

UNIVERSITY OF NAPLES FEDERICO II

DEPARTMENT OF PHARMACY



PhD in Pharmaceutical Science – XXXII cycle

**Calorimetric and spectroscopic
investigation of biomolecules for
therapeutic applications**

PhD Thesis

Federica D’Aria

Tutor:
Prof. CONCETTA GIANCOLA

PhD Coordinator:
Prof. MARIA VALERIA D’AURIA

ABSTRACT

Molecular recognition is the key for all biological processes. Such phenomena can be either intermolecular, as for the binding of a ligand to a macromolecule, or intramolecular, as for the denaturation of proteins or nucleic acids. In recent decades, DNA-ligand, protein-ligand or protein-DNA interactions have been the subject of numerous physico-chemical studies. The understanding of the energetics both of biomolecules stability and of their binding with other (bio)molecules is extremely interesting in biochemistry, biotechnology, and especially in the pharmaceutical field for a targeted structure-based drug design.

Calorimetric and spectroscopic methodologies, combined to computational studies and biological assays, are essential for drug discovery. Indeed, thermodynamic stability of macromolecules as well as the energetics of their interaction with potential drugs are an essential complement to structural data for the optimization of lead compounds.

Specifically, in this Ph.D. thesis, studies have been addressed to investigate:

- ✓ Physico-chemical factors affecting drug bioavailability (Chapter 3).
- ✓ Thermodynamic stability of G-quadruplexes (G4s) in oncogene promoters and their interactions with ligands (Chapter 4).
- ✓ Effects of epigenetic modifications on G4s stability (Chapter 5).

Chapter 3 describes how the combination of the appropriate pH, solvent, temperature, and mixing time can improve the complexation between quercetin, a natural compound characterized by interesting pharmacological activities, and hydroxypropyl- β -cyclodextrin, a commonly used drug carrier. Chapter 4 focuses on the energetics of the interaction between *KRAS* proto-oncogene G4 and new putative anticancer drugs. This study led to the identification of a series of molecules able to selectively interact with G4s and characterized by cytotoxic activity on cancer cell lines. Finally, in Chapter 5, it was investigated, through mass spectrometry experiments, the capability of two modified sequences of *KIT* proto-oncogene, containing 5-methylcytosine and 5-carboxylcytosine, to fold into G4. The results proved that, despite the epigenetic modifications, these sequences were able to fold into G4, even though with a slower kinetics, as the unmodified sequence.

LIST OF PUBLICATIONS

Paper I

“Host-guest inclusion complex of quercetin and hydroxypropyl- β -cyclodextrin”. D’Aria F., Serri C., Niccoli M., Mayol L., Quagliariello V., Iaffaioli R.V., Biondi M., Giancola C. *J Therm Anal Calorim*, **2017**, 130:451–456. doi: 10.1007/s10973-017-6135-5.

Paper II

“Thermodynamics of complex formation between hydroxypropyl- β -cyclodextrin and quercetin in water–ethanol solvents at T = 298.15 K”. Usacheva T., Kabirov D., Beregova D., Gamov G., Sharnin V., Biondi M., Mayol L., D’Aria F., Giancola C. *J Therm Anal Calorim*, **2019**, 138:417–424. doi: 10.1007/s10973-019-08136-5.

Paper III

“Selective binding of a bioactive porphyrin-based photosensitizer to the G-quadruplex from the KRAS oncogene promoter”. Caterino M., D’Aria F., Kustov A.V., Belykh D. V., Khudyaeva I. S., Starseva O. M., Berezin D. B., Pylina Y. I., Usacheva T., Amato J., Giancola C. *Int. J. Biol. Macromol.*, 2020, 145:244-251. doi: 10.1016/j.ijbiomac.2019.12.152.

Manuscript submitted

1. “Physicochemical and Biological Evaluation of Novel G-Quadruplex DNA Binders”. D’Aria F., D’Amore V.M., Di Leva F.S., Amato J., Caterino M., Russomanno P., Salerno S., Barresi E., De Leo M., Marini A. M., Taliani S., Da Settimo F., Salgado G.F., Pompili, L., Zizza, P., Shirasawa S., Novellino E., Biroccio A., Marinelli L., Giancola C. *Eur. J. Pharm. Sci.*

2. "Ligand binding to G-quadruplex DNA: new insights from ultraviolet resonance Raman spectroscopy". Di Fonzo S., Amato J., D'Aria F., Caterino M., D'Amico F., Gessini A., Brady J.W., Cesàro A., Pagano B., Giancola C. *Phys. Chem. Chem. Phys.*

LIST OF ABBREVIATIONS

A	Adenine
APS	Ammonium Persulfate
BCL2	B-cell lymphoma-2
C	Cytosine
CD	Circular Dichroism
CDs	Cyclodextrins
CHCA	α -Cyano-4-HydroxyCinnamic Acid
c-KIT	cellular- Receptor tyrosine kinase
c-MYC	cellular- MYeloCytomatosis
C_p	Heat Capacity
ΔH°_{cal}	Calorimetric enthalpy
ΔH°_{VH}	Van't Hoff enthalpy
ΔS°	Change in entropy
ΔG°	Change in Gibbs free energy
DAPI	4',6-diamidino-2-phenylindole
DDW	Double-Distilled Water
DMEM	Dulbecco Modified Eagle Medium
DMSO	Dimethyl Sulfoxide
DNA	Deoxyribonucleic Acid
DNMTs	DNA methyltransferases
DS	Degree of Substitution
DSC	Differential Scanning Calorimetry
ECL	Enhanced Chemi-luminescence
EI	Electronic Ionization
ELISA	Enzyme-linked Immunosorbent Assay
ESI	Electrospray Ionization
F	Folded
FAM	6-carboxyfluorescein

FBS	Fetal Bovine Serum
FRET	Förster Resonance Energy Transfer
G	Guanine
G4	G-quadruplex
GAPs	GTPases Activating Proteins
GEFs	Nucleotide Exchange Factors
HIF-1 α	Hypoxia-Inducible Factor 1-alpha
HP β CD	Hydroxypropyl- β -cyclodextrin
HPLC	High Performance Liquid Chromatography
HSP70	Heat Shock Protein 70
hTERT	Telomerase Reverse Transcriptase
INS	Insulin gene
ITC	Isothermal Titration Calorimetry
KRAS	Kirsten RAt Sarcoma viral oncogene homolog
MALDI	Matrix-Assisted Laser Desorption Ionization
MD	Molecular Dynamics
MW	Microwaves
NHE	Nuclease Hypersensitive Elements
NMR	Nuclear Magnetic Resonance
PAGE	Polyacrylamide Gel Electrophoresis
PBS	Phosphate Buffer Solution
PCR	Polymerase Chain Reaction
PDAC	Pancreatic Ductal Adenocarcinoma
PDT	Photodynamic Therapy
PID	Proportional Integral Derivative
QCT	Quercetin
RESP	Restrained Electrostatic Potential
RNA	Ribonucleic Acid
ROS	Reactive Oxygen Species
RT	Reverse Transcription
RT	Room Temperature
qRT-PCR	Real-Time quantitative Polymerase Chain Reaction
SD	Standard Deviation
SDS	Sodium Dodecyl Sulfate

SP	Standard Precision
SPR	Surface Plasmon Resonance
SV40	Simian Virus 40
T	Thymine
T _m	Melting Temperature
TAM	Thermal Activity Monitor
TAMRA	6-carboxytetramethylrhodamine
TED	Semiconducting Thermoelectric Devices
TEMED	Tetramethylethylenediamine
TMS	Tetramethylsilane
TLC	Thin Layer Chromatography
TOF	Time Of Flight
TSC	Sclerosis Tuberos Complex
TSS	Transcription Start Sites
Un	Unfolded
U	Uracil
VEGF	Vascular Endothelial Growth Factor
VS	Virtual Screening
WB	Western Blotting
WHO	World Health Organization

TABLE OF CONTENTS

ABSTRACT	I
LIST OF PUBLICATIONS	II
LIST OF ABBREVIATIONS	IV
CHAPTER 1 INTRODUCTION	1
1.1 Natural substances in anticancer therapy	1
1.1.1 Quercetin	2
1.1.2 Cyclodextrins	3
1.2 Nucleic Acids.....	5
1.2.1 Non-canonical DNA structures	7
1.2.2 G-quadruplexes	8
1.2.3 G-quadruplexes in telomeres and oncogene promoters	11
1.2.4 KRAS G4	12
1.2.5 Targeting G4 structure in cancer cells	14
1.3 Epigenetics of G4s	15
1.4 Aims and objectives.....	16
CHAPTER 2 METHODS	18
2.1 Circular Dichroism	18
2.2 Fluorescence Spectroscopy	21
2.3 Differential Scanning Calorimetry.....	23
2.4 Electrophoresis.....	27
2.5 Mass Spectrometry	29
CHAPTER 3 PHYSICO-CHEMICAL FACTORS AFFECTING DRUG BIOAVAILABILITY	32
3.1 A calorimetric study of host-guest inclusion complex between quercetin and hydroxypropyl- β -cyclodextrin (Paper I)	33
3.1.1 Introduction	33
3.1.2 Results and discussion	35
3.1.3 Conclusions	39
3.1.4 Experimental section.....	40

3.2 Thermodynamic studies of complex formation between hydroxypropyl- β -cyclodextrin and quercetin in water–ethanol solvents at T = 298.15 K (Paper II)	43
3.2.1 Introduction	43
3.2.2 Results and discussion	44
3.2.3 Conclusions	51
3.2.4 Experimental section	52
CHAPTER 4 THERMODYNAMIC STABILITY OF G4S IN ONCOGENE PROMOTERS AND THEIR INTERACTIONS WITH LIGANDS	55
4.1 Study on the interaction of G-quadruplex from the <i>KRAS</i> promoter and bioactive porphyrin-based photosensitizers	56
4.1.1 Introduction	56
4.1.2 Results and discussion	59
4.1.3 Conclusions	67
4.1.4 Experimental section	68
4.2 Discovery, Synthesis, Physicochemical Studies and Biological Evaluation of Novel Ligands Targeting the G-Quadruplex in the <i>KRAS</i> Proto-oncogene	72
4.2.1 Introduction	72
4.2.2 Results and discussion	73
4.2.3 Conclusions	88
4.2.4 Experimental section	89
CHAPTER 5 EFFECTS OF EPIGENETIC MODIFICATIONS ON G4S STABILITY	100
CONCLUSIONS	107
REFERENCES	110

Chapter 1

INTRODUCTION

1.1 Natural substances in anticancer therapy

Cancer is one of the major causes of death worldwide. New cancer diagnoses are about 12 million each year, and about 9.6 million people in 2018 died from this disease in the world. Currently, cancer represents the second cause of death after cardiovascular diseases. According to the World Health Organization (WHO), the most lethal kinds of cancer recognized to date are the cancer of lung (1.76 million deaths), liver (782,000 deaths), stomach (783,000 deaths), colon and rectum (862,000 deaths) and breast (627,000 deaths) (World Health Organization, 2018). There are different possibilities for the treatment of cancer, such as surgery, radiotherapy, chemotherapy and immunotherapy; these options can also be used in combination, simultaneously or sequentially.

In particular, chemotherapy is based on the use of antineoplastic drugs which can be administered by different routes (intravenously, orally, etc.) and aims at killing tumor cells. Ideally, an anticancer drug should perform its cytotoxicity selectively against the tumoral tissue. However, many anticancer drugs have low therapeutic indices and generally lack specificity; consequently, they are toxic to both cancer and normal cells, and cause strong non-specific side effects, such as myelosuppression, immunosuppression, gastrointestinal problems (e.g. nausea and vomiting), cardiotoxicity (myocardial ischemia, arrhythmias, more or less severe heart failure) and nephrotoxicity (Sissons, 1953; Przystupski et al., 2019). For this reason, in the last years, complementary and innovative medicines such as gene therapy, immunotherapy, targeted therapy, neoadjuvant therapy, and natural products, have become valid alternatives to replace classic anticancer drugs.

Especially, natural products are proven effective in patients with advanced cancer, due to their efficacy and low toxicity. The use of natural extracts from plant or animal sources, particularly in medical practice, dates back to ancient times; but it is only in the eighteenth century that the manipulation of these extracts led to the isolation of the first chemically pure substances. Recent research works indicated that natural substances could provide additional

strategies for monotherapy or combination treatments of various cancer types. Indeed, more than 60% of the current anticancer chemotherapeutic drugs used in clinic were initially developed from natural products. These substances are able to intervene at different levels in tumor growth processes: some compounds behave by preventing the activation of carcinogenic compounds; other molecules hinder the formation of blood vessels that lead to the development of cancer; still others act by stimulating the cell death of cancer cells; finally the antioxidant activity of some substances helps to counteract the onset of tumors. So, in conclusion, natural products, combined with conventional chemotherapy and radiotherapy, may enhance anticancer therapeutic efficacy and reduce the side effects (Yue et al., 2017).

1.1.1 Quercetin

In the frame of natural products used in the therapeutic field, one of the best-known phytochemical groups are the flavonoids (Lee et al., 2015). They are a class of polyphenolic compounds found in nature, ubiquitously present in photosynthesizing cells (Saito, 1974; Salunkhe et al., 1983). Flavonoids are present in fruits, vegetables, and plant-derived beverages such as tea and wine (Hertog et al., 1993). Many of them share a common three-ring structure of which two rings are aromatic and one ring is heterocyclic. The variation in the heterocyclic ring allows flavonoids to be classified in various subclasses, i.e. the flavones, isoflavones, flavonols, flavanals, flavanones, anthocyanidins and chalcones (Scalbert and Williamson, 2000). Quercetin (QCT) (3,3',4',5,7-pentahydroxyflavone) is one of the most abundant flavonoids found in many fruits and vegetables, such as broccoli, yellow onions, and apples (Boots et al., 2008). The molecular structure of quercetin is shown in Figure 1.1.

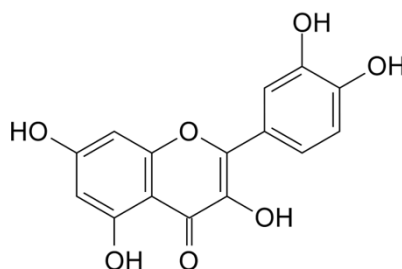


Figure 1.1. Molecular structure of quercetin.

Quercetin has antihistamine, anti-inflammatory, antiviral, immunomodulatory, and antioxidant properties (Liu et al., 2017). In recent years, more attention has focused on its

antitumor activity against different kind of tumor, including thyroid cancer, pancreatic tumor, breast cancer, hepatocellular carcinoma, prostate cancer, and gastric carcinoma cells (Lee et al., 2002; Liu et al., 2017). It has been reported that quercetin inhibits several key signaling components in cancer cells, including PI3K/Akt/mTOR, GSK-3 β , NF κ B, and heat shock protein 70 (HSP70) (Johnson et al., 2011; Wang et al., 2011). Its biological properties are based on different mechanisms like cell cycle regulation, tyrosine kinase inhibition, AMPK-Sclerosis Tuberous Complex (TSC) activation and AKT-mTOR axis inhibition (Lu et al., 2010). Recently, quercetin has been shown to inhibit self-renewal capacity of putative pancreatic cancer stem cells (Zhou et al., 2010). In other studies quercetin suppressed local and distant tumor growth and prolonged survival in murine pancreatic cancer models (Mouria et al., 2002). Furthermore, quercetin has been recently reported to have synergistic effects when combined with chemotherapeutic agents such as cisplatin, which may further improve the outcomes of the traditional chemotherapy (Brito et al., 2015a).

1.1.2 Cyclodextrins

The first reference to a molecule later identified as cyclodextrin was published by Villiers in 1891. He described a bacterial digest that he had isolated from starch (Villiers, 1891). Later, the Austrian microbiologist Franz Schardinger described two crystalline compounds that he had isolated from a bacterial digest of potato starch, α -dextrin and β -dextrin (Schardinger, 1903), now commonly called cyclodextrins (CDs). Cyclodextrins comprise a family of three well-known industrially produced major, and several rare, minor cyclic oligosaccharides. The three main cyclodextrins, α -CD, β -CD and γ -CD, are crystalline, homogeneous, non-hygroscopic substances, which contain six (α -CD), seven (β -CD) or eight (γ -CD) (α -1,4) α -d-glucopyranose bound. Due to the chair conformation of the glucopyranose units, the CDs take the shape of a truncated cone (Brewster and Loftsson, 2007).

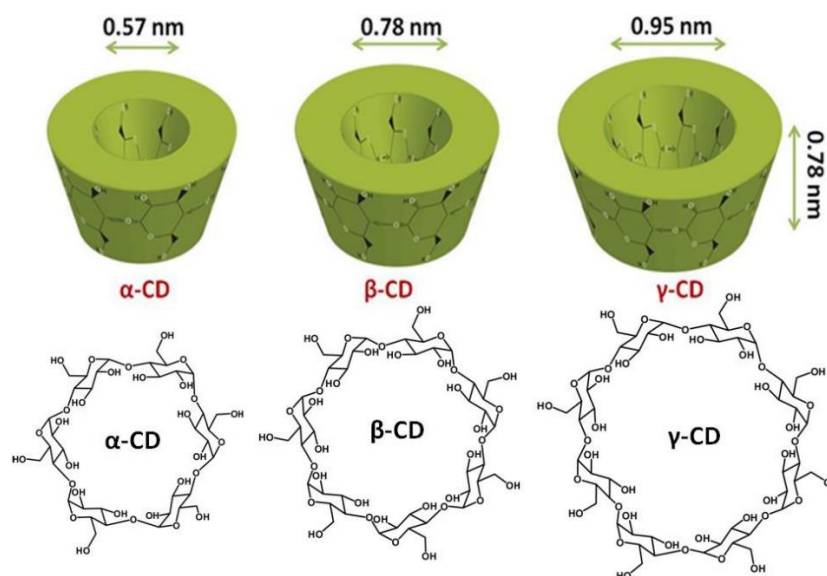


Figure 1.2. Structure and approximate geometric dimensions of α , β , and γ -CD molecules.

Because of the 4C_1 conformation of the glucopyranose units, the hydroxyl functions are orientated to the cone exterior with the primary hydroxyl groups of the sugar residues at the narrow edge of the cone and the secondary hydroxyl groups at the wider edge. The central cavity of a CD molecule has a relatively lipophilic character conferred by its coating of skeletal carbons and ethereal oxygen of the glucose residue (Lichtenthaler and Immel, 1996). Natural CDs, in particular β -CD, have a limited solubility in water, which means that the complexes resulting from the interaction of lipophilic molecules with cyclodextrins can also be poorly soluble (Brewster and Loftsson, 2007). This is believed to be due to the relatively strong intramolecular hydrogen bond in the crystal lattice. The modified cyclodextrin that has received the most attention in recent years is hydroxypropyl- β -cyclodextrin (HP β CD) in which the substitution of any of the hydroxyl groups forming the hydrogen bond with a lipophilic function, causes a considerable improvement in its solubility in water (Stella and Rajewski, 1997; Szente, 1999).

The most important pharmaceutical application of HP β CD is to complex with, and enhance the solubility of, poorly water-soluble molecules. In aqueous solution indeed, the energetically unfavored, high-enthalpy water molecules in the slightly apolar cavity of the cyclodextrin (the “host”) can be promptly replaced by appropriate “guest molecules” that are less polar than water. One, two or three cyclodextrin molecules contain one or more trapped “host” molecules. More frequently the host-guest ratio is 1:1 (Szejtli, 1998).

1.2 Nucleic Acids

Nucleic acids are biological macromolecules that play fundamental roles in cells and ensure the normal development and functioning of an organism. The most important known nucleic acids are the deoxyribonucleic acid (DNA), which contains the genetic information necessary for the biosynthesis of RNA and proteins, and the ribonucleic acid (RNA), implicated in various biological roles of coding, decoding, regulation and gene expression. The DNA is composed of different nucleotides corresponding to a phosphate group link to sugar with one of the four bases attached. The bases of DNA divide into two groups: purines [adenine (A) and guanine (G)] and pyrimidines [thymine (T) and cytosine (C)]. In RNA, thymine is replaced by uracil (U).

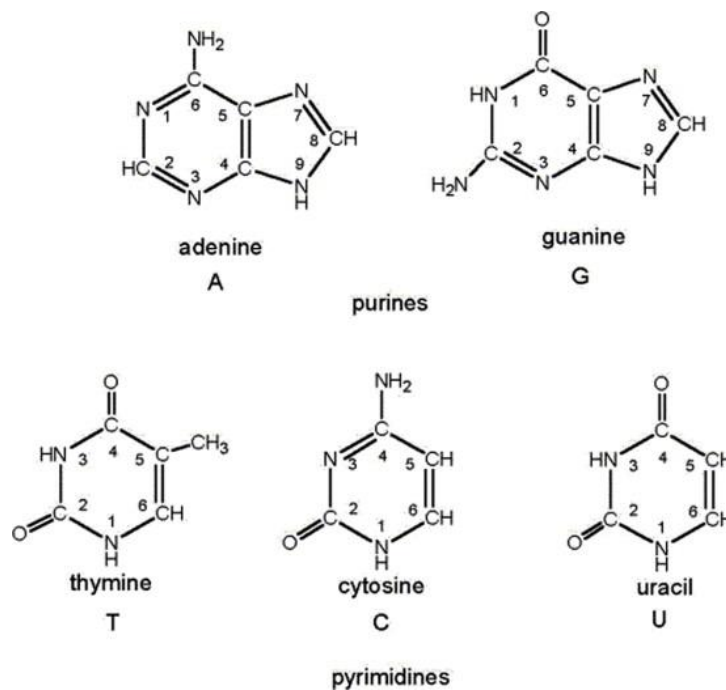


Figure 1.3. Chemical structure of different bases implicated in DNA or RNA composition.

In 1953 Watson and Crick proposed their model of the DNA double helix (Watson and Crick, 1953) which led to the current knowledge about DNA.

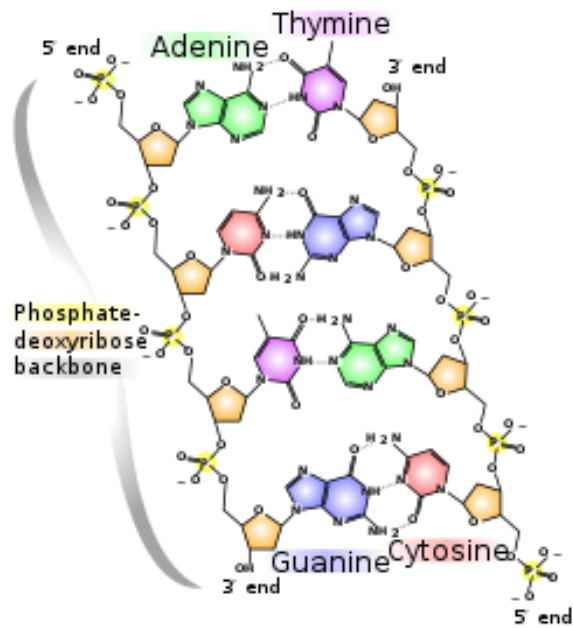


Figure 1.4. Schematic representation of base pairing in the DNA structure, discovered by Watson and Crick.

In the DNA structure, the phosphate backbone is outward facing with bases inside the structure and allowing formation of hydrogen bonds. A is complementary to T and they are linked with two hydrogen bonds and C is complementary to G with three hydrogen bonds.

Thus, all two base pairs fit neatly into the double helix. The two strands are antiparallel, with the 5'-end of one strand adjacent to the 3'-end of the other. The two strands coil around each other to form a right-handed double helix, with the base pairs in the center and the sugars and negatively charged phosphates forming the external hydrophilic backbone. The stability of the duplex derives from both base stacking and hydrogen bonding.

The model proposed by Watson and Crick was a right-handed helix reflecting the most abundant form in living cells, now known as B-DNA, whose “canonical” configuration has a broad major groove and a narrow minor groove running around the helix along the entire length of the molecule. Two additional DNA conformations have been subsequently identified, the compact A-DNA with shorter helix twisting and wider section due to the fact that it is found in dehydrated environment, and the “non-canonical”, transient, and left-handed Z-DNA (Shakked et al., 1989).

1.2.1 Non-canonical DNA structures

Under certain conditions, nucleic acids can adopt non-canonical conformations other than B-DNA. These unusual DNA structures can involve from one to four nucleic acid strands, that may arrange into hairpins, cruciform, parallel-stranded duplexes, triplexes (H-DNA), G-quadruplex (G4), i-motif and other non-B forms (Figure 1.5). It has been demonstrated that these structures are widely distributed throughout the human genome, and are enriched in critical regions (Bacolla and Wells, 2009; Biffi et al., 2013). In addition, their formation depends on the specific DNA sequence.

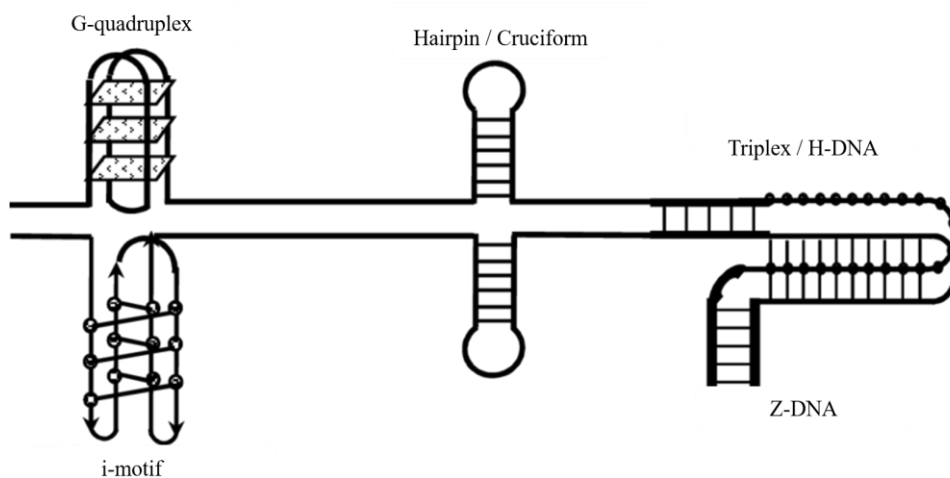


Figure 1.5. Schematic illustration showing some examples of non-canonical DNA structures.

Hydrogen bonds implicated in these structures can be Watson-Crick hydrogen bonding corresponding to the base pairing known in their helix structure but also arranged in a different configuration called Hoogsteen hydrogen bonding; in this type of hydrogen bonds, A and G are flipped and even if one of the two hydrogen bonds was identical to the one described by Watson and Crick, the other one implicated different atoms on another face of the adenine or guanine.

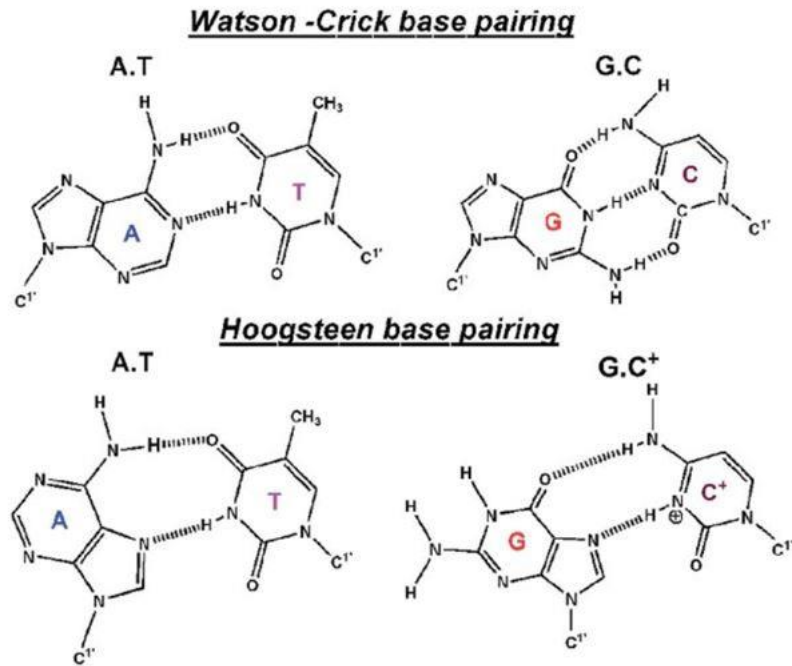


Figure 1.6. Differences between Watson-Crick base and Hoogsteen base pairing.

1.2.2 G-quadruplexes

G4s had been first suspected when Bang (Bang, 1910) observed that concentrated guanylic acid solutions form a gel, indicative of high-order structures. Gellert et al. had later proved that guanylic acid assembles into tetrameric structures by X-ray diffraction (Gellert et al., 1962). Interest in G4s has dramatically increased in recent years since when they have been proved to actually exist *in vivo* within important genome functional units (Lipps and Rhodes, 2009; Biffi et al., 2013). G4s are indeed found in telomeres and oncogene promoters, which implicates them in genome stability maintenance, gene expression and cell cycle regulation. G4s have been consequently suggested as possible targets in a novel anticancer strategy based on stabilizing G4s by small ligands (Hurley et al., 2000).

These structures are characterized by the stacking guanine quartets, known as G-tetrads, formed by a planar arrangement of four guanines stabilized by Hoogsteen hydrogen bonding and by the coordination of monovalent cations, preferentially Na^+ and K^+ (Figure 1.7) in the inner channel.

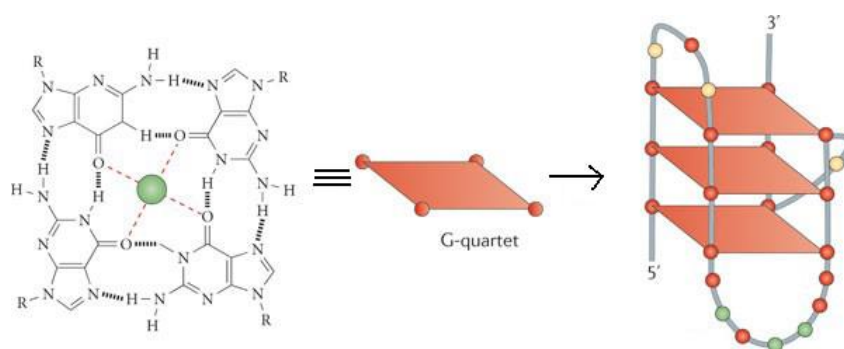


Figure 1.7. Schematic representation of the G-quartet and G quadruplex.

G4s can be classified on the basis of: 1) the number of strands; 2) the pattern of strand orientation; 3) the conformation of guanine glycosidic torsion angles; 4) the orientation of the loops (Burge et al., 2006). G4s can be unimolecular, when a single strand folds back on itself, bi- or tetra-molecular when formed by two or four strands, respectively. Then, there are four different possibilities for the relative strand orientations in the G-tetrad core:

- a) four strands are oriented in the same direction (designated a parallel-stranded core) (Figure 1.8 a);
- b) three strands are oriented in one direction and the fourth in the opposite direction (designated a “3+1” core, or hybrid core in the literature (Figure 1.8 b);
- c) two neighboring strands are oriented in one direction and the two remaining strands in the opposite direction (designated an up–up–down–down core, also called an antiparallel-stranded core in the literature - Figure 1.8 c);
- d) two strands across one diagonal are oriented in one direction and the two remaining strands across the other diagonal in the opposite direction (designated an up–down–up–down core, also called an antiparallel-stranded core in the literature) (Figure 1.8 d) (Phan, 2010).

Moreover, G-tetrads are linked by loops, which are divided in four groups (Bochman et al., 2012): 1) lateral loop, connecting two adjacent antiparallel strands (Figure 1.8 e); 2) diagonal loop, connecting two opposing antiparallel strands across the G4 plane (Figure 1.8 f); 3) double-chain-reversal loop or propeller loop, connecting two adjacent parallel strands (Figure 1.8 g); 4) V-shaped loop, connecting two corners of a G-tetrad core in which a support column is missing (Figure 1.8 h) (Dvorkin et al., 2018).

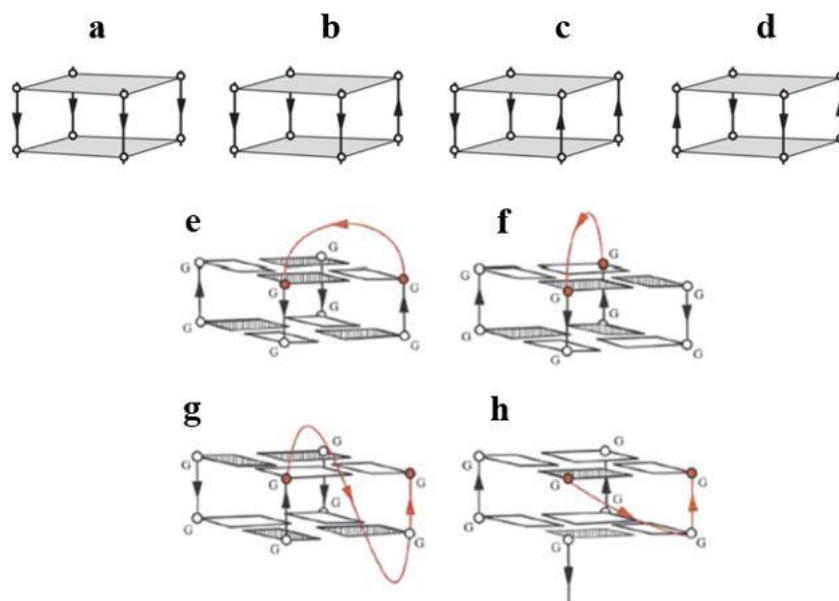


Figure 1.8 (a–d) Four types of G-tetrad cores: (a) parallel G-tetrad core, (b) (3 + 1) G-tetrad core, (c) antiparallel G-tetrad core (up–up–down–down) and (d) antiparallel G-tetrad core (up–down–up–down). (e–h) Four types of loops (colored red): (e) lateral loop, (f) diagonal loop, (g) double-chain-reversal loop and (h) V-shaped loop. Arrows indicate the strand orientations, from 5' to 3' direction.

Loops are usually short (1-7 nucleotides) and shorter loops result in more stable G4s (Williamson et al., 1989; Bugaut and Balasubramanian, 2008; Huppert, 2008; Guédin et al., 2010).

Finally, in a G-tetrad, guanosine may have two conformations: *anti* (Figure 1.9 a) and *syn* (Figure 1.9 b), determined by the rotation of the base around the N-glycosidic bond formed between N9 and C1'.

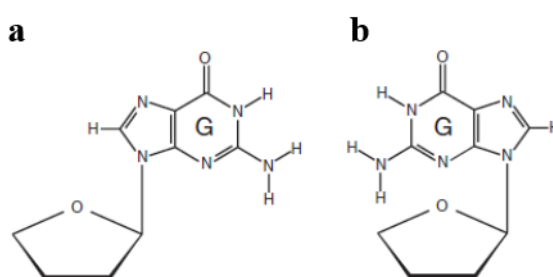


Figure 1.9: (a) *anti* conformation; (b) *syn* conformation.

Parallel quadruplexes have all the guanine glycosidic angles in *anti*-conformation, whereas antiparallel G4s have both *syn* and *anti*.

All G4s have four grooves, which are the cavities delimited by the phosphodiester backbone. Groove dimensions vary and depend on the G4 overall topology and loops nature. If all strands

are parallel, and guanosine angles are in *anti*-conformation, grooves are identical and medium-sized. If strand orientation is *syn-syn-anti-anti*, two grooves are medium-sized, one narrow-sized and one wide-sized. Lastly, if strand orientation is *syn-anti-syn-anti*, two grooves are narrow and the other two ones are wide (Burge et al., 2006; Dvorkin et al., 2018).

1.2.3 G-quadruplexes in telomeres and oncogene promoters

The proof of G4s formation *in vivo* was first observed in telomeric DNA. The first evidence was obtained *in vitro* using specific antibody for intermolecular telomeric G4 DNA of the ciliate *Stylonychia lemnae* (Schaffitzel et al., 2001). Further evidence was achieved observing that telomere end-binding proteins control the formation of G4 DNA structures *in vivo* (Paeschke et al., 2005). Telomeres are at the end of eukaryotic chromosomes and are essential for chromosomal stability and genomic integrity. Their structure and stability directly relate to cancer growth, aging and genome stability (Bodnar, 1998; Hackett et al., 2001; Neidle and Parkinson, 2002). Telomeric DNA ends are composed of both duplex and guanine-rich, 3'-overhang segments that can form G4s. Telomeres protect genome from chromosomal erosion during cell divisions and their length progressively decreases after each round of cell replication in healthy cells (Sfeir et al., 2005). The holoenzyme telomerase, a ribonucleoprotein complex with reverse transcriptase activity, elongates telomeres and is upregulated in 80-85% of human cancer cells (Greider and Blackburn, 1985; Kim et al., 2011). Bioinformatic sequence analyses have noticed that such putative G4-forming sequences are present in the genomes of different organisms (Todd et al., 2005; Rawal, 2006; Hershman et al., 2008). There is an estimate of ~700000 potential G4-forming sequences in the human genome as seen by *in silico* analyses using two different algorithms (Huppert, 2005). Gene promoters (~1 kb upstream of transcription start sites (TSS)) are particularly enriched in putative G4 motifs. G4s within gene promoters are now proved to be involved in transcription regulation (Huppert and Balasubramanian, 2007; Patel et al., 2007). The first evidence supporting the existence of unusual form of DNA in promoters dates back to 1982 and based upon the nuclease hypersensitivity of promoter elements (NHE) in the chicken β -globulin gene (Larsen and Weintraub, 1982). This form was only later associated with guanines runs G4-forming sequences have been located in promoters of genes involved in cell growth and proliferation (Rustighi et al., 2002). G4s have been reported within the promoter of several genes, like insulin (Hammond-kosack et al., 1992), *MYC* (Simonsson et al., 1998; Siddiqui-Jain et al., 2002),

VEGF (Sun, 2005), *HIF-1 α* (Armond et al., 2005), *RET* (Guo et al., 2007), *BCL-2* (Dai et al., 2006), *KIT* (Rankin et al., 2005; Fernando et al., 2006) and *KRAS* (Cogoi et al., 2004).

It has been shown that G4 formation is higher in proto-oncogene than in tumor-suppressor genes (Eddy and Maizels, 2006).

All of the available G4 structures from gene promoters have been solved using NMR and X-ray techniques (Ambrus et al., 2005; Dai et al., 2006; Phan et al., 2007; Wei et al., 2012; Agrawal et al., 2013; Marquevielle et al., 2018).

In contrast to the tandem repeats in the human telomeres, the G-rich sequences within gene promoters are often composed by G-tracts with unequal number of guanines and varying number of intervening bases. They may also contain more than four G-tracts. Each of these promoter sequences is unique in its number and length of G-tracts and intervening bases (Qin and Hurley, 2008). The promoter sequences can possibly form multiple G4s using different combinations of the G-tracts and are often a mixture of multiple conformations and loop isomers.

The G₃NG₃ (where N is whatever base) sequence is prominent in G4s from gene promoters. This motif forms a parallel-stranded G4 with a 1-nt, double-chain-reversal loop. The G₃NG₃ motif is so widespread that it has been proposed to be essential in forming a stable core in the intramolecular promoter G4s (Yang and Okamoto, 2010).

	G ₃ NG ₃				G ₃ NG ₃				
Myc2345	5'-	GGG	T	GGG	GA	GGG	T	GGG	-3'
Myc1245	5'-	GGG	A	GGG	TGGGGA	GGG	T	GGG	-3'
VEGF	5'-	GGG	C	GGG	CCGG	GGG	C	GGG	-3'
HIF-1a	5'-	GGG	A	GGG	AGAGG	GGG	C	GGG	-3'
RET	5'-	GGG	C	GGG	GCG	GGG	C	GGG	-3'
c-kit21	5'-	GGG	C	GGG	CGCGA	GGG	A	GGG	-3'
Bcl2Mid	5'-	GGG	CGC	GGG	AGGAAGG	GGG	C	GGG	-3'
Telomere	5'-	GGG	T	TAGGG	TTA	GGG	T	TAGGG	-3'

Figure 1.10. Comparison of G4-forming sequences in selected gene promoters. The telomeric sequence is also shown as a comparison. All the promoter G-rich sequences shown contain the G₃NG₃ motif; except for the BCL-2 (Bcl2Mid) sequence, they have all been shown to form parallel-stranded G-quadruplexes (Yang and Okamoto, 2010).

1.2.4 KRAS G4

Among G4-forming sequences in gene promoter regions particularly interesting is the one formed in promoter regions of *KRAS*.

KRAS encodes for the homonymous, 21 kDa GTPase that exists in two states: the active GTP-bound state and the inactive GDP-bound state. The GTPase activity is regulated positively by nucleotide exchange factors (GEFs) and negatively by GTPases activating proteins (GAPs). In the GTP-bound state, cell receives signals of proliferation, survival and differentiation (Lavrado et al., 2015; Miglietta et al., 2017).

The *KRAS* proto-oncogene is overexpressed in 30% of all human cancers and in up to 95% of pancreatic ductal adenocarcinoma (PDAC) cases (Cogoi et al., 2013). In detail, *KRAS* has a central role in controlling PDAC initiation and progression (Kang et al., 2017).

The *KRAS* promoter contains a G-rich NHE, between nt -327 and -296, which is essential for transcription. This sequence has six G-tracts and is able to form several G4 conformations (Cogoi et al., 2008; Boschi et al., 2016).

Inside the *KRAS* promoter there is a G-rich, 22-mer sequence (Figure 1.11 a) that forms a unimolecular parallel G4 (*KRAS* G4), which can be stabilized by the 16G>T mutation (Figure 1.11 b).

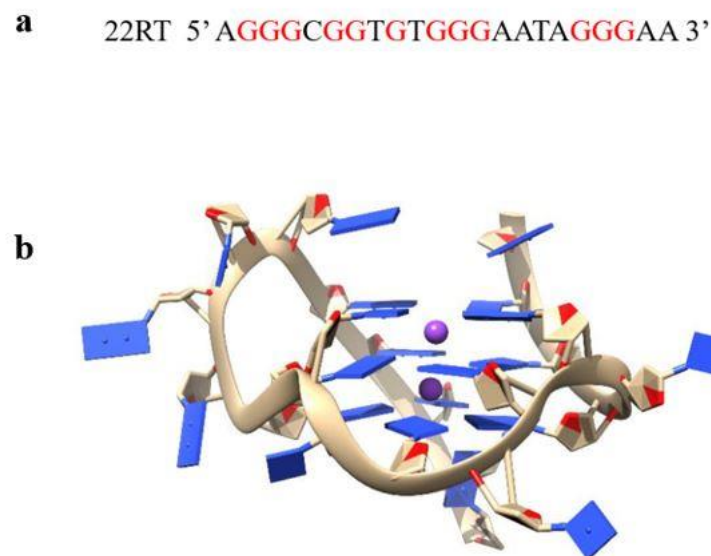


Figure 1.11. (a) *KRAS* 22-mer sequence; (b) *KRAS* G4

The *KRAS* G4 structure has recently been solved using NMR technique (Kerkour et al., 2017) and has been deposited in the Protein Data Bank (PDB Code 5I2V). It presents three G-tetrads linked through as many loops, one medium and two short double-chain-reversal loops. There are four grooves of medium size. The structure is stabilized by two K⁺ counterions coordinated between the three G-quartet planes.

1.2.5 Targeting G4 structure in cancer cells

Considering that G4s are implicated in several important biological processes, interfering with them could be worth exploring in order to find new possible therapeutic targets.

Indeed, in the last decade, G4s in oncogene promoters have also been considered as potential new targets for anticancer therapies, relying on the idea that the overexpression of oncogenes containing potential G-quadruplex structures can be deactivated by G4-binding ligands *in vivo* (Figure 1.12) (Siddiqui-Jain et al., 2002).

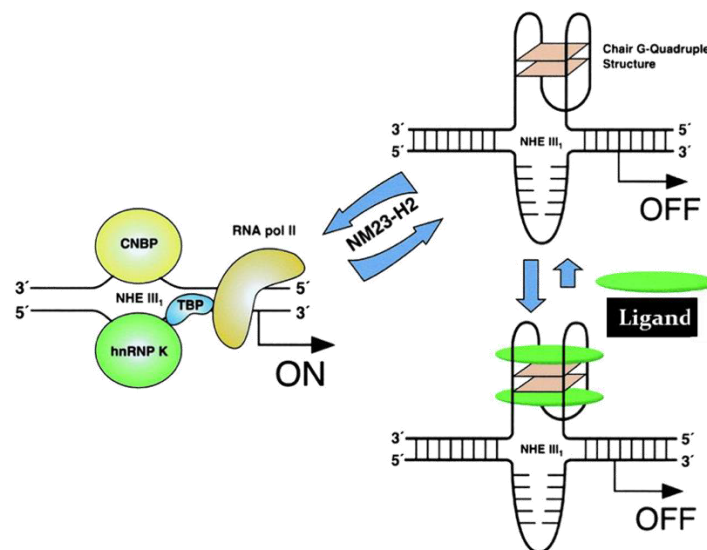


Figure 1.12. Targeting G4 to stop transcription

In these years, many molecules have been identified as ligands for G4 structures. The majority of G4 ligands in literature contains a polycyclic hetero-aromatic core able to stack with the G-tetrads, a basic side chain that interacts with the grooves/loops and the negatively charged phosphate backbone of G4 (Yang and Okamoto, 2010). The most important known G4-ligands of this kind are BRACO 19 (Figure 1.13 a) (Gowan et al., 2002), the porphyrins, among which TmPyP4 (Figure 1.13 b) (Grand et al., 2002), Pyridostatin (Figure 1.13 c) (Rodriguez et al., 2008), RHPS4 (Figure 1.13 d) (Leonetti, 2004; Phatak et al., 2007; Salvati et al., 2007) and Telomestatin (Figure 1.13 e) (Sun et al., 1997). In this frame, the Quarfloxin, a specific G4 ligand for *MYC* G4, is the first quadruplexes ligand to enter human clinical trials, even if it did not finish Phase II (Drygin et al., 2009; Brooks and Hurley, 2010). A derivative compound CX-5461 has been designed and show similar mechanism by inhibiting DNA replication and protein

translation implicating Pol I. This compound is now in advanced phase I clinical trials (Xu et al., 2017).

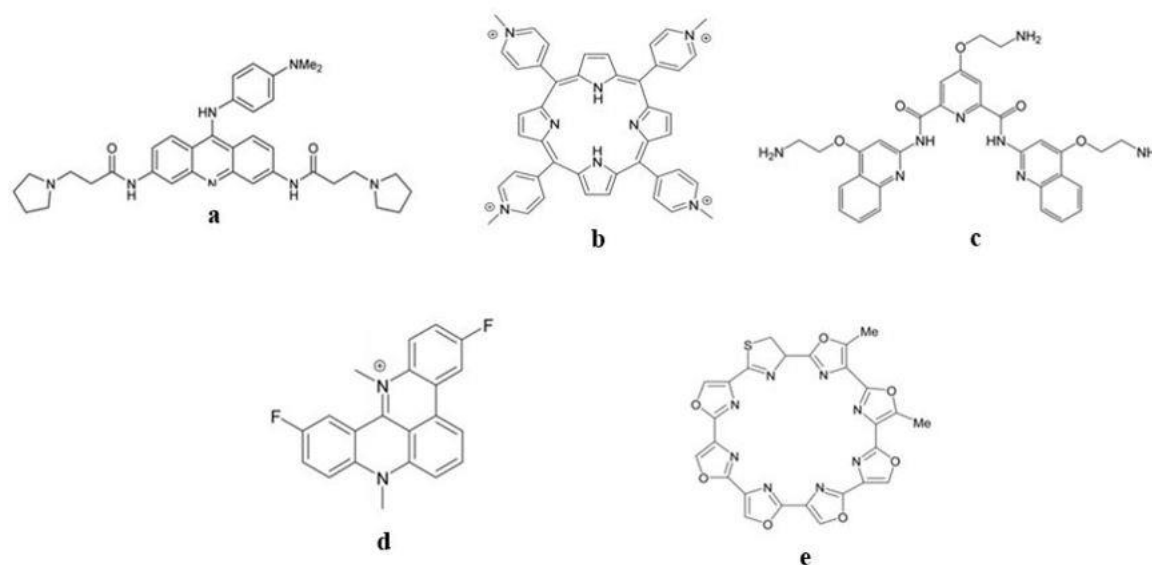


Figure 1.13. Structure of (a) BRACO19, (b) TmPyP4, (c) Pyridostatin, (d) RHPS4, and (e) Telomestatin.

1.3 Epigenetics of G4s

In the last years, G4s involvement in genomic instability has been found due to epigenetic factors. Indeed, numerous documents reported in the literature correlate the non-canonical G4 structures to epigenetic cellular processes. In this context, G4s are considered operative in pre-replication complex sites. Thousands G4 structures have been identified in human chromatin, mainly in regulatory and nucleosome-depleted regions. G4 structures are enriched in the promoters and 5' UTRs of highly transcribed genes, above all in cancer related genes and in somatic copy number amplifications (Hänsel-Hertsch et al., 2016). It is important to point out that as epigenetics influences the G4s formation and stability, likewise G4s influence epigenetic outcome. Therefore, we can consider G4 as an epigenetic event, although transient. The consequence of this linkage is a modulation not only of gene expression but of all DNA processing events, including disease onset and progression with important physiological and pathological implications (Cea et al., 2015). Specifically, DNA methylation and oxidation have been found in proximity of G4-containing strands, affecting G4 structure stability (Gros et al.,

2007; Lin et al., 2013), resulting in genomic instability that is a hallmark for many cancers. Furthermore, by interacting with DNA methyltransferases (DNMTs), or damage responders, genomic G4s contribute to nucleosome (re)positioning, histone modification, chromatin relaxation, and subsequent chromatin compaction upon replication and likely transcription (Varizhuk et al., 2019).

1.4 Aims and objectives

In that context, my research activity has been focused on the study of biomolecules for therapeutic applications through physico-chemical techniques.

On the one hand I concentrated my attention on the study of physico-chemical factors affecting drug bioavailability. The pharmacological application of several drugs is restricted by their intrinsic hydrophobicity and consequent low *in vivo* bioavailability. The therapeutic potential of small organic molecules can be unraveled by enhancing their solubility through the formation of a host-guest complex with hydroxypropyl- β -cyclodextrin. Particularly, in this thesis I focused on calorimetric studies of the host-guest inclusion complex between quercetin, a flavonoid that has many pharmacological activities, and HP β CD in water and hydroalcoholic mixtures.

On the other hand, this thesis aimed to study through physico-chemical techniques, supported by biological assays, the stability of G4 within the *KRAS* proto-oncogene and its interaction with new potential ligands. Indeed, mutations in *KRAS* are the primary cause in the development of different human cancers, particularly in the PDAC. The search for *KRAS* targeting therapies were at first based on developing direct inhibitors of *KRAS*. However, all these strategies have shown disappointing results in clinical trials because it is very difficult to design molecules able to challenge the picomolar affinity between *KRAS* and GTP/GDP. In the search for alternative strategies, the G4-forming stretch within the *KRAS* promoter turned out to be a promising target through G4 stabilization by organic ligands. For this reason, the detailed knowledge of *KRAS* G4 structure, its thermodynamics and interaction with selective ligands are essential for designing and optimizing new drugs with improved performance.

I started from two different classes of compounds. The first one was selected by Virtual Screening methodology applied to *KRAS* G4 structure and checked for their interaction with different G4s and DNA duplex. The second class of compounds has been constituted by three

water-soluble, porphyrin derivatives. The best G4-ligands were also fluorescent, allowing effective studies *in vitro* and an expected visualization in cells.

Measurements have been carried out by titration of the G4 sample with the ligand, allowing to evaluate the selectivity for G4s against DNA duplex. I used a multidisciplinary approach to study the interaction of G4s with selected drug templates, by using a combination of methodologies such as nano-calorimetry, fluorescence spectroscopy, molecular docking and biochemical assays.

This combination of techniques to the study of G4 interactions provided detailed structural and energetics information, useful to deepen the understanding of the driving forces in the molecular recognition of G4 ligand interactions under physiological conditions.

Finally, considering the crucial role of epigenetics modifications in gene regulation, the aim was to explore by mass spectrometry methodology the relationship between epigenetic modifications and the stability of the G4 in oncogene promoters. The purpose was to understand whether cytosine methylation or demethylation, influenced the ability of the sequences to fold into G4 structure.

Chapter 2

METHODS

2.1 Circular Dichroism

Circular dichroism (CD) spectroscopy is a light absorption spectroscopy that measures the difference in absorbance between the right- and left-circularly polarized light, rather than the isotropic light absorption. It is widely used to study the conformations of biomacromolecules being very sensitive to their secondary structure, and also thanks to its other advantages, like:

- very low sample amount required;
- very sensitive detection of conformational changes due to temperature, pH and solvent variations.

The electromagnetic radiation is a complex wave that propagates at the speed of light. It is made of two waves that are at right angles to each other and perpendicular to the direction of wave propagation: the magnetic (B) and the electric (E) component. Because the two components are invariably perpendicular to each other, it is an optimal approximation to consider only one of them to simplify the wave description i.e. the E-component. The wave can oscillate in any direction perpendicular to the direction of propagation. When the wave passes through a polarizer, it is polarized. Linear-polarized light occurs when the electric field vector (E) propagates in only one plane perpendicular to the direction of propagation, the direction of the vector stays constant and the magnitude oscillates (Figure 2.1A). In circularly polarized light, the E rotates around the propagation axis maintaining a constant magnitude (Figure 2.1B). Light can be circularly polarized in two directions: left and right. If the vector rotates counterclockwise when the observer looks down the axis of propagation, the light is left circularly polarized. If it rotates clockwise, it is right circularly polarized. The differential absorption of radiation polarized in two directions as function of frequency is called dichroism. For plane-polarized light this is called linear dichroism, while for circularly polarized light it is called circular dichroism.

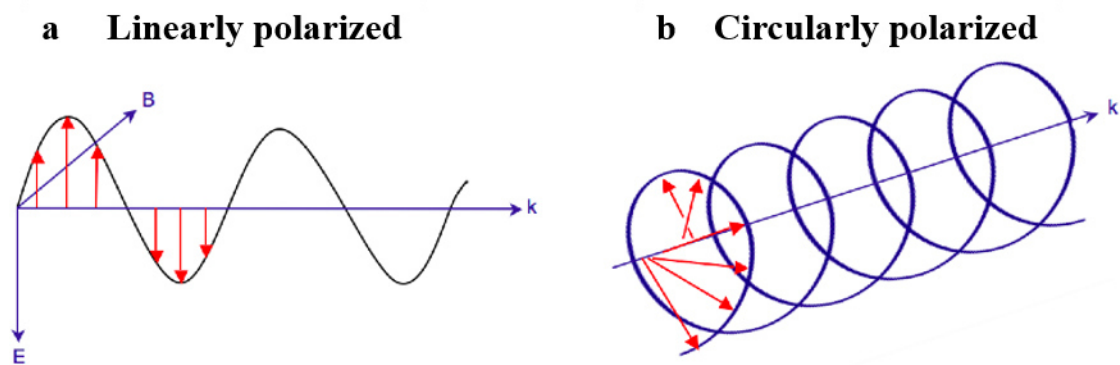


Figure 2.1. (a) linearly polarized light; (b) circularly polarized light.

Inherently asymmetric chromophores (uncommon) or symmetric chromophores in asymmetric environments interact with right- and left-circularly polarized light differently, resulting in two related phenomena. Circularly polarized light will travel through an optically active medium with different velocities due to the different indices of refraction for right- and left-circularly polarized light. This is called optical rotation or circular birefringence. Right- and left-circularly polarized light will also be absorbed to different extents at some wavelengths due to differences in extinction coefficients for the two polarized rays called circular dichroism:

$$CD = A_L - A_R \quad (1)$$

in which A_L is the absorbance of the left-polarized light, and A_R is the absorbance of the right-polarized one.

The absorbance is obtained by the Lambert-Beer law:

$$A = \epsilon l c \quad (2)$$

in which ϵ is the wavelength-dependent molar absorptivity coefficient ($M^{-1} \text{ cm}^{-1}$), l is the optical path length (cm) and c is the sample concentration (M).

During a CD measurement l and c are constant, hence the CD signal can be expressed as difference between molar absorptivity coefficients:

$$CD = \epsilon_L - \epsilon_R \quad (3)$$

An optically active sample, i.e. having different extinction coefficient toward right- and left-polarized light, introduces difference between the magnitude of the two components. The resultant E-vector no longer traces a circle over time but rather an ellipse, thus the light is elliptically polarized. Ellipticity is the unit of circular dichroism and is defined as the tangent of the ratio of the minor to major elliptical axis. The ellipticity is directly proportional to the difference between molar absorptivity coefficients of the two light components:

$$\theta = \frac{\pi\lambda(\varepsilon_R - \varepsilon_L)}{l} \quad (4)$$

in which l is the optical path and λ is the wavelength of the incident radiation.

A CD spectrum is a measure of the ellipticity vs the wavelength. The spectrum can be expressed in molar ellipticity ($[\theta]$) in order to compare spectra achieved at different concentrations:

$$([\theta]) = \frac{\theta}{[c]l} = 32.98 \Delta\varepsilon \text{ degrees } M^{-1} \text{ cm}^{-1} \quad (5)$$

A CD spectrum is recorded in the UV-Vis wavelength region. It is similar to the absorption spectrum, but it can have positive and negative bands being a difference between molar absorptivity coefficients.

The chromophores that are active to CD are intrinsically dissymmetric molecules. The dissymmetry can be structural or a consequence of the presence of a chiral center. CD can be applied only to samples that absorb in the UV-Vis region. Buffer baseline is subtracted from the CD spectrum of each sample.

For its sensitivity to stereochemical variations, CD has emerged as an important technique for studying conformational changes and supramolecular interactions. In detail, this spectroscopy has been used to investigate biological macromolecules structure and their perturbation by external factors.

Concerning the G4s, CD has been employed to study different aspects such as 3D-structures, ligand binding, kinetics of their formation and thermal melting (Randazzo et al., 2013). CD spectra of nucleic acids are very sensitive to stacking interactions between the bases. Although the topology of the folding of G4-DNA strands is very complex and many types of quadruplexes have been reported, there are three basic types of CD spectra, which have been associated to a

single specific difference in the features of the strand folding, the relative orientation of the strands, parallel (all strands have the same 5' to 3' orientation), antiparallel or hybrid.

The spectra of parallel quadruplexes have a dominant positive band at 264 nm, and a negative peak at 240 nm (Gray and Bollum, 1974; Sasisekharan, 1992). On the contrary, the spectra of antiparallel quadruplexes have a negative band at 264 nm and positive band at 290 nm (Lu et al., 1993). Finally, the spectrum of hybrid G4s is characterized not only by dominant positive bands at ~295 nm and ~265 nm, but also a negative band at ~240 nm. All these spectra present a positive band at ~210 nm (Dai et al., 2008).

2.2 Fluorescence Spectroscopy

Fluorescence spectroscopy has long been one of the most useful biophysical techniques available to scientists studying the structure and the function of biological macromolecules. Fluorescence is a spectroscopic method of analysis where the molecules are excited by irradiation at a certain wavelength and emit radiation of a different wavelength. The emission spectrum provides information for both qualitative and quantitative analysis. As shown in Figure 2.2, when light of an appropriate wavelength is absorbed by a molecule (excitation), the electronic state of the molecule changes from the ground state to one of many vibrational levels in one of the excited electronic states. The excited electronic state is usually the first excited singlet state, S1 (Figure 2.2).

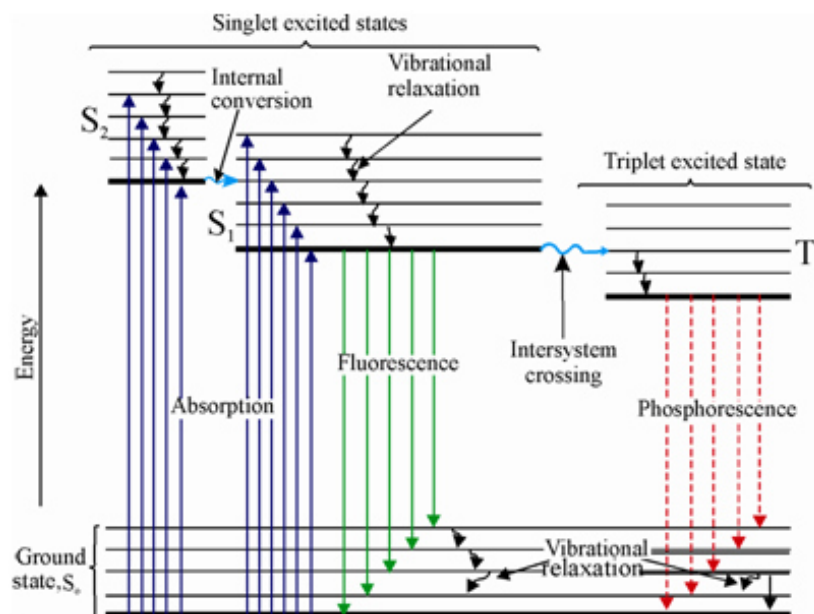


Figure 2.2. Jablonski diagram.

The fluorescence is the emission of electromagnetic radiation due to the electron transition from S_1 to S_0 . The intersystem crossing is the electron transition from S_1 to the triplet excited electronic state (T_1). The phosphorescence is the emission of radiation due to the electron transition from T_1 to S_0 . When the molecule returns to S_0 , it may be in any vibrational level and so successively a vibrational relaxation occurs.

Emission bands of a molecule have greater wavelengths compared to those of its excitation bands, it is a consequence of energy loss due to non-radiative phenomena. As a result, the fluorescence spectrum is similar to the absorption spectrum, but it is shifted to higher wavelengths and this shift is called Stokes shift.

A relevant aspect of the fluorescence is the impossibility to recover the total energy given to the molecule with the excitation. The fluorescence quantum yield (ϕ_F) provides an estimation of the energy recovered through the fluorescence process. It is defined as the ratio of the number of photons emitted to the number of photons absorbed. Possible ϕ_F values are between zero and one: the ratio is near to one if the molecule has a high fluorescence, ϕ_F is near to zero if the molecule has a low fluorescence. The fluorescent molecule is called fluorophore. Fluorophores are divided into two classes: intrinsic and extrinsic. Intrinsic fluorophores are those that occur naturally. Extrinsic are those added to a sample.

2.3 Differential Scanning Calorimetry

Differential Scanning Calorimetry (DSC) is a thermo-analytical technique in which the difference in the amount of heat required to increase the temperature of a sample and reference is measured as a function of temperature. It is the most direct and sensitive calorimetric technique used to characterize the energetics of conformational transitions of biomacromolecules and their thermal stability. DSC is a useful technique to measure, in a single measurement, thermal events such as the glass transition, melting, crystallization, cure reactions, onset of oxidation, and heats of transitions (enthalpy). In particular, the enthalpy, being a thermodynamic potential, contains information on the states to which the system can belong within the investigated temperature range (Giancola, 2008). The heat flux DSC consists of a single furnace in which the specimen and reference materials are heated or cooled together under a controlled temperature program. The sample is encapsulated in a pan, typically aluminum, and, along with an empty reference pan, sits on a thermoelectric disk surrounded by the furnace. As the furnace temperature is changed, typically at a constant rate, heat is transferred to the sample and reference.

The differential heat flow to the sample and reference is measured by area thermocouples using the thermal equivalent of Ohm's law. A material's response in a DSC is best defined by the equation below, where the amplitude of heat flow is the sum total of a heat capacity component and kinetic component of the test material.

$$q = C_p \left(\frac{dT}{dt} \right) + f(T, t) \quad (6)$$

where q = sample heat flow, C_p = sample specific heat capacity, dT/dt = heating rate, and $f(T, t)$ = kinetic response at a specific temperature, time.

The heat capacity component of the equation, $C_p (dT/dt)$, will express the specific heat capacity and changes in the heat capacity; this includes the glass transition observed in amorphous and semi-crystalline materials. Evaporation, cure reactions, crystallization, denaturation, and decomposition are expressed in the kinetic function, whereas melting, a latent heat, is an endothermic enthalpy change and may be expressed as a sum total of both heat capacity and kinetic components within the melting temperature range of a material.

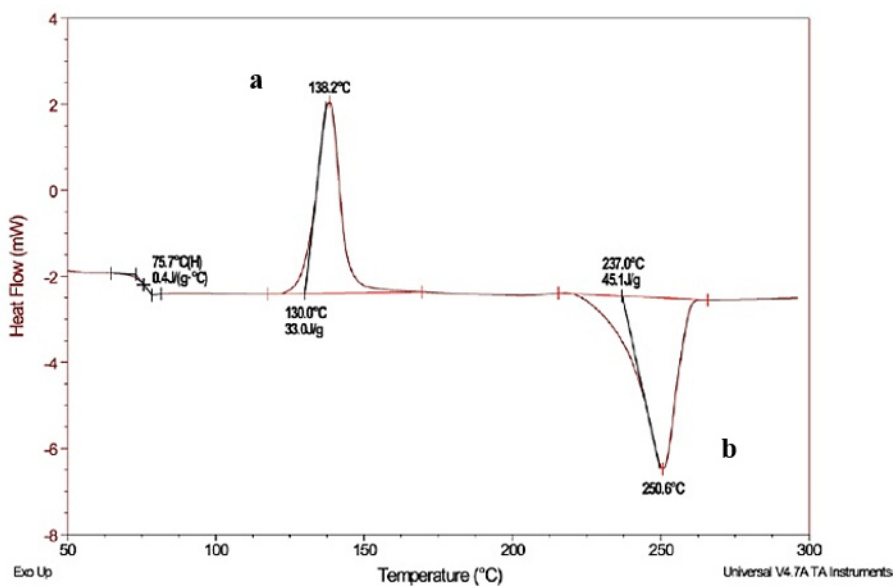


Figure 2.3 DSC thermogram (a) endothermic event (b) exothermic event.

The nano DSC, instead, consists of two cells, one for the sample and the other for the reference, with an effective volume of 300 μl . It measures the heat capacity (C_p) of a sample as a function of temperature, in comparison to a reference.

In a basic DSC experiment, the sample cell (Figure 2.4) contains a solution with the molecule of interest, while the reference cell contains only the solvent. Temperature is raised identically in the two cells at constant rate. The difference in energy required to match the temperature of the two cells is the heat either absorbed or released by molecules in the sample during a transition. These differences in input energy is a measure of molecule heat capacity.

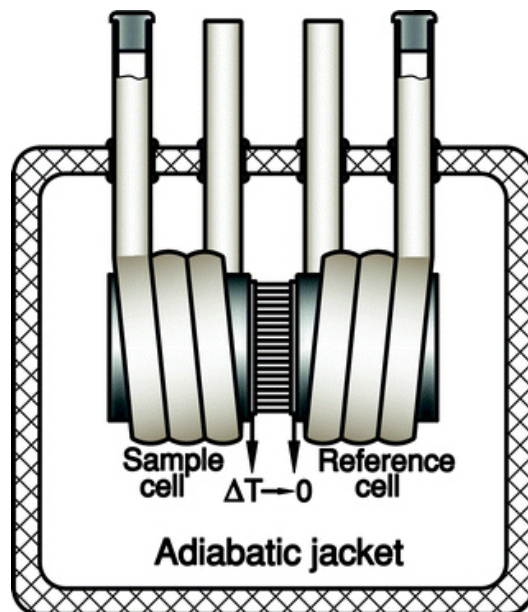


Figure 2.4. Schematic representation of a DSC cells.

An accurate buffer vs buffer (or solvent vs. solvent) baseline scan is required in this technique. A second baseline must be applied to the data to extrapolate pre- and post-transition DSC curve. The choice of this baseline is the most critical step in the analysis because it affects the value of thermodynamic parameters. Several baseline procedures are implemented in DSC software, but the simplest approach is a linear extrapolation.

After a scan sample vs. buffer, the result is a curve (Figure 2.5).

It is possible, in the case of nucleic acids, to program several consecutive heating/cooling cycles to check for reversibility. If the subsequent DSC scans of the same sample overlap, this means that the observed unfolding/folding process is fast compared to the scan rate employed in the experiment and can be considered, at each temperature, an equilibrium process; suggesting the full reversibility of the transition.

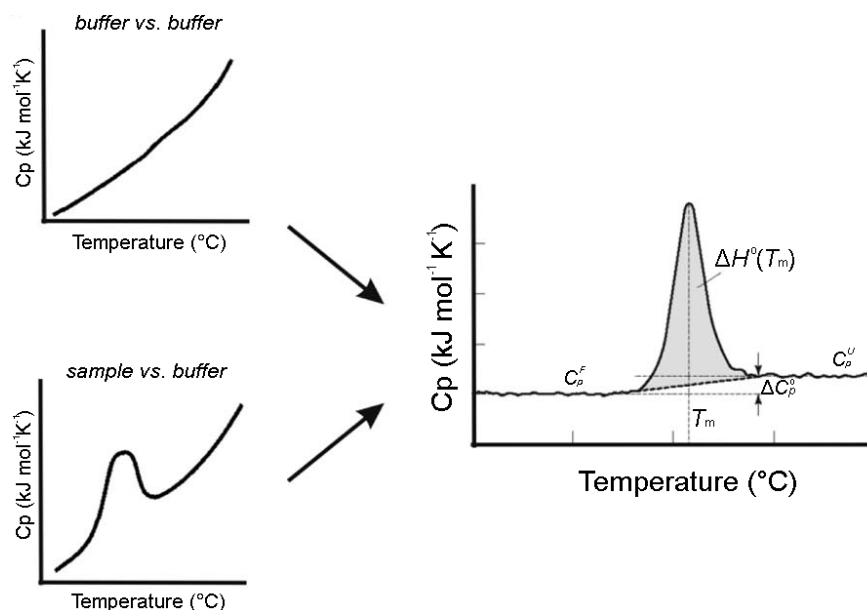


Figure 2.5. Buffer baseline scan, sample scan (on the left) and final DSC profile (on the right) after subtraction of the buffer baseline are shown. T_m is the melting temperature corresponding to the maximum of the curve, $\Delta H^o(T_m)$ is the unfolding enthalpy corresponding to the area under the curve and C_p^F and C_p^{Un} are the heat capacities of folded (F) and unfolded (Un) structures corresponding to the pre- and post-transition lines, respectively.

Thermodynamic parameters obtained from DSC experiments are quite sensitive to the structural state of biomolecules and associate with heat-induced macromolecular transitions.

The initial part of the curve provides the heat capacity (C_p^F) of the folded state; while, the final part provides the heat capacity (C_p^{Un}) of the unfolded state instead; their difference represents the ΔC_p of the molecules transition. The peak is centered at the transition melting temperature (T_m). The melting temperature is considered as the temperature at which 50% of molecules owns its folded conformation and the rest remains unfolded. Higher T_m values are representative of a more stable molecule.

Calorimetric enthalpy (ΔH_{cal}^o) is the total integrated zone below the peak, which indicates the total transition energy after suitable baseline correction:

$$\Delta H_{cal}^o(T_m) = \int_{T_i}^{T_f} C_p^o dT \quad (7)$$

in which T_i and T_f are the initial and the final temperature, respectively.

Van't Hoff enthalpy ($\Delta H^{\circ}_{\text{VH}}$) is an independent measurement of the transition enthalpy obtained assuming a two-state transition. $\Delta H^{\circ}_{\text{VH}}$ is determined through parameters derived from the experimental graph:

$$\Delta H^{\circ}_{\text{VH}} = KRT^2 \Delta C_p(T_m) / \Delta H^{\circ}_{\text{cal}}(T_m) \quad (8)$$

in which k is a constant derived from transition stoichiometry.

Information on the transition can be obtained comparing $\Delta H^{\circ}_{\text{VH}}$ with $\Delta H^{\circ}_{\text{cal}}$. If $\Delta H^{\circ}_{\text{VH}}$ is equal to $\Delta H^{\circ}_{\text{cal}}$, the transition occurs in a two-state mode. When $\Delta H^{\circ}_{\text{VH}}$ exceeds $\Delta H^{\circ}_{\text{cal}}$, the macromolecule may be associated as dimer or multimer. When $\Delta H^{\circ}_{\text{VH}}$ is less than $\Delta H^{\circ}_{\text{cal}}$, one or more intermediates are expected.

The other thermodynamic parameters are derived from these calorimetric ones. The change in entropy (ΔS°) is obtained by:

$$\Delta S^{\circ}(T_m) = \int_{T_i}^{T_f} \frac{C_p^{\circ}}{T} dT \quad (9)$$

ΔG° must be calculated at a chosen reference temperature:

$$\Delta G^{\circ}(T) = \Delta H^{\circ}(T) - T\Delta S^{\circ}(T) \quad (10)$$

2.4 Electrophoresis

Electrophoresis is a general term that describes the migration and separation of charged particles under the influence of an electric field. Most of biological molecules (e.g. amino acids, peptides, proteins, nucleotides, and nucleic acids) has ionizable groups and therefore they can be present in solution as charged species in dependence of the pH.

Gel electrophoresis (GE) is a widely used technique to separate, purify, and identify ionic or ionizable macromolecules in solution. An electrophoretic system consists of two electrodes, i.e. anode and cathode, connected by a conducting medium called electrolyte, in which the electrophoresis gel is immersed. Sample is loaded in appropriate wells and species migrate towards either electrode according to their charge.

The electric force (F_e) is given by the equation:

$$F_e = E \cdot q \quad (11)$$

in which E is the electric field and q the charge.

There is a friction that opposes to the motion generated by the electric field. The friction force is given by:

$$F_f = \gamma \cdot v \quad (12)$$

in which γ is the friction coefficient and v the migration velocity.

At constant speed:

$$F_e = F_f \quad (13)$$

from which is drawn that:

$$v = \frac{E q}{\gamma} \quad (14)$$

The electrophoretic mobility (m) is defined as:

$$m = \frac{v}{E} = \frac{q}{\gamma} \quad (15)$$

It is noted that the electrophoretic mobility exclusively depends on the particle.

In the case of a globular molecule, γ is given by:

$$\gamma = 6\pi\eta r \quad (16)$$

in which η is the medium viscosity and r the molecule radius.

Then m is:

$$m = \frac{q}{6\pi\eta r} \quad (17)$$

In conclusion, the electrophoretic mobility of a molecule is determined by its charge, dimension and shape, as well as by the medium viscosity and gel pore size. The electrophoresis allows the separation of molecules from a mixture according to their charge and size.

2.5 Mass Spectrometry

A mass spectrometer is an instrument that measures the mass / charge ratio (m/z) of ionized molecules in the gas phase. It consists of an ion source, an analyzer and a detector.

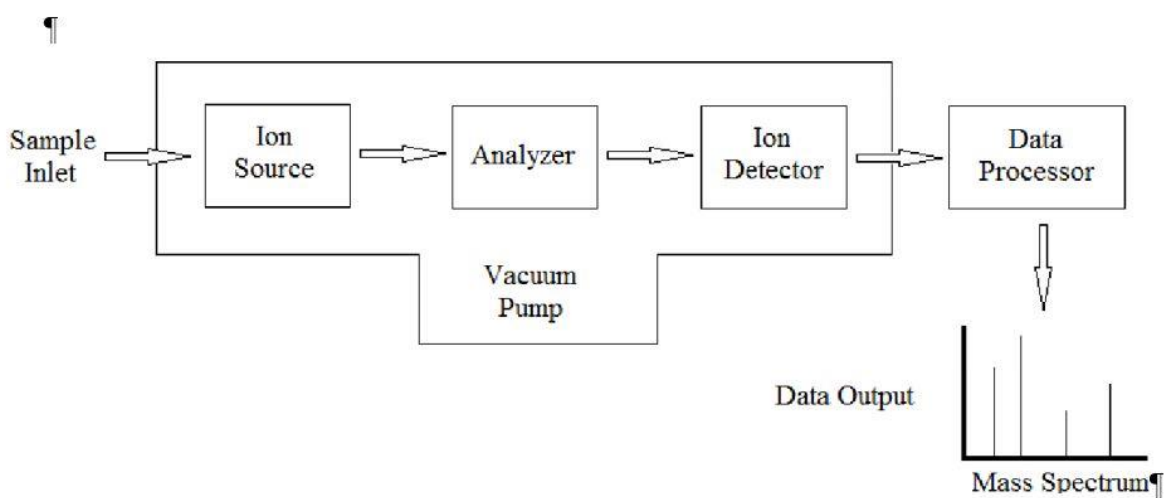


Figure 2.6. Block diagram of a mass spectrometer.

A feature of these instruments is the need for a complex high vacuum system that maintains low pressure values (from 10^{-4} to 10^{-8} torr) in all the components of the instrument, in order to allow the ions to move and make their collisions less frequent. Today mass spectrometry can not only be used for the measurement of electrons and charged elements, but also macromolecules, such as small mass metabolites, lipid molecules, peptides and even large mass compounds such as whole proteins or nucleic acids. There are many different ways of ionizing a compound, before being subjected to a magnetic or electric field within the mass analyzer.

Electronic Ionization (EI) is an example of a "hard" ionization technique, described in this way because of the highly energetic electrons used to interact with the gas or liquid for ionization. The electrons are generated from a heated metal wire in an electric circuit by thermionic emission, which are then accelerated towards the analyte. When one of these electrons collides with an analyte compound, it creates a positively charged ion by removing

an electron from the compound. This type of ionization also simultaneously results in extensive fragmentation of the analyte compound.

Matrix-Assisted Laser Desorption Ionization (MALDI) is another form of “soft” ionization that is used mainly with time-of-flight mass analyzers. It is a diffuse and powerful source for the production of intact gaseous phase ions from a wide range of large, non-volatile and thermally labile compounds such as proteins, oligonucleotides, synthetic polymers and large inorganic compounds.

Finally, the Electrospray Ionization (ESI), used in this thesis, is an ionization technique that can produce either positively or negatively charged ions. The electrospray technique allows to introduce solutions in the spectrometer and is capable of ionizing very polar and non-volatile compounds (Gaskell, 1997). There are four passages that are at the base of the ionization process: nebulization, desolvation, evaporation e ion release.

The introduction of electrospray sources was a major breakthrough in the field of biomolecule mass spectrometry (Fenn et al., 1989). Electrospray allows producing intact ions directly from large biomolecules, which have been directly taken from a solution injected in to a capillary. The softness of electrospray (the absence of fragmentation, thanks to the limited energy given by thermal heating and collisional activation) is such that even noncovalent complexes can be detected intact (Gabelica, 2010). ESI typically generates protonated and/or deprotonated molecular ions of the type $(M+nH)^{n+}$ and $(M-nH)^{n-}$, respectively. Peaks in the mass spectra are characterized by their m/z and their area. The masses of the peaks give immediate information on the stoichiometry of all complexes formed simultaneously in the solution, while in spectrophotometry methods, the stoichiometry is deduced by fitting of ligand binding curves. In addition, the relative peak areas in the mass spectra are proportional to the relative concentrations of the corresponding species in solution:

$$\frac{[X]}{[Y]} = R \times \frac{A_{(x)}}{A_{(r)}} \quad (18)$$

The easiest approximation is to consider that $R = 1$, i.e., the ratio between peak areas in the mass spectra is equal to the ratio between the concentrations of the corresponding species in solution. This is valid only if species X and Y have similar masses, shapes, hydrophobicity, and the ions produced have the same total charge. The protocol and equations can be applied to any

nucleic acid structure that can be ionized with ESI, even if the validity of the $R = 1$ hypothesis is not known.

Once the gas-phase ions have been produced, they need to be separated according to their masses, which must be determined. Ionic separation is performed by the analyzers of mass, which can be of different types. The most used ones are quadrupole mass analyzer, ion trap, Orbitrap and Time Of Flight (TOF). The quadrupole analyzer is a device which uses the stability of the trajectories in oscillating electric fields to separate ions according to their m/z ratios. The TOF analyzer consists of a vacuum tube, located halfway between the ion source and the detector. Analyzers of this type separate the ions with different m/z based on the speed at which they travel in the flight tube after being accelerated by an electric field V . The ion trap is, instead, composed of three cylindrical symmetry electrodes: applying a potential $U + V\cos\omega t$ to the intermediate electrode and positioning the other two on the earth potential ($V = 0$), a quadrupole field is generated and ions within the trap follow trajectories confined to one well defined region of space. Then, by performing a V scan, they are ejected in sequence all ions (Lavagnini et al., 2006). Two successive evolutions of this system are given by the linear ion trap (LIT, Linear Ion Trap) and by the Orbitrap (de Hoffmann and Stroobant, 2007).

The Orbitrap, that was used in this work, is an electrostatic ion trap that uses the Fourier transform to obtain mass spectra. The external part is an electrode having the shape of a barrel cut into two equal parts with a small interval. The central electrode has a spindle shape. The ions are injected tangentially through the interstice between the two parts of the external electrode. An electrostatic voltage of several kilovolts, negative for positive ions, is applied to the central electrode, while the outer electrode is at ground potential. The ions are injected with a kinetic energy of some kiloelectronvolts and start to oscillate in the trap in intricate spirals around the central electrode under the influence of an electrostatic field with a quadrilogarithmic potential distribution that is obtained by the direct current voltage and the astute geometry of the trap.

Chapter 3

PHYSICO-CHEMICAL FACTORS AFFECTING DRUG BIOAVAILABILITY

Quercetin, a flavonoid derived from many fruits and vegetables, is endowed with manifold biological properties, such as the ability to elicit a strong inhibitory effect on the growth of several tumor cell lines. Unfortunately, the pharmacological application of QCT is severely restricted by its inherent hydrophobicity and consequent low *in vivo* bioavailability. The semi-synthetic HP β CD is frequently employed to improve QCT therapeutic potential. In the following sections, I describe the thermodynamic studies on QCT- HP β CD host–guest complex formation under different solution conditions, recently published in two articles (D’Aria et al., 2017; Usacheva et al., 2019) on the Journal of Thermal Analysis and Calorimetry.

In the first publication (Paper I), made in collaboration with pharmaceutical technologists of our Department, HP β CD-QCT complex has been obtained in liquid phase, at 37 °C, under a prolonged mixing (72 h), and using two buffers at pH = 3.6 and pH = 8.0. Phase solubility and differential scanning calorimetry studies revealed that, at pH = 8.0, the complex was obtained with a 1:1 stoichiometric ratio and a strong enhancement of QCT solubility, while in acidic buffer complex formation was significantly thwarted. The affinity constant was calculated by isothermal calorimetry at pH = 8 and was found to be $489 \pm 38 \text{ M}^{-1}$, in good agreement with the value indirectly obtained from phase solubility tests $394 \pm 101 \text{ M}^{-1}$. The results confirmed the formation of the inclusion complex between QCT and HP β CD and highlight the importance of the choice of the appropriate solvent, pH, temperature, and mixing time on the formation of host guest inclusion complex with active ingredient(s) and HP β CD (D’Aria et al., 2017).

In the second publication (Paper II), made in collaboration with Russian chemists of Department of General Chemical Technology of Ivanovo State University, the heat effects of HP β CD solutions with QCT solutions in water/ethanol solvents at different concentrations were studied by calorimetric titration, and the stability of molecular complexes was assessed by UV–Vis spectrophotometry. Calorimetric titrations revealed the formation of a QCT-HP β CD host–

guest complex with a stoichiometric ratio of 1:1 in $X(\text{EtOH}) = 0.00, 0.05$ and 0.10 molar fractions of solvents at $\text{pH} = 7.0$ and $\text{pH} = 8.1$. Thermodynamic parameters of the complex formation reaction ($\lg K$; $\Delta_r H$; $T\Delta_r S$) were obtained in these experimental conditions. Differently, no complex formation was observed in water/ethanol mixed solvent when ethanol volume fraction exceeded 0.2 at neutral and alkaline pH , as well as a volume fraction higher than 0.1 at acidic pH . Furthermore, the results of differential scanning calorimetry tests, run on dried HP β CD after dissolution in hydroalcoholic solutions, indicated that ethanol and water compete for the complexation within the hydrophobic cavity of HP β CD. This explains the decreased QCT complexation efficacy in the presence of ethanol beyond 0.1 or 0.2 volume fraction (Usacheva et al., 2019).

3.1 A calorimetric study of host-guest inclusion complex between quercetin and hydroxypropyl- β -cyclodextrin (Paper I)

3.1.1 Introduction

Quercetin, also known as 3, 5, 7, 30, 40-pentahydroxyflavone, is a flavonoid containing a 3-hydroxyflavone backbone, which is very abundant in many fruits and vegetables (Apak et al., 2007) and, in particular, onions (Keli et al., 1996).

QCT is emerging as an important bioactive ingredient with manifold potential applications in pharmaceutical products since it is endowed with manifold beneficial properties, such as the reduction in systolic blood pressure (Zahedi et al., 2013), the inhibition of mast cell secretion (Shaik et al.), along with neuro-/cardioprotective (Marsh et al., 2017), antiviral (Ohnishi and Bannai, 1993), anti-inflammatory (Guardia et al., 2001), antioxidant (Zhang et al., 2016) and anticancer activities (Khonkarn et al., 2011). In particular, QCT can elicit a strong inhibitory effect on the growth of several tumor cell lines (Larocca et al., 1990; Ghasemzadeh et al., 2015; Nam et al., 2016). QCT has been proposed as an ancillary molecule in combination therapy, when administered with several chemotherapeutic drugs in the treatment of different cancers, such as topotecan (Murugan et al., 2016), cisplatin (Demiroglu-Zergeroglu et al., 2016) and sorafenib (Wang et al., 2016), just to cite a few. In a recent report, QCT has also been shown to act as a radiosensitizer (Malik et al., 2016). Notwithstanding this wide spectrum of pharmacological properties, the bioavailability profile of QCT is very poor due to its low permeability, stability and solubility in aqueous media (approximately 1.5 and $30 \mu\text{g mL}^{-1}$ in water, simulated gastric

fluid and simulated intestinal fluid) (Cai et al., 2013). For this reason the use of QCT in the pharmaceutical field is limited. The formation of inclusion complexes between QCT and solubility enhancers such as cyclodextrins is a simple way to increase the solubility of the active molecule. Actually, cyclodextrins are frequently used in the pharmaceutical field to increase the solubility of sparingly soluble compounds in water, taking advantage of their hydrophilic outer surface and hydrophobic internal cavity. The latter can encompass a wide array of sparingly water soluble molecules, therefore forming a host–guest complex and increasing the solubility, stability and overall bioavailability of the complexed molecule (Moyano-Mendez et al., 2014; Mayol et al., 2015). Mainly, three natural CDs exist, namely α , β and γ , which contain 6, 7 and 8 glucose units, respectively (Loftsson and Brewster, 1996). Among them, β -CDs is very often employed as a pharmaceutical excipient, mainly because of its cheapness, dimensions of the lipophilic cavity and ease of availability (Szejtli, 1998). Unfortunately, native β -cyclodextrins are poorly soluble in water and, also, induce adverse nephrotoxic effects when administered parenterally (Brewster and Loftsson, 2007). For this reason, chemically modified and generally safe β -cyclodextrins have been produced. In fact, semisynthetic derivatives of β -CDs possess an enhanced physical and microbiological stability, along with a lower parenteral toxicity (Szente, 1999). Among them, hydroxypropyl- β -cyclodextrin is frequently employed to improve the dissolution features and bioavailability of lipophilic drugs and, due to its improved safety, can also be used in parenteral dosage forms (Stella and Rajewski, 1997). Although the use of cyclodextrins is helpful to promote the solubilization of poorly soluble drugs, the efficiency of the complexation is generally low. For this reason, relatively large amounts of cyclodextrins are often needed to solubilize adequate amounts of drug. In this context, it is crucial to maximize complexation efficiency, and this is outstandingly important for strongly lipophilic molecules. In particular, formation of host–guest complex can be significantly ameliorated by properly adjusting the pH of the solution (Gladys et al., 2003). The aim of the present work is to improve the solubilization of QCT by forming an inclusion complex between the molecule and HP β CD. The complex has been formed in liquid phase in two different buffers at pH = 3.6 and 8.0 under mild heating (37 °C) and prolonged mixing times (72 h). The formation, stoichiometry and affinity constant of the complexes were determined by phase solubility experiments, DSC and isothermal calorimetry, to obtain quali-quantitative information on the thermodynamics of formation of the complex.

3.1.2 Results and discussion

Phase solubility experiments

Phase solubility experiments have been carried out to verify whether HP β CD is actually useful to form an inclusion complex with the guest molecule, thereby increasing its solubility. Figure 3.1 displays the molar concentration of QCT (i.e. the guest molecule) as a function of the molar concentration of the HP β CD, at pH = 3.6 and 8.0. Results indicate that, in phosphate buffer, QCT concentration is linearly increasing with increasing HP β CD concentration, while in the case of citrate buffer, the increase in QCT concentration is hardly detectable and the linearity of the dependence is less than satisfactory ($r^2 = 0.558$). The slope of the line at pH = 8.0 is 0.034 and a 6.4-fold solubility enhancement of QCT was found, thereby indicating a significant degree of interaction between QCT and HP β CD. In addition, the linear profile of the diagram points at a 1:1 stoichiometric ratio as for the formation of QCT-HP β CD complex. The affinity constant, indirectly estimated from Eq. (1), was found to be $394 \pm 101 \text{ M}^{-1}$. Differently, in the case of the acidic buffer, the results were less reliable, suggesting that the formation of the inclusion complex is strongly discouraged. This can be explained considering that the saturation concentration of QCT at pH = 8.0 is 0.039 mM, while at pH = 3.6 it is 1.04 mM. In this latter case, therefore, QCT molecules can interact much better with water molecules compared to the hydrophobic cavity of HP β CD.

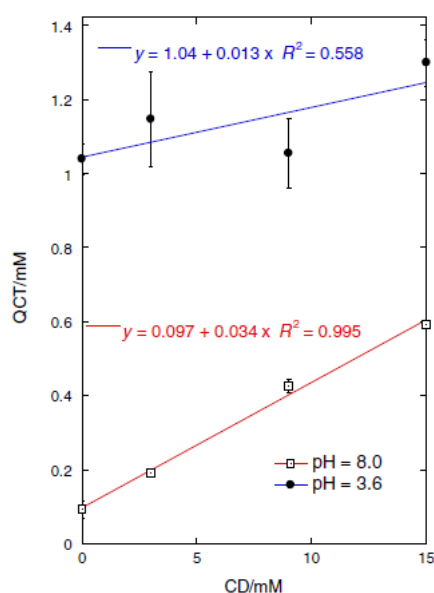


Figure 3.1. Phase solubility graph of QCT-HP β CD in phosphate (pH = 8.0) and citrate (pH = 3.6) buffers (n = 3).

Differential Scanning Calorimetry studies

DSC is frequently employed to evidence the differences in the physical mixtures between HP β CD and a drug and the putative inclusion complex. More specifically, when the melting endotherm of the complexed molecule is lost, an indication for the formation of an inclusion complex is obtained. Thus, the saturated solution used for the phase solubility, at pH 8.0 and 15 mM HP β CD concentration, was studied by DSC. More in detail, the experiments have been carried out on the raw drug, the HP β CD, as well as on the lyophilized supernatant and the precipitated mass. As reported in Figure 3.2, QCT curve showed a sharp endothermic peak at 319.9 °C (Figure 3.2 a; $\Delta H^\circ = 164.5 \pm 3.1 \text{ J g}^{-1}$), associated with the fusion of the drug while, in the case of HP β CD, two endothermic peaks at 96.8 and 331.2 °C were revealed (Figure 3.2 b). The first peak is associated with water loss, while the second one is characteristic of the thermal degradation of HP β CD. Figure 3.2 c displays the DSC trace of the putative QCT-HP β CD complex. In this case, the endothermic peak related to water loss is still present, but less important, therefore indicating the presence of a fraction of HP β CD which does not interact with the guest molecule. Interestingly, both the melting peak of QCT and the degradation peak of HP β CD were not detected when heating the lyophilized samples up to 400 °C. This flattening of DSC trace can be reasonably regarded as an evidence of the successful inclusion of QCT molecules in HP β CD cavities, to an amorphous state, or both. In Figure 3.2 d, the curve obtained by heating the lyophilized precipitated mass after phase solubility shows a behavior typical of a physical mixture, with a shift in the peak related to water loss probably due to lyophilization process. The sharp endothermic peak found at 317.1 °C, very close to the melting point of QCT, suggests the presence of free drug within the precipitate. The wide peak associated with HP β CD decomposition, on the contrary, was not found, therefore indicating a possible precipitation of the complex in the lyophilized precipitate or the formation of more stable structure during the freeze-drying process.

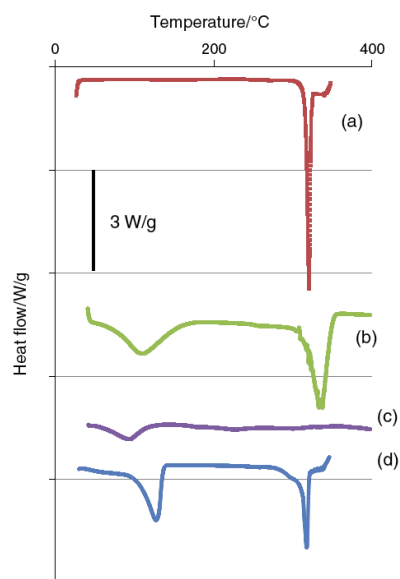


Figure 3.2. DSC curves of (a) raw QCT; (b) HP β CD; (c) QCT-HP β CD inclusion complex obtained after lyophilization of the supernatant obtained during phase solubility experiments; (d) lyophilized precipitated mass after phase solubility test; (n = 3). The endotherm is downward.

Isothermal Calorimetry measurements

The results were also confirmed by isothermal calorimetry measurements, which was used to measure the heat of inclusion complexation between HP β CD and QCT at 298.15 K. In Figure 3.3, the association enthalpy is reported as a function of the molality of quercetin, at pH = 8.0 and 298.15 K. The solid line through the points is obtained using the affinity constant and standard enthalpy evaluated by Eqs. (23) and (24). In acidic solution conditions, at pH = 3.6, small released association heats were detected that hampered the extraction of the thermodynamic parameters.

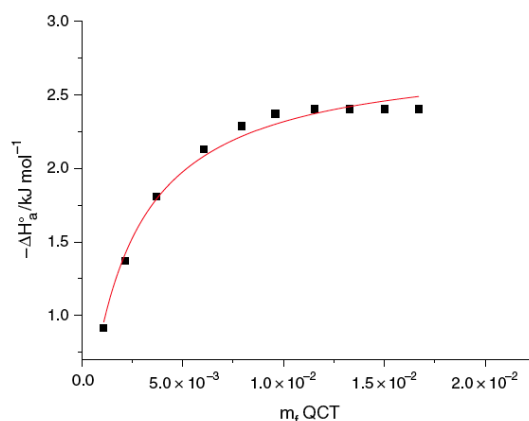


Figure 3.3. Enthalpies of association, ΔH° , as a function of the final molality of quercetin, at pH = 8.0 and 298.15 K. The experimental points are indicated by squares, while the curve was drawn employing the constant and enthalpy obtained through Eqs. (23) and (24) by the iterative least-squares method described in the experimental section.

Indeed, the thermodynamic parameters (affinity constant K_a , standard enthalpy ΔH° , entropy $T\Delta S^\circ$ and Gibbs energy ΔG°) at pH = 8.0 are shown in Table 1, together with the constant obtained by phase solubility measurements and literature data. In particular, the affinity constant obtained from calorimetry experiments is in agreement with that calculated from phase solubility experiments.

An inspection of the methodologies reported in the literature shows that phase solubility studies are largely utilized to obtain affinity constants for HP β CD-QCT complexation. However, large discrepancies were found depending on solution conditions (Table 3.1) (Pralhad and Rajendrakumar, 2004; Jullian et al., 2007; Liu et al., 2013). Liu and coworkers evaluated the apparent affinity constant for the complexation of QCT with HP β CD by phase solubility analysis and by two processing methods of fluorescence spectra analysis in Tris-HCl buffer solutions of pH 7.40 (Liu et al., 2013). Affinity constants ranging from 3110 to 4000 M^{-1} were found at 298 K, depending of the applied method and a ΔH° value of $-45.40 \text{ kJmol}^{-1}$ was obtained by Van't Hoff analysis. The high ΔH° value thus obtained led to a negative value of ΔS° . We obtained the enthalpy by direct calorimetric measurements and in a different pH solution condition, and both these factors could explain the differences in the thermodynamic parameters. These data show that the association was both enthalpically and entropically driven with a prevalence of the entropic term, therefore indicating that the hydrophobic interactions,

usually displayed by positive ΔS° , are predominant in the inclusion of QCT in the hydrophobic cavity of HP β CD.

Table 3.1. Thermodynamic parameters for the association of QCT with HP β CD at 298.15 K

Ka (M⁻¹)	ΔH° (kJ mol⁻¹)	TΔS° (kJ mol⁻¹)	ΔG° (kJ mol⁻¹)	Refs.
489 ± 38	-2.9 ± 0.1	12.5 ± 0.3	-15.3 ± 0.2	Calorimetry in this work
394 ± 101				Phase solubility in this work
3110 ± 38	-45.40 ± 1.74	-25.46 ± 0.03	-19.94 ± 0.03	(Liu et al., 2013)
1149				(Jullian et al., 2007)
532				(Pralhad and Rajendrakumar, 2004)

3.1.3 Conclusions

In this work, we have examined the formation of the inclusion complex between QCT and HP β CD aiming to study the thermodynamic parameters involved in the formation of the complex. Phase solubility studies revealed that, at pH = 8.0, QCT forms inclusion complexes with HP β CD at a 1:1 stoichiometric ratio, with a strong solubility enhancement of QCT; at pH = 3.6, on the contrary, QCT solubility is higher but little or no interaction with HP β CD occurs. The formation of the complex was also confirmed by DSC results. Furthermore, the affinity constant was calculated by means of isothermal calorimetry at pH = 8.0, and the obtained value was found to be 489 ± 38 M⁻¹, in good agreement with the value of the constant indirectly obtained from phase solubility tests (394 ± 101 M⁻¹). Taken all together, these results highlight the importance of the choice of the appropriate solvent, pH, temperature and mixing time on the formation of host guest inclusion complex with active ingredient(s) and HP β CD.

3.1.4 Experimental section

Materials

All substances were Sigma-Aldrich products. In all calorimetric measurements, the concentration of QCT was between 1.5×10^{-4} and 2.0×10^{-4} mol kg⁻¹, while the concentration range for the for HP β CD was between 2.2×10^{-3} and 2.5×10^{-2} mol kg⁻¹. The average degree of substitution of the HP β CD employed was 4.2. Solutions were prepared just before measurements employing phosphate and citrate buffers, at pH = 8.0 and 3.6, respectively.

Preparation and characterization of QCT-HP β CD complex

QCT and HP β CD were dissolved in each buffer solution at a 1:1 molar ratio and placed in a thermostatic bath under mild agitation (100 rpm) at 37 °C for 72 h. During mixing, each flask was covered with aluminum foil to prevent QCT photodegradation. The obtained QCT-HP β CD inclusion complexes were characterized by phase solubility experiments, differential scanning calorimetry curves and isothermal microcalorimetry tests, as described in the following.

Phase solubility experiments

Prior to phase solubility tests, citrate and phosphate buffer were prepared. Citrate buffer was prepared by dissolving 1.93 g of sodium citrate and 2.41 g of citric acid in 500 mL of double-distilled water (DDW). The solution was magnetically stirred for 30 min at room temperature and diluted with further DDW to a final 1 L volume. The resulting liquid was filtered through a 0.45- μ m membrane filter, and the pH was adjusted to 3.6. For phosphate buffer, 0.201 g of KCl, 7 g of NaCl, 1.42 g of Na₂HPO₄ were solubilized and the same procedure employed. The pH was adjusted to 8.0.

To verify the formation of QCT-HP β CD inclusion complexes, phase solubility experiments were carried out as follows. An excess amount of QCT was suspended in 10 mL of citrate or phosphate buffers containing HP β CD in the 3–15 mM concentration range. The suspensions were poured in capped vials, vortexed for 5 min and mixed in the dark at 37 °C in a thermostatic bath for 72 h under continuous agitation at 100 rpm. Thereafter, the solutions were filtered through a 0.45- μ m membrane and the filtered solution was analyzed by spectrophotometric assay to quantify the solubilized QCT (UV-1800, Shimadzu Laboratory World, Japan; $k = 370$

and 382 nm in citrate and phosphate buffer, respectively). The phase diagram was obtained by plotting the molar concentration of solubilized QCT against HP β CD molar concentration.

The stability constant of the QCT-HP β CD complex was calculated from the slope of the phase solubility diagram, with the equation:

$$K_c = \frac{\text{slope}}{S_0(1-\text{slope})} \quad (19)$$

where S_0 is QCT solubility in the absence of HP β CD.

Differential Scanning Calorimetry

The formation of the complex between QCT and HP β CD has been qualitatively investigated by performing thermo-analytical tests on the lyophilized solutions (24 h, 0.01 atm, -60 °C; Modulyo, Edwards, UK) obtained from phase solubility. Particularly, the heats involved in the melting of QCT, HP β CD, the inclusion complex and the recovered precipitate from phase solubility tests were determined by a differential scanning calorimeter (DSC Q20, TA Instruments, USA), preliminarily calibrated with a pure indium standard. Weighted solid samples (approximately 3–4 mg) were placed in aluminum pans and scanned from 40 to 400 °C at a constant heating rate of 10 °C min⁻¹, under an inert nitrogen atmosphere purged at a constant 50.0 mL min⁻¹ flow rate. The melting temperature (T_m) was obtained from the fusion peak.

Isothermal Calorimetry

Measurements of the experimental heats of dilution or mixing of two binary solutions containing any one of the solutes were determined at 298 K using a thermal activity monitor (TAM) from Thermometric, equipped with a flow mixing vessel. A P3 peristaltic pump from Pharmacia envoys the solutions into the calorimeter through Teflon tubes.

The values of the experimental heats (of dilution or mixing) can be obtained from the equation:

$$\Delta H = \frac{dQ/dt}{P_w} \quad (20)$$

where dQ/dt (W) is the heat flux, P_w (kg^{-1}) is the total mass flow rate of the solvent through the calorimeter, and ΔH is given in J kg^{-1} of solvent in the final solution.

The following two kinds of experiments were arranged:

1. The determination of the heat of dilution, $\Delta H_{\text{dil}} (m^i \rightarrow m^f)$, from the initial, m^i , to the final, m^f , molality of binary aqueous solutions of HP β CD or QCT, at the different concentrations employed.

2. The determination of the heat of mixing, $\Delta H_{\text{MIX}} [(m_{\text{HP}\beta\text{CD}}^i)(m_{\text{QCT}}^i) \rightarrow m_{\text{HP}\beta\text{CD}}^f, m_{\text{QCT}}^f]$ of binary aqueous solutions of QCT, with binary aqueous solutions of HP β CD.

Dilution and mixing experiments were carried out using PBS buffer as solvent. The enthalpy of mixing two binary solutions, ΔH_{MIX} , is related to the enthalpy of formation of a complex, or in general to the enthalpy of interaction between solutes, ΔH^* , and to the heats of dilution experienced by the two solutes, ΔH_{dil} , by the following equation:

$$\Delta H_{\text{MIX}} [(m_{\text{HP}\beta\text{CD}}^i)(m_{\text{QCT}}^i) \rightarrow m_{\text{HP}\beta\text{CD}}^f, m_{\text{QCT}}^f] = \Delta H^* + \Delta H_{\text{dil}} (m_{\text{HP}\beta\text{CD}}^i \rightarrow m_{\text{HP}\beta\text{CD}}^f) + \Delta H_{\text{dil}} (m_{\text{QCT}}^i \rightarrow m_{\text{QCT}}^f) \quad (21)$$

Treatment of the data

Assuming that a 1:1 complex is formed when mixing two binary solutions, the association process can be represented as follows:



ΔH^* , normalized to the total molality of the guest, m_{QCT} can be related to the actual molality of the cyclodextrin host molecule, $m_{\text{HP}\beta\text{CD}}^f$, to the standard molar enthalpy of association, ΔH_a° , and to the apparent affinity constant, K_a' , as follows (Liu et al., 2013):

$$\frac{m_{\text{QCT}}}{\Delta H^*} = \frac{1}{\Delta H_a^\circ} + \frac{1}{\Delta H_a^\circ K_a' m_{\text{HP}\beta\text{CD}}^f} \quad (23)$$

For each value of ΔH^* , the actual concentration of the host molecule is given by:

$$m_{HP\beta CD}^f = m_{HP\beta CD} - \frac{\Delta H^*}{\Delta H_{SAT}^*} * m_{QCT} \quad (24)$$

where m_{QCT} is the total stoichiometric molality of the host molecule. The standard enthalpy and the constant are obtained from Eqs. (23) and (24) by an iterative least-squares fitting. The iterations are continued until two successive values of ΔH° differ by less than 2%. The values of the free energy and entropy are obtained through the usual thermodynamic relations. The absence of any information about the activity coefficients leads to the evaluation of association parameters thermodynamically not exactly defined. Only an apparent constant, K'_a , can be determined, and consequently the standard free energy and entropy suffer of the same limitations.

3.2 Thermodynamic studies of complex formation between hydroxypropyl- β -cyclodextrin and quercetin in water–ethanol solvents at T = 298.15 K (Paper II)

3.2.1 Introduction

The formation of the host–guest complex between QCT and HP β CD in water (Figure 3.4 a, b) has been studied in detail (Liu et al., 2013; D’Aria et al., 2017).

In a recent report, QCT-HP β CD complex has also been prepared in ethanol by the co-precipitation method, resulting in a strong enhancement of QCT aqueous solubility and photostability (Savic et al., 2015). However, to the best of our knowledge, the stability of the complex has not been established to date in water and hydroalcoholic solutions.

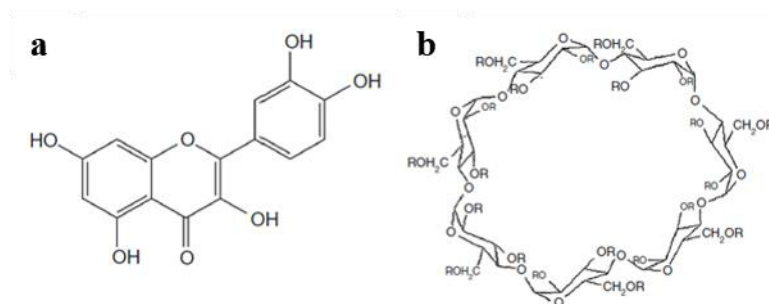


Figure 3.4. Structural formulas of: (a) quercetin, (b) hydroxypropyl- β -cyclodextrin

In a previous work, Usacheva and Sharnin found that the addition of a nonaqueous substance to water promotes the stability of the molecular complexes of crown ethers and amino

acids/peptides, leading to an increase in the exothermicity of the reactions of their formation due to a change in the solvation features of the complexes (Usacheva and Sharnin, 2015). Thus, here we used a thermodynamic approach to quantitatively analyze the influence of individual solvation factors on the stability of the complexes as previously reported (Krestov and Novosyolov, 1994). More specifically, the processes of solubilization of water-insoluble compounds by the formation of the host–guest inclusion complex with CDs can be considered as processes of competition–substitution of water molecules in the CD cavity by a guest molecule (Donz and Coleman, 1995). Hence, in the presence of co-solvent molecules, water content in the internal cavity of macrocycle will depend on the competition between the “guests” and co-solvent molecules of a mixed solvent in the CD cavity. For instance, it has been established that some minimal amount of methanol or ethanol facilitates the binding of large hydrophobic “guests” to β -cyclodextrin (Yoshii et al., 1998). In this regard, the use of non-aqueous solvent additives to water is expected to help in creating optimal conditions for the solubilization of hydrophobic molecules by CDs. Starting from these considerations, herein we have studied the formation of QCT-HP β CD inclusion complex in water–ethanol mixtures at different concentrations of ethanol so as to assess the effect of solvent composition on the formation of QCT-HP β CD complex.



To this aim, the thermodynamic parameters involved in the complex formation have been determined starting from microcalorimetry experiments carried out on the different hydroalcoholic mixtures and at different pH values.

3.2.2 Results and discussion

Previous studies focused on the complex formation between d-metal ions and amine or carboxylate complexes in aqueous–organic solvents have revealed, on the basis of the solvation-thermodynamic approach, the possibility of predicting the thermodynamic parameters of the ionic complex formation reactions in different media according to a change in the solvation state of ligands (Sharnin, 1995; Zevakin et al., 2007; Gesse et al., 2012).

In particular, the complexation in water is considered as a set of reactions of stepwise replacement of water molecules in the first solvate shell of the central ion by a ligand molecule (Sharnin, 1995). In a binary solvent, the set of reactions is more complicated, since there is a preferential solvation of reagents with one of the solvent components (Zevakin et al., 2007; Gesse et al., 2012). In the complexation of inorganic cations with crown ethers, cryptands and other macrocyclic structures, the central ion is completely or almost completely isolated from the solvent. For less stable complexes between macrocycle (host) and organic molecule (guest), the guest molecule and the solvent most probably compete for the formation of the complex with the HP β CD.

Isothermal Titration Calorimetry and UV-Vis studies

In this work, the thermodynamic parameters of the complex formation between QCT and HP β CD in water and in water/ethanol mixed solvent, at pH = 7.0 and 8.1, compared with the relevant literature data in water, are presented in Table 3.2.

Table 3.2. Thermodynamic parameters for the association of QCT with HP β CD in water and in water/ethanol mixtures

X(ETOH) molar fraction	lgK	Δ -H (kJ mol ⁻¹)	Δ -G (kJ mol ⁻¹)	Δ -S (kJ mol ⁻¹)	Methods	T (K)	pH	Refs.
0.00	3.8 ± 0.2	-4.9 ± 0.8	-21.6 ± 1.1	56.1 ± 1.4	Calorimetry	298.15	7.0	This work
	3.4 ± 0.1	-	-	-	UV-Vis spectra	298.15	7.0	
	2.7	-2.9 ± 0.1	-15.3 ± 0.2	41.6 ± 0.3	Calorimetry	298.15	8.0	(D'Aria et al., 2017a)
	2.6	-	-	-	Phase solubility	298.15	8.0	
	3.5	-45.4 ± 1.74	-19.94 ± 0.03	-85.37 ± 5.69	Phase solubility	298.15	7.4	(Liu et al., 2013)
	3.6	-	-	-	Double-reciprocal plot	298.15	7.4	(Liu et al., 2013)
	3.6	-	-	-	Nonlinear regression analysis	298.15	7.4	(Liu et al., 2013)
	3.4	-	-19.50 ± 0.02	-	Phase solubility	303.15	7.4	(Liu et al., 2013)
	3.2	-	-19.11 ± 0.01	-	Phase solubility	308.15	7.4	(Liu et al., 2013)
	3.1	-	-18.66 ± 0.02	-	Phase solubility	313.15	7.4	(Liu et al., 2013)
	3.5	-	-	-	Phase solubility	298.15	7.4	(Liu et al., 2013)
	3.2	-	-	-	Phase solubility	303.15	-	(Jullian et al., 2007)
	2.7	-	-	-	Phase solubility	298.15	-	(Pralhad and Rajendrakumar, 2004)
	4.04	-	-	-	Phase solubility	297.15	3.0	(Zheng et al., 2005)
0.05	3.7 ± 0.1	-7.6 ± 0.6	-20.9 ± 0.6	44.4 ± 0.8	Calorimetry	298.15	7.0	This work
	3.5 ± 0.1	-	-	-	Uv-Vis spectra	298.15	7.0	
0.10	3.6 ± 0.1	-7.3 ± 0.5	-20.6 ± 0.6	44.8 ± 0.8	Calorimetry	298.15	7.0, 8.1	This work
	3.3 ± 0.4	-	-	-	UV-Vis spectra	298.15	7.0	

The results of calorimetric titrations showed that the complexation occurs in water/ethanol mixtures of composition X(EtOH) = 0.00, 0.05 and 0.10 molar fraction. Conversely, no complex formation was found out when ethanol molar fraction was ≥ 0.20 at pH = 7.0 or when pH was lowered to 3.6 with a 0.10 EtOH molar fraction, according to the calorimetric titration and UV–Vis data.

The formation of the QCT-HP β CD complex can be envisaged by the total heat of complexation $\Sigma(Q_{\text{compl}})$ dependence on the concentration of HP β CD in the cell. More in detail, when the complex formed, $\Sigma(Q_{\text{compl}})$ becomes HP β CD concentration independent as observed in Figure 3.5 a–c. Differently, as shown in Figure 3.5 d, e, in the presence of weak molecular

interactions, the total heat of complexation $\Sigma(Q_{\text{compl}})$ dependence on the concentration of HP β CD in the cell is linear.

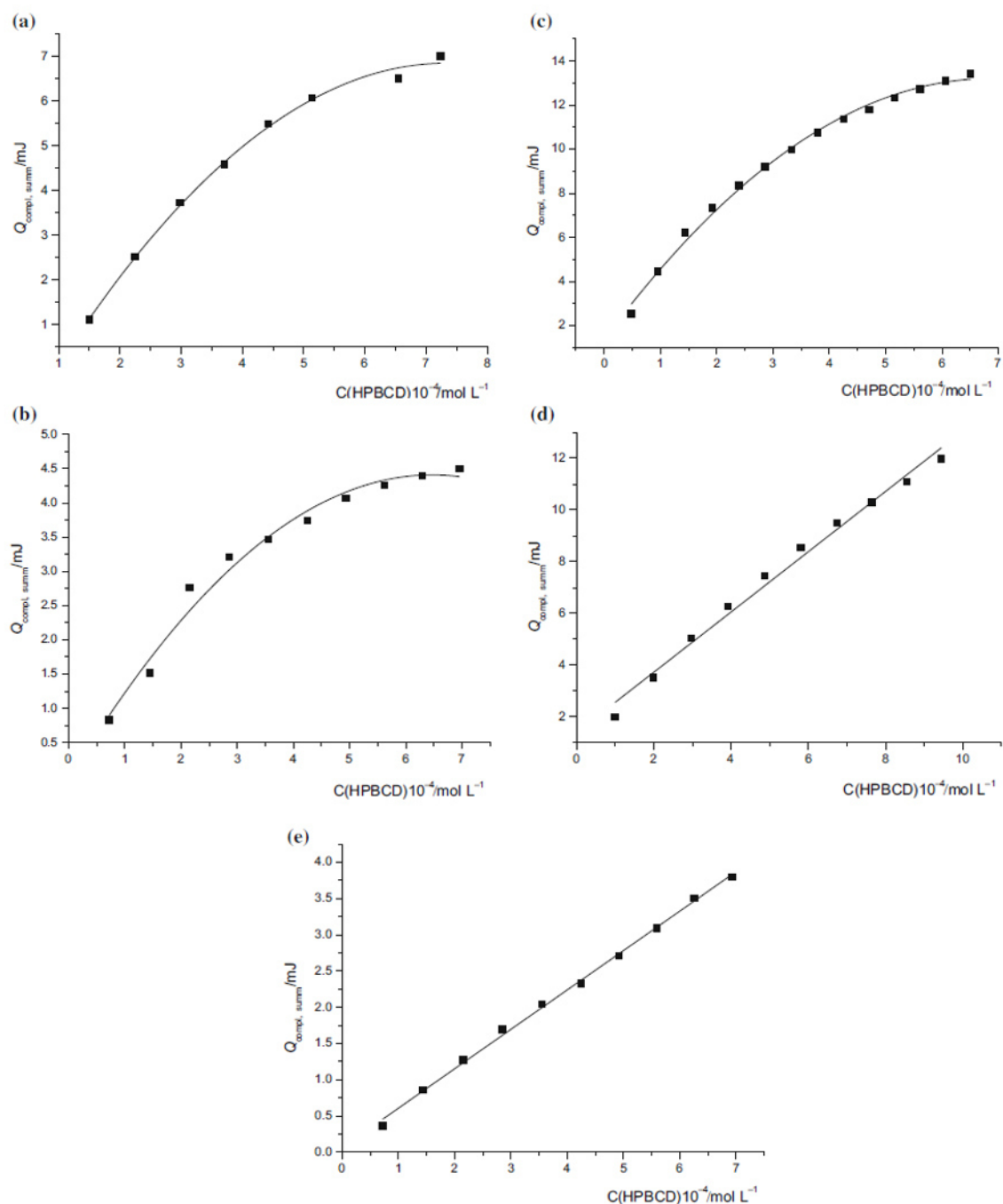


Figure 3.5. Total heat effect of the interaction between QCT and HPβCD in H₂O–EtOH solvent, depending on the total molar concentration of HPβCD in the cell, (a) in H₂O at $T = 298.15\text{ K}$, $\text{pH} = 7.0$; (b) at $X(\text{EtOH}) = 0.10$ molar fraction, at $T = 298.15\text{ K}$, $\text{pH} = 7.0$; (c) at $X(\text{EtOH}) = 0.10$ molar fraction, at $T = 298.15\text{ K}$, $\text{pH} = 8.1$; (d) at $X(\text{EtOH}) = 0.10$ molar fraction, at $T = 298.15\text{ K}$, $\text{pH} = 3.6$; (e) at $X(\text{EtOH}) = 0.20$ molar fraction, at $T = 298.15\text{ K}$, $\text{pH} = 7.0$.

Binding constants at $\text{pH} = 7.0$ were also calculated by UV–Vis titration spectra (Figure 3.6 a, b), and the results are shown in Table 3.2. An inspection of Table 3.2 shows that the

thermodynamic parameters of QCT-HP β CD complex formation have been obtained in water by various methods, under different conditions (Pralhad and Rajendrakumar, 2004; Zheng et al., 2005; Jullian et al., 2007; Liu et al., 2013; D'Aria et al., 2017). In most of them, the values of the association constants are in satisfactory agreement with each other and with our values obtained by both calorimetric and UV–Vis methods.

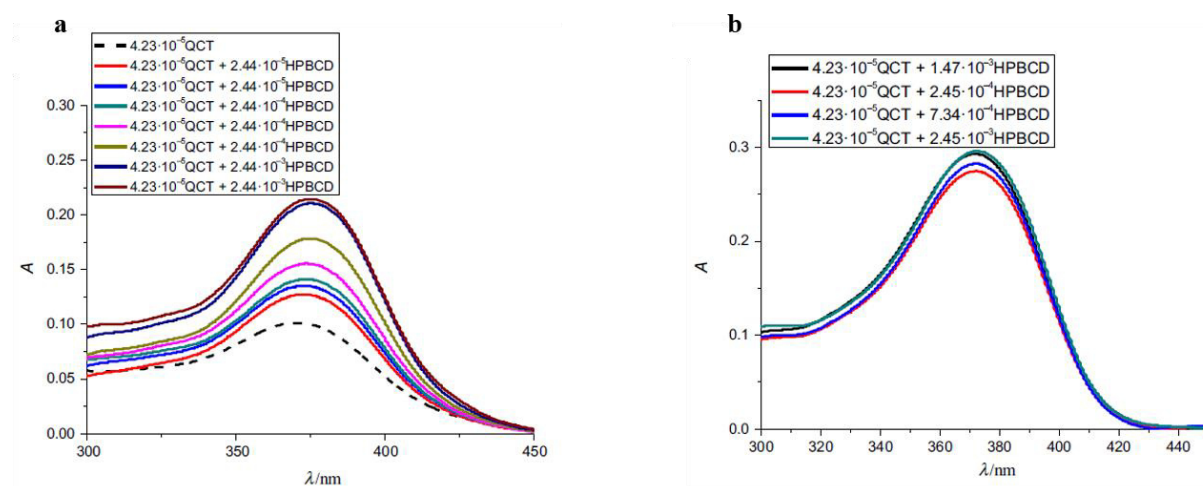


Figure 3.6. Electronic absorption spectra of HP β CD with a solution of QCT. The numbers in the legend indicate the molar concentrations of QCT and HP β CD (mol L⁻¹), (a) in H₂O at pH = 7.0, (b) in X(EtOH) = 0.10 molar fraction at pH = 7.0

In the previous paper, we found the association constant in water at pH = 8.0 (D'Aria et al., 2017), and in this work we were able to obtain calorimetric data in water at pH = 7.0. At this pH, the association constant was one order of magnitude higher and the values of Δ_rH and Δ_rS showed an increase in both the exothermicity of complexation and the entropic contribution to the Gibbs energy change for the complex formation. The different Δ_rH and Δ_rS values obtained by Liu et al. can be reasonably explained, considering that they were indirectly extracted by the phase solubility analysis at a different pH of 7.4 (Liu et al., 2013). After the addition of ethanol to water, the stability of the complex was unchanged for X(EtOH) = 0.00, 0.05 and 0.10 molar fraction. However, along with this, an increase in the exothermicity of complexation and a decrease in the entropic contribution to the Gibbs energy change of the formation reaction were detected.

In a previous publication, an insignificant effect of added DMSO on the stability of molecular complexes was found in the study of the complexation of triglycine with cryptand

[2.2.2] (Usacheva et al., 2016). This finding was discussed based on the compensation effect of the entropy/enthalpy contributions to the Gibbs energy of complexation. Furthermore, in the case of molecular complexes of crown ethers with amino acids and peptides, the addition of ethanol, DMSO and acetone resulted in an increased stability of molecular complexes and in an increase in the exothermicity of their formation reactions (Usacheva and Sharnin, 2015). These results were explained in terms of changes in solvation of guest molecules with the replacement of waters by organic solvents. Considering previous studies, we could hypothesize that moving from water to hydroalcoholic solvent, the thermodynamics of QCT-HP β CD complex formation is influenced by the change in solvation of QCT. The solubility of QCT is higher in water/ethanol mixtures than in water (Razmara et al., 2010), and this indicates that ethanol molecules displace water molecules in QCT hydration shell, affecting both the enthalpic and entropic contributions to Gibbs energy of complexation, so that the lgK for low X(EtOH) remains the same as in water. Increasing ethanol molar fraction, EtOH is able to effectively solvate QCT molecules, by subtracting them from the complexation, and competes for occupation of HP β CD cavities or fills the residual empty space of the cavity of HP β CD, as already found in another study (Boonyarattanakalin, 2015). The overall result is that, for X(EtOH) greater than 0.10 molar fraction, no complexation occurs.

Differential Scanning Calorimetry experiments

DSC scans have been run to provide further information on the physical and chemical processes occurring during heating. Commercial HP β CD displays a broad endothermic peak, which is indicative of the release of superficial and strongly retained water from the hydrophobic core at 106 °C (Figure 3.7 a) (Oprean et al., 2016; Tang et al., 2016). After HP β CD dissolution in water, the DSC peak appears at a very similar temperature (about 103.5 °C, Figure 3.7 b), therefore indicating that the same interaction occurs after immersion of HP β CD in water. The DSC peak appears at slightly lower temperatures after dissolution in 9:1 and 8:2 water/ethanol mixtures, around 100 °C (Figure 3.7 c, d). The decrease in these peak temperatures can be explained by the formation of the host–guest molecular inclusion compound that allows the replacement of the strongly retained water molecules inside the cavity by the ethanol moieties. The obtained complex mainly most probably contains superficial water molecules that are more easily released, and hence, the peak temperature decreases (Hădărugă et al., 2013). This indicates that the total water content is lower and/or weakly bound to HP β CD

after immersion in ethanolic or hydroalcoholic solvents, compared to the untreated, commercial CD. These results therefore corroborate the existence of the competition between ethanol and water for the complexation within the hydrophobic cavity of HP β CD which in turn contributes in decreasing the efficacy of QCT complexation in the presence of ethanol.

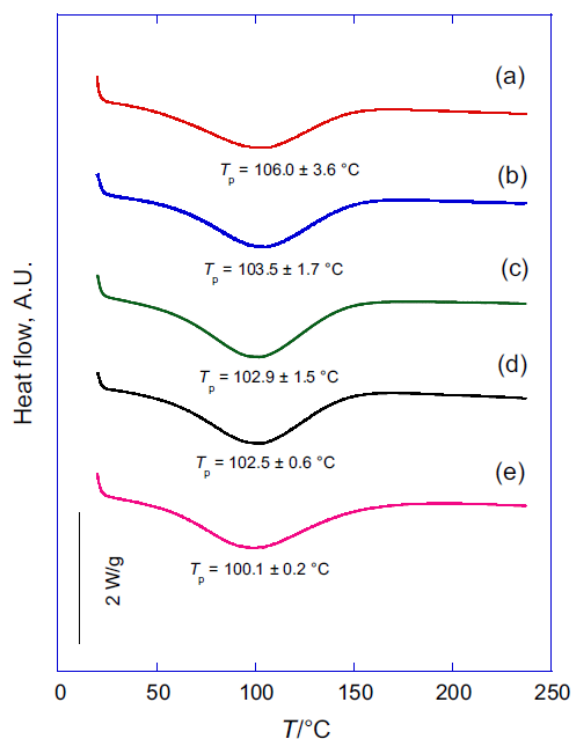


Figure 3.7. Superimposed DSC data for raw HP β CD (a) and dried HP β CD after dissolution in water (b); water/ethanol 9:1 v/v mixture (c); water/ethanol 8:2 v/v mixture (d); ethanol (e)

3.2.3 Conclusions

This work established that the addition of ethanol to water leads to an insignificant decrease in the stability of the QCT-HP β CD host-guest complex. However, along with this, there is an increase in the exothermicity of complexation and a decrease in the entropic contribution to the change of the reaction Gibbs energy. Above $X(\text{EtOH}) = 0.10$ molar fraction, no complexation occurs. It seems unexpected because the decrease in the complex stability should be more significant at increasing ethanol content in the solvent. Probably, in H₂O/EtOH solvent with 0.1 and more molar fraction of EtOH the replacement of QCT in the cavity of CD by molecules of EtOH is presented. In consequence, the complex QCT-CD does not form. This can be reasonably ascribed to the outcomes of DSC results, which showed that ethanol actively

competes for the inclusion within HP β CD cavity, therefore hampering the effective formation of QCT–HP β CD inclusion complex. Overall, the data showed that the ethanol affects QCT solvation, shifting the equilibrium far from QCT-HP β CD complex formation, and competes for occupation of HP β CD cavities. Taken altogether, these results highlight a counterintuitive conclusion, in that the expected solubility enhancement of the active molecule in the presence of ethanol did not match a higher affinity between QCT and HP β CD. However, further studies on different molecules in mixed solvents will be devoted to shed light on the thermodynamic interactions between pharmacologically active natural compounds and HP β CD.

3.2.4 Experimental section

Materials

All substances were obtained from Sigma-Aldrich. QCT and HP β CD (both $\geq 99\%$ purity) were used as received, without further purification. Rectificate grade ethyl alcohol was purified by distillation before use. The amount of water in EtOH ($\leq 5\%$ w/w) was determined from the density by accurately weighing using a pycnometer, preliminarily calibrated with ethanol on an analytical scale balance AUX220D and taking into account these measurements in the preparation of aqueous ethanol solvents. Mixed solvents were prepared with bidistilled and deaerated water by a gravimetric method.

Isothermal Titration Calorimetry

The heat effects of mixing HP β CD solutions with QCT were determined by isothermal titration calorimetry with the TAM III (TA Instruments, USA) microcalorimeter in water/ethanol mixed solvents containing $X(\text{EtOH}) = 0.00, 0.05, 0.10, 0.20, 0.50$ and 0.95 molar fractions in phosphate buffer at $\text{pH} = 3.6, 7.0$ and 8.1 and at $T = 298.15$ K. The optimal concentration conditions for the experiments, limited by the low solubility of the reagents in the water–ethanol mixtures, were previously calculated according to the RRSU program for each solvent composition. The yield of the QCT-HP β CD complex varied in the widest range of values (3–50%). The initial concentration of HP β CD in the syringe ranged from $1.45 \cdot 10^{-2}$ to $1.59 \cdot 10^{-2} \text{ mol L}^{-1}$.

The initial concentration of QCT in the cell ranged from $1.19 \cdot 10^{-4}$ to $2.25 \cdot 10^{-4} \text{ mol L}^{-1}$. The HP β CD-QCT molar ratio was in the 3–9 range. In all experiments, the composition of the

solvent in the syringe and in the cell was the same. The heat effect of mixing for solutions of HP β CD with solutions of QCT (Q_{mix}) is contributed by the heat of QCT-HP β CD complex formation (Q_{compl}), the heat of dilution of HP β CD solution ($Q_{dil 1}$) in a solvent in the cell and the heat of dilution of QCT solution placed in the cell in a solvent added from syringe ($Q_{dil 2}$):

$$Q_{mix} = Q_{compl} + Q_{dil 1} + Q_{dil 2} \quad (26)$$

The last term was considered to be negligible; therefore, it follows:

$$Q_{compl} = Q_{mix} - Q_{dil 1} \quad (27)$$

The values of lgK and Δ_rH for QCT-HP β CD complex formation have been calculated by the program HEAT developed to simultaneously calculate the enthalpies of reaction and the equilibrium constants of complex formation for systems with any stoichiometry (Borodin et al., 1985). The HEAT use and application were described in detail in previous publications for the treatment of calorimetric data of the molecular complex formation of amino acids and peptides with crown ethers and cryptand [2.2.2] mixed solvents (Usacheva and Sharnin, 2015; Usacheva et al., 2016). The algorithm for the calculation of lgK and Δ_rH used by HEAT consists in the numerical minimization of function F :

$$F = \sum_{i=1}^N \omega_i (\Delta_{compl}H - \Delta_{calc}H)_i^2 \quad (28)$$

where N is the number of experimental points; ω_i is the mass of the single measurement; and $\Delta_{compl}H$ and $\Delta_{calc}H$ are the experimental and calculated molar enthalpies of the process, respectively. In this work, all $\Delta_{compl}H$ experimental values have been considered to be determined with the same precision, so $\omega_i = 1$.

UV-Vis spectroscopy

The UV–Vis spectral data were processed using FTMT program (Borodin et al., 1985). The FTMT program applies for equilibrium modeling in solutions and data processing of spectral measurements with the purpose of determining equilibrium constants. For this, an approach based on the statistical maximum likelihood principle was used. The mathematical model of

the system sets the number and stoichiometry of the reactions, the values of the equilibrium constants, the partial molar properties of the particles or reactions and the total concentrations of the components. The calculations were performed basing the experimental dependencies of absorbance at one wavelength on the initial concentration ratio of the reagents. The molar extinction coefficients of QCT and HP β CD required for calculations in FTMT, at each pH and wavelength value, were preliminarily determined using calibration plots. The sum of mean square deviations for calculated and experimental values of optical density was in the range from 0.0001 to 0.1.

Differential Scanning Calorimetry

Aiming to verify the possible different interactions of ethanol and water with cyclodextrins, thermo-analytical tests have been run on HP β CD using a TA Q20 differential scanning calorimeter (DSC; TA Instruments, USA). In particular, DSC spectra have been obtained on HP β CD as received, and on the dry residue of HP β CD solubilized in water, ethanol and hydroalcoholic solutions (water/ethanol 9:1 and 8:2 volumetric ratios). All DSC tests have been carried out in the solid state, on the samples preliminarily dried in the hood overnight. Samples were accurately weighted (~ 5 mg) and placed in hermetic aluminum pans. Then, the samples were heated from 20 to 240 °C at 10 °C min⁻¹ under an inert nitrogen atmosphere at a constant flow rate (50 mL min⁻¹). An empty aluminum pan was used as a reference. Triplicate scans have been performed.

Chapter 4

THERMODYNAMIC STABILITY OF G4s IN ONCOGENE PROMOTERS AND THEIR INTERACTIONS WITH LIGANDS

The oncogene *KRAS* is involved in the pathogenesis of many tumors and represents thereby a relevant anticancer target. The *KRAS* P1 promoter contains a nuclease hypersensitive, guanine-rich sequence able to fold into a G4. The stabilization of this G4 structure by small molecules is emerging as a feasible approach to down-regulate *KRAS* expression. In the following, two different studies will be described on this topic.

The first research was made in collaboration with researchers of Ivanovo State University and Russian Academy of Sciences and recently published (Paper III). In that study, three water-soluble, positively charged porphyrin-like compounds were synthesized and tested for their interaction with the *KRAS* G4 by circular dichroism, fluorescence, and molecular docking calculations. For a comparison of ligands binding affinity and selectivity, TmPyP4 was taken as a reference. One out of the three tested compounds proved biological activity and selectivity for G4 over duplex DNA. It also showed to discriminate between different G4 topologies, with a preference for the parallel over antiparallel conformation. Molecular docking studies suggested a preferential binding to the 3'-end of the *KRAS* G4 driven through π - π stacking interactions. Biological assays also revealed a good photodynamic-induced cytotoxicity on HeLa cells (D'Aria et al., 2020).

The second study was the result of a fruitful collaboration between researchers of our Department and a group of the Regina Elena Cancer Institute in Rome (paper submitted).

The research is based on the identification of a set of novel stabilizing molecules through a virtual screening campaign on the *KRAS* G4 structure. CD melting experiments allowed evaluating the ligand-induced stabilization of *KRAS* G4. Several analogues of the best performing compounds were then synthesized for improving the binding affinity and the selectivity over different G4 topologies and double helix DNA. The most promising derivative

underwent fluorescence titration experiments and further computational studies to clarify its binding affinity, stoichiometry, and interaction mode. Finally, biological experiments revealed that this compound, producing an inhibitory effect on *KRAS* expression, is capable to reduce the viability of cancer cells in which activated *KRAS* drives carcinogenesis.

4.1 Study on the interaction of G-quadruplex from the *KRAS* promoter and bioactive porphyrin-based photosensitizers

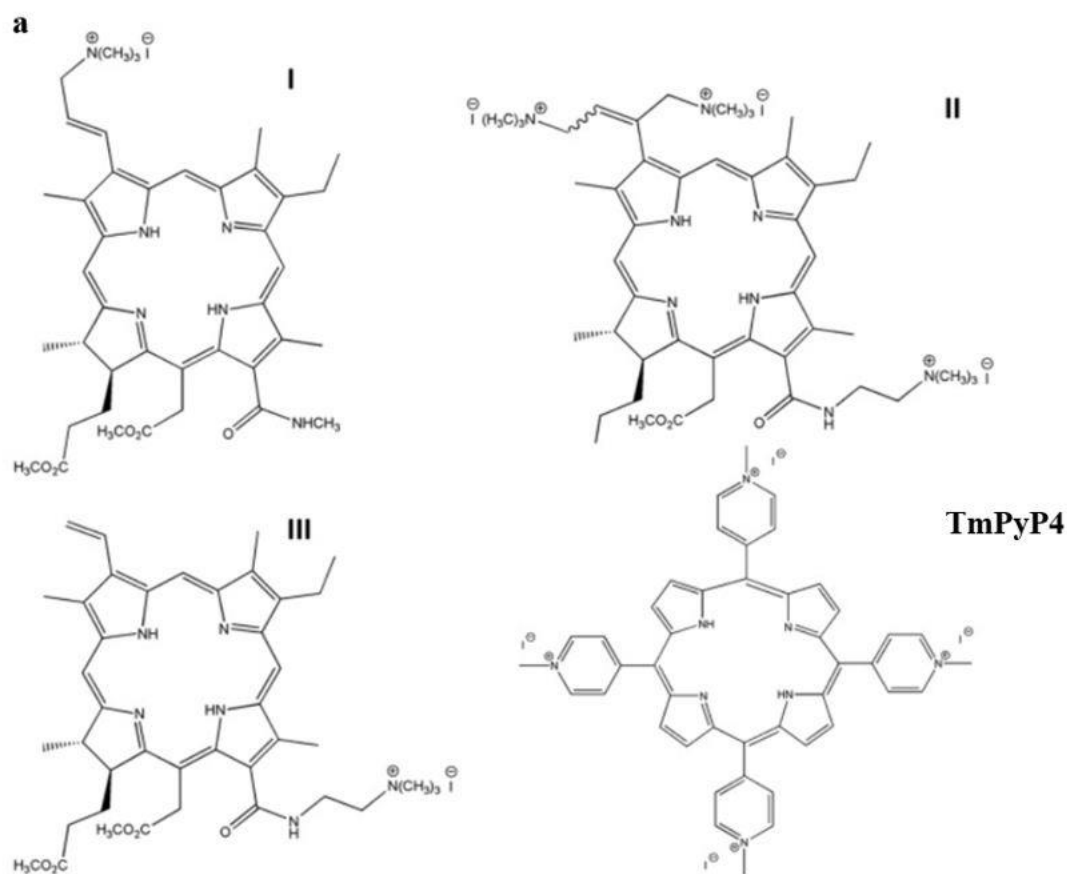
4.1.1 Introduction

Nowadays it is well known that DNA can form higher-order structures that profoundly differ from the Watson-Crick B-form. These alternative structures, triggered by different molecular environments, are now believed to act as functional signals in a number of biological processes and play important roles in the progression of several diseases (Bacolla and Wells, 2009; Zhao et al., 2010). A remarkable feature of non-canonical DNA structures is their topological polymorphism, which opens up the possibility to regulate the processes they take part in (Balasubramanian et al., 2011; Amato et al., 2014). Particularly, the higher-order DNA structures known as G-quadruplexes, are formed by guanine-rich sequences that assemble into guanine tetrads stabilized by Hoogsteen hydrogen bonds and monovalent cations (Bochman et al., 2012). Spread throughout the human genome, G4s are in the spotlight as potential druggable anticancer targets since they are enriched within key functional units, like telomeres and oncogene promoters. The stabilization of G4s by small ligands hinders telomerase-catalyzed elongation of telomeres and downregulates the expression of those genes whose promoter bears G4-forming sequences (Balasubramanian et al., 2011; Biffi et al., 2013; Murat and Balasubramanian, 2014; Moye et al., 2015). The G4-forming sequence from the *KRAS* oncogene P1 promoter stands out as a foremost example of potential anticancer G4 target, being responsible for most of the transcriptional activity (Cogoi and Xodo, 2006). *KRAS* maps at 12p12.1 (Gene ID: 3845) and encodes for a small GDP/GTP kinase (UniProt: P01116) whose point mutations account for the uncontrolled kinase activation (Hobbs et al., 2016). The mutant *KRAS* triggers several downstream pathways pushing towards uncontrolled cell proliferation, e.g. the MAPK and P13 signaling. *KRAS* is found to be the most common mutated oncogene in several cancers, particularly in colon-rectal, pancreatic, and lung cancers (di Magliano and Logsdon, 2013; Serra et al., 2014; Haigis, 2017). A direct targeting of *KRAS* and its

downstream effectors at protein level has proved difficult and unfruitful since long, mostly because of the very high affinity for GTP/GDP, although some small molecule inhibitors have been designed for an engineered *KRAS* mutant (McCormick, 2015; Zhang et al., 2018). In the search for alternative strategies, the G4-forming stretch within the *KRAS* promoter turned out to be a promising target through G4 stabilization by organic ligands (Cogoi and Xodo, 2016). The first NMR structure of this G4 was only recently reported (the 22-mer sequence bearing the 16G>T substitution for stability purpose – PDB entry 5I2V), opening the way to rational ligand design (Kerkour et al., 2017; Marquevielle et al., 2018).

Among the plethora of explored G4-binder classes, those featuring broad, planar aromatic macrocycle are the most rewarding because of hydrophobic, π - π end-stacking with the outer G-tetrad planes of G4s. Porphyrin derivatives meet these requirements and TmPyP4 (5,10,15,20-tetrakis(*N*-methyl-4-pyridyl)porphyrin) (Figure 4.1a) distinguishes in the class as the first ever G4-binder used for targeting the G4s from both the prominent *KRAS* and *MYC* oncogene promoters (Siddiqui-Jain et al., 2002; Cogoi and Xodo, 2006). Interestingly, a large body of data has shown that cationic porphyrins such as TmPyP3 and TmPyP4 also behave as photosensitizers, i.e. once irradiated with light they generate reactive oxygen species (ROS) that oxidize and degrade nucleic acids (Ren and Chaires, 1999; Freyer et al., 2007). This happens in particular at guanine, as the low ionization potential of this base makes it the major oxidation target in DNA/RNA sequences (Margolin et al., 2006; Tada-Oikawa et al., 2009).

On this basis, an attractive molecular strategy to repress oncogenic *KRAS* in pancreatic cancer cells, by combining the photosensitizing property of the porphyrin scaffold and their affinity for G-rich sequences in G4 structures, was proposed (Faudale et al., 2012). However, TmPyP4 and many of its derivatives alike, suffer from inadequate G4 vs duplex selectivity (Martino et al., 2009; Boschi et al., 2016). Thus, synthesists are seeking to design derivatives with improved binding affinity and selectivity, mostly by adding flexible aliphatic side-chains bearing positive charges that may provide further stereoselectivity and additional interactions (Romera et al., 2011).



b

KRAS G4	5'—A—G—G—G—C—G—G—T—G—T—G—G—G—A—A—T—A—G—G—G—A—A—3'
KIT-1 G4	5'—A—G—G—G—A—G—G—G—C—G—C—T—G—G—G—A—G—G—A—G—G—3'
Tel23	5'—T—A—G—G—G—T—T—A—G—G—G—T—T—A—G—G—G—T—T—A—G—G—G—3'
Hairpin	5'—C—G—A—A—T—T—C—G—T—T—T—T—C—G—A—A—T—T—C—G—3'

Figure 4.1. (a) Chemical structure of the investigated ligands and of TmPyP4. (b) List of the investigated G4-forming sequences (*KRAS* G4, *KIT-1* G4 and *Tel23*) and of the 20-mer hairpin-duplex DNA (*Hairpin*). Red-colored thymine in the *KRAS* G4 sequence represents the 16G >T substitution adopted to improve the overall G4 stability.

In this frame, we have synthesized and tested the binding properties of three porphyrin-like compounds (**I-III** Figure 4.1 a), towards the 22-mer G4-forming sequence (Figure 4.1 b) from the *KRAS* oncogene P1 promoter by means of CD and fluorescence titration. The starting scaffold chlorin e6, is a chlorophyll a derivative with a partially reduced porphyrin-like tetrapyrrolic macrocycle that is active at nanomolar range, comparable to that of verteporfin

and temoporfin: two well-known photosensitizers used in clinics (Romera et al., 2011). However, like many other photosensitizers, chlorin e6 and its ester derivatives are not very soluble in water, and this reduces the efficacy of the photodynamic therapy (PDT), a rapidly expanding therapeutic modality for treating a number of diseases, including cancer (Romera et al., 2011).

Herein, we synthesized three water-soluble, positively charged chlorin e6 derivatives (**I–III**, Figure 4.1 a), and analysed their *KRAS* G4 binding properties, particularly focusing on their selectivity for G4 over duplex DNA, and on their ability to discriminate different G4 conformations. TmPyP4 was used as a reference for ligands performance. Molecular docking calculations were also performed to support wet-lab findings. Finally, the photosensitizing properties (singlet oxygen $^1\text{O}_2$) of synthesized compounds along with their ability to induce cytotoxic effects in HeLa cells, were also investigated.

4.1.2 Results and discussion

Circular dichroism experiments

CD is a well-established method to study various aspects of G4s and of their interaction with ligands, like the presence and the overall topology adopted by a G4, and the capability of a ligand to induce a particular conformation (Berezin et al., 2015). CD is also a useful tool to investigate the thermal stability of G4s and the effect of a ligand on it.

Hence, CD was used for investigating the effects of **I–III** on the structure and thermal stability of the *KRAS* G4, as well as to check their selectivity towards other G4s and duplex DNA. TmPyP4 was also used for comparison. To check the proper folding of *KRAS* G4, its CD spectrum was recorded at 20 °C. A positive maximum at 263 nm and a negative minimum at 243 nm, which are diagnostic values of the parallel G4 topology, were observed (Figure 4.2) (Zhang et al., 2018). Next, the potential of compounds **I–III** and TmPyP4 to alter the native folding topology of *KRAS* G4 was analysed. DNA/ligand mixtures were prepared by adding an excess of each ligand to the pre-folded G4 structure. No significant variations in the CD spectrum of *KRAS* G4 were observed upon addition of each ligand. The DNA-stabilizing properties of such compounds were hence evaluated by measuring the ligand-induced change in the melting temperature (ΔT_m) of *KRAS* G4 (Figure 4.2). The results of these experiments are summarized in Table 4.1.

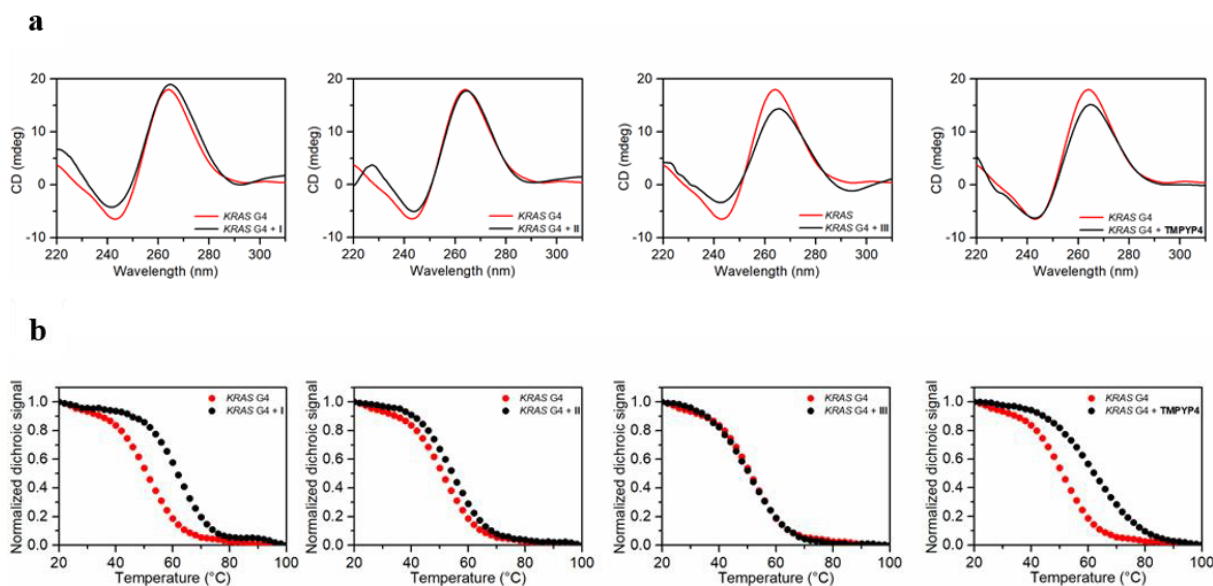


Figure 4.2. (a) CD spectra and (b) CD melting profiles of *KRAS* G4 in the absence (red) and presence (black) of each ligand (10 mol equiv. of I, II, and III; 8 mol equiv. of TmPyP4).

CD melting results show that, among the three investigated derivatives, **I** has the highest stabilizing effect on *KRAS* G4 with a ΔT_m of +11 °C. In order to compare the G4 stabilizing effect of compound **I** to that produced by TmPyP4, a CD melting experiment at 8:1 ligand/*KRAS* G4 ratio was performed, from which a ΔT_m of +10.5 °C was derived. Interestingly, this value well matches with the one observed for TmPyP4 (Table 4.1), thus indicating a similar stabilizing effect for these two ligands.

On the other hand, compound **II** induced only a negligible thermal stabilization of *KRAS* G4 ($\Delta T_m = +3$ °C) despite the presence of three positive charges. Probably, the presence of such additional charges only contributes to establish unspecific electrostatic interactions with the outer phosphate backbone, preventing **II** to effectively bind to the G4 scaffold. Compound **III** proved to be ineffective in stabilizing *KRAS* G4 altogether. We speculate that the different position and geometry of the positively charged moiety affects, in this case, the possibility of forming the additional bonds required for the overall stabilization of the G4/ligand complex.

A 20-mer hairpin-duplex DNA consisting of two self-complementary 8-mer sequences connected by a TTTT loop (*Hairpin*, Figure 4.1 b), was also investigated. The CD spectrum of such hairpin is characterized by a positive band centred at ~280 nm and a negative one at 250 nm (Figure 4.3 a) characteristic values of the duplex DNA. These bands were slightly shifted upon compound **I** addition. Conversely, compounds **II** and **III** induced significant changes to the CD band at 280 nm. In particular, no effect was observed for **I** (Figure 4.3 b), while

compound **II** was found to induce the unfolding of the duplex structure since the CD spectra of *Hairpin* in the presence of **II** at 20 and 100 °C were similar, and **III** significantly destabilized *Hairpin* (Table 4.1).

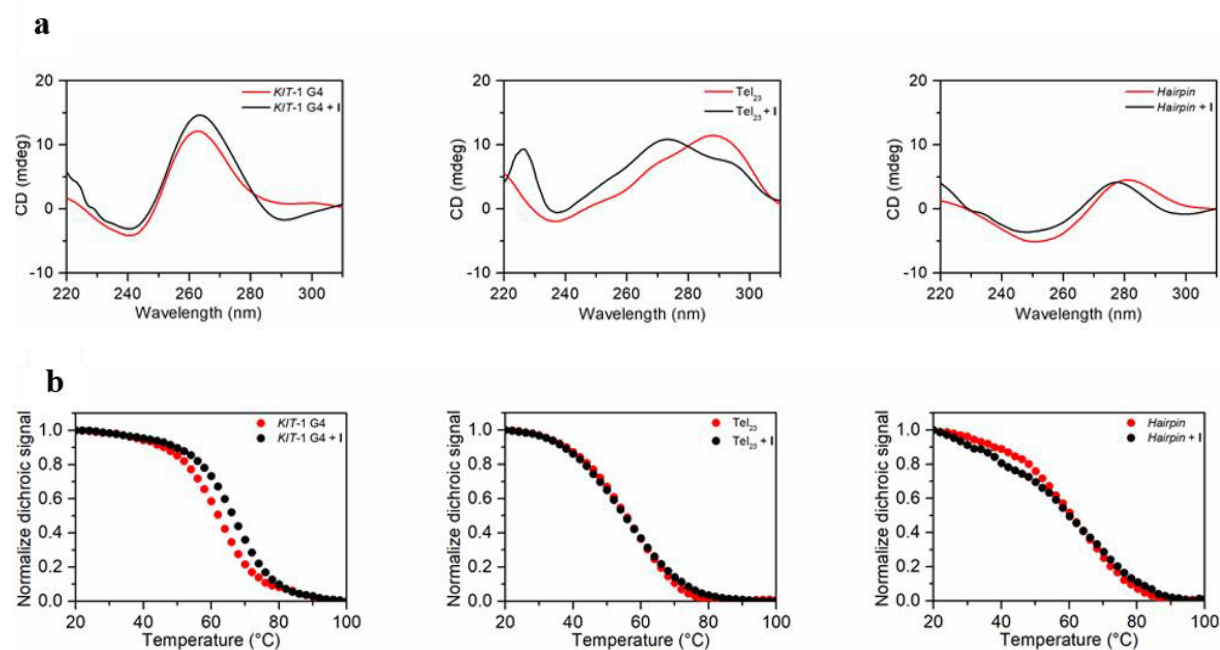


Figure 4.3.(a) CD spectra and (b) CD melting profiles for *KIT-1 G4*, *Tel23* and *Hairpin* in the absence and in the presence of **I** (10 mol equiv.) The T_m values of *KIT-1 G4*, *Tel23 G4*, and *Hairpin* in the absence of ligand were 63.0, 56.2, and 62.0 (± 0.5) °C, respectively.

Table 4.1. Ligand-induced thermal stabilization of *KRAS G4* measured by CD melting experiments.

Ligand	ΔT_m (°C) ^a	
	<i>KRAS G4</i> ^b	<i>Hairpin</i> ^b
I	+11	+1
II	+3	n.d. ^c
III	0	-21
TmPyP4	+11	n.d. ^c

^a ΔT_m values are the differences in the melting temperatures of DNA in the presence and absence of ligands. The error on ΔT_m is ± 1 °C.

^b The T_m values of *KRAS G4* and *Hairpin* in the absence of ligand were 51.0 and 62.0 (± 0.5) °C, respectively.

^c Not determined.

Overall, these results indicate **I** to be comparable to TmPyP4 in stabilizing *KRAS* G4. However, unlike TmPyP4 that is known to indiscriminately bind to G4 and duplex DNA (Ren and Chaires, 1999; Freyer et al., 2007; Brito et al., 2015b), **I** turned out to be selective.

A thorough characterization was then brought on solely for **I**, which was checked for its specificity towards other G4 structures. For this purpose, *KIT-1* and Tel₂₃ G4s were used as examples of parallel and antiparallel G4 conformations, respectively. First, CD spectra of these DNA sequences were recorded to verify their folding topologies (Figure 4.3 a). The CD spectrum of *KIT-1* G4 showed a positive band at 260 nm and a negative one at 240 nm, in agreement with the formation of a parallel G4 conformation. On the other hand, Tel₂₃ displayed a positive band at around 290 nm with a shoulder at 270 nm, and a negative band at 240 nm, according to the formation of an antiparallel (3+1) hybrid G4.

As deducible from its relative CD signature, no significant conformational changes occur to *KIT-1* G4 upon addition of **I**. Conversely, **I** induced significant changes in the CD spectrum of the Tel₂₃ G4 structure, with the decrease of the band at 290 nm and the increase of the intensity of the band around 270 nm, thus suggesting a hybrid-to-parallel conformational change.

As far as thermal stabilization effects are concerned, **I** was found to stabilize *KIT-1* G4 to a smaller extent ($\Delta T_m = +5$ °C) than *KRAS* G4, while no effects were observed for Tel₂₃ G4 (Figure 4.3 b). Interestingly, these results indicate the ability of **I** to discriminate among different G4 topologies, with a preference for the parallel conformations, and in particular for the *KRAS* G4 structure. This is also in agreement with the observed hybrid-to-parallel conformational change induced by **I** on Tel₂₃ G4.

Förster resonance energy transfer (FRET) melting assay

FRET melting analysis has been used to estimate the G4 over duplex selectivity of compound **I** and TmPyP4 (Giancola and Pagano, 2012). The doubly-labeled F-*KRAS*-T G4-forming sequence was used. FRET experiments were performed both in the absence and presence of competing *Hairpin*. FRET-melting curves (Figure 4.4) confirmed that both **I** and TmPyP4 are able to stabilize the F-*KRAS*-T G4 structure ($\Delta T_m > 15$ °C). Moreover, compound **I** showed a good degree of selectivity for the G4 over the duplex, with ΔT_m decreased by $0.7(\pm 0.6)$ °C in the presence of 10-fold excess of competing duplex (2 μ M) and of $1.7(\pm 1.0)$ °C at the level of a 50-fold excess of the duplex (10 μ M). Conversely, TmPyP4 showed less

preference to bind to G4 compared to duplex DNA. Indeed, a strong decrease of T_m of the ligand-G4 complex was observed in the presence of competing duplex (Figure 4.4).

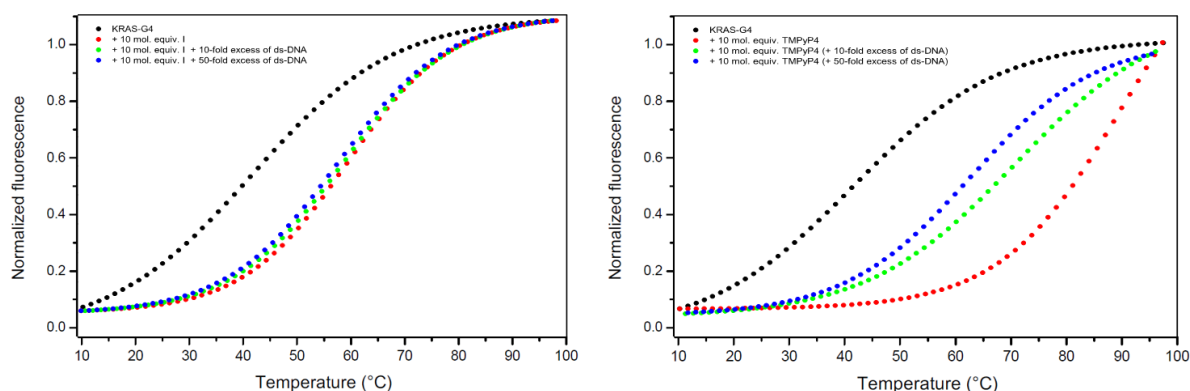


Figure 4.4. FRET-melting curves of F-KRAS-T G4 (0.2 μM) in the absence (black line) and in presence of compound **I** (left panel) and TmPyP4 (right panel) without (red line) and with 2.0 μM (green line) and 10.0 μM (blue line) hairpin-duplex DNA competitor.

Fluorescence binding experiments

Fluorescence titration experiments were carried out to quantify the ligand binding affinity for *KRAS* G4 and *KIT-1* G4. Fluorescence emission spectra of **I** in the absence and presence of increasing amount of G4s were recorded. Compound **I** has a fluorescence maximum at 668 nm when excited at 504 nm. A decrease in fluorescence intensity upon increasing DNA concentration was observed in both *KRAS* G4 and *KIT-1* G4 titrations. The binding constants were then determined from the variation of the fluorescence intensities. In particular, the binding curves were obtained by plotting the fraction of bound ligand (α) as a function of G4 concentration (Figure 4.5), and binding constants (K_b) were obtained by curve fitting to an independent and equivalent binding sites model, by means of a nonlinear regression algorithm. The results of this interpolation analysis indicate in both cases a 1:1 ligand/DNA stoichiometry, and K_b values of $17.8(\pm 4.4) \times 10^6$ and $1.9(\pm 0.6) \times 10^6 \text{ M}^{-1}$ for *KRAS* G4 and *KIT-1* G4, respectively, thus indicating a higher affinity of **I** for *KRAS* than *KIT-1* G4.

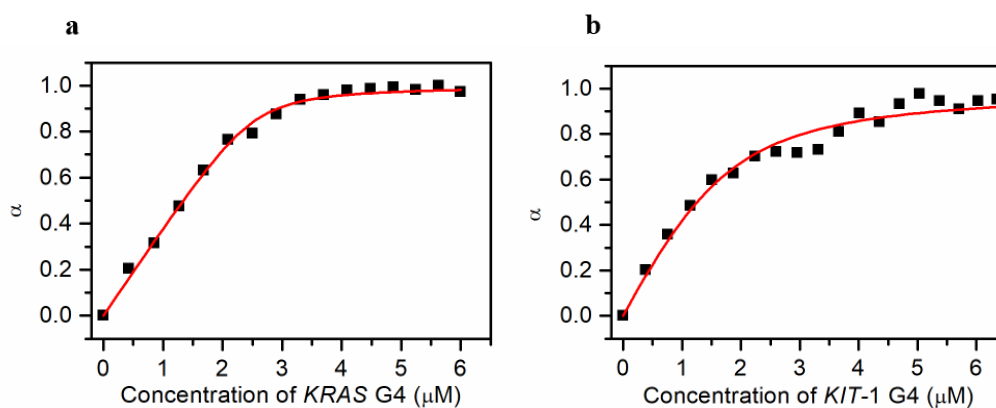


Figure 4.5. Fluorescence titration curves obtained by plotting the fraction of bound I (α) as a function of (a) *KRAS* G4 and (b) *KIT-1* G4 concentration. The experimental data (black squares) were fitted using an independent and equivalent-sites model (red lines).

Binding mode by molecular docking

Molecular Docking calculation served to further evaluate the binding mode of **I** with either *KRAS* G4 or *KIT-1* G4, exploiting the recently deposited *KRAS* G4 NMR (PDB entry 5I2V) and the *KIT-1* G4 (PDB entry 3QXR) structures. The NMR structure was also filed for *KIT-1* G4 but even though the NMR structure represents a reliable model for the *KIT* G4 *in vivo*, no significant difference occurs to the end of docking calculation, in particular at the 5' side. As for the 3' end, the NMR structure shows a slightly more relaxed loop conformation, which did not return better docking scores as compared to the X-ray structure at the 3' site ($-7.0 \text{ kcal mol}^{-1}$). The X-ray and NMR deposited models for the *KIT* G4 are significantly overlapping, with RMSD as low as 0.828 Å using Needleman-Wunsch nucleic matrix when not accounting for the residues 16-22 loop. RMSD goes up to 0.987 including the loop (data not shown). Given the limitations of molecular docking, no relevant differences were to be expected by using either structures. Figure 4.6 depicts the most energetically favoured binding poses (-7.9 and $-8.2 \text{ kcal mol}^{-1}$ for *KRAS* G4 and *KIT-1* G4, respectively). In both cases, docking models are consistent with the 1:1 stoichiometry found by fluorescence titrations, with the interaction widely driven by π - π end-stacking interactions, since the energetics of the poses on the opposite outer tetrad are severely unfavoured ($-5.6 \text{ kcal mol}^{-1}$ for *KRAS* G4, whereas no pose was found for *KIT-1* G4 – not shown). The 1:1 stoichiometry can be explained by the differences existing between the outer G4 planes. In the case of *KIT-1* G4, this is conceivably due to the hindrance to ligand interaction from the loop that crosses one of the planes. *KRAS* G4 does not feature such long, interfering loop, yet the outer G4 plane on the 5' side is less accessible to the solvent than its 3'

counterpart because of hindrance from A1 and A17. A17 is “locked” by the stacking interactions it engages with the G4 plane below, whereas A1 is seemingly less restricted to move. Although A22 is sub-orthogonal to the 3′ G4 plane with which it interacts by H-bond between N6 and O6 of either G4 or G20, this plane is still more accessible than its 5′ counterpart. A22, and A21 alike, are therefore relatively free to flip and the ligand might compete for the G4 with ease. The binding face of *KIT-1* G4 has a similar condition with A1 and C12 stacking on the G4 plane. As in the case of *KRAS* G4, A1 is free to flip whereas C12 is stuck on the G4 plane. Anyhow, these inferences have to be taken carefully as conclusive given the intrinsic limitations of molecular docking and some concerns over the deposited 5I2V NMR structure (whose A21 and A22 appear in a very unstable arrangement). Furthermore, the system does not include any significant number of flanking bases as compared to the in-vivo system, whose behaviour might sizably differ.

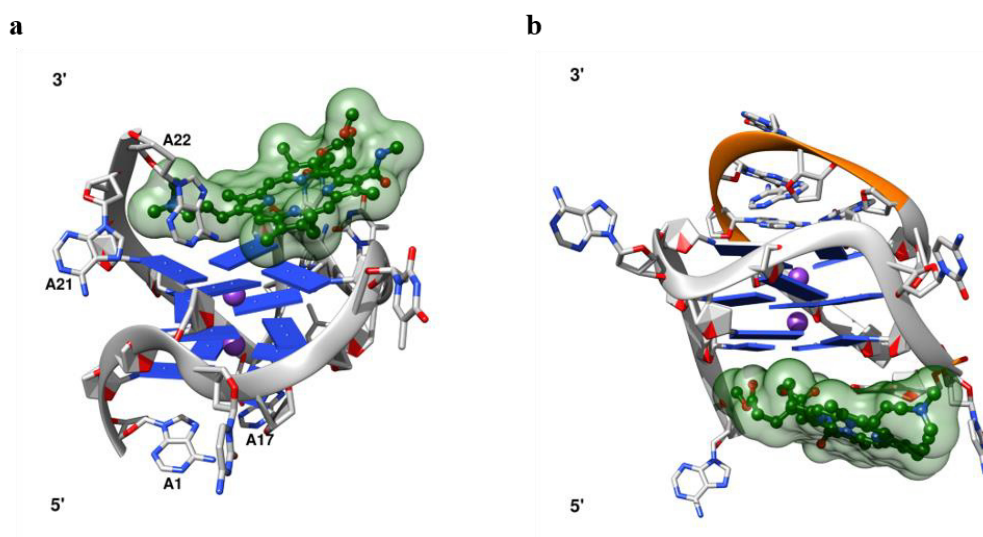


Figure 4.6. Best scoring docking poses of I with *KRAS* G4 ($-7.9 \text{ kcal mol}^{-1}$, left) and *KIT-1* G4 ($-8.2 \text{ kcal mol}^{-1}$, right). Residues engaged in guanine-tetrads are represented and filled slabs. The *KIT-1* G4 loop hindering the 3′ tetrad is highlighted in orange.

Generation of singlet oxygen

One of the most important properties of any photosensitizer is generation of singlet oxygen or other reactive oxygen species. The direct estimation of the quantum yield (γ_{Δ}) and lifetime of $^1\text{O}_2$ from compound I in pyridine and 1-octanol was performed by measuring the NIR luminescence emission of $^1\text{O}_2$ at around 1270 nm, which is considered as the “gold standard” for PDT dosimetry. The corresponding γ_{Δ} values are listed in Table 4.2. The results obtained

for compound **I** are in a good agreement with those of **II** and **III** reported by some of us in a previous study (Kustov et al., 2018), and also fall within the range of γ_{Δ} values ($\gamma_{\Delta} = 0.55 \pm 0.1$) observed for any chlorophyll photosensitizer in any weakly polar solvent.

Table 4.2. Quantum yield of singlet oxygen $^1\text{O}_2$ for I–III in 1-octanol and pyridine.^a

Compound	Solvent	
	1-Octanol	Pyridine
I	0.66	0.62
II	0.53 ^b	0.59 ^b
III	0.65 ^b	0.56 ^b

^a Experimental errors are estimated to be within 10%.

^b These values were from (Kustov et al., 2018).

Photodynamic activity of compounds I–III in HeLa cells

The photodynamic activity of **I–III** in HeLa cell line was also evaluated. Results of such experiments, reported in Table 4.3, reveal several important features of these compounds. In particular, we observed no dark-toxicity for compound **II**. We speculate that **II**, having three cationic sidechains, may be not able to efficiently penetrate HeLa cell membranes, due to its high hydrophilicity. As for the other compounds, **I** showed a low dark-toxicity at 10 μM concentration, while **III** displayed a larger dark toxic effect towards cancer cells when used at 10 μM . On the other hand, by irradiating with red light, some damage towards cancer cells was observed with **II**, but its effect was small. Conversely, the mono-cationic compounds **I** and **III** displayed a good photodynamic effect providing the inactivation of 72 and 97% of tumor cells for **I** and **III**, respectively. The killing effect for **III** was larger, however, its dark toxicity was also more pronounced. This may be ascribed to the unspecific binding of **III** to duplex DNA, with consequent off-target effects.

Table 4.3. Survival indexes for HeLa cells after treatment with compounds I–III (CPS, μM) in the dark and under irradiation with the light dose of 12 J cm^{-2} .^a

Compound	Dark toxicity			Photo-induced toxicity
	10 μM	1 μM	0.1 μM	1 μM
I	82.39 ± 3.37	100.64 ± 3.49	101.03 ± 1.71	28.02 ± 2.61
II	112.24 ± 6.98	118.96 ± 5.82	137.32 ± 4.71	84.09 ± 2.95
III	24.16 ± 2.34	93.90 ± 2.54	109.60 ± 2.73	3.17 ± 0.04

^a Survival index denotes the ratio between the number of living cells in the photosensitizer containing solution and the number of such cells in control, multiplied by 100. Uncertainties represent twice standard deviation.

4.1.3 Conclusions

The discovery of photosensitizer molecules able to selectively interact with specific noncanonical DNA structures, like G4s, could represent an important strategy to enhance the effectiveness of the PDT treatment while preventing the toxicity effects due to off-target effects. G4-forming sequences are found in the promoter regions of many oncogenes where they are deeply involved in the regulation of their transcriptional activity and, therefore, in the development and progression of cancer. This notion is pushing towards the development of G4-targeting ligands as potential anticancer drugs. However, there are no approved anticancer drugs targeting such noncanonical DNA structures to date. This is at least in part due to the non-specific binding of most of G4 ligands to duplex and/or other DNA structures (Pagano et al., 2018). Moreover, all ligands bind to a target G4 reversibly, leading only to a transient effect on the expression of the respective oncogene (Amato et al., 2018). In this context, the use of photosensitizers could represent an interesting approach to fight cancer by employing selective G4 binders that can irreversibly attack the target.

In this work, we have evaluated the interaction of three porphyrin-like photosensitizers with G4-forming DNA sequences. All three compounds were found to generate ROS in weakly polar media. Among them, compound **I** was shown to selectively stabilize G4 over duplex DNA and also displayed a marked preference for binding to parallel G4s (especially *KRAS* G4) over antiparallel ones. Indeed, CD experiments showed that **I** is a good *KRAS* G4 stabilizer that does

not affect the pre-existing architecture of the target G4 upon interaction. For this reason, its binding to G4s was investigated in more detail. Fluorescence experiments provided the binding constant K_b of $17.8 \pm 0.5 \times 10^6 \text{ M}^{-1}$ of **I** to the *KRAS* G4 and a 1:1 drug/DNA binding stoichiometry. Molecular docking results provided further insights into the recognition between **I** and the *KRAS* G4, highlighting the possible key structural elements involved in the interaction. Results of biological assays also revealed a strong enhancement of **I** activity on HeLa cells upon light exposure, providing the inactivation of around 72% of tumor cells.

Altogether, the reported results indicate that compound **I** could actually give the basis for the development of G4 ligands with effective photodynamic-induced cytotoxicity on cancer cells. The number and the position of cationic side chains can improve G4 ligand selectivity still preserving biological activity, to accomplish the desired result of achieving new potent but less toxic anticancer drug candidates.

4.1.4 Experimental section

Material and methods

Oligonucleotides were purchased from Biomers.net GmbH (Ulm/Donau, Germany). All common chemicals, reagents and solvents were purchased from Sigma Aldrich (Merck group) unless otherwise stated. ^1H NMR spectra were recorded on a Bruker Advance II spectrometer (300 MHz). CDCl_3 and $\text{DMSO-}d_6$ were used as appropriate solvents and TMS as internal standard for ^1H NMR measurements. Mass spectra were obtained with a Thermo Finnigan LCQ Flut (ESI) instrument and a MALDI FAB MS-spectrometer AXIMA Confidence (Shimadzu) using α -cyano-4-hydroxycinnamic acid (CHCA) as matrix. UV-Vis spectra were obtained at 25 °C on a Drawell G9 spectrophotometer using highly diluted compound solutions (~10 μmol).

Oligonucleotide purification and sample preparation

Synthetic oligonucleotides were purified by high performance liquid chromatography (HPLC) on a Nucleogel SAX column (Macherey–Nagel, 1000–8/46), using buffer A (20 mM $\text{KH}_2\text{PO}_4/\text{K}_2\text{HPO}_4$, 20% (v/v) CH_3CN at pH 7.0), and buffer B (1 M KCl, 20 mM $\text{KH}_2\text{PO}_4/\text{K}_2\text{HPO}_4$, 20% (v/v) CH_3CN at pH 7.0). A 30 min linear gradient from 100% A to 100% B with a 1 mL min^{-1} flow rate was used. The isolated oligomers were further desalted by Sep-pak cartridges C-18 (Waters) and lyophilized. DNA samples were then dissolved in 20 mM KH_2PO_4 buffer (pH 7.0) containing 60 mM KCl and 0.1 mM EDTA. The concentration of

oligonucleotides was determined by UV adsorption at 90 °C, using molar extinction coefficient values ϵ ($\lambda = 260$ nm) calculated by the nearest neighbour model (Cantor et al., 1970). Samples were then annealed by heating the solution at 90 °C for 5 min, then gradually cooled to room temperature, and finally incubated for 24 h, at 4 °C before data acquisition.

Circular dichroism experiments

CD experiments were performed on a Jasco J-815 spectropolarimeter (JASCO Inc., Tokyo, Japan) equipped with a PTC-423S/15 Peltier temperature controller. CD spectra were recorded at 20 °C in the wavelength range of 220–300 nm and averaged over three scans. The following parameters were used: 100 nm min⁻¹ scan rate, 4 s response time and 1 nm bandwidth. Buffer baseline was subtracted from each spectrum. A 2 μ M oligonucleotide concentration was used. CD melting experiments were carried out in the 20–100 °C temperature range at 1 °C min⁻¹ heating rate, following changes of CD signal at the wavelength of maximum intensity (263 nm for *KRAS* and *KIT-1* G4s, 288 nm for Tel23 G4, and 280 nm for hairpin-duplex DNA). The melting temperatures (T_m) were determined from curve fit using Origin 7.0 software. CD spectra and melting experiments were recorded both in the absence and presence of each ligand. DNA/ligand mixtures were obtained by adding 10 mol equiv. (20 μ M) of **I–III** to the folded DNA structures. TMPyP4 was used at 8:1 ligand/DNA ratio, since at higher ligand concentrations a turbidity of the relative solution occurred. The stock solutions of ligands were 10 mM in DMSO. ΔT_m values were determined as the difference in the melting temperature of the DNA structures with and without ligands. Each experiment was performed in duplicate and the reported values averaged.

Förster resonance energy transfer melting assay

A FP-8300 spectrofluorometer (Jasco) equipped with a Peltier temperature controller accessory (Jasco PCT-818) was used to run FRET melting assays. Experiments were performed by using the G4 forming sequence F-*KRAS*-T, which has the donor FAM (6-carboxyfluorescein, F) and the acceptor TAMRA (6-carboxytetramethylrhodamine, T) fluorophores covalently attached. Labeled oligonucleotide was purchased from Biomers (Germany) and used without further purification. F-*KRAS*-T was prepared as a 1 μ M solution in 20 mM KH₂PO₄ buffer (pH 7.0) containing 60 mM KCl and 0.1 mM EDTA, then annealed by heating to 90 °C for 5 min and followed by cooling to room temperature overnight, and

finally stored at 4 °C for 24 h before data acquisition. Measurements were performed exciting at 492 nm and detecting at 522 nm in a sealed quartz cuvette with a path length of 1 cm. Both slits were set at 5 nm. The final concentration of F-*KRAS*-T G4 was 0.2 μM. Experiments were performed in the presence of compound **I** (2.0 μM) without and with 2.0 or 10.0 μM of the 20-mer hairpin duplex DNA (*Hairpin*) competitor. In addition, a blank with no compound or competitor was also analyzed.

The fluorescence melting of F-*KRAS*-T G4 was monitored at 0.5 °C min⁻¹ over the 10–100 °C range. FAM emission was normalized between 0 and 1. Data analysis was carried out using Origin 7.0 software.

Fluorescence titration experiments

Fluorescence experiments were performed at 20 °C on a Varian Cary Eclipse (Varian Inc., CA, USA) spectrofluorometer equipped with a Jasco PCT-818 Peltier (Jasco Inc., MA, USA) temperature controller accessory. A 1 cm path length, sealed quartz cuvette was used. Both excitation and emission slits were set at 5 nm. The titrations were carried out by stepwise addition (5 μL) of a DNA solution (100 μM) to a cell containing a fixed ligand concentration (2 μM). Excitation wavelength was set at 504 nm and emission spectra were recorded in the wavelength range of 514–750 nm. After each addition of DNA, the solution was stirred and allowed to equilibrate for 5 min before data collection. The fraction of bound ligand (α) at each point of the titration was calculated following fluorescence changes at the maximum of intensity. Titration curves were obtained by plotting α as a function of the DNA concentration. The equilibrium binding constants (K_b) were estimated by fitting the resulting curves to an independent and equivalent binding site model (Giancola and Pagano, 2012). The experiments were repeated in triplicate, and the results are presented as the mean \pm SD

Molecular docking

Molecular docking calculations were brought out using as target models the NMR structure of *KRAS* G4, and the X-ray structure of *KIT*-1 G4 (PDB entries 5I2V and 3QXR, respectively). The 2D model of **I** was drawn using ChemDraw and the 3D coordinates were generated by the online SMILE Translator service. DockPrep tool from Chimera package was used for preparing the structures and the ligand, for Gasteiger partial charges assignment and polar hydrogens addition (Lang et al., 2009). All torsions were set as rotatable.

Box grids encompassing the whole G4s were defined and centred by AutoDock Tools (100 × 100 × 100 at 27.25, y = 27.37, z = 23.00 for *KRAS* G4; 70 × 70 × 70 at x = -4.50, y = 11.67, z = -11.09 for *KIT-1* G4). Ten AutoDock Vina 1.1.2 (Trott and Olson, 2009) runs for each model were performed by using random seeds, exhaustiveness 20, with each run returning 20 poses. The *KRAS* G4 underwent 500 conjugated gradient minimization steps prior docking.

Singlet oxygen quantum yield determination

The singlet oxygen ($^1\text{O}_2$) quantum yield (γ_Δ) of compounds **I–III** was determined as previously described (Berezin et al., 2015; Kustov et al., 2018). Time-resolved photoluminescence of $^1\text{O}_2$ was measured at 1270 nm using the LIF-200 pulsed laser fluorimeter equipped with a nitrogen laser. A pulse frequency of 30 Hz, 20 μJ of energy and 2 ns impulse duration were used. The γ_Δ values were estimated both in pyridine and 1-octanol with a comparative method using *meso*-tetraphenylporphyrin as an appropriate standard (Kustov et al., 2018):

$$\frac{\gamma_\Delta}{\gamma_{\Delta st}} = I_0 \cdot \frac{D}{I_{0st}} \cdot D_{st} \quad (29)$$

where γ_Δ , I_0 , D and $\gamma_{\Delta st}$, I_{0st} , D_{st} were the quantum yield, the initial intensity of luminescence obtained from decay kinetics at $\tau = 0$, and the optical density of a solution of an appropriate photosensitizer and H2TPP, respectively.

Biological assays

Toxicity of **I–III** towards tumor cell lines in the dark and under light irradiation was investigated using the HeLa cell model. HeLa cells were cultured at 37 °C in the DMEM/F12 growth medium (PAA Laboratories GmbH, Cölbe, Austria) containing 10% v/v of fetal bovine serum (FBS) (HyClone, Logan, UT, USA) without antibiotics and under 5% CO_2 . All manipulations were similar to those described before (Pylyna et al., 2017). Briefly, compounds **I–III** were dissolved in pure DMSO (Amresco, USA) and an appropriate amount of their stock solution was added to the growth medium containing 5000 cells for each plate, in order to reach final photosensitizer concentrations between 0.1 and 10 μM . Experiments to determine dark toxicity were run incubating the plates with HeLa cells for 72 h in the dark. For the analysis of light toxicity, cells incubated with the appropriate photosensitizer were exposed to red light for

20 min. A light diode panel emitting at $\lambda = 662 \pm 15$ nm and a total light dose of 12 J cm^{-2} were used. After irradiation, cells were incubated again for 70 h. Next, growth medium was removed, and cell culture washed with 200 μL of phosphate buffer solution (PBS). Immediately, 100 μL of a fluorescein diacetate solution (Sigma, USA) was added into each well and the plates were left inside the CO_2 incubator for 40 min. The relative number of living cells was determined by means of fluorescence intensity measurements using the “Fluorat-02-Panorama” spectrofluorometer (LTD “Lumex”, Russia) (Pylina et al., 2017). Excitation and emission wavelengths were set at 485 nm and 520 nm, respectively. Cell survival (%) was evaluated as ratio of the fluorescence intensity measured in the well containing the investigated compound with respect to the control well containing pure DMSO. All experiments were repeated 8–10 times.

4.2 Discovery, Synthesis, Physicochemical Studies and Biological Evaluation of Novel Ligands Targeting the G-Quadruplex in the KRAS Proto-oncogene

4.2.1 Introduction

As mentioned above, the NHE within the *KRAS* P1 promoter features a G-rich sequence that folds into a G4 whose stabilization by small molecules offers a convenient alternative to downregulate *KRAS* at gene-level (Jordano and Perucho, 1986; Hoffman et al., 1990; Cogoi et al., 2008; Cogoi and Xodo, 2016). Diverse classes of compounds have been tested to this end, such as porphyrins, acridines, anthraquinones, phenanthrolines, perylenes and quinolines (Monchaud and Teulade-Fichou, 2008; Alzeer et al., 2009; Lavrado et al., 2015; Boschi et al., 2016; Calabrese et al., 2018; Carvalho et al., 2018; Pattanayak et al., 2018; D’Aria et al., 2020). The majority of these compounds share polycyclic and heteroaromatic moieties that grant decent selectivity over the duplex DNA, mainly due to stronger π - π stacking interactions with the guanine tetrads.

Herein, initially, the thermal stability of *KRAS* G4 (Kerkour et al., 2017) was studied by CD and DSC. Then, using the recently solved NMR structure of the *KRAS* G4 a structure-based virtual screening (VS) was performed with the aim to find novel chemotypes as *KRAS* G4 stabilizers. Subsequently, the most promising VS hits were tested for their binding and stabilizing abilities by thermal melting experiments. The best performing compounds were then selected for likewise lead optimization program. The newly synthesized molecules were again

evaluated for their *KRAS* G4 stabilizing properties and then assayed for selectivity toward both diverse G4 topologies and duplex DNA, i.e. the G4 from the *KIT* promoter (*KIT* G4; sequence: AGGGAGGGCGCTGGGAGGAGGG), the 23-mer telomeric G4 (Tel23; sequence: TAGGGTTAGGGTTAGGGTTAGGG), and the 20-mer hairpin DNA (sequence: CGAATTCGTTTTTCGAATTCG). The best performing derivative underwent further fluorescence assays and molecular dynamics calculations to gain insight into the stoichiometry and binding affinity of its interaction with *KRAS* G4 and to disclose its binding mode to this DNA motif. Finally, biological analyses revealed that the selected compound, **19**, is effective in downregulating *KRAS* gene expression, with a consequent cytotoxic effect in cancer cells in which activated *KRAS* acts as a driver oncogene. Altogether, these data indicate our compound as a very promising template to generate a new class of potent and selective G4-ligands for *KRAS* targeting in anticancer therapy.

4.2.2 Results and discussion

Thermodynamic stability of *KRAS* G4

The *KRAS* G4 was studied using CD and DSC to determine its thermodynamic stability to be used as a reference for assessing ligands performances.

CD spectroscopy was used to record the CD spectrum and the CD melting curve of *KRAS* G4. The CD spectrum of *KRAS* G4 solution was recorded in the 220-360 nm range at 20 °C (Figure 4.7).

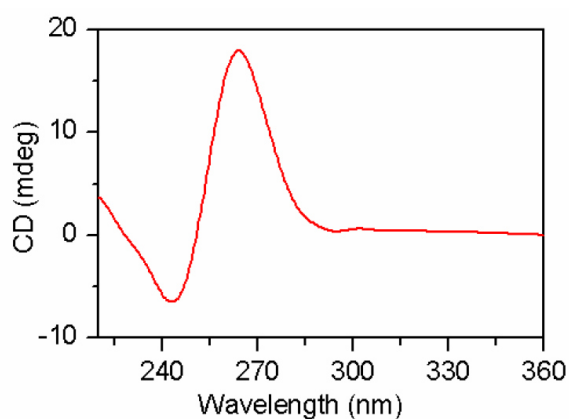


Figure 4.7. CD spectrum of *KRAS* G4

The spectrum exhibits the typical peaks of a parallel G4, i.e. maximum at 264 nm and minimum at 241 nm.

CD heating/cooling profiles were recorded in the 20–100 °C range at 1 °C/min heating rate using the same solution (Figure 4.8):

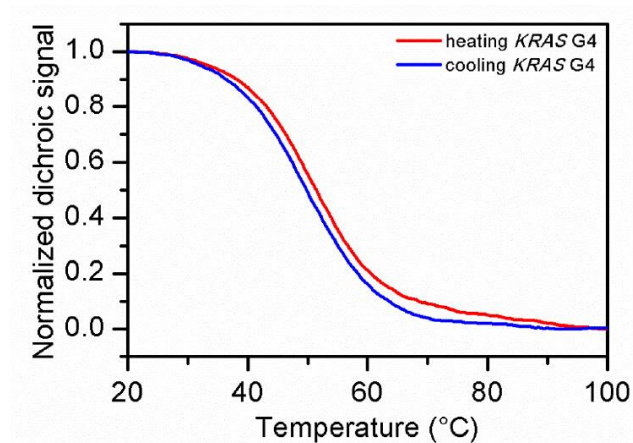


Figure 4.8. CD heating/cooling profiles of *KRAS G4*

The heating/cooling profiles overlap indicating a reversible process. The T_m was determined as 51 ± 0.5 °C.

DSC experiments were carried out to study the thermodynamic stability of *KRAS G4*. The obtained DSC melting profiles are shown in Figure 4.9.

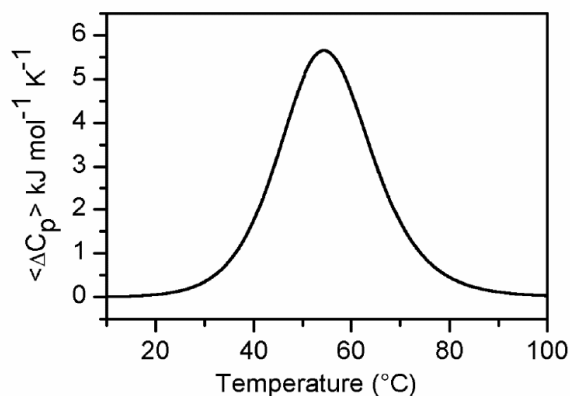


Figure 4.9. DSC curve of *KRAS G4*

The G4 thermodynamic parameters derived from this curve are reported in Table 4.4.

Table 4.4. Thermodynamic parameters* for *KRAS* G4 determined by DSC.

ΔH° (kJ/mol K)	ΔS° (kJ/mol K)	$\Delta G^\circ_{37^\circ\text{C}}$ (kJ/mol)	T_m ($^\circ\text{C}$)
150	0.459	13	53

*The error on thermodynamic parameters is within 5%. The error on T_m is ± 1 .

As reported in literature, each G-tetrad contributes an average $\sim 60\text{--}80$ kJ/mol to a total ΔH° (Mergny et al., 2006).

The obtained ΔH° value is slightly lower than expected. This could be due to a not optimal G-quartet stacking interactions.

The $\Delta H^\circ_{\text{VH}}$ is comparable to the ΔH° , that indicated a two-state transition. In agreement with CD, DSC indicates a reversible transition as successive scans overlap.

Virtual screening

As briefly reported in the introduction, the solved *KRAS* G4 NMR structure (PDB code: 5I2V (Kerkour et al., 2017)) was here used as target for a structure-based virtual screening campaign aimed at identifying brand new *KRAS* G4 stabilizers. Indeed, this G4 motif possesses two wide stacking surfaces and four grooves of medium size that can potentially be recognized by small organic molecules (Kerkour et al., 2017). For VS calculations, we employed the Glide software (Friesner et al., 2004; Halgren et al., 2004) to dock compounds from both an in-house virtual library and the commercial Asinex Platinum Collection database. Notably, the latter library is composed of all the compounds designed so far by our research group against common anticancer targets including kinases, integrins, chemokine receptors and nucleic acids. Advantageously, these compounds are either already available in stock or can be easily resynthesized. Moreover, for many molecules, a number of analogues are already present allowing a rapid structure-activity relationship analysis. Both the libraries only included compounds endowed with lead-like pharmacokinetic properties, according to the Lipinski's rule of five. For each of these molecules, the possible tautomeric and protonation states in the pH range 7.4 ± 1.5 were predicted. Then, the libraries were filtered to discard all the neutral and negatively charged compounds and all the molecules featuring less than two aromatic rings. In fact, positively charged moieties and extended aromatic systems are generally required to establish favorable contacts with the DNA phosphate backbone and with the G-tetrads stacking

surfaces, respectively (Di Leva et al., 2013, 2014; Castillo-González et al., 2015). Thus, two final subsets of 875 and 14,510 potential ligands were obtained and submitted to VS calculations. The search area included the whole *KRAS* G4 structure, and the Glide Standard Precision (SP) scoring function (Friesner et al., 2004; Halgren et al., 2004) was used to perform docking and score the predicted binding modes. For each compound, only the best scored docking pose was selected. For each database, the best 15% of the ranked solutions was subjected to a careful visual inspection to evaluate the predicted interaction mode with *KRAS* G4. In particular, the formation of π -stacking or polar interactions (i.e. salt bridges) with the target DNA was evaluated. Finally, the selected compounds were further inspected for good chemical binding geometry. Based on these criteria, 12 hits, 4 chosen from the in-house database (**1-4**, Figure 4.10) and 8 selected from Asinex Platinum Collection library and then purchased from the vendor (**5-12**, Figure 4.10), were tested in biophysical assays to verify their G4 binding properties.

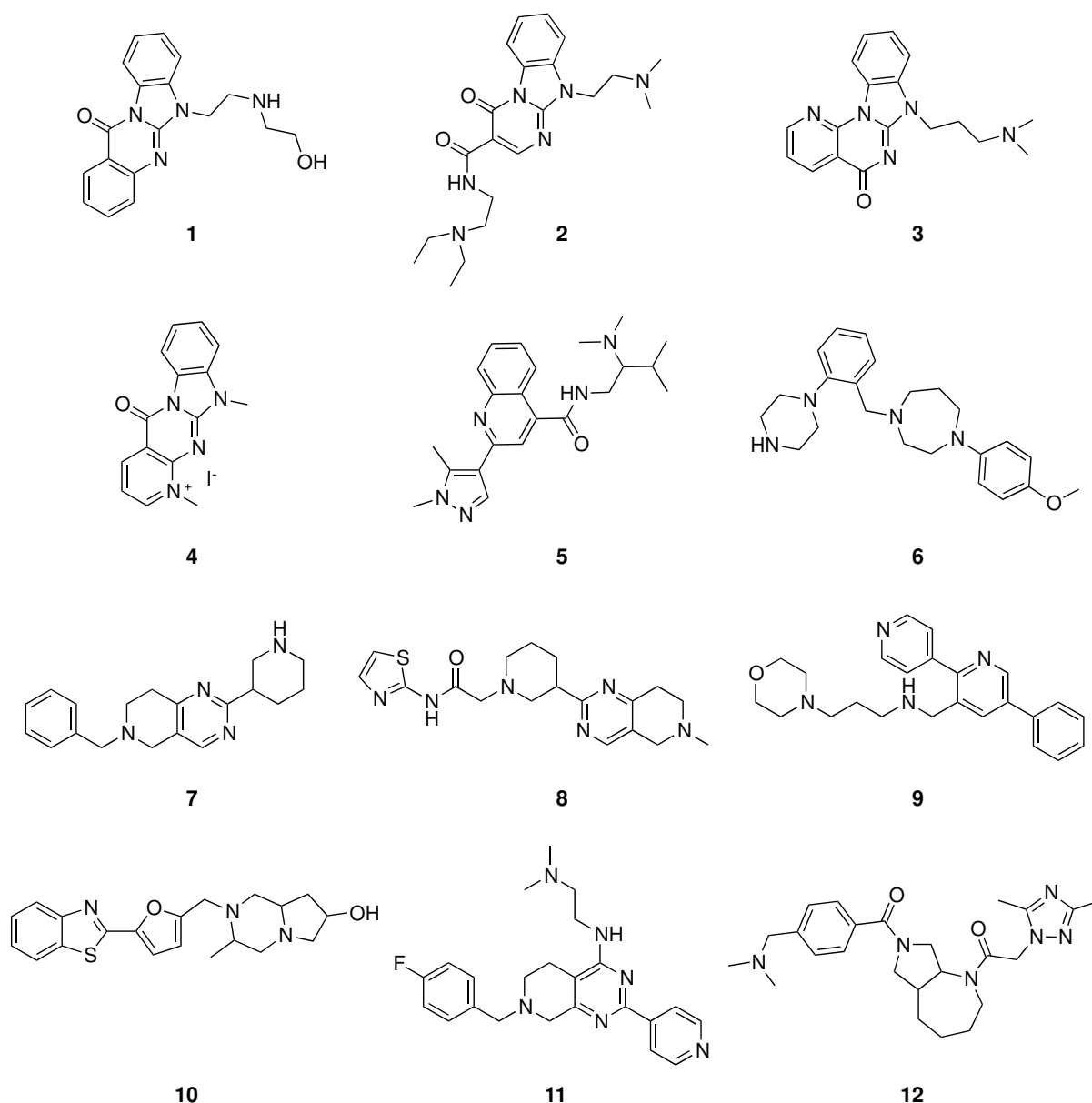


Figure 4.10. Chemical structures of VS hits 1-4 from the in-house library and 5-12 from the Asinex Platinum Collection.

CD Experiments of the selected hits (1-12) with *KRAS* G4

Initially, the conformation of *KRAS* G4 was proved by circular dichroism (CD) spectroscopy. The CD spectrum displayed a positive band at 264 nm and a negative band at 240 nm, which is the characteristic CD profile of parallel-stranded quadruplexes (Zhang et al., 2010). Notably, no CD spectra change has to be reported for *KRAS* G4 upon ligand binding.

The stabilizing effect of each of the selected hits (1-12) on *KRAS* G4 was then measured in terms of ΔT_m by CD thermal melting experiments at 264 nm (Figure 4.11). Compounds 1 and 4 proved the best, albeit not fully satisfactory, stabilizing effect on *KRAS* G4 ($\Delta T_m = +4.5$ °C

and $\Delta T_m = +7.5$ °C, respectively; Figure 4.12). Subsequently, the selectivity of these compounds against the 20-mer hairpin DNA was assessed through CD thermal melting experiments at 280 nm. These assays showed that both **1** and **4** have poor stabilizing effects ($\Delta T_m = 0$ °C and $\Delta T_m = +1$ °C, respectively) on the duplex DNA, thus prompting their selection as hit compounds for chemical optimization.

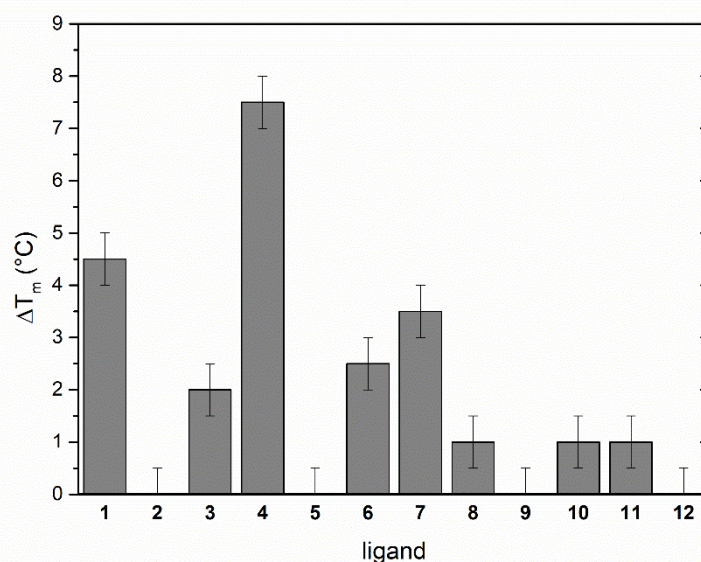


Figure 4.11. ΔT_m of *KRAS* G4 upon interaction with VS hits.

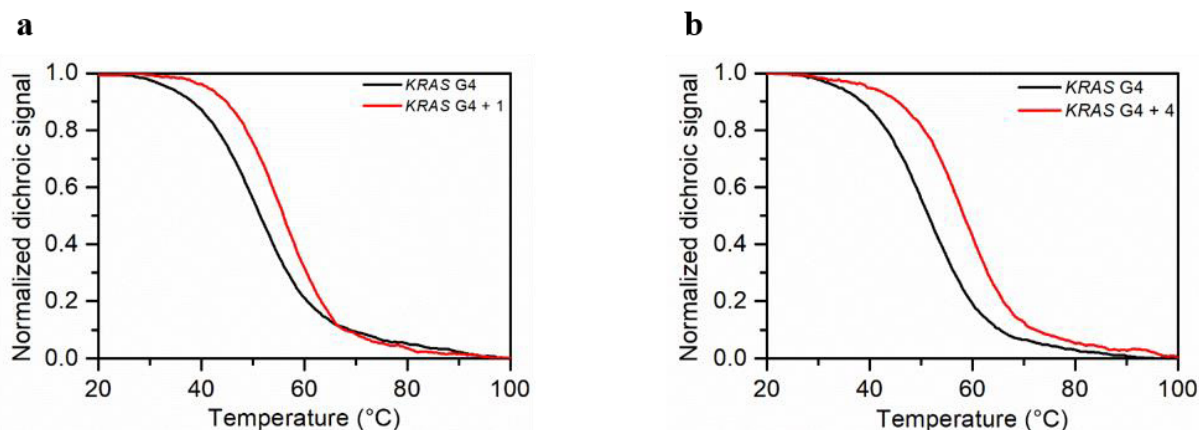


Figure 4.12. Normalized CD thermal denaturation of *KRAS* G4 in the absence and in the presence of **1** (a) and **4** (b).

Hit Optimization

In our lead optimization program, we intended to investigate the influence of side chains of different length and nature on the binding of **1** and **4** to the target DNA as well as on their

G4/duplex selectivity. In this perspective, we first selected from our in-house database a set of four analogues of **1** (compounds **13-16**, Chart 2), featuring a terminal amino group in place of the hydroxyl function. In fact, as briefly reported in the introduction, our in-house library offers the advantage that many compounds already possess a number of analogues, so a rapid SAR analysis is possible.

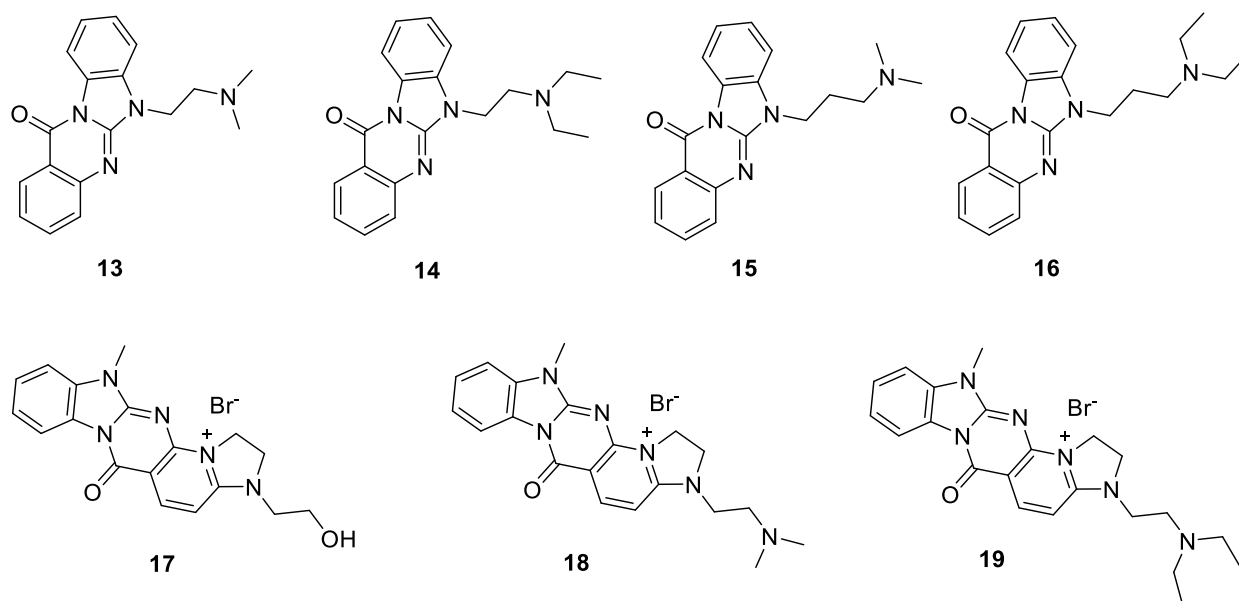
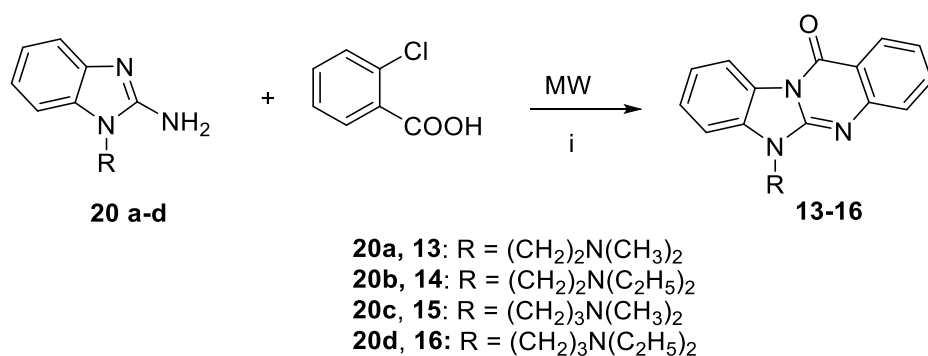


Figure 4.13. Chemical structures of derivatives **13-19**.

The synthesis of **13-16**, which has been already described in a previous paper (Dalla Via et al., 2001), was here improved using microwaves (MW), allowing the obtainment of the desired products with higher yields and shorter time reaction (12 min *versus* 5-7 h, Scheme 1). In particular, a MW-assisted Ullmann condensation reaction between the appropriate 1-dialkylaminoalkyl-2-aminobenzimidazole **20 a-d** (Dalla Via et al., 2001) and the commercially available 2-chlorobenzoic acid (Scheme 1) was performed. After cooling, the reaction mixture was poured into ice and the precipitated crude 6-(aminoalkyl)benzo[4,5]imidazo[2,1-*b*]quinazolin-12(6*H*)-ones **13-16** were collected and purified by recrystallization from ethanol.

Scheme 1*

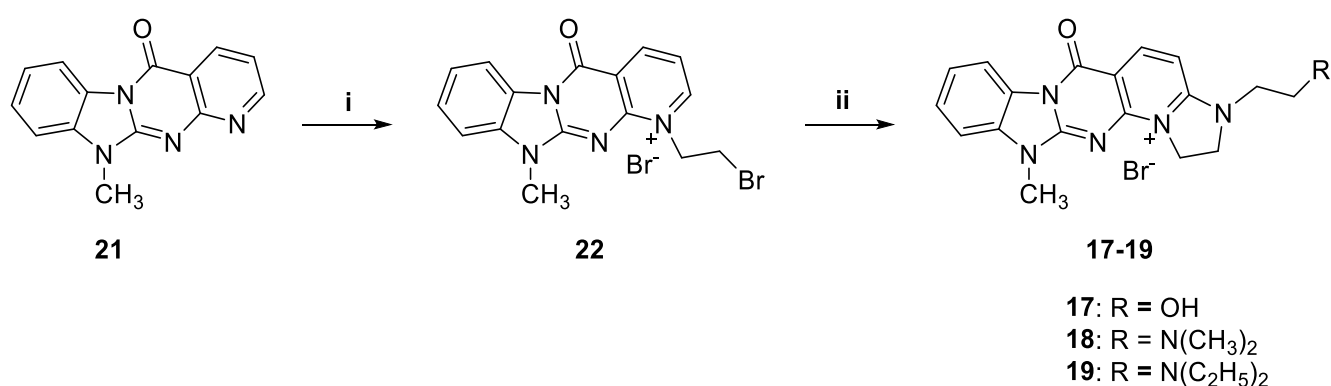


*Reagent and conditions: (i) K₂CO₃, CuBr, KI, DMF, 150 °C, P = 10 bar, power = 40-150 W, ramp t = 2 min, t = 12 min.

Parallel to the synthesis of **13-16**, we thought to combine some structural features of the two selected hits **1** and **4** by designing a derivative in which the pendant side chain of **1** was inserted at the positively charged pyridine nitrogen of **4** (**17**, Scheme 2). Furthermore, two analogues featuring the side chain of **13** and **14** were also designed (**18** and **19**, Scheme 2) to extend the SAR around this structural combination.

In this vein, the synthetic procedure previously developed by us for the preparation of **4** (Caroti et al., 1987) was applied starting from the 11-methylbenzo[4,5]imidazo[1,2-*a*]pyrido[2,3-*d*]pyrimidin-5(11*H*)-one **21** (Caroti et al., 1987) with few modifications (Scheme 2).

Scheme 2*



*Reagents and conditions: (i) 1,2-dibromoethane, 90 °C; (ii) H₂N(CH₂)₂R, ethanol, reflux.

Reaction of compound **21** with an excess of 1,2-dibromoethane at 90 °C for 40 h furnished **22**, which was suspended in ethanol and added with an excess of the appropriate amine. The

reaction mixture was refluxed for 4 h and then filtered to give crude products, finally purified by recrystallization from ethanol. A deep analysis of the spectral data allowed us to unequivocally assign to the obtained compounds **17-19** the structures outlined in Scheme 2, featuring a fused pentacyclic system. Actually, this is in agreement with literature data (Parenty et al., 2005, 2007) that report the reaction between a primary amine and a 2-bromoethylpyridinium derivative to proceed via a nucleophilic attack, followed by a cyclisation and an oxidation step, leading to a dihydroimidazopyridinium compound. Although the obtained derivatives **17-19** possessed an unexpected structure, they were considered for biological evaluation, as their structural features still met the requirements to act as G4 stabilizing molecules, that is a positively charged moiety and an extended aromatic system.

Biophysical assays on 13-19

Compounds **13-19** were tested on *KRAS* G4 and duplex hairpin DNA, evaluating ΔT_m by CD thermal melting experiments (Figures 4.14, 4.15). In the subset of derivatives **13-16**, all the compounds with the exception of **13** showed improved *KRAS* G4 stabilizing properties compared to the hit **1** and maintained satisfactory selectivity over duplex hairpin (Figure 4.14).

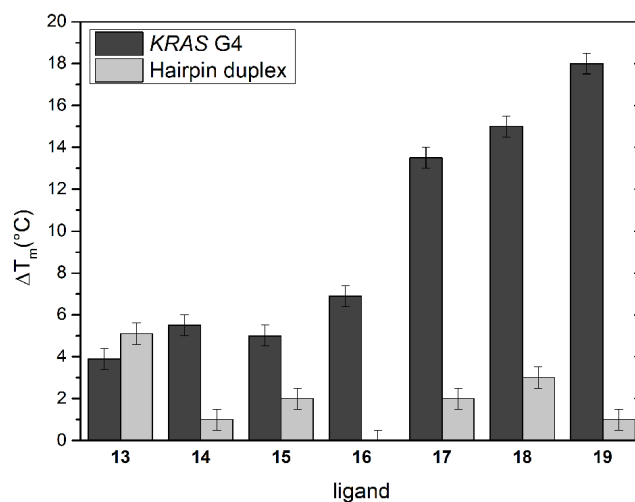


Figure 4.14. Ligand-induced thermal stabilization of *KRAS* G4 and hairpin duplex measured by CD melting experiments.

More interesting results were observed for the pentacyclic derivatives **17-19**, with all the three compounds recording substantial performance improvement ($\Delta T_m > 10$ °C) with respect to the parent hit **4**. Also, these compounds showed high *KRAS* G4/duplex DNA selectivity ratio

(Figure 4.14). In view of these data, **17-19** were further tested for selectivity over the parallel *KIT* G4 and hybrid-1 Tel23.

Table 4.5. Comparison of 17, 18 and 19 ΔT_m with *KRAS* G4 and control sequences.

ligand	<i>KRAS</i> G4	<i>KIT</i> G4	Tel23
	$\Delta T_m \pm 0.5$ °C	$\Delta T_m \pm 0.5$ °C	$\Delta T_m \pm 0.5$ °C
17	+ 13.5	+ 7.0	+ 2.5
18	+ 15.0	+ 10.0	+ 5.5
19	+ 18.0	+ 10.5	+ 7.5

These ligands showed a preferential binding to parallel G4s rather antiparallel one (Table 4.5). All of them turned out to increase the *KRAS* G4 thermal stability with a larger extent compared to the other G4s. In particular, **19** was the most potent *KRAS* G4 stabilizing agent of the series and was thereby selected for further analysis (Figure 4.15).

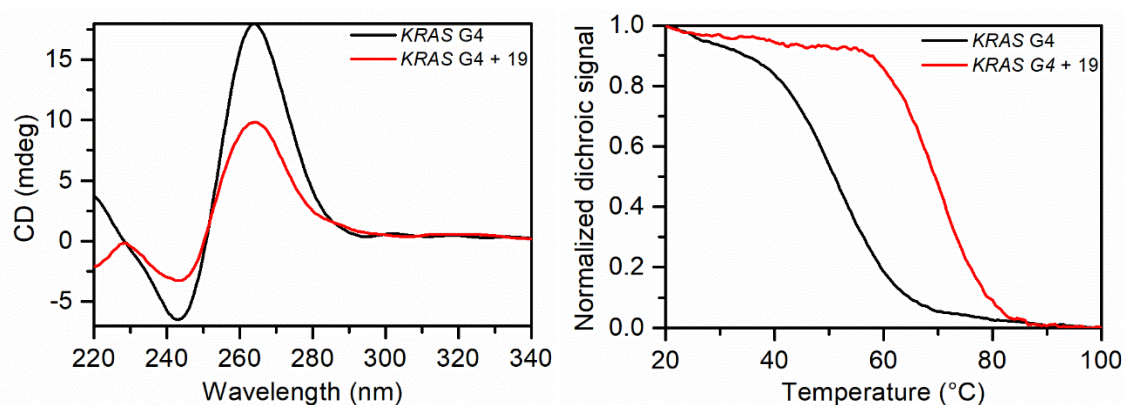


Figure 4.15 CD spectra (left panel) and melting profiles (right panel) of *KRAS* G4 without (blackline) and with (redline) **19.**

Fluorescence titration experiments were thus performed for gaining information on the binding affinity and stoichiometry of the interaction between *KRAS* G4 and **19** (Figure 4.16) (Shirasawa et al., 1993; Thiriet and Hayes, 2005; Giancola and Pagano, 2012; Pagano et al., 2012).

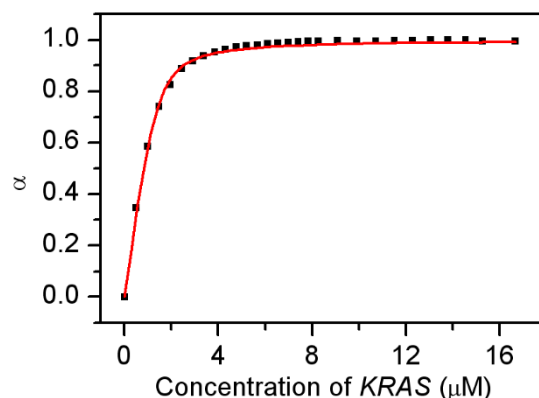


Figure 4.16. Fluorescence titration of **19 with *KRAS* G4.**

Results of fluorescence analysis showed a stoichiometry ratio of 1:1 *KRAS* G4/**19** and a binding constant (K_b) of $7.2 \pm 0.4 \cdot 10^6 \text{ M}^{-1}$. In order to strengthen the CD results, fluorescence experiments were also performed with *KIT* G4, revealing an interaction of 1:1 *KIT* G4/**19** with $K_b = 2.3 \pm 0.5 \cdot 10^6 \text{ M}^{-1}$, which is threefold lower compared to that of *KRAS* G4.

To investigate the *KRAS* G4/**19** complex behaviour upon addition of different amounts of **19** a non-denaturing gel electrophoresis experiment was performed. *KRAS* G4 moves as a single band in the gel, thus suggesting the presence of a unimolecular structure and the absence of high-order DNA structures. The addition of **19** to the *KRAS* G4 did not affect the G4 mobility at all investigated ratios (Figure 4.17), in agreement with the stoichiometry revealed by the fluorescence assay.

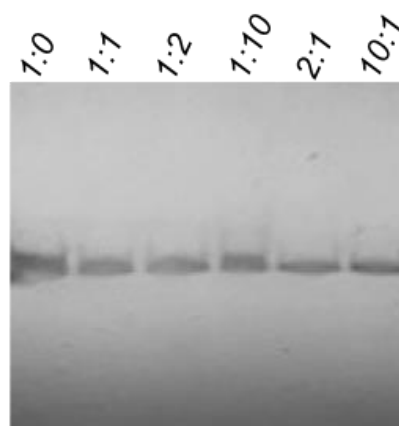


Figure 4.17. PAGE analysis of *KRAS* G4 complexes with compounds **19 prepared at different DNA/ligand ratios.**

Computational studies

In order to investigate at the atomic level the binding mode of the newly synthesized derivatives to *KRAS* G4, molecular modeling studies were carried out on the most promising compound of the series, **19**. Initially, molecular docking of this compound was performed in the *KRAS* G4 NMR structure (PDB code: 5I2V) (Kerkour et al., 2017). Docking calculations predicted two similar binding modes in which the ligand stacks at the 3' region of the target DNA to interact with residues G9, G13, and A22. However, the two poses differ in the arrangement of the ligand planar scaffold which is mutually flipped by 180°. The stability and energetics of this pose were further investigated through more accurate calculations. In particular, to fully take into account the receptor flexibility and the water and ions effects, each of the two docking-predicted 19/DNA complexes was submitted to 1.5 μ s molecular dynamics (MD) simulations in explicit solvent. A comparison between the ligand RMSD plot computed for the two MD trajectories showed that only one of the two docking solutions (pose A) evolves in a stable binding conformation over the simulated time scale. In fact, starting from this pose, in the first half of the MD run the ligand experiences a slight rearrangement to reach a well-defined binding mode, which is conserved throughout the rest of the simulation. In fact, this pose is stabilized by tight interactions with the DNA. Specifically, **19** lies at the G4 3' end where it engages favorable π -stacking with G9, G13 and G20 (Figure 4.18).

Furthermore, the *N,N*-(diethyl)aminoethyl group establishes a salt bridge with the phosphate backbone of A14 (Figure 4.19) or A22 (Figure 4.19). It is also interesting to note that **19** can form additional stacking interactions with the terminal A22, which shifts from its initial position to be packed against the ligand aromatic scaffold. Remarkably, these contacts stabilize not only the ligand binding conformation but also the overall *KRAS* G4 architecture.

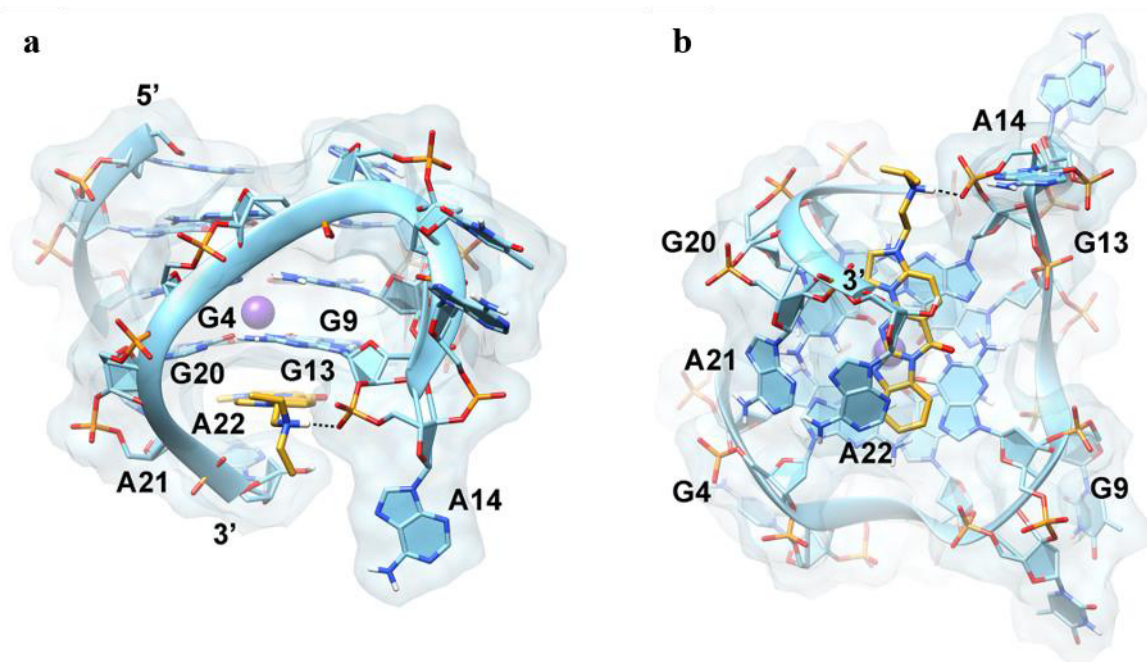


Figure 4.18. Front (a) and bottom (b) view of the MD predicted binding pose of 19 (yellow sticks) at the NMR structure of the G-quadruplex (PDB code: 5IV2, Kerkour et al., 2017). DNA is shown as cyan cartoons and transparent surface. Nucleotides are highlighted as sticks, aromatic rings are filled with thin slabs, while K⁺ ions are depicted as purple spheres. Hydrogen bonds are represented as dashed black lines.

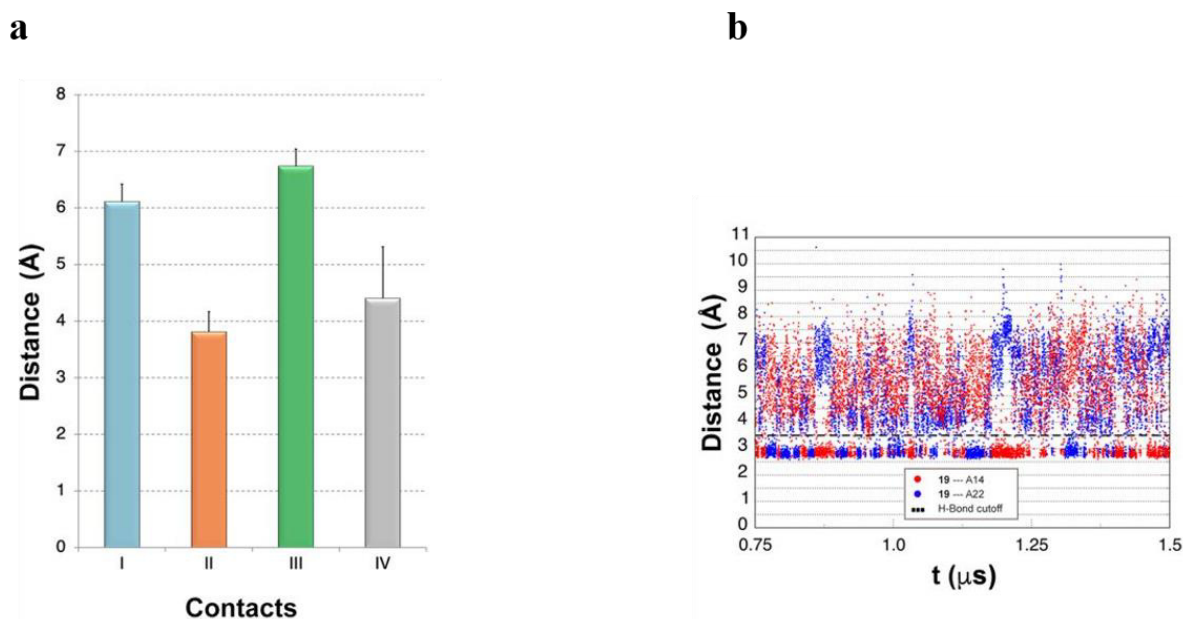


Figure 4.19 (a) Interatomic distances (mean ± S.D.) representative of the ligand (polycyclic nucleus - center of mass)/DNA residues (aromatic ring centroid) stacking interactions along the second half of the MD calculations on docking pose A: (I) G9, cyan bar; (II) G13, orange bar; (III) G20, green bar; (IV) A22, gray bar. (b) Distance between the ligand diethylamino group (N) and representative A14 and A22 phosphate oxygens along the MD simulations.

Biological Assays

To verify the biological relevance of our finding, we assayed the capability of **19** to inhibit KRAS expression in tumor cells. To this aim, HCT116 colorectal cancer cells were treated with **19** at 2 μM concentration, which is the compound IC_{50} calculated by viability assay. Also, the effect on KRAS expression was evaluated at both gene and protein level. As reported in Figure 4.20 a, qRT-PCR analyses revealed that treatment of HCT116 colorectal cancer cells with **19** (2 μM for 24, 48 or 72 h) reduced the mRNA levels of *KRAS* up to 40%, when compared to their untreated counterpart. Subsequently, the effect of **19** on KRAS expression was validated also in terms of protein expression. As evidenced in Figure 4.20b, treatment of the cells for 72 h with 2 μM of **19** determined the reduction of KRAS levels of about 30%. Remarkably, in contrast to other G4 ligands, treatment of cells with 2 μM of **19** for 24 h did not produce any increase in the phosphorylation levels of histone H2AX, a hallmark of DNA double-strand breaks (Thiriet and Hayes, 2005), reinforcing the idea that the selected compound can be selective for the G4 structure present at gene promoter level. Since KRAS is considered a driver oncogene, we also evaluated whether **19** was able to affect the viability of two KRAS isogenic tumor cell lines HK2-6 and HKE-3, derived from the HCT116 cells and carrying the mutated ($\text{KRAS}^{\text{G13D/G13D}}$) or wild-type ($\text{KRAS}^{\text{wt/wt}}$) gene alleles, respectively (Shirasawa et al., 1993; Del Curatolo et al., 2018). Briefly, the two cell lines were treated with different concentrations of **19** (ranging from 1 to 10 μM) and the number of viable cells was evaluated by crystal violet assay (Figure 4.20). Remarkably, these experiments clearly evidenced that the cytotoxic effect of **19** on the HKE-3 cells ($\text{IC}_{50} > 10 \mu\text{M}$) was lower than that produced on HK2-6 cells ($\text{IC}_{50} = 2.78 \mu\text{M}$), indicating that our compound is more effective in cells in which the mutated KRAS acts as driver oncogene.

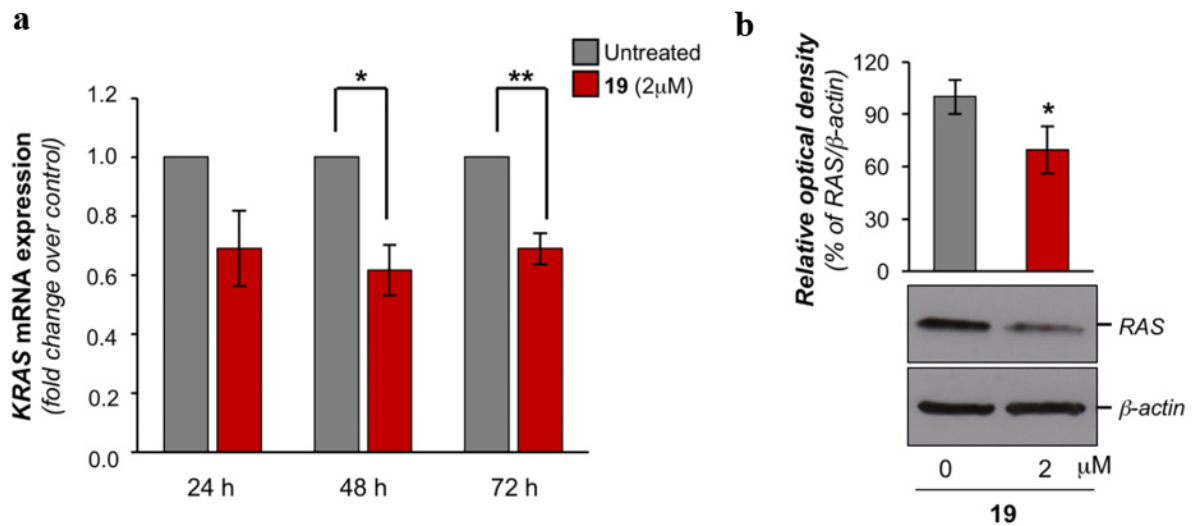


Figure 4.20. (a) Gene expression of *KRAS* was evaluated by qPCR in HCT116 cells untreated or treated with 2 μM of 19 for the indicated times (24, 48 and 72 h). Results are expressed as fold change of mRNA levels in treated cells over their controls, after β-actin normalization. Histograms are shown as mean ± SD (**p* = 0.0149, ***p* = 0.0081; Student's t-test). (b) Protein expression was evaluated by Western Blot (WB) analysis. Upper panel, histogram showing the relative optical density of *KRAS* expression evaluated by Image-J quantification tool and normalized for β-actin. The graph shows the mean ± SD (**p* = 0.0352; Student's t-test). Lower panel, representative WB images of *KRAS*, γH2AX and β-actin.

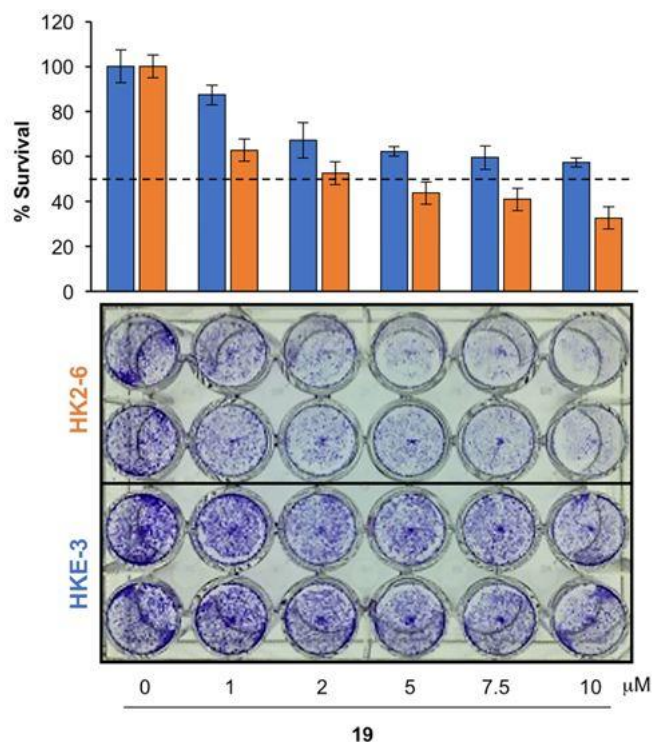


Figure 4.21. HK2-6 and HKE-3 cells were treated with compound **19** at the indicated doses for 72 h. Viable cell number was determined by colorimetric crystal violet assay. Histogram shows the mean values \pm SD.

These data indicate that **19** would represent the prototype of a new class of compounds that, inhibiting the expression of *KRAS* gene, might in principle counteract *KRAS*-mutated tumors that are refractory to treatment with anti-EGFR antibodies (e.g. cetuximab and panitumumab), so far devoid of valid therapeutic treatments (Siravegna et al., 2015).

4.2.3 Conclusions

The stabilization of G4 DNA motifs in oncogene promoters by small molecules has emerged in the last years as a promising strategy to control aberrant protein expression in cancer cells. Among the druggable oncogene is *KRAS*, which codifies for the homonymous kinase and is mutated and overexpressed in a high percentage of tumors. Here a VS campaign led to the discovery of new chemotypes able to recognize and stabilize the *KRAS* G4 gene promoter. The chemical optimization of the identified molecules resulted in a set of derivatives which were extensively characterized for their G4 stabilizing properties. Particularly one of these analogues, namely **19**, showed a high affinity for the *KRAS* G4 and good selectivity against duplex DNA and other G4 forming sequences. Subsequent fluorescence titration experiments

on the *KRAS* G4/**19** complex showed a 1:1 stoichiometry ratio and a ligand/DNA binding constant of about $7.2 \times 10^6 \text{ M}^{-1}$. Molecular dynamics simulations studies provided not only structural insights into the binding mode of **19** to *KRAS* G4 but also the molecular basis for the stabilization of the target DNA by this compound. Finally, biological assays demonstrated that **19** exerts cytotoxic effects, at low micromolar concentration, in tumor cells expressing constitutively active forms of mutated *KRAS*. In conclusion, our data indicate that **19** can represent the prototype of a novel class of antitumoral drugs able to inhibit the expression of the *KRAS* driver oncogene, which has long been considered undruggable. In this perspective, the development of a new class of anti-*KRAS* molecules would represent an important curative opportunity for a subclass of patients for whom effective therapies are still missing.

4.2.4 Experimental section

Differential scanning calorimetry

DSC measurements were carried out on a nano-DSC (TA Instruments, New Castle, DE, USA) using a 204 μM G4 sample in a 60 mM KCl, 20 mM KH_2PO_4 , 0.1 mM EDTA buffer at pH 7.0. Three heating/cooling cycles were recorded in the 10–100 $^\circ\text{C}$ range, 0.5 $^\circ\text{C}/\text{min}$ scan rate, using 600 s equilibration time prior each heating and 300 s before each cooling. The same method was used for buffer vs buffer scans to obtain the baseline, which subtracted from sample vs buffer scan to obtain the thermodynamic parameters. The corrected thermograms were then normalized per mole of DNA to obtain the corresponding molar heat capacity curves. Model-free enthalpy ($\Delta H^\circ(T_m)$) for the overall unfolding of DNA structure was estimated by integrating the area under the heat capacity versus temperature curves and represent the average of at least three different heating experiments. T_m values correspond to the maximum of each thermogram peak. DSC curves provided the van't Hoff enthalpy ($\Delta H^\circ_{\text{vH}}$), calculated assuming a simple two-state transition (Pagano et al., 2013).

Virtual screening

For our study, an in-house virtual database of 5,858 compounds and the commercially available Asinex Platinum Collection library (<http://www.asinex.com>) of 9,216 molecules were selected. All the possible tautomeric and protonation states in the pH range 7.4 ± 1.5 were generated for each compound using Epik (Shelley et al., 2007; Greenwood et al., 2010) for a total amount of 7,924 and 17,500 structures, respectively, for the in-house and the Asinex libraries. A filtering

procedure was then applied to provide a more focused set of ligands. Specifically, all the molecules having at least two aromatic rings and a positive total charge were retained, resulting in two final subsets containing, respectively, 875 and 14,280 structures. Concerning the target macromolecule, we selected the NMR structure of the *KRAS* G-quadruplex structure (PDB code: 5IV2, (Kerkour et al., 2017)) that was prepared through the Protein Preparation Wizard implemented in Maestro Suite 2019 (Madhavi Sastry et al., 2013). During the preparation, all water molecules were deleted, hydrogen atoms were added, and the complex was minimized. The docking search area was set on the centre of mass of the macromolecule so as to enclose the entire G-quadruplex. The interaction grids were thus computed through the grid generation tool of Glide 6.7 (Friesner et al., 2004; Halgren et al., 2004). The OPLS 2005 force field (Banks et al., 2005) was employed for docking. The results from each of the two sets of calculations were evaluated and ranked based on the Glide SP scoring function (Friesner et al., 2004; Halgren et al., 2004). Thus, the top-ranked compounds (the best 15 %) of each subset were visually inspected for their binding modes and for good chemical geometry. Compounds 1-4 were retrieved from our in-house library, while compounds 5-12 were purchased from the Asinex vendor. Compounds purity (> 95 %) was determined by HPLC, according to the procedure described in the chemistry section.

DNA synthesis and sample preparation

The sequences d(AGGGCGGTGTGGGAATAGGGAA) (*KRAS* G4), d(AGGGAGGGCGCTGGGAGGAGGG) (*KIT* G4), d(TAGGGTTAGGGTTAGGGTTAGGG) (Tel23), and d(CGAATTCGTTTTTCGAATTCG) (hairpin duplex), were synthesized on a ABI394 DNA/RNA synthesizer (Applied Biosystem, Foster City, CA, USA) by using the standard DNA synthesis protocol on solid phase at the 5- μ mol scale (Oliviero et al., 2008). A concentrated ammonia aqueous solution at 55 °C for 12 h was used to DNA detachment from support and removal of the semi-permanent protection groups. The combined filtrates and washings were concentrated under reduced pressure, dissolved in water, and purified by HPLC on a Nucleogel SAX column (Macherey-Nagel, 1000-8/46), using buffer A consisting of 20 mM KH₂PO₄/ K₂HPO₄ aqueous solution (pH 7.0), containing 20% (v/v) CH₃CN, buffer B consisting of 1 M KCl, 20 mM KH₂PO₄/ K₂HPO₄ aqueous solution (pH 7.0), containing 20% (v/v) CH₃CN, and a linear gradient from 0% to

100% B for 30 min with a flow rate 1 mL min⁻¹. The fractions of the oligomers were collected and successively desalted by Sep-Pak cartridges (C-18).

Oligonucleotide samples were prepared by dissolving the lyophilized DNAs in potassium phosphate buffer (60 mM KCl, 20 mM KH₂PO₄, 0.1 mM EDTA, pH 7.0). The solutions were heated at 90 °C for 5 min and slowly cooled to room temperature. The annealing procedure was followed by overnight storage at 4 °C prior to use. The concentration of the oligonucleotides was evaluated by UV measurements at 260 nm, at a temperature of 90 °C, using molar extinction coefficient values calculated by the nearest-neighbor model (Cantor et al., 1970). Stock solutions of putative ligands were prepared at 10 mM concentration in DMSO. Appropriate amounts of ligand were added to the oligonucleotide solutions to obtain the desired ligand/DNA ratio, followed by mix at 20 °C for 10 min before data acquisition.

Circular dichroism

CD spectra were recorded on a Jasco J-815 spectropolarimeter (JASCO Inc., Tokyo, Japan) equipped with a PTC-423S/15 Peltier temperature controller. All the spectra were recorded at 20 °C in the 220-360 nm wavelength range and averaged over three scans. The scan rate was 100 nm min⁻¹, with a 4 s response and 1 nm bandwidth. Buffer baseline was subtracted from each spectrum. Sample concentration was 2 μM for all DNA samples. CD spectra of DNA/ligand mixtures were obtained by adding 10 mol equiv of ligand. CD melting experiments were carried out in the 20-100 °C range at 1 °C min⁻¹ heating rate and followed at an appropriate wavelength for each DNA sample (*KRAS* G4 and *KIT* G4 at 264 nm, Tel23 at 289 nm, and the duplex hairpin at 280 nm). The melting temperatures (T_m) were determined from curve fit using Origin 7.0 software (OriginLab Corp., Northampton, MA, USA). CD melting experiments were recorded on DNA samples both in the absence and presence of each ligand to obtain ΔT_m values, determined as:

$$\Delta T_m = T_{m,DNA/ligand} - T_{m,DNA} \quad (30)$$

where $T_{m,DNA/ligand}$ is measured on ligand/DNA mixtures (10 mol equiv), $T_{m,DNA}$ is from the standalone DNA sample. All experiments were performed in duplicate and the reported values are the average of two measurements.

Chemistry

The uncorrected melting points were determined using a Reichert Köfler hot-stage apparatus. NMR spectra were obtained on a Bruker AVANCE 400 (^1H , 400 MHz, ^{13}C , 100 MHz) in DMSO- d_6 or in CDCl_3 . The coupling constants are given in Hertz. Magnesium sulfate was used as the drying agent. Evaporations were made in vacuo (rotating evaporator). Analytical Thin Layer Chromatography (TLC) have been carried out on Merck 0.2 mm precoated silica gel aluminum sheets (60 F-254). Silica gel 60 (230–400 mesh) was used for column chromatography. ESI-MS/MS were obtained in positive ion mode from a LCQ Advantage ThermoFinnigan spectrometer (ThermoFinnigan, USA). Microwave assisted reactions were carried out in BIOTAGE Initiator 2.5 microwave apparatus. Reagents, starting materials, and solvents were purchased from commercial suppliers and used as received. The following compounds were obtained according to methods previously described: 6-(2-((2-hydroxyethyl)amino)ethyl)benzo[4,5]imidazo[2,1-*b*]quinazolin-12(6*H*)-one (**1**) (Dalla Via et al., 2001), *N*,10-bis(2-(diethylamino)ethyl)-4-oxo-4,10-dihydrobenzo[4,5]imidazo[1,2-*a*]pyrimidine-3-carboxamide (**2**) (Da Settimo et al., 2003), 7-(3-(dimethylamino)propyl)benzo[4,5]imidazo[1,2-*a*]pyrido[3,2-*e*]pyrimidin-5(7*H*)-one (**3**) (Da Settimo et al., 1998), 1,11-dimethyl-5-oxo-5,11-dihydrobenzo[4,5]imidazo[1,2-*a*]pyrido[2,3-*d*]pyrimidin-1-ium iodide (**4**) (Dalla Via et al., 2001), 1-dialkylaminoalkyl-2-aminobenzimidazoles (**20a-d**) (Dalla Via et al., 2001) and 11-methylbenzo[4,5]imidazo[1,2-*a*]pyrido[2,3-*d*]pyrimidin-5(11*H*)-one (**21**) (Caroti et al., 1987). The structural characterization of previously described target compounds **1-4** and **13-16** has been herein implemented by ^{13}C NMR data.

6-(2-((2-Hydroxyethyl) amino)ethyl)benzo[4,5]imidazo[2,1-*b*]quinazolin-12(6*H*)-one (**1**). ^{13}C NMR (100 MHz, DMSO- d_6): δ 42.27, 47.17, 51.77, 60.78, 109.94, 115.53, 116.60, 122.03, 122.97, 125.63, 125.93, 126.42, 126.84, 132.53, 134.82, 146.87, 149.48, 159.61.

N,10-Bis(2-(diethylamino)ethyl)-4-oxo-4,10-dihydrobenzo[4,5]imidazo[1,2-*a*]pyrimidine-3-carboxamide (**2**). ^{13}C NMR (100 MHz, CDCl_3): δ 12.07, 12.30, 37.62, 41.93, 47.59, 47.64, 50.90, 52.08, 107.16, 110.11, 117.73, 123.80, 125.95, 127.10, 131.54, 149.75, 159.34, 160.27, 164.85.

7-(3-(Dimethylamino)propyl)benzo[4,5]imidazo[1,2-*a*]pyrido[3,2-*e*]pyrimidin-5(7*H*)-one (**3**). ^{13}C NMR (100 MHz, CDCl_3): δ 26.29, 40.57, 45.51, 56.43, 110.08, 114.96, 116.30, 122.20, 123.86, 125.64, 126.49, 131.49, 138.65, 149.20, 151.00, 152.71, 168.85.

1,11-Dimethyl-5-oxo-5,11-dihydrobenzo[4,5]imidazo[1,2-a]pyrido[2,3-d]pyrimidin-1-ium iodide (4). ¹³C NMR (100 MHz, DMSO-*d*₆): δ 29.14, 42.02, 111.34, 115.39, 116.96, 124.60, 124.80, 127.30, 131.50, 144.78, 148.79, 150.44, 152.52, 156.86.

General procedure for the synthesis of 6-(aminoalkyl) benzo[4,5]imidazo[2,1-b]quinazolin-12(6H)-one derivatives 13-16. A mixture of the appropriate 1-dialkylaminoalkyl-2-aminobenzimidazole **20a-d** (0.50 mmol), 2-chlorobenzoic acid (0.078 g, 0.50 mmol), cuprous bromide (0.004 g, 0.030 mmol), anhydrous potassium carbonate (0.083 g, 0.60 mmol) and a catalytic amount of potassium iodide in 1.0 mL of dimethylformamide was irradiated at a T = 150 °C, P = 10 bar, power = 40-150 Watt, *ramp* time = 2 min for 12 min. After cooling the reaction mixture was poured into ice. The precipitated crude products **13-16** were collected and purified by recrystallization from ethanol.

6-(2-(Dimethylamino) ethyl)benzo[4,5]imidazo[2,1-b]quinazolin-12(6H)-one (13). Yield: 70%; m.p. 161-162 °C: (Dalla Via et al., 2001) m.p. 160-165 °C); ¹³C NMR (100 MHz, CDCl₃): δ 40.44, 45.88, 56.75, 108.51, 116.62, 117.12, 122.37, 123.17, 126.02, 126.20, 126.35, 127.26, 131.99, 134.59, 146.69, 149.55, 160.31.

6-(2-(Diethylamino) ethyl)benzo[4,5]imidazo[2,1-b]quinazolin-12(6H)-one (14). Yield: 65%; m.p. 143-144 °C: (Dalla Via et al., 2001) m.p. 140-145 °C); ¹³C NMR (100 MHz, CDCl₃): δ 11.49, 40.13, 47.70, 50.07, 108.78, 116.60, 117.16, 122.47, 123.26, 126.00, 126.16, 126.47, 127.33, 131.99, 134.65, 146.68, 149.53, 160.32.

6-(3-(Dimethylamino) propyl)benzo[4,5]imidazo[2,1-b]quinazolin-12(6H)-one (15). Yield: 55%; m.p. 163-164 °C: (Dalla Via et al., 2001) m.p. 163-165 °C); ¹³C NMR (100 MHz, CDCl₃): δ 25.85, 40.31, 45.25, 56.51, 108.55, 116.61, 117.10, 122.39, 123.21, 126.01, 126.12, 126.42, 127.30, 132.15, 134.66, 146.74, 149.60, 160.34.

6-(3-(Diethylamino) propyl)benzo[4,5]imidazo[2,1-b]quinazolin-12(6H)-one (16). Yield: 65%; m.p. 131-133 °C: (Dalla Via et al., 2001) m.p. 130-135 °C); ¹³C NMR (100 MHz, CDCl₃): δ 10.64, 24.99, 40.57, 46.96, 50.27, 108.59, 116.66, 117.14, 122.53, 123.29, 125.93, 126.14, 126.52, 127.35, 131.93, 134.71, 146.77, 149.52, 160.30.

General synthetic procedures for 3-(2-substituted ethyl) -12-methyl-6-oxo-2,3,6,12-tetrahydro-1H-benzo[4,5]imidazo[1,2-a]imidazo[1',2':1,6]pyrido[2,3-d]pyrimidin-14-ium bromide 17-19. The appropriate amine (10.0 mmol) was added dropwise to a suspension of **22** (0.110 g, 0.25 mmol) in 10 ml of ethanol and the mixture was refluxed for 4 h. After

cooling, the resulting suspension was filtered and the crude products obtained were purified by recrystallization from ethanol.

3-(2-Hydroxyethyl)-12-methyl-6-oxo-2,3,6,12-tetrahydro-1H-benzo[4,5]imidazo[1,2-a]imidazo [1',2':1,6]pyrido[2,3-d]pyrimidin-14-ium bromide (17). Yield: 45%; ¹H NMR (400 MHz, DMSO-*d*₆): δ 3.71 (s, 4H), 3.87 (s, 3H), 4.20 (t, *J* = 10.0 Hz, 2H), 4.65 (t, *J* = 10.0 Hz, 2H), 5.07 (s, 1H), 6.95 (d, *J* = 9.2 Hz, 1H), 7.53 (t, *J* = 7.4 Hz, 1H), 7.65 (t, *J* = 7.6 Hz, 1H), 7.83 (d, *J* = 8.0 Hz, 1H), 8.47-8.51 (m, 2H); ¹³C NMR (100 MHz, DMSO-*d*₆): δ 28.90, 45.40, 48.39, 48.60, 57.74, 100.68, 100.81, 110.96, 115.36, 123.97, 125.22, 126.64, 131.48, 141.79, 148.96, 151.43, 156.47, 156.61. ESI-MS/MS *m/z* 336 [M]⁺. Anal. Calcd. for C₁₈H₁₈BrN₅O₂ (%): C, 51.94; H, 4.36; N, 16.82. Found: C, 52.01; H, 4.29; N, 16.75.

3-(2-(Dimethylamino)ethyl)-12-methyl-6-oxo-2,3,6,12-tetrahydro-1H-benzo[4,5]imidazo[1,2-a]imidazo[1',2':1,6]pyrido[2,3-d]pyrimidin-14-ium bromide (18). Yield: 49%; ¹H NMR (400 MHz, DMSO-*d*₆): δ 2.23 (s, 6H), 2.56 (t, *J* = 6.0 Hz, 2H), 3.74 (t, *J* = 6.0 Hz, 2H), 3.86 (s, 3H), 4.19 (t, *J* = 9.8 Hz, 2H), 4.64 (t, *J* = 10 Hz, 2H), 7.00 (d, *J* = 9.2 Hz, 1H), 7.54 (t, *J* = 7.2 Hz, 1H), 7.64 (t, *J* = 7.2 Hz, 1H), 7.82 (d, *J* = 8.0 Hz, 1H), 8.45-8.50 (m, 2H); ¹³C NMR (100 MHz, DMSO-*d*₆): δ 28.78, 43.44, 45.22, 48.26, 55.62, 100.14, 100.80, 110.84, 115.21, 123.86, 125.03, 126.53, 131.31, 141.85, 148.76, 151.34, 156.06, 156.28. ESI-MS/MS *m/z* 363 [M]⁺. Anal. Calcd. for C₂₀H₂₃BrN₆O (%): C, 54.18; H, 5.23; N, 18.96. Found: C, 54.32; H, 5.19; N, 18.81.

3-(2-(Diethylamino)ethyl)-12-methyl-6-oxo-2,3,6,12-tetrahydro-1H-benzo[4,5]imidazo[1,2-a]imidazo[1',2':1,6]pyrido[2,3-d]pyrimidin-14-ium bromide (19). Yield: 50%; ¹H NMR (400 MHz, DMSO-*d*₆): δ 0.93 (t, *J* = 7.0 Hz, 6H), 2.53 (q, *J* = 7.2 Hz, 4H), 2.68 (t, *J* = 5.6 Hz, 2H), 3.70 (t, *J* = 5.8 Hz, 2H), 3.86 (s, 3H), 4.21 (t, *J* = 10 Hz, 2H), 4.66 (t, *J* = 9.8 Hz, 2H), 6.96 (d, *J* = 9.2 Hz, 1H), 7.52 (t, *J* = 7.6 Hz, 1H), 7.64 (t, *J* = 7.8 Hz, 1H), 7.82 (d, *J* = 8.0 Hz, 1H), 8.45-8.50 (m, 2H); ¹³C NMR (100 MHz, DMSO-*d*₆): δ 11.79, 28.90, 44.12, 45.33, 46.30, 48.54, 49.65, 100.54, 100.85, 110.97, 115.34, 123.97, 125.17, 126.63, 131.44, 141.72, 148.91, 151.45, 156.21, 156.45. ESI-MS/MS *m/z* 391 [M]⁺. Anal. Calcd. for C₂₂H₂₇BrN₆O (%): C, 56.05; H, 5.77; N, 17.83. Found: C, 56.21; H, 5.71; N, 17.68.

1-(2-bromoethyl)-11-methyl-5-oxo-5,11-dihydrobenzo[4,5]imidazo[1,2-a]pyrido[2,3-d]pyrimidin-1-ium bromide 22. Compound **21** (0.215 g, 0.86 mmol) was suspended in 1.5 mL of 1,2-dibromoethane (17.0 mmol). The resulting mixture was heated at 90 °C for 40 h.

During this time an additional amount of 1,2-dibromoethane (0.2 ml) was slowly added. After cooling, the suspension was filtered to give a yellow solid, which was purified by recrystallization from ethanol. Yield: 65%; ^1H NMR (400 MHz, $\text{DMSO-}d_6$): δ 3.97 (s, 3H), 4.17 (t, $J = 6.0$ Hz, 2H), 5.25 (t, $J = 6.0$ Hz, 2H), 7.63 (t, $J = 6.8$ Hz, 1H), 7.72 (t, $J = 7.0$ Hz, 1H), 7.76-7.79 (m, 1H), 7.91 (d, $J = 8.0$ Hz, 1H), 8.49 (d, $J = 8.0$ Hz, 1H), 9.20 (d, $J = 6.0$ Hz, 1H), 9.26 (dd, $J = 1.8$ Hz, $J = 7.8$ Hz, 1H).

Fluorescence

Fluorescence experiments were performed at 20 °C on an FP-8300 spectrofluorimeter (Jasco Inc., Tokyo, Japan) equipped with a Peltier temperature controller accessory (Jasco PCT-818). A 1 cm path length, sealed quartz cuvette was used. Both excitation and emission slits were set at 5 nm. The ligand solutions had a concentration in the 1.5-2.0 μM range in phosphate buffer and were prepared by weighting using an analytical scale. The titrations were carried out by stepwise additions of DNA (5 μL at 100 μM) to a cell containing a fixed concentration (1.5-2.0 μM) of ligand. The solution was stirred and allowed to equilibrate for 5 min after each addition. Emission spectra were recorded by exciting each compound at the appropriate wavelength. The fraction of bound ligand (α) at each point of the titration was calculated following fluorescence changes at the maximum of intensity:

$$\alpha = \frac{I_{\lambda} - I_{\lambda}^{\max}}{I_{\lambda}^{\min} - I_{\lambda}^{\max}} \quad (31)$$

in which λ is the wavelength of the ligand maximum emission; I_{λ} is the fluorescence intensity at each point of titration; I_{λ}^{\max} is the fluorescence intensity of the ligand alone; and I_{λ}^{\min} is the fluorescence intensity of the saturated sample.

Titration curves were obtained by plotting α versus the DNA G4 concentration. The equilibrium binding constant (K_b) and the stoichiometry of the binding (n) were estimated by fitting the resulting curve to an independent and equivalent binding site model (Eq. 14) (Cummaro et al., 2011).

$$\alpha = 1/2L_0 \left[\left(L_0 + nQ_0 + \frac{1}{K_b} \right) - \sqrt{\left(L_0 + nQ_0 + \frac{1}{K_b} \right)^2 - 4L_0nQ_0} \right] \quad (32)$$

in which α is the bound ligand fraction, L_0 is the total ligand concentration, and Q_0 is the added G4 concentration. Appropriate excitation wavelength was used for each ligand. Experiments were repeated twice, and the results are reported as the mean \pm SD.

Native polyacrylamide gel electrophoresis analysis

Native gel electrophoreses were carried out in 15% (w/v) polyacrylamide gel. An 89 mM Tris HCl, 89 mM boric acid 10 \times TB solution at pH 7.0 was used as a run buffer, Ammonium persulfate (APS) as a radical initiator, tetramethylethylenediamine (TEMED) as a radical stabilizer and bromophenol blue as a run marker. Stock ligand solutions concentration was 10 mM in DMSO. Two native gel electrophoreses were carried out in excess of either the ligand or the oligonucleotide. In the first case, an oligonucleotide concentration of 50 μ M for each sample and an increasing amount (1, 2, 10 mol equiv) of ligand were used. In the second case, an oligonucleotide concentration of 50 μ M for each sample and an increasing amount (0.01, 0.02, 0.1 mol equiv) of ligand were used. The total volume loaded in each well was 10 μ L. Gels were imaged by UV-shadowing, using 254 nm exposure wavelength (Amato et al., 2014a).

Molecular Dynamics

Docking simulations on compound **19** were performed applying the same protocol followed in VS calculations. Prior to docking, the ligand tridimensional structure was generated with the Maestro Build Panel, and its tautomeric and protonation states at physiological pH (7.4 ± 1.5) were then predicted by the software Epik (Shelley et al., 2007; Greenwood et al., 2010).

The docking predicted 19/*KRAS* G4 complexes were solvated in a 12.0 \AA layer cubic water box using the TIP3P water model parameters (Jorgensen et al., 1983). 19 K^+ cations were used to neutralize the system, with two of these ions placed at the centre of the G-tetrads. Further 2 K^+ and 2 Cl^- ions were added to reach the standard 150 mM KCl concentration. The *parmbsc1* (Ivani et al., 2016) and *gaff* (Wang et al., 2004) Amber force fields were used to parameterize the nucleic acid and ligand, respectively. Amber charges were applied to the DNA and water molecules, whereas ligand charges were computed using the restrained electrostatic potential (RESP) fitting procedure (Bayly et al., 1993). The ESP was first calculated by means of the Gaussian package using a 6-31G* basis set at B3LYP level of theory, and then the RESP charges were obtained by a two-stages fitting procedure using Antechamber (Wang et al., 2006). The NAMD 2.9 (Phillips et al., 2005) code was used to perform the simulations. A cutoff

of 10 Å was used for short-range interactions. The long-range electrostatic interactions were computed by means of the particle mesh Ewald method using a 1.0 Å grid spacing in periodic boundary conditions. Each system was minimized and heated up to 300 K while putting harmonic constraints, which were gradually released along the thermalization process. Then, production runs were performed in the NPT ensemble at 1 atm and 300 K.

Cell lines, culture conditions and treatments

HCT116 colorectal cancer cells were obtained by Dr Vogelstein, Johns Hopkins University. HK2–6 and HKE-3 were kindly provided by Dr. Shirasawa and performed by gene targeting technique (Shirasawa et al., 1993). BJ-EHLT derived from the transformation of BJ human fibroblasts with telomerase reverse transcriptase (hTERT) and simian virus 40 (SV40) early region. All the cells were grown in high glucose Dulbecco modified eagle medium (DMEM; Euroclone) supplemented with L-glutamine, penicillin/streptomycin and 10% fetal bovine serum (FBS, Hyclone). The G-quadruplex ligand EMICORON (Franceschin et al., 2012; Zizza et al., 2019) was used at 1 µM for 24 h.

Real-time PCR

To quantify gene expression by real-time quantitative polymerase chain reaction (qRT-PCR), total RNA was isolated from cell pellets by using TRIzol reagent (Ambion). The quality of the extracted RNA was assessed by 1% agarose gel electrophoresis and from the A_{260}/A_{280} absorbance ratio (Nanodrop 1000, ThermoFisher Scientific). Reverse transcription (RT) from 500 ng of RNA was performed using the QuantiTect Reverse Transcription Kit (Qiagen) according to the manufacturer's instructions. Real-time qRT-PCRs were performed on the obtained cDNAs by using Fast power SYBR green master mix (Apply Biosystem) on 7900HT Fast Real-Time PCR System (Applied Biosystem) thermocycler. For each sample 5 µl of the 1:10 diluted cDNA was mixed with 0.5 µl of each primer (10 µM), 10 µl of the SYBR green master mix and water at final volume of 20 µl. Standard qPCR thermal parameters were used: one cycle of 95 °C for 10 min then 40 cycles of 95 °C for 15 sec and 60 °C for 1 min followed by dissociation curve (95 °C for 15sec, 60 °C for 1 min, 95 °C for 15 sec).

Primer pairs (KRAS: FW 5'-ACACAAAACAGGCTCAGGACT-3'; REV: 5'-TGTCGGATCTCCCTCACCAA-3' and β-actin: FW 5'-AGCACTGTGTTGGCGTACAG-3';

REV: 5'-TCCCTGGAGAAGAGCTACGA-3') were synthesized by Integrated DNA Technologies (BVBA Leuven, Belgium).

All experiments were run in triplicate and the gene expression levels were normalized to the β -actin.

Western Blotting

For western blot analysis total cell lysates were prepared as previously reported (Biroccio et al., 2003). The proteins were fractionated by SDS-polyacrylamide gel electrophoresis and transferred to nitrocellulose membrane (Amersham, Arlington Heights, USA). Membranes were probed with primary antibodies and the signal was detected using peroxidase-conjugated anti-mouse or anti-rabbit secondary antibodies (Jackson Immunoresearch Labs, Inc., Baltimore, USA). The enhanced chemi-luminescence (ECL) system (Thermo Scientific) was used for detection. The following primary antibodies were used: rabbit mAb anti-RAS (D2C1, Cell Signaling Technology Beverly, MA, USA) and mouse mAb anti- β -actin (clone AC-15, Sigma, St. Louis, USA).

Clonogenic assay

HCT116 cells, were seeded in 35 mm-Petri dishes at the clonogenic density of 300 cells/plate in DMEM medium with 10% FBS and, after 24 h, cells were treated with DMSO (negative control) or the indicated dose of **19**. After 10 days, the cells were stained with 2% methylene blue in 50% ethanol and the number of colonies was counted. Surviving fractions were calculated as the ratio of absolute survival of the treated sample/absolute survival of the untreated sample.

Viability assay (Crystal Violet)

HK2-6 and HKE-3 cells were seeded in a 24-well plate at a density of 7×10^4 for well. After 24 h, the cells were treated with compounds **19** at different doses for 72 h. Then cells were washed twice in PBS and fixed with 4% formaldehyde for 15' at RT. After washing, 500 μ l of crystal violet staining solution (Sigma) was added to each well, and incubated for 30' at RT. Finally, the plates were rinsed twice with water, air-dried at RT, and the cell pellets were dissolved in 400 μ l of Acetic Acid. One hundred μ l of each sample were transferred to a 96-well plate and the optical density of each well was measured at 570 nm (OD570) with an ELISA

reader (Thermo Scientific). The average absorbance in each condition was used to calculate the survival expressed as percent of treated vs untreated condition. IC₅₀ (the dose necessary to reduce the survival of 50%) was calculated by Calcsyn software.

Immunofluorescence microscopy

BJ-EHLT cells were fixed in 2% formaldehyde in PBS for 10 min at Room Temperature (RT) and permeabilized in 0.25% Triton X-100 in PBS for 5 min at RT. For immune-labeling, cells were incubated with the mouse anti- γ H2AX (Millipore, Billerica, MA, USA) primary antibody 2h at RT, washed twice in PBS and finally incubated with the anti-mouse IgG (H+L), F(ab')₂ Fragment (Alexa Fluor 555 Conjugate) secondary antibodies for 1 h. Nuclei were stained with 4',6-diamidino-2-phenylindole (DAPI, Sigma). Fluorescence signals were recorded by using a Leica DMIRE2 microscope equipped with a Leica DFC 350FX camera and elaborated by Leica FW4000 deconvolution software (Leica, Solms, Germany). For quantitative analysis of γ H2AX positivity, at least 250 cells on triplicate slices were scored.

Chapter 5

EFFECTS OF EPIGENETIC MODIFICATIONS ON G4s STABILITY

In this chapter, I introduce the research activity that I conducted in the Dr. Valérie Gabelica's laboratory at the Institute Européen de Chimie et Biologie (IECB) in Pessac, Brdeaux (France). During this period, I studied the mass spectrometry characterization of G-quadruplex folding of sequences having epigenetic interest. In particular, I focused my attention on G4 that forms in the promoter region of *KIT*, called *KIT-1* G4.

Epigenetics concerns hereditary changes in gene regulation that are not related to changes in DNA sequence itself. DNA methylation, histone modification, chromatin remodeling and micro RNA are just some of several mechanism that mediate epigenetic phenomena (Tammen et al., 2013). Among those, DNA methylation and histone modifications are the most studied epigenetic mediators. DNA methylation is a chemical modification by a methyl group added on C5 position of cytosine in DNA molecule. It occurs almost exclusively at CpG dinucleotides where a cytosine nucleotide occurs next to a guanine nucleotide (Bird, 2002; Jones and Liang, 2009). Although most CpG dinucleotides are methylated, the genome also contains CpG islands (CGIs), short CpG-rich genomic regions, which are usually unmethylated. CGIs are the key epigenomic elements in mammalian genome. Initially, CGIs were defined as the regions of the genome characterized by a lower level of DNA methylation (Bird et al., 1985), but later, based on the CpG content of the DNA sequence, CGIs were defined as the segments of the genome that show increased level of CpG dinucleotides and GC content (Gardiner-Garden and Frommer, 1987; Takai and Jones, 2002). Another modification that can be had on the cytosines present in these regions is the demethylation of the 5-methylcytosine processed by thymine DNA glycosylase. Therefore, the 5-carboxylcytosine appears to be involved in the epigenetic regulation of the genome.

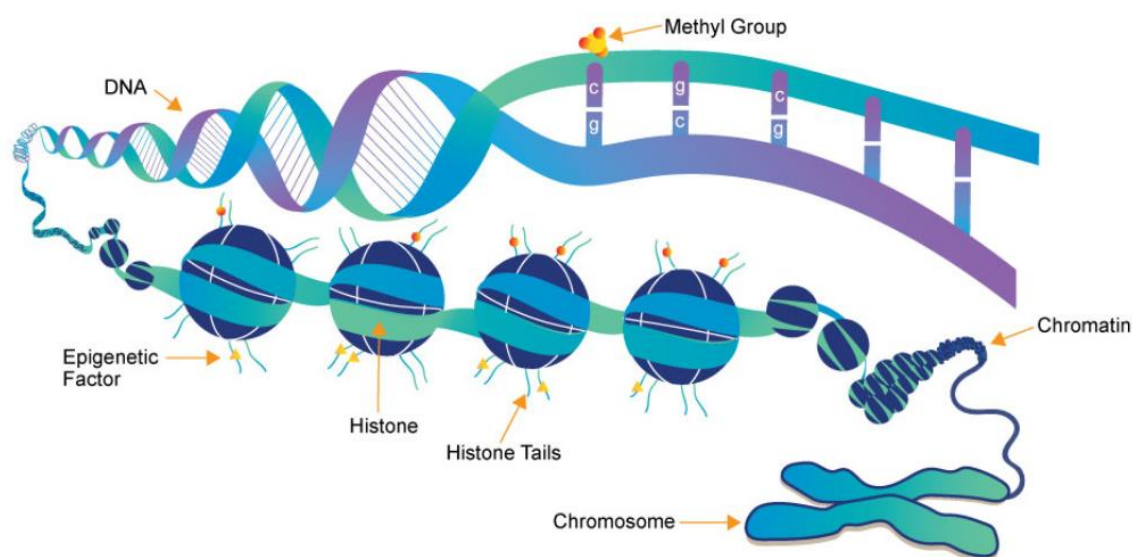


Figure 5.1. Representation of the chromatin structure, including histones and DNA, which become available to epigenetic marks.

Recent evidences support the role of G4 motifs in biological settings that are determined by epigenetic events. It is well-known that G4s have a regulatory role in recombination (Mani et al., 2009), DNA replication (Paeschke et al., 2011), initiation of double strand break (De and Michor, 2011), telomere maintenance and protein binding (Paeschke et al., 2010; Sissi et al., 2011; Bochman et al., 2012). Nucleotide composition of the G-quadruplex sequence is an important criterion for effective folding of the structural motif. The effect of a replacement of a guanine in a G-track with methylated one on the stability of human telomeric G-quadruplexes was also examined (Mekmaysy et al., 2008). Results showed that methylation not only decreases the stability of G-quadruplexes, but also changes their folded structures.

Because G4 structures are also found in the promoters of many genes and these regions are often enriched for the dinucleotide 5'-CpG-3', it will be very likely to find epigenetic modifications in these regions. Little is known about the relationship between cytosine modification in DNA and the formation or function of G4 in these regions.

For this reason, during my stay at IECB, I studied the stability of *KIT-1* G4 from with modified cytosines by mass spectrometry. The two analyzed sequences are shown in Figure 5.2.

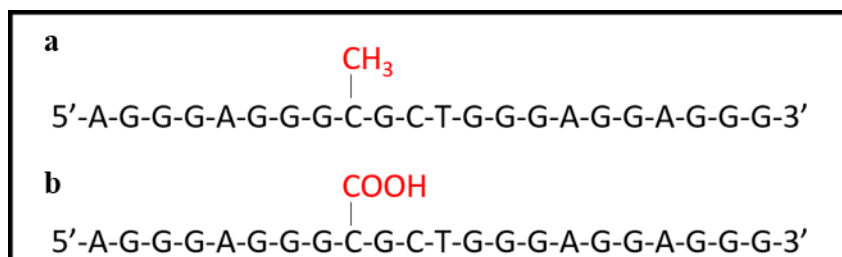


Figure 5.2. Investigated sequences: (a) *KIT-1* G4 modified with 5-methylcytosine (*KIT-1*-G4-Me), (b) *KIT-1* G4 modified with 5-carboxylcytosine (*KIT-1*- G4-COOH).

We carried out mass spectrometry experiment to check whether these sequences, despite the modified bases, were able to fold into G4 in the same way as *KIT-1* G4 without modifications.

Thanks to the high-resolution mass spectrometry, an independent signal is detected for each potassium binding stoichiometry, allowing non-ambiguous stoichiometry determination. Figure 5.3 (a-c) shows representative mass spectra (zoom on the 4⁻ charge state) obtained upon KCl titration of three *KIT-1* G4 sequences (*KIT-1* G4, *KIT-1* G4-Me and *KIT-1* G4-COOH). After subtracting the non-specific adducts contribution we quantify the concentration of specific K⁺ complexes of each stoichiometry for each point in the titration. After this subtraction, only 1-K⁺ and 2-K⁺ specific complexes remain.

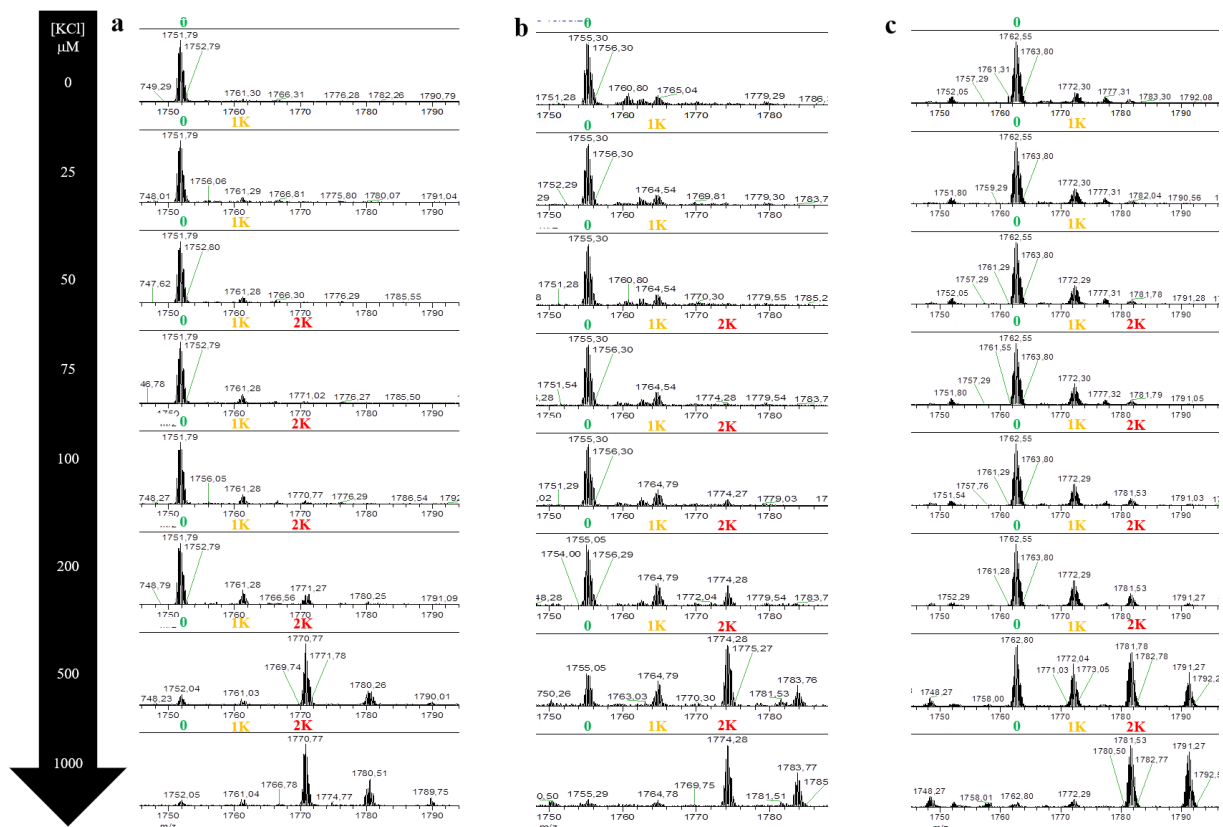


Figure 5.3. Mass spectrometry titration (20 °C) of 10 μM (a) *KIT-1* G4, (b) *KIT-1* G4-Me and (c) *KIT-1* G4-COOH, in 100 mM TMAA with increasing amount of KCl (zoom on the 4⁺ charge state).

The mass spectra of a sequence with the same number of bases as *KIT-1* G4 but which is unable to fold into G4 was used to subtract non-specific adducts (Figure 5.4).

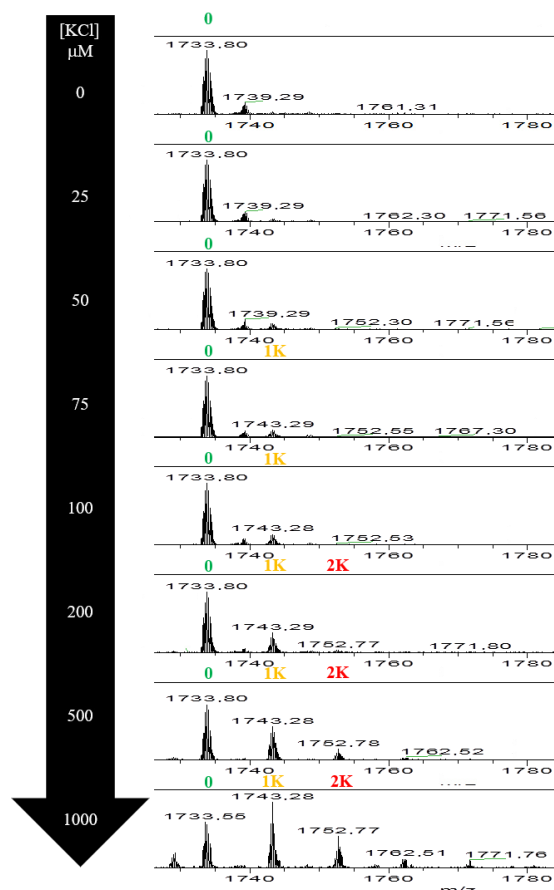


Figure 5.4. Mass spectrometry titration (20°C) of 10 μM 22nonG4 in 100 mM TMAA with increasing amount of KCl (zoom on the 4- charge state).

The results show the formation of the G4 for all three investigated sequences, as the peak of the unfolded sequence disappears already after the addition of KCl 500 μM . Furthermore, mass spectra suggest a propensity to parallel topological arrangement, since the sequences predominantly adopt a 2- K^+ binding stoichiometry in sub-mM KCl concentrations.

To confirm the formation of G4 and the predominant topology for the three sequences we monitored the same titration experiment by circular dichroism experiments.

The results (Figure 5.5 a-c) demonstrate that without KCl in solution the DNA sequences are not folded into G4. Instead, the CD spectra change upon KCl addition to the DNA, indicating a structural change induced by K^+ binding. For all the sequences the folding into parallel G4 occurs at high KCl concentration, as anticipated based on MS results.

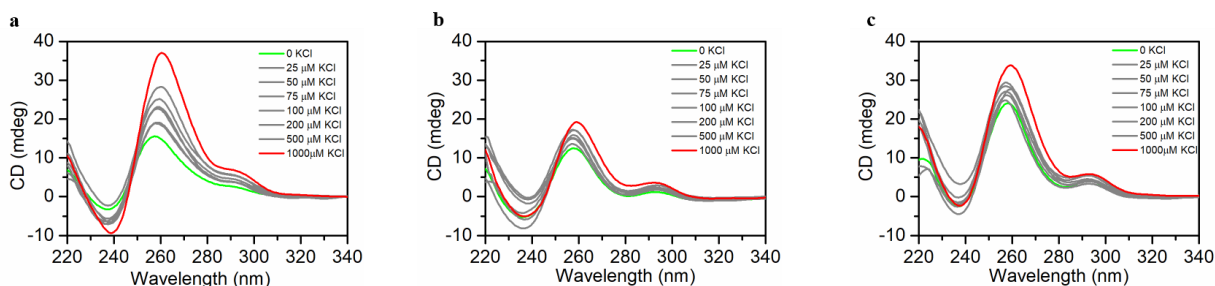


Figure 5.5. CD titration (20°C) of 10 μM (a) *KIT-1*, (b) *KIT-1-Me* and (c) *KIT-1-COOH* in 100 mM TMAA with increasing amount of KCl (0 in green, 25, 50, 75, 100, 200, 500 in grey and 1000 μM in red).

Finally, we performed the kinetic experiments (Figure 5.6 a-c) with ESI-MS to check if the formation time of the G4 was the same for all the sequences, after adding KCl.

On the minute to the hour time scale, we followed the potassium binding stoichiometry by ESI-MS at room temperature. The spectra were recorded when KCl was added to the solution (t0). After subtraction of the nonspecific adducts, we distinguished and quantify three different stoichiometries (0-K⁺, 1-K⁺ and 2-K⁺) as a function of reaction time.

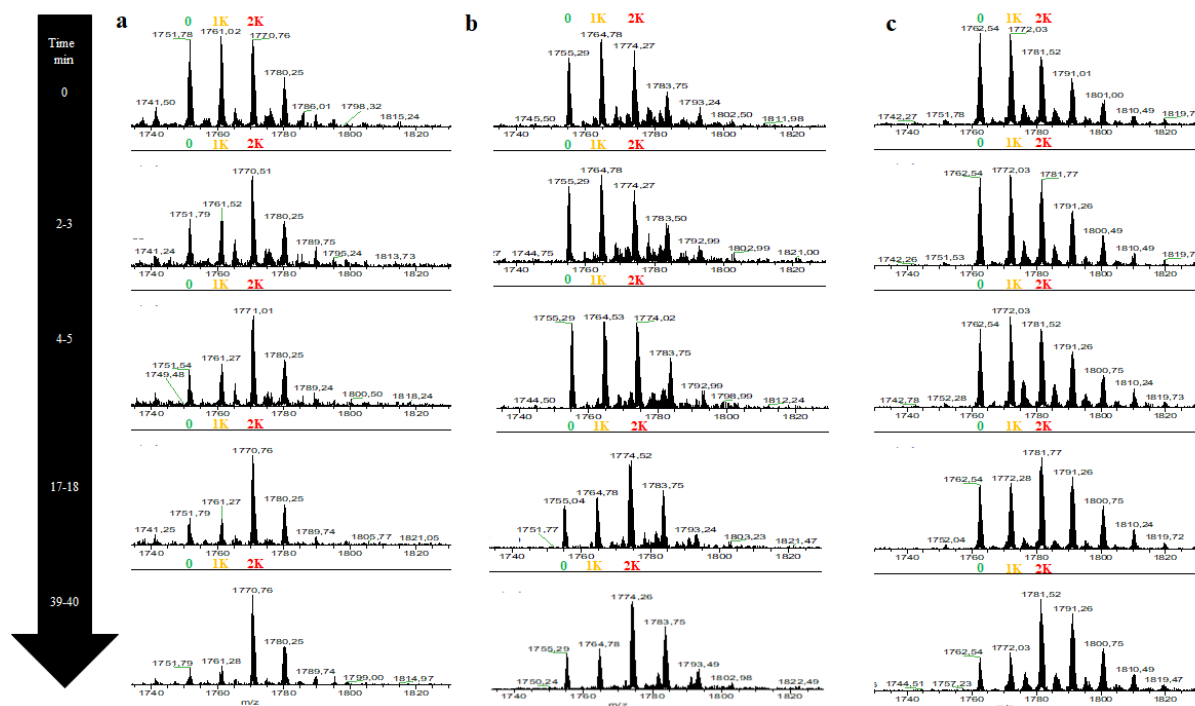


Figure 5.6. Kinetics of K⁺ binding monitored by ESI-MS of 30 μM (a) *KIT-1* G4, (b) *KIT-1* G4-Me and (c) *KIT-1* G4-COOH in 100 mM TMAA after adding KCl to reach a concentration of 1mM KCl.

The results show that the formation of G4 is faster for *KIT-1* G4 compared to the two modified sequences. In fact, for *KIT-1* G4 the complete formation of the G4 occurs already after 17-18 minutes, while for the other two sequences it takes place after 39-40 minutes (Figure 5.6).

The research is in progress in our laboratory, at the Department of Pharmacy of University of Naples Federico II. The future perspectives will be to complete the research, studying the thermodynamic stability of the modified structures through DSC and CD melting experiments.

CONCLUSIONS

This thesis has been focused on the study of biomolecules for therapeutic applications through physico-chemical methodologies, combined with biological assays. Physico-chemical techniques have been important to study the stability of biomolecules and the energetics of their interaction with potential drugs. Biological studies have been essential to assess their activity in cells.

In the first part of my thesis, the research activity was addressed to study the physico-chemical factors affecting drug bioavailability, in the second one the attention was focused on the interaction between potential drugs and DNA G4s. Finally, in the third part of the thesis, the influence of epigenetic modifications on the stability of G4 structures was studied through mass spectrometry experiments.

As concern the first part, the thermodynamics of the formation of the QCT-HP β CD complex in water and in water/ethanol mixtures has been investigated using calorimetric and spectroscopic techniques. Phase solubility experiments, supported by DSC measurements, have shown that the formation of the complex in water is improved at pH 8.0. Moreover, the affinity constant at this pH was calculated by isothermal calorimetry. Then, we studied the formation of the complex in hydroalcoholic solutions. The experiments showed that above 0.10 molar fraction molar of EtOH the complex did not form, probably because ethanol competes with quercetin for inclusion within the cavity of HP β CD. Indeed, the low content of ethanol in hydroalcoholic solvents and a slightly basic pH contributed to a better encapsulation of QCT in the cavity of HP β CD. This work was made in collaboration with pharmaceutical technologists of our Department and Russian chemists of Department of General Chemical Technology of Ivanovo State University.

As concern the second part, many small organic molecules were studied for their interaction with DNA G4s and tested in cells for their biological activity.

First, three porphyrin-like compounds were synthesized and tested on *KRAS* G4, in collaboration with researchers of Ivanovo State University and Russian Academy of Sciences. The capability of these molecules to thermally stabilize *KRAS* G4 has been studied through CD

melting experiments. Then, the binding affinity and the binding mode of the best compound have been investigated by fluorescence and molecular docking experiments. The interaction between TmPyP4, a well-known G4 ligand, and *KRAS* G4 was taken as a reference system. Finally, photodynamic measurements performed on the best compound and thorough biological tests conducted on all the compounds studied using HeLa cells, proved that this compound represents a model for the development of G4 ligands with photodynamic-induced cytotoxicity on cancer cells.

Moreover, a set of putative ligands able to target *KRAS* G4 was discovered in collaboration with researchers of our Department and a group of the Regina Elena Cancer Institute in Rome. This set of ligands were identified through High-Throughput Virtual Screening, starting from the recently determined *KRAS* G4 NMR structure as molecular docking target. The affinity of this compounds for *KRAS* G4 was quickly screened by CD melting experiments. The compounds found to be promising from these first experiments were then optimized and their binding properties to *KRAS* G4 were determined by means of CD. One compound was successfully found to be a promising *KRAS* G4 binder. Successively, fluorescence titrations, PAGE, molecular dynamics and biological assays proved that this compound represents a good starting point for further optimization.

Interestingly, in the past years, various studies have focused on the study of the interaction between quercetin and several G4 forming DNA sequences showing the beneficial effects of this flavonoid on some cancer cell lines (Bhattacharjee et al., 2017; Tawani et al., 2017). To our knowledge, the interaction between quercetin and *KRAS* G4 has never been investigated, thus this could be considered as a starting point for a future study where the use of the QCT-HP β CD complex, described in the first part of the thesis, could be of relevance for the development of new anticancer therapies.

Finally, in the third part of the thesis, during my stay at the Institute Européen de Chimie et Biologie in Bordeaux, I investigated through mass spectrometry experiments the influence of epigenetic modifications on the stability of G4 structures. Particularly, I studied the sequence able to fold into G4 of *KIT* proto-oncogene modified with 5-methylcytosine and 5-carboxylcytosine. The experiments proved that there is no difference in the formation of the G4 between the sequences with and without modifications. In addition, kinetic experiments showed that the formation of G4 is faster for unmodified sequence compared to the two modified ones. The future perspectives on this work foresee their thermodynamic characterization, through CD

and DSC methodologies. Lastly, an interesting development of this research could be the study of the *KIT-1* G4 sequence with an increased number of methylations and/or carboxylations in CG domains tight before and after the G4 sequence.

REFERENCES

- Agrawal, P., Hatzakis, E., Guo, K., Carver, M., and Yang, D. (2013). Solution structure of the major G-quadruplex formed in the human VEGF promoter in K⁺: insights into loop interactions of the parallel G-quadruplexes. *Nucleic Acids Res.* 41, 10584–10592. doi:10.1093/nar/gkt784.
- Alzeer, J., Vummidi, B. R., Roth, P. J. â. C., and Luedtke, N. W. (2009). Guanidinium-Modified Phthalocyanines as High-Affinity G-Quadruplex Fluorescent Probes and Transcriptional Regulators. *Angew. Chemie Int. Ed.* 48, 9362–9365. doi:10.1002/anie.200903685.
- Amato, J., Iaccarino, N., Pagano, B., Morigi, R., Locatelli, A., Leoni, A., et al. (2014a). Bis-indole derivatives with antitumor activity turn out to be specific ligands of human telomeric G-quadruplex. *Front. Chem.* 2, 1–8. doi:10.3389/fchem.2014.00054.
- Amato, J., Iaccarino, N., Randazzo, A., Novellino, E., and Pagano, B. (2014b). Noncanonical DNA Secondary Structures as Drug Targets: the Prospect of the i-Motif. *ChemMedChem* 9, 2026–2030. doi:10.1002/cmdc.201402153.
- Amato, J., Pagano, A., Capasso, D., Di Gaetano, S., Giustiniano, M., Novellino, E., et al. (2018). Targeting the BCL2 Gene Promoter G-Quadruplex with a New Class of Furopyridazinone-Based Molecules. *ChemMedChem* 13, 406–410. doi:10.1002/cmdc.201700749.
- Ambrus, A., Chen, D., Dai, J., Jones, R. A., and Yang, D. (2005). Solution structure of the biologically relevant G-quadruplex element in the human c-MYC promoter. Implications for G-quadruplex stabilization. *Biochemistry* 44, 2048–2058. doi:10.1021/bi048242p.
- Apak, R., Güçlü, K., Demirata, B., Özyürek, M., Çelik, S., Bektaşoğlu, B., et al. (2007). Comparative Evaluation of Various Total Antioxidant Capacity Assays Applied to Phenolic Compounds with the CUPRAC Assay. *Molecules* 12, 1496–1547. doi:10.3390/12071496.
- Armond, R. De, Wood, S., Sun, D., Hurley, L. H., and Ebbinghaus, S. W. (2005). Evidence for the Presence of a Guanine Quadruplex Forming Region within a Polypurine Tract of the Hypoxia Inducible Factor 1 R Promoter †. 16341–16350. doi:10.1021/bi051618u.
- Bacolla, A., and Wells, R. D. (2009). Non-B DNA conformations as determinants of mutagenesis and human disease. *Mol. Carcinog.* 48, 273–285. doi:10.1002/mc.20507.
- Balasubramanian, S., Hurley, L. H., and Neidle, S. (2011). Targeting G-quadruplexes in gene promoters: a novel anticancer strategy? *Nat. Rev. Drug Discov.* 10, 261–275.
- Bang, I. (1910). Untersuchungen über die Guanylsäure. *Biochem. Z.* 26, 293–311.
- Banks, J. L., Beard, H. S., Cao, Y., Cho, A. E., Damm, W., Farid, R., et al. (2005). Integrated Modeling Program, Applied Chemical Theory (IMPACT). *J. Comput. Chem.* 26, 1752–1780. doi:10.1002/jcc.20292.
- Bayly, C. I., Cieplak, P., Cornell, W., and Kollman, P. A. (1993). A well-behaved electrostatic potential based method using charge restraints for deriving atomic charges: the RESP model. *J. Phys. Chem.* 97, 10269–10280. doi:10.1021/j100142a004.
- Berezin, D. B., Karimov, D. R., Venediktov, E. A., Kustov, A. V., Makarov, V. V., and Romanenko, Y. V. (2015). The Synthesis and Singlet Oxygen Generation Study of 13(1)-N-Piperazinyl Chlorin e6-15(2),17(3)-Dimethyl Ester. *Macroheterocycles* 8, 384–388. doi:10.6060/mhc151088b.
- Bhattacharjee, S., Sengupta, P. K., and Bhowmik, S. (2017). Exploring the preferential interaction of quercetin with VEGF promoter G-quadruplex DNA and construction of a pH-dependent DNA-based logic gate. *RSC Adv.* 7, 37230–37240. doi:10.1039/C7RA05930B.
- Biffi, G., Tannahill, D., McCafferty, J., and Balasubramanian, S. (2013). Quantitative visualization of DNA G-quadruplex structures in human cells. *Nat. Chem.* 5, 182–186. doi:10.1038/nchem.1548.
- Bird, A. (2002). DNA methylation patterns and epigenetic memory. *Genes Dev.* 16, 6–21.

doi:10.1101/gad.947102.

- Bird, A., Taggart, M., Frommer, M., Miller, O. J., and Macleod, D. (1985). A fraction of the mouse genome that is derived from islands of nonmethylated, CpG-rich DNA. *Cell* 40, 91–99. doi:10.1016/0092-8674(85)90312-5.
- Biroccio, A., Amodei, S., Antonelli, A., Benassi, B., and Zupi, G. (2003). Inhibition of c-Myc Oncoprotein Limits the Growth of Human Melanoma Cells by Inducing Cellular Crisis. *J. Biol. Chem.* 278, 35693–35701. doi:10.1074/jbc.M304597200.
- Bochman, M. L., Paeschke, K., and Zakian, V. A. (2012). DNA secondary structures: stability and function of G-quadruplex structures. *Nat. Rev. Genet.* 13, 770–780. doi:10.1038/nrg3296.
- Bodnar, A. G. (1998). Extension of Life-Span by Introduction of Telomerase into Normal Human Cells. *Science* (80-.). 279, 349–352. doi:10.1126/science.279.5349.349.
- Boonyarattanakalin, K. (2015). Influence of Ethanol as Co-Solvent in Cyclodextrin Inclusion Complexation: A Molecular Dynamics Study. *Sci. Pharm.* 83, 387–399. doi:10.3797/scipharm.1412-08.
- Boots, A. W., Haenen, G. R. M. M., and Bast, A. (2008). Health effects of quercetin: From antioxidant to nutraceutical. *Eur. J. Pharmacol.* 585, 325–337. doi:10.1016/j.ejphar.2008.03.008.
- Borodin, V. A., Vasil'ev, V. P., and Kozlovskii, E. V. (1985). *Mathematical Problems of Chemical Thermodynamics*. Novosibirsk: Nauka.
- Boschi, E., Davis, S., Taylor, S., Butterworth, A., Chirayath, L. A., Purohit, V., et al. (2016). Interaction of a Cationic Porphyrin and Its Metal Derivatives with G-Quadruplex DNA. *J. Phys. Chem. B* 120, 12807–12819. doi:10.1021/acs.jpcc.6b09827.
- Brewster, M. E., and Loftsson, T. (2007). Cyclodextrins as pharmaceutical solubilizers. *Adv. Drug Deliv. Rev.* 59, 645–666. doi:10.1016/j.addr.2007.05.012.
- Brito, A., Ribeiro, M., Abrantes, A., Pires, A., Teixeira, R., Tralhao, J., et al. (2015a). Quercetin in Cancer Treatment, Alone or in Combination with Conventional Therapeutics? *Curr. Med. Chem.* 22, 3025–3039. doi:10.2174/0929867322666150812145435.
- Brito, H., Martins, A. C., Lavrado, J., Mendes, E., Francisco, A. P., Santos, S. A., et al. (2015b). Targeting KRAS Oncogene in Colon Cancer Cells with 7-Carboxylate Indolo[3,2-b]quinoline Tri-Alkylamine Derivatives. *PLoS One* 10, e0126891. doi:10.1371/journal.pone.0126891.
- Brooks, T. A., and Hurley, L. H. (2010). Targeting MYC Expression through G-Quadruplexes. *Genes Cancer* 1, 641–649. doi:10.1177/1947601910377493.
- Bugaut, A., and Balasubramanian, S. (2008). A sequence-independent study of the influence of short loop lengths on the stability and topology of intramolecular DNA G-quadruplexes. *Biochemistry* 47, 689–697. doi:10.1021/bi701873c.
- Burge, S., Parkinson, G. N., Hazel, P., Todd, A. K., and Neidle, S. (2006). Quadruplex DNA: Sequence, topology and structure. *Nucleic Acids Res.* 34, 5402–5415. doi:10.1093/nar/gkl655.
- Cai, X., Fang, Z., Dou, J., Yu, A., and Zhai, G. (2013). Bioavailability of Quercetin: Problems and Promises. *Curr. Med. Chem.* 20, 2572–2582. doi:10.2174/09298673113209990120.
- Calabrese, D. R., Zlotkowski, K., Alden, S., Hewitt, W. M., Connelly, C. M., Wilson, R. M., et al. (2018). Characterization of clinically used oral antiseptics as quadruplex-binding ligands. *Nucleic Acids Res.* 46, 2722–2732. doi:10.1093/nar/gky084.
- Cantor, C. R., Warshaw, M. M., and Shapiro, H. (1970). Oligonucleotide interactions. III. Circular dichroism studies of the conformation of deoxyoligonucleolides. *Biopolymers* 9, 1059–1077. doi:10.1002/bip.1970.360090909.
- Caroti, P., Ceccotti, C., Da Settimo, A., Palla, F., and Primofiore, G. (1987). ChemInform Abstract: Synthesis of 5,11-Dihydro-5-oxopyrido(2',3':4,5)pyrimido(1,2-a)benzimidazoles as Potential Antitumor Agents. *ChemInform* 18. doi:10.1002/chin.198744221.
- Carvalho, J., Pereira, E., Marquevielle, J., Campello, M. P. C., Mergny, J.-L., Paulo, A., et al. (2018). Fluorescent light-up acridine orange derivatives bind and stabilize KRAS-22RT G-quadruplex. *Biochimie* 144, 144–152. doi:10.1016/j.biochi.2017.11.004.
- Castillo-González, D., Mergny, J.-L., De Rache, A., Pérez-Machado, G., Cabrera-Pérez, M. A., Nicolotti, O., et al. (2015). Harmonization of QSAR Best Practices and Molecular Docking Provides an Efficient Virtual Screening Tool for Discovering New G-Quadruplex Ligands. *J.*

- Chem. Inf. Model.* 55, 2094–2110. doi:10.1021/acs.jcim.5b00415.
- Cea, V., Cipolla, L., and Sabbioneda, S. (2015). Replication of Structured DNA and its implication in epigenetic stability. *Front. Genet.* 6. doi:10.3389/fgene.2015.00209.
- Cogoi, S., Paramasivam, M., Spolaore, B., and Xodo, L. E. (2008). Structural polymorphism within a regulatory element of the human KRAS promoter: formation of G4-DNA recognized by nuclear proteins. *Nucleic Acids Res.* 36, 3765–3780. doi:10.1093/nar/gkn120.
- Cogoi, S., Quadrifoglio, F., and Xodo, L. E. (2004). G-rich Oligonucleotide Inhibits the Binding of a Nuclear Protein to the Ki- ras Promoter and Strongly Reduces Cell Growth in Human Carcinoma Pancreatic Cells †. 21, 2512–2523. doi:10.1021/bi035754f.
- Cogoi, S., and Xodo, L. E. (2006). G-quadruplex formation within the promoter of the KRAS proto-oncogene and its effect on transcription. *Nucleic Acids Res.* 34, 2536–2549. doi:10.1093/nar/gkl286.
- Cogoi, S., and Xodo, L. E. (2016). G4 DNA in ras genes and its potential in cancer therapy. *Biochim. Biophys. Acta - Gene Regul. Mech.* 1859, 663–674. doi:10.1016/j.bbagr.2016.02.002.
- Cogoi, S., Zorzet, S., Rapozzi, V., Géci, I., Pedersen, E. B., and Xodo, L. E. (2013). MAZ-binding G4-decoy with locked nucleic acid and twisted intercalating nucleic acid modifications suppresses KRAS in pancreatic cancer cells and delays tumor growth in mice. *Nucleic Acids Res.* 41, 4049–4064. doi:10.1093/nar/gkt127.
- Cummaro, A., Fotticchia, I., Franceschin, M., Giancola, C., and Petraccone, L. (2011). Binding properties of human telomeric quadruplex multimers: A new route for drug design. *Biochimie* 93, 1392–1400. doi:10.1016/j.biochi.2011.04.005.
- D’Aria, F., Caterino, M., Kustov, A. V., Belykh, D. V., Khudyaeva, I. S., Starseva, O. M., et al. (2020). Selective binding of a bioactive porphyrin-based photosensitizer to the G-quadruplex from the KRAS oncogene promoter. *Int. J. Biol. Macromol.* 145, 244–251. doi:10.1016/j.ijbiomac.2019.12.152.
- D’Aria, F., Serri, C., Niccoli, M., Mayol, L., Quagliariello, V., Iaffaioli, R. V., et al. (2017a). Host-guest inclusion complex of quercetin and hydroxypropyl- β -cyclodextrin: A calorimetric study. *J. Therm. Anal. Calorim.* 130, 451–456. doi:10.1007/s10973-017-6135-5.
- D’Aria, F., Serri, C., Niccoli, M., Mayol, L., Quagliariello, V., Iaffaioli, R. V., et al. (2017b). Host-guest inclusion complex of quercetin and hydroxypropyl- β -cyclodextrin. *J. Therm. Anal. Calorim.* 130, 451–456. doi:10.1007/s10973-017-6135-5.
- Da Settimo, A., Da Settimo, F., Marini, A. M., Primofiore, G., Salerno, S., Viola, G., et al. (1998). Synthesis, DNA binding and in vitro antiproliferative activity of purinoquinazoline, pyridopyrimidopurine and pyridopyrimidobenzimidazole derivatives as potential antitumor agents. *Eur. J. Med. Chem.* 33, 685–696. doi:10.1016/S0223-5234(98)80027-5.
- Da Settimo, A., Primofiore, G., Da Settimo, F., Marini, A. M., Taliani, S., Salerno, S., et al. (2003). Synthesis of pyrimido[1,2- a]benzimidazol-4(10 H)-one derivatives and evaluation of their interactions with DNA. *J. Heterocycl. Chem.* 40, 1091–1096. doi:10.1002/jhet.5570400620.
- Dai, J., Carver, M., and Yang, D. (2008). Polymorphism of human telomeric quadruplex structures. *Biochimie* 90, 1172–1183. doi:10.1016/j.biochi.2008.02.026.
- Dai, J., Chen, D., Jones, R. A., Hurley, L. H., and Yang, D. (2006). NMR solution structure of the major G-quadruplex structure formed in the human BCL2 promoter region. 34, 0–11. doi:10.1093/nar/gkl610.
- Dalla Via, L., Gia, O., Marciani Magno, S., Da Settimo, A., Marini, A. M., Primofiore, G., et al. (2001). Synthesis, in vitro antiproliferative activity and DNA-interaction of benzimidazoquinazoline derivatives as potential anti-tumor agents. *Farm.* 56, 159–167. doi:10.1016/S0014-827X(01)01079-5.
- de Hoffmann, E., and Stroobant, V. (2007). *Mass Spectrometry - Principles and Applications*. Third. , ed. J. Wiley.
- De, S., and Michor, F. (2011). DNA secondary structures and epigenetic determinants of cancer genome evolution. *Nat. Struct. Mol. Biol.* 18, 950–955. doi:10.1038/nsmb.2089.
- Del Curatolo, A., Conciatori, F., Cesta Incani, U., Bazzichetto, C., Falcone, I., Corbo, V., et al. (2018). Therapeutic potential of combined BRAF/MEK blockade in BRAF-wild type preclinical tumor

- models. *J. Exp. Clin. Cancer Res.* 37, 140. doi:10.1186/s13046-018-0820-5.
- Demiroglu-Zergeroglu, A., Ergene, E., Ayvali, N., Kuete, V., and Sivas, H. (2016). Quercetin and Cisplatin combined treatment altered cell cycle and mitogen activated protein kinase expressions in malignant mesotelioma cells. *BMC Complement. Altern. Med.* 16, 281. doi:10.1186/s12906-016-1267-x.
- Di Leva, F. S., Novellino, E., Cavalli, A., Parrinello, M., and Limongelli, V. (2014). Mechanistic insight into ligand binding to G-quadruplex DNA. *Nucleic Acids Res.* 42, 5447–5455. doi:10.1093/nar/gku247.
- Di Leva, F. S., Zizza, P., Cingolani, C., D'Angelo, C., Pagano, B., Amato, J., et al. (2013). Exploring the Chemical Space of G-Quadruplex Binders: Discovery of a Novel Chemotype Targeting the Human Telomeric Sequence. *J. Med. Chem.* 56, 9646–9654. doi:10.1021/jm401185b.
- di Magliano, M. P., and Logsdon, C. D. (2013). Roles for KRAS in Pancreatic Tumor Development and Progression. *Gastroenterology* 144, 1220–1229. doi:10.1053/j.gastro.2013.01.071.
- Donz, C., and Coleman, A. W. (1995). Solvent effects in competition between guest molecules for β -cyclodextrin. *J. Incl. Phenom. Mol. Recognit. Chem.* 23, 11–21. doi:10.1007/BF00706945.
- Drygin, D., Siddiqui-Jain, A., O'Brien, S., Schwaebe, M., Lin, A., Bliesath, J., et al. (2009). Anticancer Activity of CX-3543: A Direct Inhibitor of rRNA Biogenesis. *Cancer Res.* 69, 7653–7661. doi:10.1158/0008-5472.CAN-09-1304.
- Dvorkin, S. A., Karsisiotis, A. I., and Webba da Silva, M. (2018). Encoding canonical DNA quadruplex structure. *Sci. Adv.* 4, eaat3007. doi:10.1126/sciadv.aat3007.
- Eddy, J., and Maizels, N. (2006). Gene function correlates with potential for G4 DNA formation in the human genome. *Nucleic Acids Res.* 34, 3887–3896. doi:10.1093/nar/gk1529.
- Faudale, M., Cogoi, S., and Xodo, L. E. (2012). Photoactivated cationic alkyl-substituted porphyrin binding to g4-RNA in the 5'-UTR of KRAS oncogene represses translation. *Chem. Commun.* 48, 874–876. doi:10.1039/C1CC15850C.
- Fenn, J., Mann, M., Meng, C., Wong, S., and Whitehouse, C. (1989). Electrospray ionization for mass spectrometry of large biomolecules. *Science (80-.)*. 246, 64–71. doi:10.1126/science.2675315.
- Fernando, H., Reszka, A. P., Huppert, J., Ladame, S., Rankin, S., Venkitaraman, A. R., et al. (2006). A Conserved Quadruplex Motif Located in a Transcription Activation Site of the Human c-kit Oncogene. 7854–7860. doi:10.1021/bi0601510.
- Franceschin, M., Rizzo, A., Casagrande, V., Salvati, E., Alvino, A., Altieri, A., et al. (2012). Aromatic Core Extension in the Series of N-Cyclic Bay-Substituted Perylene G-Quadruplex Ligands: Increased Telomere Damage, Antitumor Activity, and Strong Selectivity for Neoplastic over Healthy Cells. *ChemMedChem* 7, 2144–2154. doi:10.1002/cmde.201200348.
- Freyer, M. W., Buscaglia, R., Kaplan, K., Cashman, D., Hurley, L. H., and Lewis, E. A. (2007). Biophysical Studies of the c-MYC NHE III1 Promoter: Model Quadruplex Interactions with a Cationic Porphyrin. *Biophys. J.* 92, 2007–2015. doi:10.1529/biophysj.106.097246.
- Friesner, R. A., Banks, J. L., Murphy, R. B., Halgren, T. A., Klicic, J. J., Mainz, D. T., et al. (2004). Glide: A New Approach for Rapid, Accurate Docking and Scoring. 1. Method and Assessment of Docking Accuracy. *J. Med. Chem.* 47, 1739–1749. doi:10.1021/jm0306430.
- Gabelica, V. (2010). “Determination of Equilibrium Association Constants of Ligand–DNA Complexes by Electrospray Mass Spectrometry,” in, 89–101. doi:10.1007/978-1-60327-418-0_6.
- Gardiner-Garden, M., and Frommer, M. (1987). CpG Islands in vertebrate genomes. *J. Mol. Biol.* 196, 261–282. doi:10.1016/0022-2836(87)90689-9.
- Gaskell, S. J. (1997). Electrospray: Principles and Practice. *J. Mass Spectrom.* 32, 677–688. doi:10.1002/(SICI)1096-9888(199707)32:7<677::AID-JMS536>3.3.CO;2-7.
- Gellert, M., Lipsett, M. N., and Davies, D. R. (1962). HELIX FORMATION BY GUANYLIC ACID. *Proc. Natl. Acad. Sci.* 48, 2013–2018. doi:10.1073/pnas.48.12.2013.
- Gesse, Z. F., Repkin, G. I., Isaeva, V. A., and Sharnin, V. A. (2012). The influence of reagents solvation on enthalpy change of glycine-ion protonation and silver(I) glycine-ion complexation in aqueous-dimethylsulfoxide solutions. *J. Therm. Anal. Calorim.* 110, 1457–1462. doi:10.1007/s10973-011-2127-z.
- Ghasemzadeh, A., Jaafar, H. Z. E., Rahmat, A., and Ashkani, S. (2015). Secondary metabolites

- constituents and antioxidant, anticancer and antibacterial activities of *Etlingera elatior* (Jack) R.M.Sm grown in different locations of Malaysia. *BMC Complement. Altern. Med.* 15, 335. doi:10.1186/s12906-015-0838-6.
- Giancola, C. (2008). A convenient tool for studying the stability of proteins and nucleic acids: Differential scanning calorimetry. *J. Therm. Anal. Calorim.* 91, 79–85. doi:10.1007/s10973-007-8436-6.
- Giancola, C., and Pagano, B. (2012). “Energetics of Ligand Binding to G-Quadruplexes,” in *Quadruplex Nucleic Acids*, 211–242. doi:10.1007/128_2012_347.
- Gladys, G., Claudia, G., and Marcela, L. (2003). The effect of pH and triethanolamine on sulfoxazole complexation with hydroxypropyl- β -cyclodextrin. *Eur. J. Pharm. Sci.* 20, 285–293. doi:10.1016/S0928-0987(03)00202-1.
- Gowan, S. M., Harrison, J. R., Patterson, L., Valenti, M., Read, M. a, Neidle, S., et al. (2002). A G-quadruplex-interactive potent small-molecule inhibitor of telomerase exhibiting in vitro and in vivo antitumor activity. *Mol. Pharmacol.* 61, 1154–1162. doi:10.1124/mol.61.5.1154.
- Grand, C. L., Han, H., Muñoz, R. M., Weitman, S., Von Hoff, D. D., Hurley, L. H., et al. (2002). The cationic porphyrin TMPyP4 down-regulates c-MYC and human telomerase reverse transcriptase expression and inhibits tumor growth in vivo. *Mol. Cancer Ther.* 1, 565–73. Available at: <http://www.ncbi.nlm.nih.gov/pubmed/12479216>.
- Gray, D. M., and Bollum, F. J. (1974). A circular dichroism study of poly dG, poly dC, and poly dG:dC. *Biopolymers* 13, 2087–2102. doi:10.1002/bip.1974.360131011.
- Greenwood, J. R., Calkins, D., Sullivan, A. P., and Shelley, J. C. (2010). Towards the comprehensive, rapid, and accurate prediction of the favorable tautomeric states of drug-like molecules in aqueous solution. *J. Comput. Aided. Mol. Des.* 24, 591–604. doi:10.1007/s10822-010-9349-1.
- Greider, C. W., and Blackburn, E. H. (1985). Identification of a specific telomere terminal transferase activity in tetrahymena extracts. *Cell* 43, 405–413. doi:https://doi.org/10.1016/0092-8674(85)90170-9.
- Gros, J., Rosu, F., Amrane, S., De Cian, A., Gabelica, V., Lacroix, L., et al. (2007). Guanines are a quartet’s best friend: impact of base substitutions on the kinetics and stability of tetramolecular quadruplexes. *Nucleic Acids Res.* 35, 3064–3075. doi:10.1093/nar/gkm111.
- Guardia, T., Rotelli, A. E., Juarez, A. O., and Pelzer, L. E. (2001). Anti-inflammatory properties of plant flavonoids. Effects of rutin, quercetin and hesperidin on adjuvant arthritis in rat. *Farm.* 56, 683–687. doi:10.1016/S0014-827X(01)01111-9.
- Guédin, A., Gros, J., Alberti, P., and Mergny, J.-L. (2010). How long is too long? Effects of loop size on G-quadruplex stability. *Nucleic Acids Res.* 38, 7858–7868. doi:10.1093/nar/gkq639.
- Guo, K., Pourpak, A., Beetz-Rogers, K., Gokhale, V., Sun, D., and Hurley, L. H. (2007). Formation of Pseudosymmetrical G-Quadruplex and i-Motif Structures in the Proximal Promoter Region of the RET Oncogene. *J. Am. Chem. Soc.* 129, 10220–10228. doi:10.1021/ja072185g.
- Hackett, J. A., Feldser, D. M., and Greider, C. W. (2001). Telomere Dysfunction Increases Mutation Rate and Genomic Instability. 106, 275–286.
- Hădărugă, N. G., Hădărugă, D. I., and Isengard, H.-D. (2013). “Surface water” and “strong-bonded water” in cyclodextrins: a Karl Fischer titration approach. *J. Incl. Phenom. Macrocycl. Chem.* 75, 297–302. doi:10.1007/s10847-012-0143-7.
- Haigis, K. M. (2017). KRAS Alleles: The Devil Is in the Detail. *Trends in Cancer* 3, 686–697. doi:10.1016/j.trecan.2017.08.006.
- Halgren, T. A., Murphy, R. B., Friesner, R. A., Beard, H. S., Frye, L. L., Pollard, W. T., et al. (2004). Glide: A New Approach for Rapid, Accurate Docking and Scoring. 2. Enrichment Factors in Database Screening. *J. Med. Chem.* 47, 1750–1759. doi:10.1021/jm030644s.
- Hammond-kosack, M. C. U., Dobrinski, B., Lurz, R., Docherty, K., and Kilpatrick, M. W. (1992). The human insulin gene linked polymorphic region exhibits an altered DNA structure. 20, 231–236.
- Hänsel-Hertsch, R., Beraldi, D., Lensing, S. V., Marsico, G., Zyner, K., Parry, A., et al. (2016). G-quadruplex structures mark human regulatory chromatin. *Nat. Genet.* 48, 1267–1272. doi:10.1038/ng.3662.
- Hershman, S. G., Chen, Q., Lee, J. Y., Kozak, M. L., Yue, P., Wang, L.-S., et al. (2008). Genomic

- distribution and functional analyses of potential G-quadruplex-forming sequences in *Saccharomyces cerevisiae*. *Nucleic Acids Res.* 36, 144–156. doi:10.1093/nar/gkm986.
- Hertog, M. G. L., Hollman, P. C. H., Katan, M. B., and Kromhout, D. (1993). Intake of potentially anticarcinogenic flavonoids and their determinants in adults in the Netherlands. *Nutr. Cancer* 20, 21–29. doi:10.1080/01635589309514267.
- Hobbs, G. A., Der, C. J., and Rossman, K. L. (2016). RAS isoforms and mutations in cancer at a glance. *J. Cell Sci.* 129, 1287–1292. doi:10.1242/jcs.182873.
- Hoffman, E. K., Trusko, S. P., Murphy, M., and George, D. L. (1990). An S1 nuclease-sensitive homopurine/homopyrimidine domain in the c-Ki-ras promoter interacts with a nuclear factor. *Proc. Natl. Acad. Sci.* 87, 2705–2709. doi:10.1073/pnas.87.7.2705.
- Huppert, J. L. (2005). Prevalence of quadruplexes in the human genome. *Nucleic Acids Res.* 33, 2908–2916. doi:10.1093/nar/gki609.
- Huppert, J. L. (2008). Four-stranded nucleic acids: structure, function and targeting of G-quadruplexes. *Chem. Soc. Rev.* 37, 1375. doi:10.1039/b702491f.
- Huppert, J. L., and Balasubramanian, S. (2007). G-quadruplexes in promoters throughout the human genome. 35, 406–413. doi:10.1093/nar/gkl1057.
- Hurley, L. H., Wheelhouse, R. T., Sun, D., Kerwin, S. M., Salazar, M., Fedoroff, O. Y., et al. (2000). G-quadruplexes as targets for drug design. *Pharmacol. Ther.* 85, 141–158. doi:10.1016/S0163-7258(99)00068-6.
- Ivani, I., Dans, P. D., Noy, A., Pérez, A., Faustino, I., Hospital, A., et al. (2016). Parmbsc1: a refined force field for DNA simulations. *Nat. Methods* 13, 55–58. doi:10.1038/nmeth.3658.
- Johnson, J. L., Rupasinghe, S. G., Stefani, F., Schuler, M. A., and Gonzalez de Mejia, E. (2011). Citrus Flavonoids Luteolin, Apigenin, and Quercetin Inhibit Glycogen Synthase Kinase-3 β Enzymatic Activity by Lowering the Interaction Energy Within the Binding Cavity. *J. Med. Food* 14, 325–333. doi:10.1089/jmf.2010.0310.
- Jones, P. A., and Liang, G. (2009). Rethinking how DNA methylation patterns are maintained. *Nat. Rev. Genet.* 10, 805–811. doi:10.1038/nrg2651.
- Jordano, J., and Perucho, M. (1986). Chromatin structure of the promoter region of the human c-K-ras gene. *Nucleic Acids Res.* 14, 7361–7378. doi:10.1093/nar/14.18.7361.
- Jorgensen, W. L., Chandrasekhar, J., Madura, J. D., Impley, R. W., and Klein, M. L. (1983). Comparison of simple potential functions for simulating liquid water. *J. Chem. Phys.* 79, 926–935.
- Jullian, C., Moyano, L., Yañez, C., and Olea-Azar, C. (2007). Complexation of quercetin with three kinds of cyclodextrins: An antioxidant study. *Spectrochim. Acta Part A Mol. Biomol. Spectrosc.* 67, 230–234. doi:10.1016/j.saa.2006.07.006.
- Kang, R., Xie, Y., Zhang, Q., Hou, W., Jiang, Q., Zhu, S., et al. (2017). Intracellular HMGB1 as a novel tumor suppressor of pancreatic cancer. *Cell Res.* 27, 916–932. doi:10.1038/cr.2017.51.
- Keli, S. O., Hertog, M. G., Feskens, E. J., and Kromhout, D. (1996). Dietary flavonoids, antioxidant vitamins, and incidence of stroke: the Zutphen study. *Arch. Intern. Med.* 156, 637–42. Available at: <http://www.ncbi.nlm.nih.gov/pubmed/8629875>.
- Kerkour, A., Marquevielle, J., Ivashchenko, S., Yatsunyk, L. A., Mergny, J.-L., and Salgado, G. F. (2017). High-resolution three-dimensional NMR structure of the KRAS proto-oncogene promoter reveals key features of a G-quadruplex involved in transcriptional regulation. *J. Biol. Chem.* 292, 8082–8091. doi:10.1074/jbc.M117.781906.
- Khonkarn, R., Mankhetkorn, S., Hennink, W. E., and Okonogi, S. (2011). PEG-OCL micelles for quercetin solubilization and inhibition of cancer cell growth. *Eur. J. Pharm. Biopharm.* 79, 268–275. doi:10.1016/j.ejpb.2011.04.011.
- Kim, N. W., Piatyszek, M. A., Prowse, K. R., Harley, C. B., West, M. D., Ho, P. L. C., et al. (2011). Specific Association of Human Telomerase Activity with Immortal Cells and Cancer. 266, 2011–2016.
- Krestov, G., and Novosyolov, N. (1994). *Ionic Solvation*. Ellis Horw. New York: Prentice Hall.
- Kühnau, J. “The Flavonoids. A Class of Semi-Essential Food Components: Their Role in Human Nutrition,” in, 117–191. doi:10.1159/000399407.
- Kustov, A. V., Belykh, D. V., Smirnova, N. L., Venediktov, E. A., Kudayarova, T. V., Kruchin, S. O.,

- et al. (2018). Synthesis and investigation of water-soluble chlorophyll pigments for antimicrobial photodynamic therapy. *Dye. Pigment.* 149, 553–559. doi:10.1016/j.dyepig.2017.09.073.
- Lang, P. T., Brozell, S. R., Mukherjee, S., Pettersen, E. F., Meng, E. C., Thomas, V., et al. (2009). DOCK 6: Combining techniques to model RNA-small molecule complexes. *RNA* 15, 1219–1230. doi:10.1261/rna.1563609.
- Larocca, L. M., Piantelli, M., Leone, G., Sica, S., Teofili, L., Panici, P. B., et al. (1990). Type II oestrogen binding sites in acute lymphoid and myeloid leukaemias: growth inhibitory effect of oestrogen and flavonoids. *Br. J. Haematol.* 75, 489–495. doi:10.1111/j.1365-2141.1990.tb07787.x.
- Larsen, A., and Weintraub, H. (1982). An altered DNA conformation detected by S1 nuclease occurs at specific regions in active chick globin chromatin. *Cell* 29, 609–622. doi:https://doi.org/10.1016/0092-8674(82)90177-5.
- Lavagnini, I., Magno, F., Seraglia, R., and Traldi, P. (2006). *Quantitative Applications of Mass Spectrometry*. doi:10.1002/0470029021.
- Lavrado, J., Brito, H., Borralho, P. M., Ohnmacht, S. A., Kim, N.-S., Leitão, C., et al. (2015). KRAS oncogene repression in colon cancer cell lines by G-quadruplex binding indolo[3,2-c]quinolines. *Sci. Rep.* 5, 9696. doi:10.1038/srep09696.
- Lee, J., Han, S.-I., Yun, J.-H., and Kim, J. H. (2015). Quercetin 3-O-glucoside suppresses epidermal growth factor-induced migration by inhibiting EGFR signaling in pancreatic cancer cells. *Tumor Biol.* 36, 9385–9393. doi:10.1007/s13277-015-3682-x.
- Lee, L.-T., Huang, Y.-T., Hwang, J.-J., Lee, P.-P. H., Ke, F.-C., Nair, M. P., et al. (2002). Blockade of the epidermal growth factor receptor tyrosine kinase activity by quercetin and luteolin leads to growth inhibition and apoptosis of pancreatic tumor cells. *Anticancer Res.* 22, 1615–27. Available at: <http://www.ncbi.nlm.nih.gov/pubmed/12168845>.
- Leonetti, C. (2004). Biological Activity of the G-Quadruplex Ligand RHPS4 (3,11-Difluoro-6,8,13-trimethyl-8H-quino[4,3,2-kl]acridinium methosulfate) Is Associated with Telomere Capping Alteration. *Mol. Pharmacol.* 66, 1138–1146. doi:10.1124/mol.104.001537.
- Lichtenthaler, F., and Immel, S. (1996). The Lipophilicity Patterns of Cyclodextrins and of Non-glucose Cyclooligosaccharides. *J. Incl. Phenom. Mol. Recognit. Chem.* 25, 3–16.
- Lin, J., Hou, J., Xiang, H., Yan, Y., Gu, Y., Tan, J., et al. (2013). Stabilization of G-quadruplex DNA by C-5-methyl-cytosine in bcl-2 promoter: Implications for epigenetic regulation. *Biochem. Biophys. Res. Commun.* 433, 368–373. doi:10.1016/j.bbrc.2012.12.040.
- Lipps, H. J., and Rhodes, D. (2009). G-quadruplex structures: in vivo evidence and function. doi:10.1016/j.tcb.2009.05.002.
- Liu, M., Dong, L., Chen, A., Zheng, Y., Sun, D., Wang, X., et al. (2013). Inclusion complexes of quercetin with three β -cyclodextrins derivatives at physiological pH: Spectroscopic study and antioxidant activity. *Spectrochim. Acta Part A Mol. Biomol. Spectrosc.* 115, 854–860. doi:10.1016/j.saa.2013.07.008.
- Liu, Y., Tang, Z.-G., Lin, Y., Qu, X.-G., Lv, W., Wang, G.-B., et al. (2017). Effects of quercetin on proliferation and migration of human glioblastoma U251 cells. *Biomed. Pharmacother.* 92, 33–38. doi:10.1016/j.biopha.2017.05.044.
- Loftsson, T., and Brewster, M. E. (1996). Pharmaceutical Applications of Cyclodextrins. 1. Drug Solubilization and Stabilization. *J. Pharm. Sci.* 85, 1017–1025. doi:10.1021/js950534b.
- Lu, J., Wu, D., Zheng, Y., Hu, B., Zhang, Z., Shan, Q., et al. (2010). Quercetin activates AMP-activated protein kinase by reducing PP2C expression protecting old mouse brain against high cholesterol-induced neurotoxicity. *J. Pathol.* 222, 199–212. doi:10.1002/path.2754.
- Lu, M., Guo, Q., and Kallenbach, N. R. (1993). Thermodynamics of G-tetraplex formation by telomeric DNAs. *Biochemistry* 32, 598–601. doi:10.1021/bi00053a027.
- Madhavi Sastry, G., Adzhigirey, M., Day, T., Annabhimoju, R., and Sherman, W. (2013). Protein and ligand preparation: parameters, protocols, and influence on virtual screening enrichments. *J. Comput. Aided. Mol. Des.* 27, 221–234. doi:10.1007/s10822-013-9644-8.
- Malik, A., Sultana, M., Qazi, A., Qazi, M. H., Parveen, G., Waquar, S., et al. (2016). Role of Natural Radiosensitizers and Cancer Cell Radioresistance: An Update. *Anal. Cell. Pathol.* 2016, 1–8.

doi:10.1155/2016/6146595.

- Mani, P., Yadav, V. K., Das, S. K., and Chowdhury, S. (2009). Genome-Wide Analyses of Recombination Prone Regions Predict Role of DNA Structural Motif in Recombination. *PLoS One* 4, e4399. doi:10.1371/journal.pone.0004399.
- Margolin, Y., Cloutier, J.-F., Shafirovich, V., Geacintov, N. E., and Dedon, P. C. (2006). Paradoxical hotspots for guanine oxidation by a chemical mediator of inflammation. *Nat. Chem. Biol.* 2, 365–366. doi:10.1038/nchembio796.
- Marquevielle, J., Kumar, M. V. V., Mergny, J.-L., and Salgado, G. F. (2018). 1H, 13C, and 15N chemical shift assignments of a G-quadruplex forming sequence within the KRAS proto-oncogene promoter region. *Biomol. NMR Assign.* 12, 123–127. doi:10.1007/s12104-017-9793-0.
- Marsh, D. T., Das, S., Ridell, J., and Smid, S. D. (2017). Structure-activity relationships for flavone interactions with amyloid β reveal a novel anti-aggregatory and neuroprotective effect of 2',3',4'-trihydroxyflavone (2-D08). *Bioorg. Med. Chem.* 25, 3827–3834. doi:10.1016/j.bmc.2017.05.041.
- Martino, L., Pagano, B., Fotticchia, I., Neidle, S., and Giancola, C. (2009). Shedding Light on the Interaction between TMPyP4 and Human Telomeric Quadruplexes. *J. Phys. Chem. B* 113, 14779–14786. doi:10.1021/jp9066394.
- Mayol, L., Serri, C., Menale, C., Crispi, S., Piccolo, M. T., Mita, L., et al. (2015). Curcumin loaded PLGA–poloxamer blend nanoparticles induce cell cycle arrest in mesothelioma cells. *Eur. J. Pharm. Biopharm.* 93, 37–45. doi:10.1016/j.ejpb.2015.03.005.
- McCormick, F. (2015). KRAS as a Therapeutic Target. *Clin. Cancer Res.* 21, 1797–1801. doi:10.1158/1078-0432.CCR-14-2662.
- Mekmaysy, C. S., Petraccone, L., Garbett, N. C., Ragazzon, P. A., Gray, R., Trent, J. O., et al. (2008). Effect of O 6 -Methylguanine on the Stability of G-Quadruplex DNA. *J. Am. Chem. Soc.* 130, 6710–6711. doi:10.1021/ja801976h.
- Mergny, J., Gros, J., De Cian, A., Bourdoncle, A., Rosu, F., Saccà, B., et al. (2006). “Energetics, kinetics and dynamics of quadruplex folding,” in *Quadruplex Nucleic Acids*, eds. S. Neidle and S. Balasubramanian (Cambridge: Royal Society of Chemistry), 31–80.
- Miglietta, G., Cogoi, S., Marinello, J., Capranico, G., Tikhomirov, A. S., Shchekotikhin, A., et al. (2017). RNA G-Quadruplexes in Kirsten Ras (KRAS) Oncogene as Targets for Small Molecules Inhibiting Translation. *J. Med. Chem.* 60, 9448–9461. doi:10.1021/acs.jmedchem.7b00622.
- Monchaud, D., and Teulade-Fichou, M. P. (2008). A hitchhiker’s guide to G-quadruplex ligands. *Org. Biomol. Chem.* 6, 627–636. doi:10.1039/b714772b.
- Mouria, M., Gukovskaya, A. S., Jung, Y., Buechler, P., Hines, O. J., Reber, H. A., et al. (2002). Food-derived polyphenols inhibit pancreatic cancer growth through mitochondrial cytochrome C release and apoptosis. *Int. J. Cancer* 98, 761–769. doi:10.1002/ijc.10202.
- Moyano-Mendez, J. R., Fabbrocini, G., De Stefano, D., Mazzella, C., Mayol, L., Scognamiglio, I., et al. (2014). Enhanced antioxidant effect of trans -resveratrol: potential of binary systems with polyethylene glycol and cyclodextrin. *Drug Dev. Ind. Pharm.* 40, 1300–1307. doi:10.3109/03639045.2013.817416.
- Moye, A. L., Porter, K. C., Cohen, S. B., Phan, T., Zyner, K. G., Sasaki, N., et al. (2015). Telomeric G-quadruplexes are a substrate and site of localization for human telomerase. *Nat. Commun.* 6, 1–12. doi:10.1038/ncomms8643.
- Murat, P., and Balasubramanian, S. (2014). Existence and consequences of G-quadruplex structures in DNA. *Curr. Opin. Genet. Dev.* 25, 22–29. doi:10.1016/j.gde.2013.10.012.
- Murugan, C., Rayappan, K., Thangam, R., Bhanumathi, R., Shanthi, K., Vivek, R., et al. (2016). Combinatorial nanocarrier based drug delivery approach for amalgamation of anti-tumor agents in breast cancer cells: an improved nanomedicine strategy. *Sci. Rep.* 6, 34053. doi:10.1038/srep34053.
- Nam, J.-S., Sharma, A., Nguyen, L., Chakraborty, C., Sharma, G., and Lee, S.-S. (2016). Application of Bioactive Quercetin in Oncotherapy: From Nutrition to Nanomedicine. *Molecules* 21, 108. doi:10.3390/molecules21010108.
- Neidle, S., and Parkinson, G. (2002). Telomere maintenance as a target for anticancer drug discovery. *Nat. Rev. Drug Discov.* 1, 383–393. doi:10.1038/nrd793.

- Ohnishi, E., and Bannai, H. (1993). Quercetin potentiates TNF-induced antiviral activity. *Antiviral Res.* 22, 327–331. doi:10.1016/0166-3542(93)90041-G.
- Oliviero, G., D’Errico, S., Borbone, N., Amato, J., Piccialli, V., Varra, M., et al. (2008). Synthesis of N-1-alkyl analogues of cyclic inosine diphosphate ribose (CIDPR) by a new solid phase approach. *Nucleic Acids Symp. Ser.* 52, 573–574. doi:10.1093/nass/nrn290.
- Oprean, C., Mioc, M., Csányi, E., Ambrus, R., Bojin, F., Tatu, C., et al. (2016). Improvement of ursolic and oleanolic acids’ antitumor activity by complexation with hydrophilic cyclodextrins. *Biomed. Pharmacother.* 83, 1095–1104. doi:10.1016/j.biopha.2016.08.030.
- Paeschke, K., Capra, J. A., and Zakian, V. A. (2011). DNA Replication through G-Quadruplex Motifs Is Promoted by the *Saccharomyces cerevisiae* Pif1 DNA Helicase. *Cell* 145, 678–691. doi:10.1016/j.cell.2011.04.015.
- Paeschke, K., McDonald, K. R., and Zakian, V. A. (2010). Telomeres: Structures in need of unwinding. *FEBS Lett.* 584, 3760–3772. doi:10.1016/j.febslet.2010.07.007.
- Paeschke, K., Simonsson, T., Postberg, J., Rhodes, D., and Lipps, H. J. (2005). Telomere end-binding proteins control the formation of G-quadruplex DNA structures in vivo. 12, 847–854. doi:10.1038/nsmb982.
- Pagano, A., Iaccarino, N., Abdelhamid, M. A. S., Brancaccio, D., Garzarella, E. U., Di Porzio, A., et al. (2018). Common G-Quadruplex Binding Agents Found to Interact With i-Motif-Forming DNA: Unexpected Multi-Target-Directed Compounds. *Front. Chem.* 6. doi:10.3389/fchem.2018.00281.
- Pagano, B., Cosconati, S., Gabelica, V., Petraccone, L., De Tito, S., Marinelli, L., et al. (2012). State-of-the-art methodologies for the discovery and characterization of DNA G-quadruplex binders. *Curr. Pharm. Des.* 18, 1880–1899. doi:1381-6128/12.
- Pagano, B., Randazzo, A., Fotticchia, I., Novellino, E., Petraccone, L., and Giancola, C. (2013). Differential scanning calorimetry to investigate G-quadruplexes structural stability. *Methods* 64, 43–51. doi:10.1016/j.ymeth.2013.02.018.
- Parenty, A. D. C., Smith, L. V., and Cronin, L. (2005). An unusual substitution reaction directed by an intramolecular re-arrangement. *Tetrahedron* 61, 8410–8418. doi:10.1016/j.tet.2005.06.074.
- Parenty, A. D. C., Song, Y.-F., Richmond, C. J., and Cronin, L. (2007). A General and Efficient Five-Step One-Pot Procedure Leading to Nitrogen-Bridgehead Heterocycles Containing an Imidazole Ring. *Org. Lett.* 9, 2253–2256. doi:10.1021/ol070263z.
- Patel, D. J., Phan, A. T., and Kuryavyi, V. (2007). Human telomere , oncogenic promoter and 5’ -UTR G-quadruplexes : diverse higher order DNA and RNA targets for cancer therapeutics. *Nucleic Acids Res.* 35, 7429–7455. doi:10.1093/nar/gkm711.
- Pattanayak, R., Barua, A., Das, A., Chatterjee, T., Pathak, A., Choudhury, P., et al. (2018). Porphyrins to restrict progression of pancreatic cancer by stabilizing KRAS G-quadruplex: In silico, in vitro and in vivo validation of anticancer strategy. *Eur. J. Pharm. Sci.* 125, 39–53. doi:10.1016/j.ejps.2018.09.011.
- Phan, A. T. (2010). Human telomeric G-quadruplex : structures of DNA and RNA sequences. 277, 1107–1117. doi:10.1111/j.1742-4658.2009.07464.x.
- Phan, A. T., Kuryavyi, V., Burge, S., Neidle, S., and Patel, D. J. (2007). Structure of an unprecedented G-quadruplex scaffold in the human c-kit promoter. *J. Am. Chem. Soc.* 129, 4386–4392. doi:10.1021/ja068739h.
- Phatak, P., Cookson, J. C., Dai, F., Smith, V., Gartenhaus, R. B., Stevens, M. F. G., et al. (2007). Telomere uncapping by the G-quadruplex ligand RHPS4 inhibits clonogenic tumour cell growth in vitro and in vivo consistent with a cancer stem cell targeting mechanism. *Br. J. Cancer* 96, 1223–1233. doi:10.1038/sj.bjc.6603691.
- Phillips, J. C., Braun, R., Wang, W., Gumbart, J., Tajkhorshid, E., Villa, E., et al. (2005). Scalable molecular dynamics with NAMD. *J. Comput. Chem.* 26, 1781–1802. doi:10.1002/jcc.20289.
- Pralhad, T., and Rajendrakumar, K. (2004). Study of freeze-dried quercetin-cyclodextrin binary systems by DSC, FT-IR, X-ray diffraction and SEM analysis. *J. Pharm. Biomed. Anal.* 34, 333–9. doi:10.1016/S0731-7085(03)00529-6.
- Przystupski, D., Niemczura, M. J., Górska, A., Supplitt, S., Kotowski, K., Wawryka, P., et al. (2019). In Search of Panacea—Review of Recent Studies Concerning Nature-Derived Anticancer Agents.

- Nutrients* 11, 1426. doi:10.3390/nu11061426.
- Pylina, Y., Shadrin, D., Shevchenko, O., Startseva, O., Velegzhaninov, I., Belykh, D., et al. (2017). Dark and Photoinduced Cytotoxic Activity of the New Chlorophyll-a Derivatives with Oligoethylene Glycol Substituents on the Periphery of Their Macrocycles. *Int. J. Mol. Sci.* 18, 103. doi:10.3390/ijms18010103.
- Qin, Y., and Hurley, L. H. (2008). Structures, folding patterns, and functions of intramolecular DNA G-quadruplexes found in eukaryotic promoter regions. 90. doi:10.1016/j.biochi.2008.02.020.
- Randazzo, A., Spada, G. P., and Da Silva, M. W. (2013). Circular dichroism of quadruplex structures. *Top. Curr. Chem.* 330, 67–86. doi:10.1007/128-2012-331.
- Rankin, S., Reszka, A. P., Huppert, J., Zloh, M., Parkinson, G. N., Todd, K., et al. (2005). Putative DNA Quadruplex Formation within the Human c-kit Oncogene. *J Am Chem Soc* 127, 10584–10589. doi:10.1021/ja050823u.Putative.
- Rawal, P. (2006). Genome-wide prediction of G4 DNA as regulatory motifs: Role in Escherichia coli global regulation. *Genome Res.* 16, 644–655. doi:10.1101/gr.4508806.
- Razmara, R. S., Daneshfar, A., and Sahraei, R. (2010). Solubility of Quercetin in Water + Methanol and Water + Ethanol from (292.8 to 333.8) K. *J. Chem. Eng. Data* 55, 3934–3936. doi:10.1021/je9010757.
- Ren, J., and Chaires, J. B. (1999). Sequence and Structural Selectivity of Nucleic Acid Binding Ligands †. *Biochemistry* 38, 16067–16075. doi:10.1021/bi992070s.
- Rodriguez, R., Müller, S., Yeoman, J. A., Trentesaux, C., Riou, J. F., and Balasubramanian, S. (2008). A novel small molecule that alters shelterin integrity and triggers a DNA-damage response at telomeres. *J. Am. Chem. Soc.* 130, 15758–15759. doi:10.1021/ja805615w.
- Romera, C., Bombarde, O., Bonnet, R., Gomez, D., Dumy, P., Calsou, P., et al. (2011). Improvement of porphyrins for G-quadruplex DNA targeting. *Biochimie* 93, 1310–1317. doi:10.1016/j.biochi.2011.06.008.
- Rustighi, A., Tessari, M. A., Vascotto, F., Sgarra, R., Giancotti, V., and Manfioletti, G. (2002). A Polypyrimidine/Polypurine Tract within the Hmga2 Minimal Promoter: A Common Feature of Many Growth-Related Genes †. *Biochemistry* 41, 1229–1240. doi:10.1021/bi011666o.
- Saito, K. (1974). Possible site of flavonoid synthesis in the photosynthetic apparatus (Short Communication). *Biochem. J.* 144, 431–432. doi:10.1042/bj1440431.
- Salunkhe, D. K., Jadhav, S. J., Kadam, S. S., Chavan, J. K., and Luh, B. S. (1983). Chemical, biochemical, and biological significance of polyphenols in cereals and legumes. *C R C Crit. Rev. Food Sci. Nutr.* 17, 277–305. doi:10.1080/10408398209527350.
- Salvati, E., Leonetti, C., Rizzo, A., Scarsella, M., Mottolese, M., Galati, R., et al. (2007). Telomere damage induced by the G-quadruplex ligand RHPS4 has an antitumor effect. *J. Clin. Invest.* 117, 3236–3247. doi:10.1172/JCI32461.
- Sasisekharan, V. (1992). Hairpin and parallel. *Nucleic Acids Res.* 20, 4061–4067.
- Savic, I. M., Nikolic, V. D., Savic-Gajic, I., Nikolic, L. B., Radovanovic, B. C., and Mladenovic, J. D. (2015). Investigation of properties and structural characterization of the quercetin inclusion complex with (2-hydroxypropyl)- β -cyclodextrin. *J. Incl. Phenom. Macrocycl. Chem.* 82, 383–394. doi:10.1007/s10847-015-0500-4.
- Scalbert, A., and Williamson, G. (2000). Dietary Intake and Bioavailability of Polyphenols. *J. Nutr.* 130, 2073S-2085S. doi:10.1093/jn/130.8.2073S.
- Schaffitzel, C., Berger, I., Postberg, J., Hanes, J., Lipps, H. J., and Plu, A. (2001). In vitro generated antibodies specific for telomeric guanine-quadruplex DNA react with Stylonychia lemnae macronuclei.
- Schardinger, F. (1903). Über Thermophile Bakterien aus verschiedenen Speisen und Milch, sowie über einige Umsetzungsprodukte derselben in kohlenhydrathaltigen Nährlösungen, darunter kristallisierte Polysaccharide (Dextrine) aus Stärke. *Z. Unters. Nahr. Genussm* 6, 865–880.
- Serra, R. W., Fang, M., Park, S. M., Hutchinson, L., and Green, M. R. (2014). A KRAS-directed transcriptional silencing pathway that mediates the CpG island methylator phenotype. *Elife* 3. doi:10.7554/eLife.02313.
- Sfeir, A. J., Chai, W., Shay, J. W., and Wright, W. E. (2005). Telomere-End Processing: the Terminal

- Nucleotides of Human Chromosomes. 18, 131–138. doi:10.1016/j.molcel.2005.02.035.
- Shaik, Y. B., Castellani, M. L., Perrella, A., Conti, F., Salini, V., Tete, S., et al. Role of quercetin (a natural herbal compound) in allergy and inflammation. *J. Biol. Regul. Homeost. Agents* 20, 47–52. Available at: <http://www.ncbi.nlm.nih.gov/pubmed/18187018>.
- Shakkeed, Z., Guerstein-Guzikevich, G., Eisenstein, M., Frolow, F., and Rabinovich, D. (1989). The conformation of the DNA double helix in the crystal is dependent on its environment. *Nature* 342, 456–460. doi:10.1038/342456a0.
- Sharnin, V. A. (1995). Thermochemistry of formation of copper(II)-ethylenediamine complexes and solvation of reagents in aqueous organic solvents. *J. Therm. Anal.* 45, 721–728. doi:10.1007/BF02548887.
- Shelley, J. C., Cholleti, A., Frye, L. L., Greenwood, J. R., Timlin, M. R., and Uchimaya, M. (2007). Epik: a software program for pK a prediction and protonation state generation for drug-like molecules. *J. Comput. Aided. Mol. Des.* 21, 681–691. doi:10.1007/s10822-007-9133-z.
- Shirasawa, S., Furuse, M., Yokoyama, N., and Sasazuki, T. (1993). Altered growth of human colon cancer cell lines disrupted at activated Ki-ras. *Science* (80-.). 260, 85–88. doi:10.1126/science.8465203.
- Siddiqui-Jain, A., Grand, C. L., Bearss, D. J., and Hurley, L. H. (2002). Direct evidence for a G-quadruplex in a promoter region and its targeting with a small molecule to repress c-MYC transcription. *Proc. Natl. Acad. Sci.* 99, 11593–11598. doi:10.1073/pnas.182256799.
- Simonsson, T., Pecinka, P., and Kubista, M. (1998). DNA tetraplex formation in the control region of c-myc. 26, 1167–1172.
- Siravegna, G., Mussolin, B., Buscarino, M., Corti, G., Cassingena, A., Crisafulli, G., et al. (2015). Clonal evolution and resistance to EGFR blockade in the blood of colorectal cancer patients. *Nat. Med.* 21, 795–801. doi:10.1038/nm.3870.
- Sissi, C., Gatto, B., and Palumbo, M. (2011). The evolving world of protein-G-quadruplex recognition: A medicinal chemist's perspective. *Biochimie* 93, 1219–1230. doi:10.1016/j.biochi.2011.04.018.
- Sissons, H. A. (1953). THE SPREAD OF TUMOURS IN THE HUMAN BODY By R. A. Willis, M.D, D.Sc., F.R.C.P., Professor of Pathology in the University of Leeds; formerly Pathologist to the Alfred Hospital, and to the Austin Hospital for Chronic Diseases, Melbourne. Second edition. 10x7. *J. Bone Joint Surg. Br.* 35-B, 337–337. doi:10.1302/0301-620X.35B2.337.
- Stella, V. J., and Rajewski, R. A. (1997). Cyclodextrins: their future in drug formulation and delivery. *Pharm. Res.* 14, 556–67. doi:10.1023/a:1012136608249.
- Sun, D. (2005). Facilitation of a structural transition in the polypurine/polypyrimidine tract within the proximal promoter region of the human VEGF gene by the presence of potassium and G-quadruplex-interactive agents. *Nucleic Acids Res.* 33, 6070–6080. doi:10.1093/nar/gki917.
- Sun, D., Thompson, B., Cathers, B. E., Salazar, M., Kerwin, S. M., Trent, J. O., et al. (1997). Inhibition of human telomerase by a G-Quadruplex-Interactive compound. *J. Med. Chem.* 40, 2113–2116. doi:10.1021/jm970199z.
- Szejtli, J. (1998). Introduction and General Overview of Cyclodextrin Chemistry. *Chem. Rev.* 98, 1743–1754. doi:10.1021/cr970022c.
- Szente, L. (1999). Highly soluble cyclodextrin derivatives: chemistry, properties, and trends in development. *Adv. Drug Deliv. Rev.* 36, 17–28. doi:10.1016/S0169-409X(98)00092-1.
- Tada-Oikawa, S., Oikawa, S., Hirayama, J., Hirakawa, K., and Kawanishi, S. (2009). DNA Damage and Apoptosis Induced by Photosensitization of 5,10,15,20-Tetrakis (N -methyl-4-pyridyl)-21 H ,23 H -porphyrin via Singlet Oxygen Generation. *Photochem. Photobiol.* 85, 1391–1399. doi:10.1111/j.1751-1097.2009.00600.x.
- Takai, D., and Jones, P. A. (2002). Comprehensive analysis of CpG islands in human chromosomes 21 and 22. *Proc. Natl. Acad. Sci.* 99, 3740–3745. doi:10.1073/pnas.052410099.
- Tammen, S. A., Friso, S., and Choi, S.-W. (2013). Epigenetics: The link between nature and nurture. *Mol. Aspects Med.* 34, 753–764. doi:10.1016/j.mam.2012.07.018.
- Tang, P., Tang, B., Wang, Q., Xu, K., Xiong, X., and Li, H. (2016). Effect of hydroxypropyl- β -cyclodextrin on the bounding of salazosulfapyridine to human serum albumin. *Int. J. Biol. Macromol.* 92, 105–115. doi:10.1016/j.ijbiomac.2016.07.033.

- Tawani, A., Mishra, S. K., and Kumar, A. (2017). Structural insight for the recognition of G-quadruplex structure at human c-myc promoter sequence by flavonoid Quercetin. *Sci. Rep.* 7, 3600. doi:10.1038/s41598-017-03906-3.
- Thiriet, C., and Hayes, J. J. (2005). Chromatin in need of a fix: Phosphorylation of H2AX connects chromatin to DNA repair. *Mol. Cell* 18, 617–622. doi:10.1016/j.molcel.2005.05.008.
- Todd, A. K., Johnston, M., and Neidle, S. (2005). Highly prevalent putative quadruplex sequence motifs in human DNA. *Nucleic Acids Res.* 33, 2901–2907. doi:10.1093/nar/gki553.
- Trott, O., and Olson, A. J. (2009). AutoDock Vina: Improving the speed and accuracy of docking with a new scoring function, efficient optimization, and multithreading. *J. Comput. Chem.*, NA-NA. doi:10.1002/jcc.21334.
- Usacheva, T., Kabirov, D., Beregova, D., Gamov, G., Sharnin, V., Biondi, M., et al. (2019). Thermodynamics of complex formation between hydroxypropyl- β -cyclodextrin and quercetin in water–ethanol solvents at T = 298.15 K. *J. Therm. Anal. Calorim.* 138, 417–424. doi:10.1007/s10973-019-08136-5.
- Usacheva, T. R., Pham Thi, L., Terekhova, I. V., Kumeev, R. S., and Sharnin, V. A. (2016). Thermodynamics of molecular complexation of glycyl–glycyl–glycine with cryptand [2.2.2] in water–dimethylsulfoxide solvent at 298.15 K. *J. Therm. Anal. Calorim.* 126, 307–314. doi:10.1007/s10973-016-5383-0.
- Usacheva, T. R., and Sharnin, V. A. (2015). A thermodynamic study of reactions of amino acids with crown ethers in nonaqueous media as examples of guest–host molecular complex formation. *Russ. Chem. Bull.* 64, 2536–2544. doi:10.1007/s11172-015-1189-7.
- Varizhuk, A., Isaakova, E., and Pozmogova, G. (2019). DNA G-Quadruplexes (G4s) Modulate Epigenetic (Re)Programming and Chromatin Remodeling. *BioEssays* 41, 1900091. doi:10.1002/bies.201900091.
- Villiers, A. (1891). Sur la fermentation de la féculé par l’action du ferment butyrique. *Compt. Rend. Acad. Sci* 112, 536–538.
- Wang, C., Su, L., Wu, C., Wu, J., Zhu, C., and Yuan, G. (2016). RGD peptide targeted lipid-coated nanoparticles for combinatorial delivery of sorafenib and quercetin against hepatocellular carcinoma. *Drug Dev. Ind. Pharm.* 42, 1938–1944. doi:10.1080/03639045.2016.1185435.
- Wang, J. M., Wolf, R. M., Caldwell, J. W., Kollman, P. a, and Case, D. a (2004). Development and testing of a general amber force field. *J. Comput. Chem.* 25, 1157–1174. doi:10.1002/jcc.20035.
- Wang, J., Wang, W., Kollman, P. A., and Case, D. A. (2006). Automatic atom type and bond type perception in molecular mechanical calculations. *J. Mol. Graph. Model.* 25, 247–260. doi:10.1016/j.jmgm.2005.12.005.
- Wang, K., Liu, R., Li, J., Mao, J., Lei, Y., Wu, J., et al. (2011). Quercetin induces protective autophagy in gastric cancer cells: Involvement of Akt-mTOR- and hypoxia-induced factor 1 α -mediated signaling. *Autophagy* 7, 966–978. doi:10.4161/auto.7.9.15863.
- Watson, J. D., and Crick, F. H. D. (1953). A Structure for Deoxyribose Nucleic Acid. *Nature* 171, 737–738.
- Wei, D., Parkinson, G. N., Reszka, A. P., and Neidle, S. (2012). Crystal structure of a c-kit promoter quadruplex reveals the structural role of metal ions and water molecules in maintaining loop conformation. *Nucleic Acids Res.* 40, 4691–4700. doi:10.1093/nar/gks023.
- Williamson, J. R., Raghuraman, M. K., and Cech, T. R. (1989). Monovalent cation-induced structure of telomeric DNA: The G-quartet model. *Cell* 59, 871–880. doi:https://doi.org/10.1016/0092-8674(89)90610-7.
- World Health Organization (2018). World Cancer Report.
- Xu, H., Di Antonio, M., McKinney, S., Mathew, V., Ho, B., O’Neil, N. J., et al. (2017). CX-5461 is a DNA G-quadruplex stabilizer with selective lethality in BRCA1/2 deficient tumours. *Nat. Commun.* 8, 14432. doi:10.1038/ncomms14432.
- Yang, D., and Okamoto, K. (2010). Structural insights into G-quadruplexes: towards new anticancer drugs. *Future Med. Chem.* 2, 619–646. doi:10.4155/fmc.09.172.
- Yoshii, H., Kometani, T., Furuta, T., Watanabe, Y., Linko, Y.-Y., and Linko, P. (1998). Formation of Inclusion Complexes of Cyclodextrin with Ethanol under Anhydrous Conditions. *Biosci.*


- Biotechnol. Biochem.* 62, 2166–2170. doi:10.1271/bbb.62.2166.
- Yue, Q., Gao, G., Zou, G., Yu, H., and Zheng, X. (2017). Natural Products as Adjunctive Treatment for Pancreatic Cancer: Recent Trends and Advancements. *Biomed Res. Int.* 2017, 1–13. doi:10.1155/2017/8412508.
- Zahedi, M., Ghiasvand, R., Feizi, A., Asgari, G., and Darvish, L. (2013). Does Quercetin Improve Cardiovascular Risk factors and Inflammatory Biomarkers in Women with Type 2 Diabetes: A Double-blind Randomized Controlled Clinical Trial. *Int. J. Prev. Med.* 4, 777–85. doi:24049596.
- Zevakin, M. A., Grazhdan, K. V., Dushina, S. V., and Sharnin, V. A. (2007). Thermodynamic characteristics of reagents and reaction of Ag⁺–nicotinamide complex formation in water–ethanol media. *J. Mol. Liq.* 131–132, 163–167. doi:10.1016/j.molliq.2006.08.036.
- Zhang, D.-H., Fujimoto, T., Saxena, S., Yu, H.-Q., Miyoshi, D., and Sugimoto, N. (2010). Monomorphic RNA G-Quadruplex and Polymorphic DNA G-Quadruplex Structures Responding to Cellular Environmental Factors. *Biochemistry* 49, 4554–4563. doi:10.1021/bi1002822.
- Zhang, Y., Larraufie, M.-H., Musavi, L., Akkiraju, H., Brown, L. M., and Stockwell, B. R. (2018). Design of Small Molecules That Compete with Nucleotide Binding to an Engineered Oncogenic KRAS Allele. *Biochemistry* 57, 1380–1389. doi:10.1021/acs.biochem.7b01113.
- Zhang, Y., Yang, F., Jamali, M., and Peng, Z. (2016). Antioxidant Enzyme Activities and Lipid Oxidation in Rape (*Brassica campestris* L.) Bee Pollen Added to Salami during Processing. *Molecules* 21, 1439. doi:10.3390/molecules21111439.
- Zhao, J., Bacolla, A., Wang, G., and Vasquez, K. M. (2010). Non-B DNA structure-induced genetic instability and evolution. *Cell. Mol. Life Sci.* 67, 43–62. doi:10.1007/s00018-009-0131-2.
- Zheng, Y., Haworth, I. S., Zuo, Z., Chow, M. S. S., and Chow, A. H. L. (2005). Physicochemical and Structural Characterization of Quercetin- β -Cyclodextrin Complexes. *J. Pharm. Sci.* 94, 1079–1089. doi:10.1002/jps.20325.
- Zhou, W., Kallifatidis, G., Baumann, B., Rausch, V., Mattern, J., Gladkich, J., et al. (2010). Dietary polyphenol quercetin targets pancreatic cancer stem cells. *Int. J. Oncol.* 37, 551–61. doi:10.3892/ijo_00000704.
- Zizza, P., Dinami, R., Porru, M., Cingolani, C., Salvati, E., Rizzo, A., et al. (2019). TRF2 positively regulates SULF2 expression increasing VEGF-A release and activity in tumor microenvironment. *Nucleic Acids Res.* 47, 3365–3382. doi:10.1093/nar/gkz041.

Published Papers

Papers I – II - III

Host–guest inclusion complex of quercetin and hydroxypropyl- β -cyclodextrin

A calorimetric study

Federica D’Aria¹ · Carla Serri² · Marcella Niccoli³ · Laura Mayol^{1,4,5} · Vincenzo Quagliariello⁶ · Rosario Vincenzo Iaffaioli⁶ · Marco Biondi^{1,4,5}  · Concetta Giancola¹

Received: 16 December 2016 / Accepted: 1 February 2017 / Published online: 16 February 2017
© Akadémiai Kiadó, Budapest, Hungary 2017

Abstract Quercetin (QCT), a flavonoid derived from many fruits and vegetables, is endowed with manifold biological properties, such as the ability to elicit a strong inhibitory effect on the growth of several tumor cell lines. Unfortunately, the pharmacological application of QCT is severely restricted by its inherent hydrophobicity and consequent low in vivo bioavailability. The therapeutic potential of QCT can be unraveled by enhancing its solubility through the formation of a host–guest complex with hydroxypropyl- β -cyclodextrin (HP β CD). In this study, HP β CD-QCT complex has been obtained in liquid phase, at 37 °C and under a prolonged mixing (72 h), and using two buffers at pH = 3.6 and pH = 8.0. Phase solubility and differential scanning calorimetry (DSC) studies revealed that, at pH = 8.0, the complex was obtained with

a 1:1 stoichiometric ratio and a strong enhancement of QCT solubility, while in acidic buffer complex formation was significantly thwarted. The affinity constant was calculated by isothermal calorimetry at pH = 8 and was found to be $489 \pm 38 \text{ M}^{-1}$, in good agreement with the value indirectly obtained from phase solubility tests $394 \pm 101 \text{ M}^{-1}$. The results confirmed the formation of the inclusion complex between QCT and HP β CD and highlight the importance of the choice of the appropriate solvent, pH, temperature and mixing time on the formation of host guest inclusion complex with active ingredient(s) and HP β CD.

Keywords Quercetin · Hydroxypropyl- β -cyclodextrin · DSC · Isothermal Calorimetry · Inclusion complex · Phase solubility

✉ Marco Biondi
mabiondi@unina.it

- ¹ Dipartimento di Farmacia, Università degli Studi di Napoli Federico II, Via D. Montesano 49, 80131 Naples, Italy
- ² Dipartimento di Scienze del Farmaco e Prodotti per la Salute, Università degli Studi di Messina, Piazza Pugliatti 1, 98122 Messina, Italy
- ³ Dipartimento di Scienze Chimiche, Università degli Studi di Napoli Federico II, Strada Comunale Cinthia 26, 80126 Naples, Italy
- ⁴ Centro di Ricerca Interdipartimentale sui Biomateriali (CRIB), Università degli Studi di Napoli Federico II, P.le V. Tecchio 80, 80125 Naples, Italy
- ⁵ Consorzio Interuniversitario INBB: Laboratorio Nazionale Interferenti Endocrini, Via Pietro Castellino 111, 80128 Naples, Italy
- ⁶ Dipartimento di Oncologia Addominale, Istituto Nazionale per lo Studio e la Cura dei Tumori, Fondazione “G. Pascale”-IRCCS, 80131 Naples, Italy

Introduction

Quercetin (QCT), also known as 3, 5, 7, 3', 4'-pentahydroxyflavone, is a flavonoid of vegetal origin, which is very abundant in many fruits and vegetables [1] and, in particular, in onions [2].

QCT is emerging as an important bioactive ingredient with manifold potential applications in pharmaceutical products since it is endowed with some interesting biological activities and is well known mainly for its strong antioxidant properties [3]. In addition, QCT possesses further interesting features, such as cardiovascular protection [4], along with antiviral [5], anti-inflammatory [6] and anticancer [7] activity. In particular, QCT can elicit a strong inhibitory effect on the growth of several tumor cell lines [8–10]. QCT has been proposed as an ancillary molecule in combination therapy, when administered with

several chemotherapeutic drugs in the treatment of different cancers, such as topotecan [11], cisplatin [12] and sorafenib [13], just to cite a few. In a recent report, QCT has also been shown to act as a radiosensitizer [14].

Notwithstanding this wide spectrum of pharmacological properties, the use of QCT in the pharmaceutical field is hampered by its strong hydrophobicity, which greatly limits the bioavailability and absorption profiles of this phytochemical, especially after oral administration. The formation of inclusion complexes between QCT and solubility enhancers such as cyclodextrins is a simple way to increase the solubility of the active molecule.

Actually, cyclodextrins are frequently used in the pharmaceutical field to increase the solubility of sparingly soluble compounds in water, taking advantage of their hydrophilic outer surface and hydrophobic internal cavity. The latter can encompass a wide array of sparingly water soluble molecules, therefore forming a host–guest complex and increasing the solubility, stability and overall bioavailability of the complexed molecule [15–17]. Among cyclodextrins, β -cyclodextrin is very often employed as a pharmaceutical excipient, mainly because of its cheapness, dimensions of the lipophilic cavity and ease of availability [18]. More in detail, β -cyclodextrin is a cyclic oligosaccharide with a frusto-conical architecture, composed of seven α -D-glucopyranose units linked by (α -1, 4) glycosidic bonds [19].

Unfortunately, native β -cyclodextrins are poorly soluble in water and, also, induce adverse nephrotoxic effects when administered parenterally [20]. For this reason, chemically modified and generally safe β -cyclodextrins have been produced. Among them, semi-synthetic hydroxypropyl- β -cyclodextrin (HP β CD) is frequently employed to improve the dissolution features and bioavailability of lipophilic drugs and, due to its improved safety, can also be used in parenteral dosage forms [21].

Although the use of cyclodextrins is helpful to promote the solubilization of poorly soluble drugs, the efficiency of the complexation is generally low. For this reason, relatively large amounts of cyclodextrins are often needed to solubilize adequate amounts of drug. In this context, it is crucial to maximize complexation efficiency, and this is outstandingly important for strongly lipophilic molecules. In particular, formation of host–guest complex can be significantly ameliorated by properly adjusting the pH of the solution [22].

The aim of the present work is to improve the solubilization of QCT by forming an inclusion complex between the molecule and HP β CD. The complex has been formed in liquid phase in two different buffers at pH = 3.6 and 8.0 under mild heating (37 °C) and prolonged mixing times (72 h). The formation, stoichiometry and affinity constant of the complexes were determined by phase solubility

experiments, differential scanning calorimetry (DSC) and isothermal calorimetry, to obtain qualitative information on the thermodynamics of formation of the complex.

Experimental

Materials

All substances were Sigma-Aldrich products. In all calorimetric measurements, the concentration of quercetin (QCT) was between 1.5×10^{-4} and 2.0×10^{-4} mol kg⁻¹, while the concentration range for the for HP β CD was between 2.2×10^{-3} and 2.5×10^{-2} mol kg⁻¹. The average degree of substitution (DS) of the HP β CD employed was 4.2. Solutions were prepared just before measurements employing phosphate and citrate buffers, at pH = 8.0 and 3.6, respectively.

Preparation and characterization of quercetin: hydroxypropyl- β cyclodextrin-complex

QCT and HP β CD were dissolved in each buffer solution at a 1:1 molar ratio and placed in a thermostatic bath under mild agitation (100 rpm) at 37 °C for 72 h. During mixing, each flask was covered with aluminum foil to prevent QCT photodegradation.

The obtained QCT-HP β CD inclusion complexes were characterized by phase solubility experiments, differential scanning calorimetry curves and isothermal microcalorimetry tests, as described in the following.

Phase solubility experiments

Prior to phase solubility tests, citrate and phosphate buffer were prepared. Citrate buffer was prepared by dissolving 1.93 g of sodium citrate and 2.41 g of citric acid in 500 mL of bidistilled water (DDW). The solution was magnetically stirred for 30 min at room temperature and diluted with further DDW to a final 1 L volume. The resulting liquid was filtered through a 0.45- μ m membrane filter, and the pH was adjusted to 3.6. For phosphate buffer, 0.201 g of KCl, 7 g of NaCl, 1.42 g of Na₂HPO₄ were solubilized and the same procedure employed. The pH was adjusted to 8.0.

To verify the formation of QCT-HP β CD inclusion complexes, phase solubility experiments were carried out as described in the following. An excess amount of QCT was suspended in 10 mL of citrate or phosphate buffer solutions containing HP β CD in the 3–15 mM concentration range. The suspensions were poured in capped vials, vortexed for 5 min and mixed in the dark at 37 °C in a

thermostatic bath for 72 h under continuous agitation at 100 rpm. Thereafter, the solutions were filtered through a 0.45-μm membrane and the filtered solution was analyzed by spectrophotometric assay to quantify the solubilized QCT (UV-1800, Shimadzu Laboratory World, Japan; $\lambda = 370$ and 382 nm in citrate and phosphate buffer, respectively). The phase diagram was obtained by plotting the molar concentration of solubilized QCT against HPβCD molar concentration.

The stability constant of the QCT-HPβCD complex was calculated from the slope of the phase solubility diagram, with the equation:

$$K_c = \frac{\text{slope}}{S_0(1 - \text{slope})} \quad (1)$$

where S_0 is QCT solubility in the absence of HPβCD.

Differential scanning calorimetry (DSC)

The formation of the complex between QCT and HPβCD has been qualitatively investigated by performing thermo-analytical tests on the lyophilized solutions (24 h, 0.01 atm, -60 °C; Modulyo, Edwards, UK) obtained from phase solubility. Particularly, the heats involved in the melting of QCT, HPβCD, the inclusion complex and the recovered precipitate from phase solubility tests were determined by a differential scanning calorimeter (DSC; DSC Q20, TA Instruments, USA), preliminarily calibrated with a pure indium standard. Accurately weighted solid samples (approximately 3–4 mg) were placed in aluminum pans and scanned from 40 to 400 °C at a constant heating rate of 10 °C min⁻¹, under an inert nitrogen atmosphere purged at a constant 50.0 mL min⁻¹ flow rate. The melting temperature (T_m) was obtained from the fusion peak.

Isothermal calorimetry

Measurements of the experimental heats of dilution or mixing of two binary solutions containing any one of the solutes were determined at 298 K using a thermal activity monitor (TAM) from Thermometric, equipped with a flow mixing vessel. A P3 peristaltic pump from Pharmacia envoys the solutions into the calorimeter through Teflon tubes.

The values of the experimental heats (of dilution or mixing) can be obtained from the equation:

$$\Delta H = \left(\frac{\frac{dQ}{dt}}{P_w} \right) \quad (2)$$

where $\frac{dQ}{dt}$ (W) is the heat flux, P_w (kg⁻¹) is the total mass flow rate of the solvent through the calorimeter, and ΔH is given in J kg⁻¹ of solvent in the final solution.

The following two kinds of experiments were arranged:

1. The determination of the heat of dilution, ΔH_{dil} ($m^i \rightarrow m^f$), from the initial, m^i , to the final, m^f , molality of binary aqueous solutions of HPβCD or QCT, at the different concentrations employed.
2. The determination of the heat of mixing, ΔH_{MIX} [$(m_{\text{HP}\beta\text{CD}}^i)(m_{\text{QCT}}^i) \rightarrow m_{\text{HP}\beta\text{CD}}^f, m_{\text{QCT}}^f$] of binary aqueous solutions of QCT, with binary aqueous solutions of HPβCD.

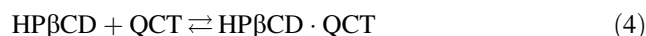
Dilution and mixing experiments were carried out using PBS buffer as solvent.

The enthalpy of mixing two binary solutions, ΔH_{MIX} , is related to the enthalpy of formation of a complex, or in general to the enthalpy of interaction between solutes, ΔH^* , and to the heats of dilution experienced by the two solutes, ΔH_{dil} , by the following equation:

$$\begin{aligned} \Delta H_{\text{MIX}} & \left[(m_{\text{HP}\beta\text{CD}}^i)(m_{\text{QCT}}^i) \rightarrow m_{\text{HP}\beta\text{CD}}^f, m_{\text{QCT}}^f \right] \\ & = \Delta H^* + \Delta H_{\text{dil}}(m_{\text{HP}\beta\text{CD}}^i \rightarrow m_{\text{HP}\beta\text{CD}}^f) \\ & \quad + \Delta H_{\text{dil}}(m_{\text{QCT}}^i \rightarrow m_{\text{QCT}}^f) \end{aligned} \quad (3)$$

Treatment of the data

Assuming that a 1:1 complex is formed when mixing two binary solutions, the association process can be represented as follows:



ΔH^* , normalized to the total molality of the guest, m_{QCT} can be related to the actual molality of the cyclodextrin host molecule, $m_{\text{HP}\beta\text{CD}}^f$, to the standard molar enthalpy of association, ΔH_a° , and to the apparent affinity constant, K_a' , as follows [23]:

$$\frac{m_{\text{QCT}}}{\Delta H^*} = \frac{1}{\Delta H_a^\circ} + \frac{1}{\Delta H_a^\circ K_a' m_{\text{HP}\beta\text{CD}}^f} \quad (5)$$

For each value of ΔH^* , the actual concentration of the host molecule is given by:

$$m_{\text{HP}\beta\text{CD}}^f = m_{\text{HP}\beta\text{CD}} - \left(\frac{\Delta H^*}{\Delta H_{\text{SAT}}^*} \right) * m_{\text{QCT}} \quad (6)$$

where m_{QCT} is the total stoichiometric molality of the host molecule. The standard enthalpy and the constant are obtained from Eqs. (5) and (6) by an iterative least-squares fitting. The iterations are continued until two successive values of ΔH_a° differ by less than 2%. The values of the free energy and entropy are obtained through the usual thermodynamic relations. The absence of any information about the activity coefficients leads to the evaluation of

association parameters thermodynamically not exactly defined. Only an apparent constant, K'_a , can be determined, and consequently the standard free energy and entropy suffer of the same limitations.

Results and discussion

Phase solubility experiments have been carried out to verify whether HP β CD is actually useful to form an inclusion complex with the guest molecule, thereby increasing its solubility. Figure 1 displays the molar concentration of QCT (i.e. the guest molecule) as a function of the molar concentration of the HP β CD, at pH = 3.6 and 8.0. Results indicate that, in phosphate buffer, QCT concentration is linearly increasing with increasing HP β CD concentration, while in the case of citrate buffer, the increase in QCT concentration is hardly detectable and the linearity of the dependence is less than satisfactory ($r^2 = 0.558$). The slope of the line at pH = 8.0 is 0.034 and a 6.4-fold solubility enhancement of QCT was found, thereby indicating a significant degree of interaction between QCT and HP β CD. In addition, the linear profile of the diagram points at a 1:1 stoichiometric ratio as for the formation of QCT-HP β CD complex. The affinity constant, indirectly estimated from Eq. (1), was found to be $394 \pm 101 \text{ M}^{-1}$. Differently, in the case of the acidic buffer, the results were less reliable, suggesting that the

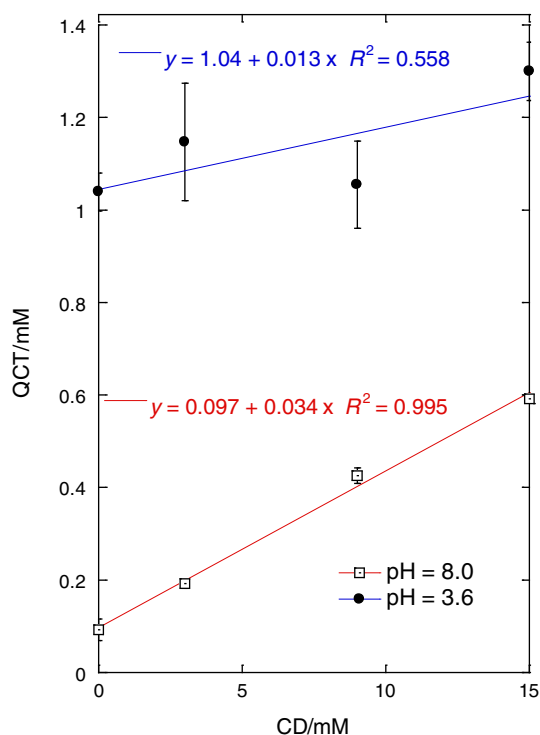


Fig. 1 Phase solubility graph of QCT-HP β CD in phosphate (pH = 8.0) and citrate (pH = 3.6) buffers ($n = 3$)

formation of the inclusion complex is strongly discouraged. This can be explained considering that the saturation concentration of QCT at pH = 8.0 is 0.039 mM, while at pH = 3.6 it is 1.04 mM. In this latter case, therefore, QCT molecules can interact much better with water molecules compared to the hydrophobic cavity of HP β CD.

DSC is frequently employed to evidence the differences in the physical mixtures between HP β CD and a drug and the putative inclusion complex. More specifically, when the melting endotherm of the complexed molecule is lost, an indication for the formation of an inclusion complex is obtained. Thus, the saturated solution used for the phase solubility, at pH 8 and 15 mM HP β CD concentration, was studied by DSC. More in detail, the experiments have been carried out on the raw drug, the HP β CD, as well as on the lyophilized supernatant and the precipitated mass. As reported in Fig. 2, QCT curve showed a sharp endothermic peak at 319.9 °C (Fig. 2a; $\Delta H^\circ = 164.5 \pm 3.1 \text{ J g}^{-1}$), associated with the fusion of the drug while, in the case of HP β CD, two endothermic peaks at 96.8 and 331.2 °C were revealed (Fig. 2b). The first peak is associated with water loss, while the second one is characteristic of the thermal degradation of HP β CD. Figure 2c displays the DSC trace

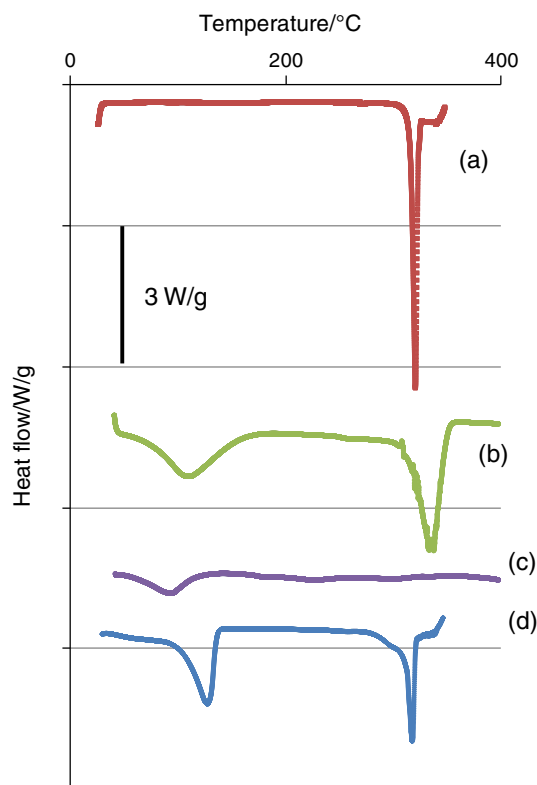


Fig. 2 DSC curves of (a) raw QCT; (b) HP β CD; (c) QCT-HP β CD inclusion complex obtained after lyophilization of the supernatant obtained during phase solubility experiments; (d) lyophilized precipitated mass after phase solubility test; ($n = 3$). The endotherm is downward

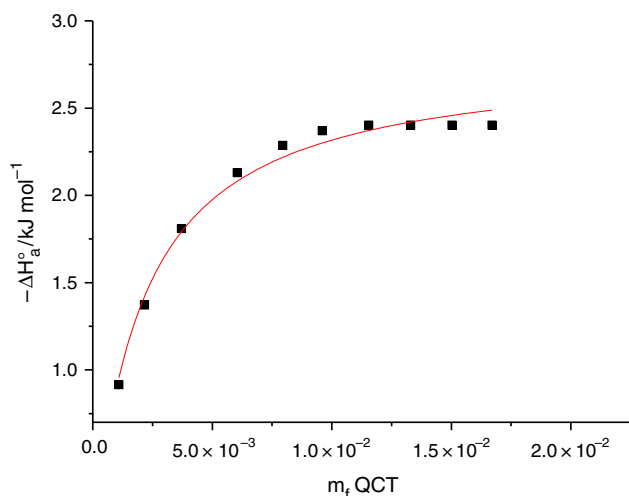


Fig. 3 Enthalpies of association, ΔH° , as a function of the final molality of quercetin, at pH = 8.4 and 298.15 K. The experimental points are indicated by squares, while the curve was drawn employing the constant and enthalpy obtained through Eqs. 5 and 6 by the iterative least-squares method described in the experimental section

of the putative QCT-HP β CD complex. In this case, the endothermic peak related to water loss is still present, but less important, therefore indicating the presence of a fraction of HP β CD which does not interact with the guest molecule. Interestingly, both the melting peak of QCT and the degradation peak of HP β CD were not detected when heating the lyophilized samples up to 400 °C. This flattening of DSC trace can be reasonably regarded as an evidence of the successful inclusion of QCT molecules in HP β CD cavities, to an amorphous state, or both. In Fig. 2d, the curve obtained by heating the lyophilized precipitated mass after phase solubility shows a behavior typical of a physical mixture, with a shift in the peak related to water loss probably due to lyophilization process. The sharp endothermic peak found at 317.1 °C, very close to the melting point of QCT, suggests the presence of free drug within the precipitate. The wide peak associated with HP β CD decomposition, on the contrary, was not found, therefore indicating a possible precipitation of the complex in the lyophilized precipitate or the formation of more stable structure during the freeze-drying process.

These results were also confirmed by isothermal calorimetry measurements, which was used to measure the heat of inclusion complexation between HP β CD and QCT at 298.15 K. In Fig. 3, the association enthalpy is reported as a function of the molality of quercetin, at pH = 8 and 298.15 K. The solid line through the points is obtained using the affinity constant and standard enthalpy evaluated by Eqs. 5 and 6. In acidic solution conditions, at pH = 3.6, small released association heats were detected that hampered the extraction of the thermodynamic parameters.

Table 1 Thermodynamic parameters for the association of QCT with HP β CD at 298.15 K

K'_a/M^{-1}	$\Delta H^\circ/kJ\ mol^{-1}$	$T\Delta S^\circ/kJ\ mol^{-1}$	$\Delta G^\circ/kJ\ mol^{-1}$	Refs.
489 ± 38	-2.9 ± 0.1	12.5 ± 0.3	-15.3 ± 0.2	
394 ± 101				
3110 ± 38	-45.40 ± 1.74	-25.46 ± 0.03	-19.94 ± 0.03	[23]
1419				[24]
532				[25]

Indeed, the thermodynamic parameters (affinity constant K'_a , standard enthalpy ΔH° , entropy $T\Delta S^\circ$ and Gibbs energy ΔG°) at pH = 8.0 are shown in Table 1, together with the constant obtained by phase solubility measurements and literature data. In particular, the affinity constant obtained from calorimetry experiments is in agreement with that calculated from phase solubility experiments.

An inspection of the methodologies reported in the literature shows that phase solubility studies are largely utilized to obtain affinity constants for HP β CD·QCT complexation. However, large discrepancies were found depending on solution conditions (Table 1) [23–25].

Liu and coworkers evaluated the apparent affinity constant for the complexation of QCT with HP β CD by phase solubility analysis and by two processing methods of fluorescence spectra analysis in Tris-HCl buffer solutions of pH 7.40 [23]. Affinity constants ranging from 3110 to 4000 M^{-1} were found at 298 K, depending of the applied method and a ΔH° value of $-45.40\ kJmol^{-1}$ was obtained by Van't Hoff analysis. The high ΔH° value thus obtained led to a negative value of ΔS° . We obtained the enthalpy by direct calorimetric measurements and in a different pH solution condition, and both these factors could explain the differences in the thermodynamic parameters. These data show that the association was both enthalpically and entropically driven with a prevalence of the entropic term, therefore indicating that the hydrophobic interactions, usually displayed by positive ΔS° , are predominant in the inclusion of QCT in the hydrophobic cavity of HP β CD.

Conclusions

In this work, we have examined the formation of the inclusion complex between QCT and HP β CD aiming to study the thermodynamic parameters involved in the formation of the complex. Phase solubility studies revealed that, at pH = 8.0, QCT forms inclusion complexes with HP β CD at a 1:1 stoichiometric ratio, with a strong solubility enhancement of QCT; at pH = 3.6, on the contrary, QCT solubility is higher but little or no interaction with HP β CD occurs. The formation of the complex was also confirmed by DSC results. Furthermore, the affinity

constant was calculated by means of isothermal calorimetry at pH = 8, and the obtained value was found to be $489 \pm 38 \text{ M}^{-1}$, in good agreement with the value of the constant indirectly obtained from phase solubility tests ($394 \pm 101 \text{ M}^{-1}$). Taken all together, these results highlight the importance of the choice of the appropriate solvent, pH, temperature and mixing time on the formation of host guest inclusion complex with active ingredient(s) and HP β CD.

References

- Apak R, Guclu K, Demirata B, Ozyurek M, Celik SE, Bektasoglu B, Berker KI, Ozyurt D. Comparative evaluation of various total antioxidant capacity assays applied to phenolic compounds with the CUPRAC assay. *Molecules*. 2007;12:1496–547.
- Keli SO, Hertog MG, Feskens EJ, Kromhout D. Dietary flavonoids, antioxidant vitamins, and incidence of stroke: the Zutphen study. *Arch Intern Med*. 1996;156:637–42.
- Zhang Y, Yang F, Jamali MA, Peng Z. Antioxidant enzyme activities and lipid oxidation in rape (*Brassica campestris* L.) bee pollen added to salami during processing. *Molecules*. 2016;21:1439–52.
- Formica JV, Regelson W. Review of the biology of Quercetin and related bioflavonoids. *Food Chem Toxicol*. 1995;33:1061–80.
- Ohnishi E, Bannai H. Quercetin potentiates TNF-induced antiviral activity. *Antiviral Res*. 1993;22:327–31.
- Guardia T, Rotelli AE, Juarez AO, Pelzer LE. Anti-inflammatory properties of plant flavonoids. Effects of rutin, quercetin and hesperidin on adjuvant arthritis in rat. *Farmacol*. 2001;56:683–7.
- Khonkarn R, Mankhetkorn S, Hennink WE, Okonogi S. PEG-OCL micelles for quercetin solubilization and inhibition of cancer cell growth. *Eur J Pharm Biopharm*. 2011;79:268–75.
- Ghasemzadeh A, Jaafar HZ, Rahmat A, Ashkani S. Secondary metabolites constituents and antioxidant, anticancer and antibacterial activities of *Etilingera elatior* (Jack) RM Sm grown in different locations of Malaysia. *BMC Complement Altern Med*. 2015;15:335–45.
- Scambia G, Ranelletti FO, Panici PB, Piantelli M, Bonanno G, De VR, Ferrandina G, Rumi C, Larocca LM, Mancuso S. Inhibitory effect of quercetin on OVCA 433 cells and presence of type II oestrogen binding sites in primary ovarian tumours and cultured cells. *Br J Cancer*. 1990;62:942–6.
- Larocca LM, Piantelli M, Leone G, Sica S, Teofili L, Panici PB, Scambia G, Mancuso S, Capelli A, Ranelletti FO. Type II oestrogen binding sites in acute lymphoid and myeloid leukemias: growth inhibitory effect of oestrogen and flavonoids. *Br J Haematol*. 1990;75:489–95.
- Murugan C, Rayappan K, Thangam R, Bhanumathi R, Shanthy K, Vivek R, Thirumurugan R, Bhattacharyya A, Sivasubramanian S, Gunasekaran P, Kannan S. Combinatorial nanocarrier based drug delivery approach for amalgamation of anti-tumor agents in breast cancer cells: an improved nanomedicine strategies. *Sci Rep*. 2016;6:34053–70.
- Demiroglu-Zergeroglu A, Ergene E, Ayvali N, Kuete V, Sivas H. Quercetin and Cisplatin combined treatment altered cell cycle and mitogen activated protein kinase expressions in malignant mesothelioma cells. *BMC Complement Altern Med*. 2016;16:281–7.
- Wang C, Su L, Wu C, Wu J, Zhu C, Yuan G. RGD peptide targeted lipid-coated nanoparticles for combinatorial delivery of sorafenib and quercetin against hepatocellular carcinoma. *Drug Dev Ind Pharm*. 2016;42:1938–44.
- Malik A, Sultana M, Qazi A, Qazi MH, Parveen G, Waqar S, Ashraf AB, Rasool M. Role of natural radiosensitizers and cancer cell radioresistance: an update. *Anal Cell Pathol (Amst)*. 2016;2016:6146595–603.
- Moyano-Mendez JR, Fabbrocini G, De SD, Mazzella C, Mayol L, Scognamiglio I, Carnuccio R, Ayala F, La Rotonda MI, De RG. Enhanced antioxidant effect of trans-resveratrol: potential of binary systems with polyethylene glycol and cyclodextrin. *Drug Dev Ind Pharm*. 2014;40:1300–7.
- Miro A, d'Angelo I, Nappi A, La MP, Biondi M, Mayol L, Musto P, Russo R, La Rotonda MI, Ungaro F, Quaglia F. Engineering poly(ethylene oxide) buccal films with cyclodextrin: a novel role for an old excipient? *Int J Pharm*. 2013;452:283–91.
- Mayol L, Serri C, Menale C, Crispi S, Piccolo MT, Mita L, Giarra S, Forte M, Saija A, Biondi M, Mita DG. Curcumin loaded PLGA-poloxamer blend nanoparticles induce cell cycle arrest in mesothelioma cells. *Eur J Pharm Biopharm*. 2015;93:37–45.
- Szejtli J. Introduction and general overview of cyclodextrin chemistry. *Chem Rev*. 1998;98:1743–54.
- Corrigan OI, Stanley CT. Mechanism of drug dissolution rate enhancement from beta-cyclodextrin-drug systems. *J Pharm Pharmacol*. 1982;34:621–6.
- Brewster ME, Loftsson T. Cyclodextrins as pharmaceutical solubilizers. *Adv Drug Deliv Rev*. 2007;59:645–66.
- Stella VJ, Rajewski RA. Cyclodextrins: their future in drug formulation and delivery. *Pharm Res*. 1997;14:556–67.
- Gladys G, Claudia G, Marcela L. The effect of pH and triethanolamine on sulfisoxazole complexation with hydroxypropyl-beta-cyclodextrin. *Eur J Pharm Sci*. 2003;20:285–93.
- Liu M, Dong L, Chen A, Zheng Y, Sun D, Wang X, Wang B. Inclusion complexes of quercetin with three beta-cyclodextrins derivatives at physiological pH: spectroscopic study and antioxidant activity. *Spectrochim Acta A Mol Biomol Spectrosc*. 2013;115:854–60.
- Jullian C, Moyano L, Yanez C, Olea-Azar C. Complexation of quercetin with three kinds of cyclodextrins: an antioxidant study. *Spectrochim Acta A Mol Biomol Spectrosc*. 2007;67:230–4.
- Pralhad T, Rajendrakumar K. Study of freeze-dried quercetin-cyclodextrin binary systems by DSC, FT-IR, X-ray diffraction and SEM analysis. *J Pharm Biomed Anal*. 2004;34:333–9.



Thermodynamics of complex formation between hydroxypropyl- β -cyclodextrin and quercetin in water–ethanol solvents at $T = 298.15$ K

Tatiana Usacheva¹ · Dzhovidon Kabirov¹ · Diana Beregova¹ · George Gamov¹ · Valentin Sharnin¹ · Marco Biondi^{2,3} · Laura Mayol^{2,3} · Federica D'Aria² · Concetta Giancola²

Received: 14 August 2018 / Accepted: 16 February 2019 / Published online: 11 March 2019
© Akadémiai Kiadó, Budapest, Hungary 2019

Abstract

Quercetin (QCT) is a flavonoid possessing many activities, such as neuro-/cardioprotective, anti-inflammatory and anti-cancer, but its pharmacological application is severely curtailed by its low water solubility and in vivo bioavailability. The formation of a QCT–hydroxypropyl- β -cyclodextrin (HP β CD) host–guest complex is promising to improve QCT therapeutic potential. Therefore, here the heat effects of HP β CD solutions with QCT solutions in water–ethanol solvents at different concentrations were studied by calorimetric titration, and the stability of molecular complexes was assessed by UV–Vis spectrophotometry. Calorimetric titrations revealed the formation of a QCT/HP β CD host–guest complex with a stoichiometric ratio of 1:1 in $X(\text{EtOH}) = 0.00, 0.05$ and 0.10 molar fractions of solvents at $\text{pH} = 7.0$ and $\text{pH} = 8.1$. Thermodynamic parameters of the complex formation reaction ($\lg K$; $\Delta_r H$; $T\Delta_r S$) were obtained in these experimental conditions. Differently, no complex formation was noticed in water–ethanol mixed solvent when ethanol volume fraction exceeded 0.2 at neutral and alkaline pH , as well as a volume fraction higher than 0.1 at acidic pH . Furthermore, the results of differential scanning calorimetry tests run on dried HP β CD after dissolution in hydroalcoholic solutions indicated that ethanol and water compete for the complexation within the hydrophobic cavity of HP β CD. This explains the decreased QCT complexation efficacy in the presence of ethanol beyond 0.1 or 0.2 volume fraction.

Keywords Quercetin · Hydroxypropyl- β -cyclodextrin · Isothermal calorimetry · UV–Vis spectrophotometry · Inclusion complexation · Water–ethanol solvents

Introduction

Quercetin (QCT 3,5,7,3',40'-pentahydroxyflavone; Fig. 1a) is a flavonoid, containing a 3-hydroxyflavone backbone, that can be found in numerous fruits, vegetables and grains [1]. QCT is endowed with manifold beneficial properties,

such as the reduction in systolic blood pressure [2], the inhibition of mast cell secretion [3] and in vitro production of cyclooxygenase and lipoxygenase [4], along with neuro-/cardioprotective [5, 6], antiviral [7], anti-inflammatory [8] and anticancer [9–12] activities. All these features have prompted the study of QCT as a potential molecule to be used in the pharmaceutical field. However, the bioavailability profile of QCT is very poor due to its low permeability, stability and solubility in aqueous media (approximately 1.5 and $30 \mu\text{g mL}^{-1}$ in water, simulated gastric fluid and simulated intestinal fluid) [13].

In general, the bioavailability of active molecules can be improved by loading them into liposomes [14], nanoparticles [15] or micelles [16] or by forming inclusion complexes with cyclodextrins (CDs) [17]. The latter are supramolecular structures commonly employed to promote the in vitro and in vivo solubility of poorly water-soluble molecules and hence their therapeutic index. CDs are

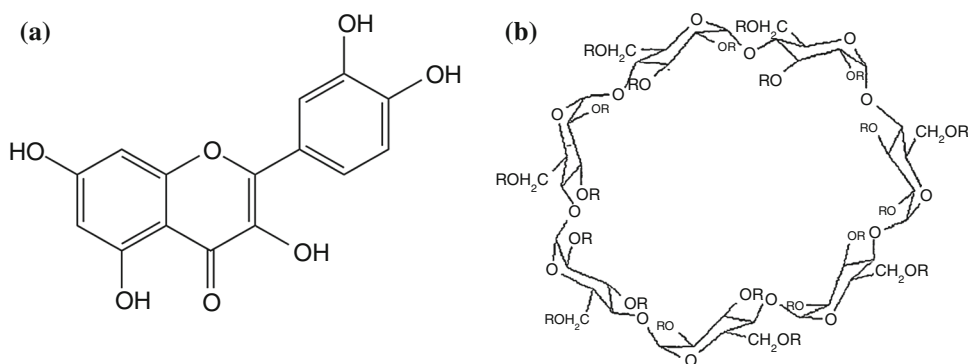
✉ Tatiana Usacheva
oxt@isuct.ru

¹ Department of General Chemical Technology, Faculty of Inorganic Chemistry and Technology, Ivanovo State University of Chemistry and Technology, Sheremetevsky Avenue 7, Ivanovo, Russian Federation 153000

² Department of Pharmacy, University of Naples Federico II, Via Domenico Montesano 49, 80131 Naples, Italy

³ Interdisciplinary Research Centre on Biomaterials – CRIB, Università di Napoli Federico II, P.le Tecchio, 80, Naples, Italy

Fig. 1 Structural formulas of: **a** quercetin, **b** hydroxypropyl- β -cyclodextrin



cyclic oligosaccharides with a frusto-conical architecture, consisting of glucopyranose units, bound by α -(1,4) glycoside bonds. Taking advantage of their hydrophilic outer surface and lipophilic internal cavity, CDs can interact with a wide array of host molecules forming inclusion complexes through non-covalent bonds [18]. Mainly, three natural CDs exist, namely α , β and γ , which contain 6, 7 and 8 glucose units, respectively [19]. The α -CD cavity is generally too small to allow an efficient complexation of most drugs, while γ -CDs are rather expensive. Thus, β -CDs are most frequently used in pharmaceutical applications, mainly due to their prompt availability and cavity size that can fit numerous drugs [20]. Amorphous, non-crystallizable semisynthetic derivatives of β -CDs possess an enhanced physical and microbiological stability, along with a lower parenteral toxicity [21, 22].

The formation of the host–guest complex between QCT and (2-hydroxypropyl)- β -cyclodextrin (HP β CD; Fig. 1b) has been studied in detail in water [17, 23]. In a recent report, QCT/HP β CD complex has also been prepared in ethanol by the co-precipitation method, resulting in a strong enhancement of QCT aqueous solubility and photostability [24]. However, to the best of our knowledge, the stability of the complex has not been established to date in water and hydroalcoholic solutions.

In a previous work, we found that the addition of a non-aqueous substance to water promotes the stability of the molecular complexes of crown ethers and amino acids/peptides, leading to an increase in the exothermicity of the reactions of their formation due to a change in the solvation features of the complexes [25]. Thus, here we used a thermodynamic approach to quantitatively analyze the influence of individual solvation factors on the stability of the complexes as previously reported [26]. More specifically, the processes of solubilization of water-insoluble compounds by the formation of the host–guest inclusion complex with CDs can be considered as processes of competition–substitution of water molecules in the CD cavity by a guest molecule [27]. Hence, in the presence of co-solvent molecules, water content in the internal cavity

of macrocycle will depend on the competition between the “guests” and co-solvent molecules of a mixed solvent in the CD cavity. For instance, it has been established that some minimal amount of methanol or ethanol facilitates the binding of large hydrophobic “guests” to β -cyclodextrin [28]. In this regard, the use of non-aqueous solvent additives to water is expected to help in creating optimal conditions for the solubilization of hydrophobic molecules by CDs. Starting from these considerations, herein we have studied the formation of QCT/HP β CD inclusion complex in water–ethanol mixtures at different concentrations of ethanol so as to assess the effect of solvent composition on the formation of QCT/HP β CD complex.



To this aim, the thermodynamic parameters involved in the complex formation have been determined starting from microcalorimetry experiments carried out on the different hydroalcoholic mixtures and at different pH values.

Materials and methods

Materials

All substances were obtained from Sigma-Aldrich. QCT and HP β CD (both $\geq 99\%$ purity) were used as received, without further purification. Rectificate grade ethyl alcohol was purified by distillation before use. The amount of water in EtOH ($\leq 5\%$ w/w) was determined from the density by accurately weighing using a pycnometer, preliminarily calibrated with ethanol on an analytical scale balance AUX220D, and taking into account these measurements in the preparation of aqueous ethanol solvents. Mixed solvents were prepared with bidistilled and deaerated water by a gravimetric method.

Methods

Isothermal titration calorimetry

The heat effects of mixing HP β CD solutions with QCT were determined by isothermal titration calorimetry with the TAM III (TA Instruments, USA) microcalorimeter in water–ethanol mixed solvents containing X(EtOH) = 0.00, 0.05, 0.10, 0.20, 0.50 and 0.95 molar fractions in phosphate buffer at pH = 3.6, 7.0 and 8.1 and at $T = 298.15$ K.

The optimal concentration conditions for the experiments, limited by the low solubility of the reagents in the water–ethanol mixtures, were previously calculated according to the RRSU program [29] for each solvent composition. The yield of the QCT/HP β CD complex varied in the widest range of values (3–50%).

The initial concentration of HP β CD in the syringe ranged from $1.45 \cdot 10^{-2}$ to $1.59 \cdot 10^{-2}$ mol L $^{-1}$. The initial concentration of QCT in the cell ranged from $1.19 \cdot 10^{-4}$ to $2.25 \cdot 10^{-4}$ mol L $^{-1}$. The HP β CD/QCT molar ratio was in the 3–9 range. In all experiments, the composition of the solvent in the syringe and in the cell was the same.

The heat effect of mixing for solutions of HP β CD with solutions of QCT (Q_{mix}) is contributed by the heat of QCT/HP β CD complex formation (Q_{compl}), the heat of dilution of HP β CD solution ($Q_{\text{dil } 1}$) in a solvent in the cell and the heat of dilution of QCT solution placed in the cell in a solvent added from syringe ($Q_{\text{dil } 2}$):

$$Q_{\text{mix}} = Q_{\text{compl}} + Q_{\text{dil } 1} + Q_{\text{dil } 2} \quad (2)$$

The last term was considered to be negligible; therefore, it follows:

$$Q_{\text{compl}} = Q_{\text{mix}} - Q_{\text{dil } 1} \quad (3)$$

The values of $\lg K$ and $\Delta_r H$ for QCT/HP β CD complex formation have been calculated by the program HEAT developed to simultaneously calculate the enthalpies of reaction and the equilibrium constants of complex formation for systems with any stoichiometry [30]. The HEAT use and application were described in detail in previous publications for the treatment of calorimetric data of the molecular complex formation of amino acids and peptides with crown ethers and cryptand [2.2.2] mixed solvents [25, 31]. The algorithm for the calculation of $\lg K$ and $\Delta_r H$ used by HEAT consists in the numerical minimization of function F :

$$F = \sum_{i=1}^N \omega_i (\Delta_{\text{compl}} H - \Delta_{\text{calc}} H)_i^2 \quad (4)$$

where N is the number of experimental points; ω_i is the mass of the single measurement; and $\Delta_{\text{compl}} H$ and $\Delta_{\text{calc}} H$ are the experimental and calculated molar

enthalpies of the process, respectively. In this work, all $\Delta_{\text{compl}} H$ experimental values have been considered to be determined with the same precision, so $w_i = 1$.

UV–Vis spectroscopy

The UV–Vis spectral data were processed using FTMT program [30]. The FTMT program applies for equilibrium modeling in solutions and data processing of spectral measurements with the purpose of determining equilibrium constants. For this, an approach based on the statistical maximum likelihood principle was used. The mathematical model of the system sets the number and stoichiometry of the reactions, the values of the equilibrium constants, the partial molar properties of the particles or reactions and the total concentrations of the components.

The calculations were performed basing the experimental dependencies of absorbance at one wavelength on the initial concentration ratio of the reagents. The molar extinction coefficients of QCT and HP β CD required for calculations in FTMT, at each pH and wavelength value, were preliminarily determined using calibration plots. The sum of mean square deviations for calculated and experimental values of optical density was in the range from 0.0001 to 0.1.

Differential scanning calorimetry

Aiming to verify the possible different interactions of ethanol and water with cyclodextrins, thermoanalytical tests have been run on HP β CD using a TA Q20 differential scanning calorimeter (DSC; TA Instruments, USA). In particular, DSC spectra have been obtained on HP β CD as received, and on the dry residue of HP β CD solubilized in water, ethanol and hydroalcoholic solutions (water/ethanol 9:1 and 8:2 volumetric ratios). All DSC tests have been carried out in the solid state, on the samples preliminarily dried in the hood overnight. Samples were accurately weighted (~ 5 mg) and placed in hermetic aluminum pans. Then, the samples were heated from 20 to 240 °C at 10 °C min $^{-1}$ under an inert nitrogen atmosphere at a constant flow rate (50 mL min $^{-1}$). An empty aluminum pan was used as a reference. Triplicate scans have been performed.

Results and discussion

Previous studies focused on the complex formation between d -metal ions and amine or carboxylate complexes in aqueous–organic solvents have revealed, on the basis of the solvation–thermodynamic approach, the possibility of predicting the thermodynamic parameters of the ionic

Table 1 Thermodynamic parameters for the association of QCT with HP β CD in water and in water/ethanol mixtures

X(EtOH) molar fraction	lgK	$\Delta_r H/kJ mol^{-1}$	$\Delta_r G/kJ mol^{-1}$	$\Delta_r S/J mol^{-1} K$	Methods	T/K	pH	References
0.00	3.8 ± 0.2	-4.9 ± 0.8	-21.6 ± 1.1	56.1 ± 1.4	Calorimetry	298.15	7.0	This work
	3.4 ± 0.1	–	–	–	UV–Vis spectra	298.15	7.0	
	2.7	-2.9 ± 0.1	-15.3 ± 0.2	41.6 ± 0.3	Calorimetry	298.15	8.0	[23]
	2.6	–	–	–	Phase solubility analysis	298.15	8.0	[23]
	3.5	-45.4 ± 1.74	-19.94 ± 0.03	-85.37 ± 5.69	Phase solubility analysis	298.15	7.4	[17]
	3.6	–	–	–	Double-reciprocal plot	298.15	7.4	[17]
	3.6	–	–	–	Nonlinear regression analysis	298.15	7.4	[17]
	3.4	–	-19.50 ± 0.02	–	Phase solubility analysis	303.15	7.4	[17]
	3.2	–	-19.11 ± 0.01	–	Phase solubility analysis	308.15	7.4	[17]
	3.1	–	-18.66 ± 0.02	–	Phase solubility analysis	313.15	7.4	[17]
	3.5	–	–	–	Phase solubility analysis	298.15	7.4	[17]
	3.2	–	–	–	Phase solubility analysis	303.15	–	[35]
	2.7	–	–	–	Phase solubility analysis	298.15	–	[36]
	4.04	–	–	–	Phase solubility analysis	297.15	3	[37]
0.05	3.7 ± 0.1	-7.6 ± 0.6	-20.9 ± 0.6	44.4 ± 0.8	Calorimetry	298.15	7.0	This work
	3.5 ± 0.1	–	–	–	UV–Vis spectra	298.15	7.0	
0.10	3.6 ± 0.1	-7.3 ± 0.5	-20.6 ± 0.6	44.8 ± 0.8	Calorimetry	298.15	7.0, 8.1	This work
	3.3 ± 0.4	–	–	–	UV–Vis spectra	298.15	7.0	

complex formation reactions in different media according to a change in the solvation state of ligands [32–34]. In particular, the complexation in water is considered as a set of reactions of stepwise replacement of water molecules in the first solvate shell of the central ion by a ligand molecule [32]. In a binary solvent, the set of reactions is more complicated, since there is a preferential solvation of reagents with one of the solvent components [33, 34]. In the complexation of inorganic cations with crown ethers, cryptands and other macrocyclic structures, the central ion is completely or almost completely isolated from the solvent. For less stable complexes between macrocycle (host) and organic molecule (guest), the guest molecule and the solvent most probably compete for the formation of the complex with the HP β CD.

In this work, the thermodynamic parameters of the complex formation between QCT and HP β CD in water and in ethanol/water mixed solvent, at pH = 7.0 and 8.1, compared with the relevant literature data in water are

presented in Table 1. The results of calorimetric titrations showed that the complexation occurs in ethanol/water mixtures of composition X(EtOH) = 0.00, 0.05 and 0.10 molar fraction. Conversely, no complex formation was found out when ethanol molar fraction was ≥ 0.20 at pH = 7.0 or when pH was lowered to 3.6 with a 0.10 EtOH molar fraction, according to the calorimetric titration and UV–Vis data.

The formation of the QCT/HP β CD complex can be envisaged by the total heat of complexation $\Sigma(Q_{\text{compl}})$ dependence on the concentration of HP β CD in the cell. More in detail, when the complex formed, $\Sigma(Q_{\text{compl}})$ becomes HP β CD concentration independent as observed in Fig. 2a–c. Differently, as shown in Fig. 2d, e, in the presence of weak molecular interactions, the total heat of complexation $\Sigma(Q_{\text{compl}})$ dependence on the concentration of HP β CD in the cell is linear. Binding constants at pH = 7.0 were also calculated by UV–Vis titration spectra (Fig. 3a, b), and the results are shown in Table 1.

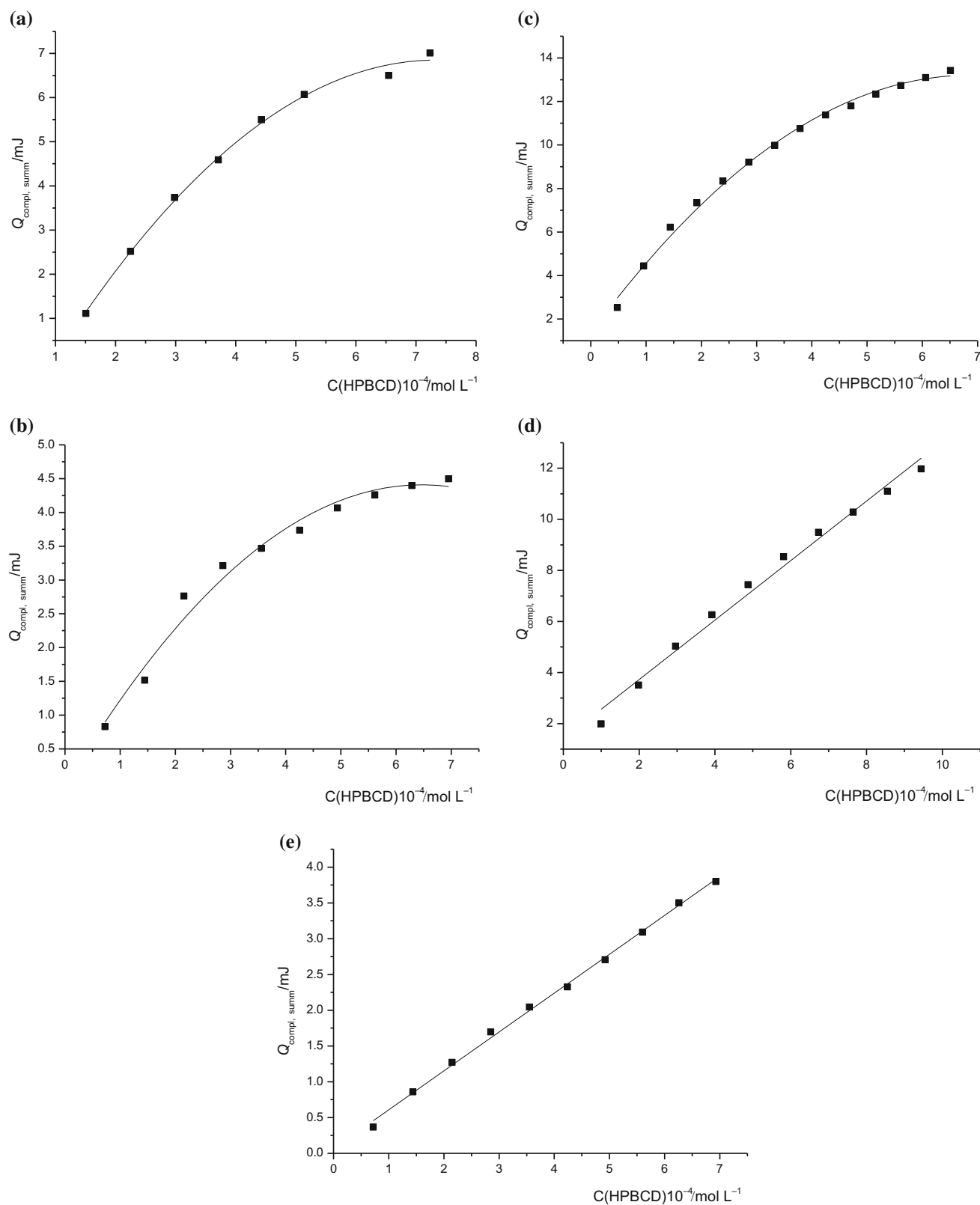


Fig. 2 a–e Total heat effect of the interaction between QCT and HP β CD in H₂O–EtOH solvent, depending on the total molar concentration of HP β CD in the cell, **a**—in H₂O at $T = 298.15 \text{ K}$, $\text{pH} = 7.0$; **b**—at $X(\text{EtOH}) = 0.10$ molar fraction, at $T = 298.15 \text{ K}$,

$\text{pH} = 7.0$; **c**—at $X(\text{EtOH}) = 0.10$ molar fraction, at $T = 298.15 \text{ K}$, $\text{pH} = 8.1$; **d**—at $X(\text{EtOH}) = 0.10$ molar fraction, at $T = 298.15 \text{ K}$, $\text{pH} = 3.6$; **e**—at $X(\text{EtOH}) = 0.20$ molar fraction, at $T = 298.15 \text{ K}$, $\text{pH} = 7.0$

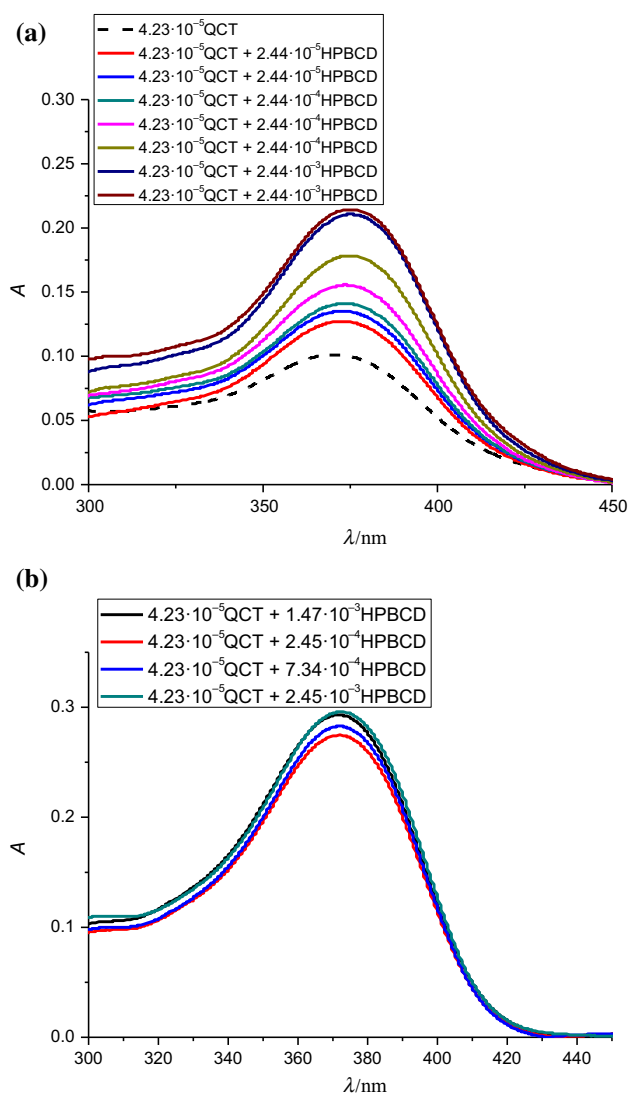


Fig. 3 Electronic absorption spectra of HP β CD with a solution of QCT. The numbers in the legend indicate the molar concentrations of QCT and HP β CD (mol L^{-1}), **a**—in H_2O at $\text{pH} = 7.0$, **b**—in $X(\text{EtOH}) = 0.10$ molar fraction at $\text{pH} = 7.0$

An inspection of Table 1 shows that the thermodynamic parameters of QCT/HP β CD complex formation have been obtained in water by various methods, under different conditions [17, 23, 35–37]. In most of them, the values of the association constants are in satisfactory agreement with each other and with our values obtained by both calorimetric and UV–Vis methods. In our previous paper, we found the association constant in water at $\text{pH} = 8.0$ [23], and in this work we were able to obtain calorimetric data in water at $\text{pH} = 7.0$. At this pH , the association constant was one order of magnitude higher and the values of $\Delta_r H$ and $\Delta_r S$ showed an increase in both the exothermicity of complexation and the entropic contribution to the Gibbs energy change for the complex formation.

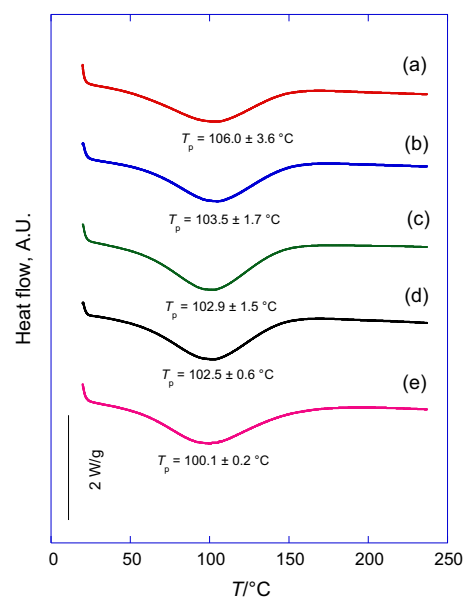


Fig. 4 Superimposed DSC data for raw HP β CD (**a**) and dried HP β CD after dissolution in water (**b**); water/ethanol 9:1 v/v mixture (**c**); water/ethanol 9:1 v/v mixture (**d**); ethanol (**e**)

The different $\Delta_r H$ and $\Delta_r S$ values obtained by Liu et al. can be reasonably explained, considering that they were indirectly extracted by the phase solubility analysis at a different pH of 7.4 [17]. After the addition of ethanol to water, the stability of the complex was unchanged for $X(\text{EtOH}) = 0.00, 0.05$ and 0.10 molar fraction. However, along with this, an increase in the exothermicity of complexation and a decrease in the entropic contribution to the Gibbs energy change of the formation reaction were detected.

In a previous publication, an insignificant effect of added DMSO on the stability of molecular complexes was found in the study of the complexation of triglycine with cryptand [2.2.2] [31]. This finding was discussed based on the compensation effect of the entropy/enthalpy contributions to the Gibbs energy of complexation. Furthermore, in the case of molecular complexes of crown ethers with amino acids and peptides, the addition of ethanol, DMSO and acetone resulted in an increased stability of molecular complexes and in an increase in the exothermicity of their formation reactions [25]. These results were explained in terms of changes in solvation of guest molecules with the replacement of waters by organic solvents.

Considering previous studies, we could hypothesize that moving from water to hydroalcoholic solvent, the thermodynamics of QCT/HP β CD complex formation is influenced by the change in solvation of QCT. The solubility of QCT is higher in ethanol/water mixtures than in water [41], and this indicates that ethanol molecules displace water molecules in QCT hydration shell, affecting both the

enthalpic and entropic contributions to Gibbs energy of complexation, so that the $\lg K$ for low $X(\text{EtOH})$ remains the same as in water. Increasing ethanol molar fraction, EtOH is able to effectively solvate QCT molecules, by subtracting them from the complexation, and competes for occupation of HP β CD cavities or fills the residual empty space of the cavity of HP β CD, as already found in another study [42]. The overall result is that, for $X(\text{EtOH})$ greater than 0.10 molar fraction, no complexation occurs.

DSC scans have been run to provide further information on the physical and chemical processes occurring during heating. Commercial HP β CD displays a broad endothermic peak, which is indicative of the release of superficial and strongly retained water from the hydrophobic core at 106 °C (Fig. 4) [38, 39]. After HP β CD dissolution in water, the DSC peak appears at a very similar temperature (about 103.5 °C), therefore indicating that the same interaction occurs after immersion of HP β CD in water. The DSC peak appears at slightly lower temperatures after dissolution in 9:1 and 8:2 water/ethanol mixtures, around 100°. The decrease in these peak temperatures can be explained by the formation of the host–guest molecular inclusion compound that allows the replacement of the strongly retained water molecules inside the cavity by the ethanol moieties. The obtained complex mainly most probably contains superficial water molecules that are more easily released, and hence, the peak temperature decreases [40]. This indicates that the total water content is lower and/or weakly bound to HP β CD after immersion in ethanolic or hydroalcoholic solvents, compared to the untreated, commercial CD. These results therefore corroborate the existence of the competition between ethanol and water for the complexation within the hydrophobic cavity of HP β CD which in turn contributes in decreasing the efficacy of QCT complexation in the presence of ethanol.

Conclusions

In this work, it has been established that the addition of ethanol to water leads to an insignificant decrease in the stability of the QCT/HP β CD host–guest complex. However, along with this, there are an increase in the exothermicity of complexation and a decrease in the entropic contribution to the change of the reaction Gibbs energy. Above $X(\text{EtOH}) = 0.10$ molar fraction, no complexation occurs. It seems unexpected because the decrease in the complex stability should be more significant at increasing ethanol content in the solvent. Probably, in H_2O –EtOH solvent with 0.1 and more molar fraction of EtOH the replacement of QCT in the cavity of CD by molecules of EtOH is presented. In consequence, the complex QCT–CD

does not form. This can be reasonably ascribed to the outcomes of DSC results, which showed that ethanol actively competes for the inclusion within HP β CD cavity, therefore hampering the effective formation of QCT–HP β CD inclusion complex. Overall, the data showed that the ethanol affects QCT solvation, shifting the equilibrium far from QCT/HP β CD complex formation, and competes for occupation of HP β CD cavities. Taken altogether, these results highlight a counterintuitive conclusion, in that the expected solubility enhancement of the active molecule in the presence of ethanol did not match a higher affinity between QCT and HP β CD. However, further studies on different molecules in mixed solvents will be devoted to shed light on the thermodynamic interactions between pharmacologically active natural compounds and HP β CD.

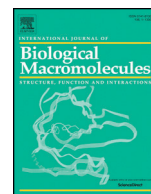
Acknowledgements The calorimetric measurements presented in this work were carried out at the Institute of Thermodynamics and Kinetics of Chemical Processes of the Ivanovo State University of Chemistry and Technology (ISUCT) using the equipment of the Center for Collective Use of ISUCT. The study was carried out under grant of Council on grants of the President of the Russian Federation (Project 14.Z56.18.877-MK). The authors thank the University of Naples Federico II for the financial support of their collaboration contributed to the preparation of this paper.

References

1. D'Andrea G. Quercetin: a flavonol with multifaceted therapeutic applications? *Fitoterapia*. 2015;106:256–71.
2. Zahedi M, Ghiasvand R, Feizi A, Asgari G, Darvish L. Does quercetin improve cardiovascular risk factors and inflammatory biomarkers in women with type 2 diabetes: a double-blind randomized controlled clinical trial. *Int J Prev Med*. 2013;4:777–85.
3. Shaik YB, Castellani ML, Perrella A, Conti F, Salini V, Tete S, Madhappan B, Vecchiet J, De Lutiis MA, Caraffa A, Cerulli G. Role of quercetin (a natural herbal compound) in allergy and inflammation. *J Biol Regul Homeost Agents*. 2006;20:47–52.
4. Kim HP, Mani I, Iversen L, Ziboh VA. Effects of naturally-occurring flavonoids and biflavonoids on epidermal cyclooxygenase and lipooxygenase from guinea-pigs. *Prostaglandins Leukot Essent Fatty Acids*. 1998;58:17–24.
5. Marsh DT, Das S, Ridell J, Smid SD. Structure-activity relationships for flavone interactions with amyloid β reveal a novel anti-aggregatory and neuroprotective effect of 2',3',4'-trihydroxyflavone (2-D08). *Bioorg Med Chem*. 2017;25:3827–34.
6. Formica JV, Regelson W. Review of the biology of quercetin and related bioflavonoids. *Food Chem Toxicol*. 1995;33:1061–80.
7. Ohnishi E, Bannai H. Quercetin potentiates TNF-induced antiviral activity. *Antivir Res*. 1993;22:327–31.
8. Guardia T, Rotelli AE, Juarez AO, Pelzer LE. Anti-inflammatory properties of plant flavonoids. Effects of rutin, quercetin and hesperidin on adjuvant arthritis in rat. *Farmacologia*. 2001;56:683–7.
9. Khonkarn R, Mankhetkorn S, Hennink WE, Okonogi S. PEG-OCL micelles for quercetin solubilization and inhibition of cancer cell growth. *Eur J Pharm Biopharm*. 2011;79:268–75.
10. Ghasemzadeh A, Jaafar HZ, Rahmat A, Ashkani S. Secondary metabolites constituents and antioxidant, anticancer and antibacterial activities of *Etilingera elatior* (Jack) R.M.Sm grown

- in different locations of Malaysia. *BMC Complement Altern Med*. 2015;15:335–45.
11. Scambia G, Ranelletti FO, Panici PB, Piantelli M, Bonanno G, De Vincenzo R, Ferrandina G, Rumi C, Larocca LM, Mancuso S. Inhibitory effect of quercetin on OVCA 433 cells and presence of type II oestrogen binding sites in primary ovarian tumours and cultured cells. *Br J Cancer*. 1990;62:942–6.
 12. Larocca LM, Piantelli M, Leone G, Sica S, Teofili L, Panici PB, Scambia G, Mancuso S, Capelli A, Ranelletti FO. Type II oestrogen binding sites in acute lymphoid and myeloid leukaemias: growth inhibitory effect of oestrogen and flavonoids. *Br J Haematol*. 1990;75:489–95.
 13. Cai X, Fang Z, Dou J, Yu A, Zhai G. Bioavailability of quercetin: problems and promises. *Curr Med Chem*. 2013;20:2572–82.
 14. Park SN, Lee MH, Kim SJ, Yu ER. Preparation of quercetin and rutin-loaded ceramide liposomes and drug-releasing effect in liposome-in-hydrogel complex system. *Biochem Biophys Res Commun*. 2013;435(3):361–6.
 15. Bose S, Du Y, Takhistov P, Michniak-Kohn B. Formulation optimization and topical delivery of quercetin from solid lipid based nanosystems. *Int J Pharm*. 2013;441:56–66.
 16. Gao X, Wang B, Wei X, Men K, Zheng F, Zhou Y, Zheng Y, Gou M, Huang M, Guo G, Huang N, Qian Z, Wei Y. Anticancer effect and mechanism of polymer micelle-encapsulated quercetin on ovarian cancer. *Nanoscale*. 2012;4:7021–30.
 17. Liu M, Dong L, Chen A, Zheng Y, Sun D, Wang X, Wang B. Inclusion complexes of quercetin with three β -cyclodextrins derivatives at physiological pH: spectroscopic study and antioxidant activity. *Spectrochim Acta A Mol Biomol Spectrosc*. 2013;115:854–60.
 18. Challa R, Ahuja A, Ali J, Khar RK. Cyclodextrins in drug delivery: an updated review. *AAPS PharmSciTech*. 2005;6:E329–57.
 19. Loftsson T, Brewster ME. Pharmaceutical applications of cyclodextrins. 1. Drug solubilization and stabilization. *J Pharm Sci*. 1996;85:1017–25.
 20. Szejtli J. Cyclodextrin in drug formulations: part I. *Pharm Technol Int*. 1991;3:15–23.
 21. Szente L, Szejtli J. Highly soluble cyclodextrin derivatives: chemistry, properties, and trends in development. *Adv Drug Deliv Rev*. 1999;36:17–38.
 22. Matsuda H, Arima H. Cyclodextrins in transdermal and rectal delivery. *Adv Drug Deliv Rev*. 1999;36:81–99.
 23. D'Aria F, Serri C, Niccoli M, Mayol L, Quagliariello V, Iaffaioli RV, Biondi M, Giancola C. Host–guest inclusion complex of quercetin and hydroxypropyl- β -cyclodextrin. *J Therm Anal Calorim*. 2017;130:451–6.
 24. Savic IM, Nikolic VD, Savic-Gajic I, Nikolic LB, Radovanovic BC, Mladenovic JD. Investigation of properties and structural characterization of the quercetin inclusion complex with (2-hydroxypropyl)- β -cyclodextrin. *J Incl Phenom Macrocycl Chem*. 2015;82:383–94.
 25. Usacheva TR, Sharnin VA. A thermodynamic study of reactions of amino acids with crown ethers in nonaqueous media as examples of guest-host molecular complex formation. *Russ Chem Bulletin*. 2015;64:2536–44.
 26. Krestov GA, Novosyolov NP. Ionic solvation. New York: Ellis Horwood Ed; 1994.
 27. Donze C, Coleman AW. Solvent effects in competition between guest molecules for β -cyclodextrin. *J Incl Phenom Mol Recogn Chem*. 1995;23:11–21.
 28. Yoshii H, Kometani T, Furuta T, Watanabe Y, Linko YY, Linko P. Formation of inclusion complexes of cyclodextrin with ethanol under anhydrous conditions. *Biosci Biotechnol Biochem*. 1998;62:2166–70.
 29. Vasiliev VP, Borodin VA, Kozlovsky EV. The use of computers in chemical-analytical calculations, vol. 112. Moscow: Higher Education school; 1993 **in Russian**.
 30. Borodin VA, Vasil'ev VP, Kozlovskii EV. Mathematical problems of chemical thermodynamics, vol. 219. Novosibirsk: Nauka; 1985 **(in Russian)**.
 31. Usacheva TR, Pham Thi L, Terekhova IV, Kumeev RS, Sharnin VA. Thermodynamics of molecular complexation of glycyl-glycyl-glycine with cryptand [2.2.2] in water–dimethylsulfoxide solvent at 298.15 K. *J Therm Anal Calorim*. 2016;126:307–14.
 32. Sharnin VA. Thermochemistry of formation of copper (II)-ethylenediamine complexes and solvation of reagents in aqueous organic solvents. *J Therm Anal Calorim*. 1995;45:721–8.
 33. Zevakin MA, Grazhdan KV, Dushina SV, Sharnin VA. Thermodynamic characteristics of reagents and reaction of Ag^+ –nicotinamide complex formation in water-ethanol media. *J Mol Liq*. 2007;131–132:163–7.
 34. Gesse ZF, Repkin GI, Isaeva VA, Sharnin VA. The influence of reagents solvation on enthalpy change of glycine-ion protonation and silver(I) glycine-ion complexation in aqueous-dimethylsulfoxide solutions. *J Therm Anal Calorim*. 2013;110:1457–62.
 35. Jullian C, Moyano L, Yanez C, Olea-Azar C. Complexation of quercetin with three kinds of cyclodextrins: an antioxidant study. *Spectrochim Acta A Mol Biomol Spectrosc*. 2007;67:230–4.
 36. Pralhad T, Rajendrakumar K. Study of freeze-dried quercetin–cyclodextrin binary systems by DSC, FT-IR, X-ray diffraction and SEM analysis. *J Pharm Biomed Anal*. 2004;34:333–9.
 37. Zheng Y, Haworth IS, Zuo Z, Chow MS, Chow AH. Physicochemical and structural characterization of quercetin- β -cyclodextrin complexes. *J Pharm Sci*. 2005;94:1079–89.
 38. Oprean C, MIOC M, Csányi E, Ambrus R, Bojin F, Tatu C, Cristea M, Ivan A, Danciu C, Dehelean C, Paunescu V, Soica C. Improvement of ursolic and oleanolic acids' antitumor activity by complexation with hydrophilic cyclodextrins. *Biomed Pharmacother*. 2016;83:1095–104.
 39. Tang P, Tang B, Wang Q, Xu K, Xiong X, Li H. Effect of hydroxypropyl- β -cyclodextrin on the bounding of salazosulfapyridine to human serum albumin. *Int J Biol Macromol*. 2016;92:105–15.
 40. Hădărugă NG, Hădărugă DI, Isengard HD. “Surface water” and “strong-bonded water” in cyclodextrins: a Karl Fischer titration approach. *J Incl Phenom Macrocycl Chem*. 2013;75:297–302.
 41. Razmara RS, Daneshfar A, Sahraei R. Solubility of quercetin in water + methanol and water + ethanol from (292.8 to 333.8) K. *J Chem*. 2010;55:3934–6.
 42. Kanokthip B, Helmut V, Peter W, Luckhana L. Influence of ethanol as a co-solvent in cyclodextrin inclusion complexation: a molecular dynamics study. *Sci Pharm*. 2015;83:387–99.

Publisher's Note Springer Nature remains neutral with regard to jurisdictional claims in published maps and institutional affiliations.



Selective binding of a bioactive porphyrin-based photosensitizer to the G-quadruplex from the *KRAS* oncogene promoter

Marco Caterino^{a,1,2}, Federica D'Aria^{a,1}, Andrey V. Kustov^{b,c}, Dmitrii V. Belykh^d, Irina S. Khudyaeva^d, Olga M. Starseva^d, Dmitriy B. Berezin^c, Yana I. Pylina^e, Tatiana Usacheva^f, Jussara Amato^{a,*}, Concetta Giancola^{a,*}

^a Department of Pharmacy, University of Naples Federico II, via D. Montesano 49, 80131 Naples, Italy

^b Krestov Institute of Solution Chemistry of Russian Academy of Sciences, Ivanovo, Russian Federation

^c Ivanovo State University of Chemistry and Technology, Institute of Macroheterocyclic Compounds, Ivanovo, Russian Federation

^d Institute of Chemistry of Komi Science Center of the Ural Branch of the Russian Academy of Sciences, Syktyvkar, Russian Federation

^e Institute of Biology of Komi Scientific Center of the Ural Branch of the Russian Academy of Sciences, Syktyvkar, Russian Federation

^f Ivanovo State University of Chemistry and Technology, Department of General Chemical Technology, Ivanovo, Russian Federation

ARTICLE INFO

Article history:

Received 29 August 2019

Received in revised form 7 October 2019

Accepted 17 December 2019

Available online 20 December 2019

Keywords:

G-quadruplex

Ligands

Chlorins

Biophysics

Singlet oxygen generation

Photodynamic activity

ABSTRACT

Background: The G-quadruplex-forming sequence within the *KRAS* proto-oncogene P1 promoter is a promising target for anticancer therapy. Porphyrin derivatives are among the most rewarding G-quadruplex binders. They can also behave as photosensitizers.

Methods: Three water-soluble, positively charged porphyrin-like compounds were synthesized and tested for their interaction with the *KRAS* G-quadruplex by circular dichroism, fluorescence, and molecular docking calculations. For a comparison of ligands binding affinity and selectivity, TMPyP4 was taken as a reference.

Results: One out of the three tested compounds proved biological activity and selectivity for G-quadruplex over duplex DNA. It also showed to discriminate between different G-quadruplex topologies, with a preference for the parallel over antiparallel conformation. Molecular docking studies suggested a preferential binding to the 3'-end of the *KRAS* G-quadruplex driven through π - π stacking interactions. Biological assays also revealed a good photodynamic-induced cytotoxicity on HeLa cells.

Conclusions: The reported results show that these porphyrin-like compounds could actually give the basis for the development of G-quadruplex ligands with effective photodynamic-induced cytotoxicity on cancer cells.

General significance: The possibility of obtaining photosensitizers with improved physico-chemical features and able to selectively target G-quadruplexes is a very interesting perspective to develop new therapeutic agents.

© 2019 Elsevier B.V. All rights reserved.

1. Introduction

The structural polymorphism of DNA enables secondary arrangements, other than the canonical Watson-Crick base pairing, that bring biological information further to primary sequence. G-quadruplex (G4) structures are formed in guanine-rich sequences that self-assemble into (at least two) π – π stacking guanine tetrads stabilized by Hoogsteen hydrogen bonds and monovalent cations [1]. Spread throughout the human genome, G4s are in the spotlight as potential druggable anticancer targets since they are enriched within key functional units, like telomeres and oncogene promoters. The stabilization of G4s by small ligands hinders telomerase-catalyzed elongation of

telomeres and downregulates the expression of those genes whose promoter bears G4-forming sequences [2–5]. The G4-forming sequence from the *KRAS* oncogene P1 promoter stands out as a foremost example of potential anticancer G4 target, being responsible for most of the transcriptional activity [6]. *KRAS* maps at 12p12.1 (Gene ID: 3845) and encodes for a small GDP/GTP kinase (UniProt: P01116) whose point mutations account for the uncontrolled kinase activation [7]. The mutant *KRAS* triggers several downstream pathways pushing towards uncontrolled cell proliferation, e.g. the MAPK and P13 signaling. *KRAS* is found to be the most common mutated oncogene in several cancers, particularly in colon-rectal, pancreatic, and lung cancers [8–10]. To directly targeting *KRAS* has proved difficult because it is very hard to design molecules able to challenge the picomolar affinity between *KRAS* and GTP/GDP, although some small molecule inhibitors have been designed for an engineered *KRAS* mutant [11,12]. In the search for alternative strategies, the G4-forming stretch within the *KRAS* promoter turned out to be a promising target through G4 stabilization by organic ligands

* Corresponding authors.

E-mail addresses: jussara.amato@unina.it (J. Amato), giancola@unina.it (C. Giancola).

¹ These authors contributed equally to this work.

² Department of Food Science, Cornell University, Ithaca, 14853, NY, United States.

[13]. The first NMR structure of this G4 was only recently reported (the 22-mer sequence bearing the 16G>T substitution for stability purpose – PDB entry 5I2V), opening the way to rational ligand design [14,15].

Among the plethora of explored G4-binder classes, those featuring broad, planar aromatic macrocycle are the most rewarding because of hydrophobic, $\pi - \pi$ end-stacking with the outer G-tetrad planes of G4s. Porphyrin derivatives meet these requirements and TMPyP4 (5,10,15,20-tetrakis(*N*-methyl-4-pyridyl)porphyrin) (Fig. 1) distinguishes in the class as the first ever G4-binder used for targeting the G4s from both the prominent *KRAS* and *MYC* oncogene promoters [6,16]. Interestingly, a large body of data has shown that cationic porphyrins such as TMPyP3 and TMPyP4 also behave as photosensitizers, i.e. once irradiated with light they generate reactive oxygen species (ROS) that oxidize and degrade nucleic acids [17,18]. This happens in

particular at guanine, as the low ionization potential of this base makes it the major oxidation target in DNA/RNA sequences [19,20]. On this basis, an attractive molecular strategy to repress oncogenic *KRAS* in pancreatic cancer cells, by combining the photosensitizing property of the porphyrin scaffold and their affinity for G-rich sequences in G4 structures, was proposed [21]. However, TMPyP4 and many of its derivatives alike, suffer from inadequate G4 vs duplex selectivity [22,23]. Thus, synthesists are seeking to design derivatives with improved binding affinity and selectivity, mostly by adding flexible aliphatic side-chains bearing positive charges that may provide further stereoselectivity and additional interactions [24].

In this frame, we have synthesized and tested the binding properties of three porphyrin-like compounds (I-III, Figs. 1A and SI) towards the 22-mer G4-forming sequence (Fig. 1B) from the *KRAS* oncogene P1

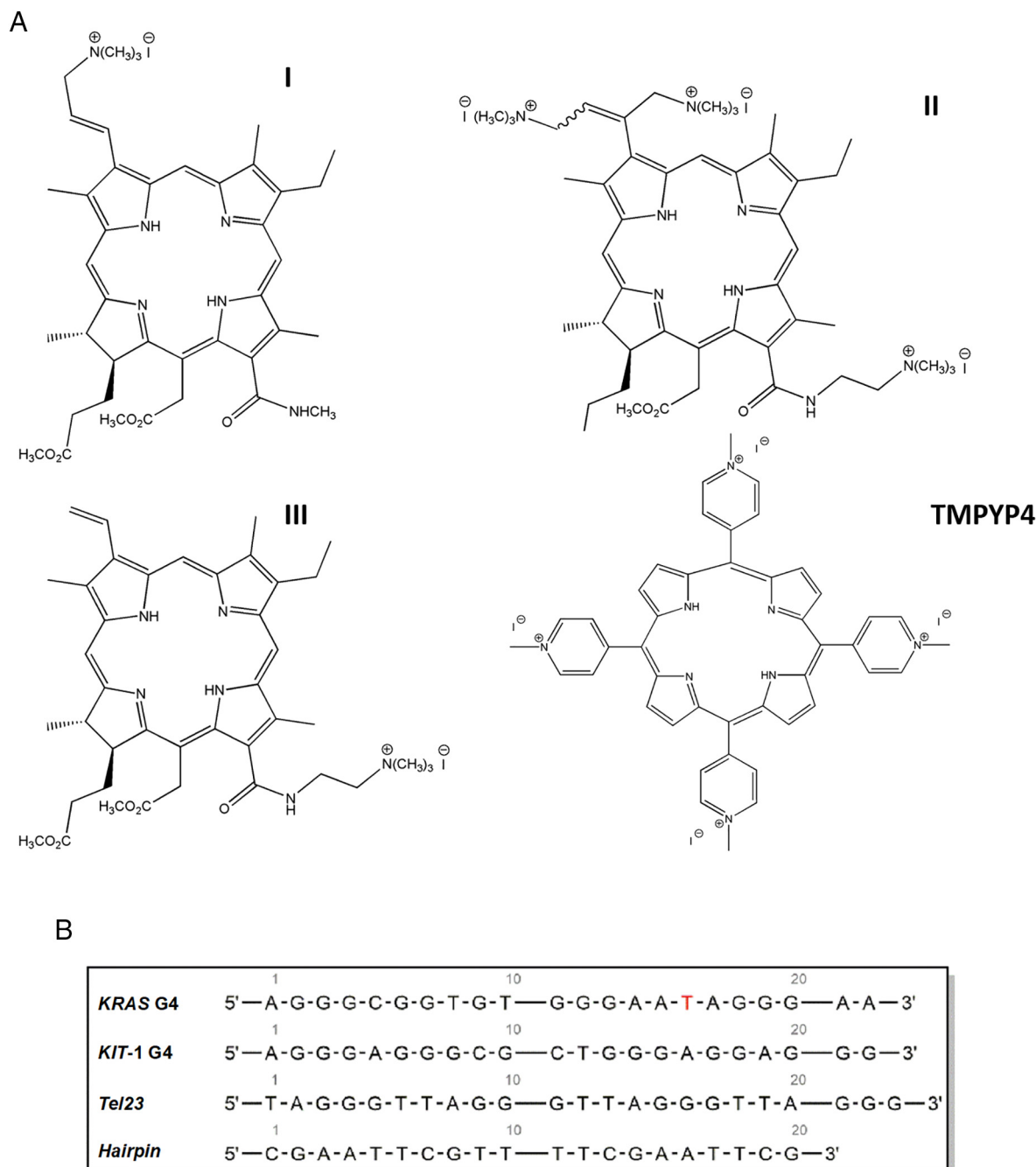


Fig. 1. (A) Chemical structure of the investigated ligands and of TMPyP4. (B) List of the investigated G4-forming sequences (*KRAS*, *KIT-1* and *Tel23*) and of the 20-mer hairpin-duplex DNA (*Hairpin*). Red-colored thymine in the *KRAS* G4 sequence represents the 16G > T substitution adopted to improve the overall G4 stability.

promoter (*KRAS* G4) by means of circular dichroism (CD) and fluorescence titration. The starting scaffold chlorin e_6 , is a chlorophyll *a* derivative with a partially reduced porphyrin-like tetrapyrrolic macrocycle that is active at nanomolar range, comparable to that of verteporfin and temoporfin: two well-known photosensitizers used in clinics [24]. However, like many other photosensitizers, chlorin e_6 and its ester derivatives are not very soluble in water, and this reduces the efficacy of the photodynamic therapy (PDT), a rapidly expanding therapeutic modality for treating a number of diseases, including cancer [24].

Herein, we synthesized three water-soluble, positively charged chlorin e_6 derivatives (**I–III**, Fig. 1), and analyzed their *KRAS* G4-binding properties, particularly focusing on their selectivity for G4 over duplex DNA, and on their ability to discriminate different G4 conformations. TMPyP4 was used as a reference for ligands performance. Molecular docking calculations were also performed to support wet-lab findings. Finally, the photosensitizing properties (singlet oxygen 1O_2) of synthesized compounds along with their ability to induce cytotoxic effects in HeLa cells, were also investigated.

2. Materials and methods

Oligonucleotides were purchased from *Biomers.net* GmbH (Ulm/Donau, Germany). All common chemicals, reagents and solvents were purchased from Sigma Aldrich (Merck group) unless otherwise stated. 1H NMR spectra were recorded on a Bruker Advance II spectrometer (300 MHz). $CDCl_3$ and $DMSO-d_6$ were used as appropriate solvents and TMS as internal standard for 1H NMR measurements. Mass spectra were obtained with a Thermo Finnigan LCQ Flut (ESI) instrument and a MALDI FAB MS-spectrometer AXIMA Confidence (Shimadzu) using α -cyano-4-hydroxycinnamic acid (CHCA) as matrix. UV-Vis spectra were obtained at 25 °C on a Drawell G9 spectrophotometer using highly diluted compound solutions (~10 μ mol).

2.1. General procedures for the synthesis of compounds **I–III**

I was obtained by chemical functionalization of *methylpheophorbide a* (**1**), following the procedure described in the Supplementary Material and according to the scheme reported in Fig. S1. The exocyclic opening in the *methylpheophorbide a* molecule with methylamine (**2**), and the aminomethylation of the vinyl group with the Eschenmoser salt (**3**), were performed on the first and second stage of functionalization, respectively. After purification by column chromatography on silica gel, **3** was reacted with methyl iodide to obtain the corresponding cationic form (**4**, also referred to as compound **I**). This was precipitated, washed with hexane and dried under vacuum at 77 °C for several days to obtain pure compound **I**. Compounds **1–3** and **I** were characterized by 1H NMR and MS analyses (Figs. S2–S9). Compounds **II** and **III** were synthesized according to the procedures described elsewhere [25].

2.2. Oligonucleotide purification and sample preparation

Synthetic oligonucleotides were purified by high performance liquid chromatography (HPLC) on a Nucleogel SAX column (Macherey–Nagel, 1000–8/46), using buffer A (20 mM KH_2PO_4/KH_2PO_4 , 20% (v/v) CH_3CN at pH 7.0), and buffer B (1 M KCl, 20 mM KH_2PO_4/KH_2PO_4 , 20% (v/v) CH_3CN at pH 7.0). A 30 min linear gradient from 100% A to 100% B with a 1 mL min^{-1} flow rate was used. The isolated oligomers were further desalted by Sep-pak cartridges C-18 (Waters) and lyophilized. DNA samples were then dissolved in 20 mM KH_2PO_4 buffer (pH 7.0) containing 60 mM KCl and 0.1 mM EDTA. The concentration of oligonucleotides was determined by UV adsorption at 90 °C, using molar extinction coefficient values ϵ ($\lambda = 260$ nm) calculated by the nearest neighbor model [26]. Samples were then annealed by heating the solution at 90 °C for 5 min, then gradually cooled to room temperature, and finally incubated for 24 h, at 4 °C before data acquisition.

2.3. Circular dichroism experiments

Circular dichroism (CD) experiments were performed on a Jasco J-815 spectropolarimeter equipped with a PTC-423S/15 Peltier temperature controller. CD spectra were recorded at 20 °C in the wavelength range of 220–300 nm and averaged over three scans. The following parameters were used: 100 $nm\ min^{-1}$ scan rate, 4 s response time and 1 nm bandwidth. Buffer baseline was subtracted from each spectrum. A 2 μ M oligonucleotide concentration was used. CD melting experiments were carried out in the 20–100 °C temperature range at 1 °C min^{-1} heating rate, following changes of CD signal at the wavelength of maximum intensity (263 nm for *KRAS* and *KIT-1* G4s, 288 nm for Tel_{23} G4, and 280 nm for hairpin-duplex DNA). The melting temperatures (T_m) were determined from curve fit using Origin 7.0 software. CD spectra and melting experiments were recorded both in the absence and presence of each ligand. DNA/ligand mixtures were obtained by adding 10 mol equiv. (20 μ M) of **I–III** to the folded DNA structures. TMPyP4 was used at 8:1 ligand/DNA ratio, since at higher ligand concentrations a turbidity of the relative solution occurred. The stock solutions of ligands were 10 mM in DMSO. ΔT_m values were determined as the difference in the melting temperature of the DNA structures with and without ligands. Each experiment was performed in duplicate and the reported values averaged.

2.4. Förster resonance energy transfer (FRET) melting assay

A FP-8300 spectrofluorometer (Jasco) equipped with a Peltier temperature controller accessory (Jasco PCT-818) was used to run FRET melting assays. Experiments were performed by using the G4 forming sequence F-*KRAS*-T, which has the donor FAM (6-carboxyfluorescein, F) and the acceptor TAMRA (6-carboxytetramethylrhodamine, T) fluorophores covalently attached. Labeled oligonucleotide was purchased from Biomers (Germany) and used without further purification. F-*KRAS*-T was prepared as a 1 μ M solution in 20 mM KH_2PO_4 buffer (pH 7.0) containing 60 mM KCl and 0.1 mM EDTA, then annealed by heating to 90 °C for 5 min and followed by cooling to R.T. overnight, and finally stored at 4 °C for 24 h before data acquisition. Measurements were performed exciting at 492 nm and detecting at 522 nm in a sealed quartz cuvette with a path length of 1 cm. Both slits were set at 5 nm. The final concentration of F-*KRAS*-T G4 was 0.2 μ M. Experiments were performed in the presence of compound **I** (2.0 μ M) without and with 2.0 or 10.0 μ M of the 20-mer hairpin duplex DNA (*Hairpin*) competitor. In addition, a blank with no compound or competitor was also analyzed. The fluorescence melting of F-*KRAS*-T G4 was monitored at 0.5 °C min^{-1} over the 10–100 °C range. FAM emission was normalized between 0 and 1. Data analysis was carried out using Origin 7.0 software.

2.5. Fluorescence titration experiments

Fluorescence experiments were performed at 20 °C on a Varian Cary Eclipse (Varian Inc., CA, USA) spectrofluorometer equipped with a Jasco PCT-818 Peltier (Jasco Inc., MA, USA) temperature controller accessory. A 1 cm path length, sealed quartz cuvette was used. Both excitation and emission slits were set at 5 nm. The titrations were carried out by stepwise addition (5 μ L) of a DNA solution (100 μ M) to a cell containing a fixed ligand concentration (2 μ M). Excitation wavelength was set at 504 nm and emission spectra were recorded in the wavelength range of 514–750 nm. After each addition of DNA, the solution was stirred and allowed to equilibrate for 5 min before data collection. The fraction of bound ligand (α) at each point of the titration was calculated following fluorescence changes at the maximum of intensity. Titration curves were obtained by plotting α as a function of the DNA concentration. The equilibrium binding constants (K_b) were estimated by fitting the resulting curves to an independent and equivalent binding site model [27]. The experiments were repeated in triplicate, and the results are presented as the mean \pm S.D.

2.6. Molecular docking

Molecular docking calculations were brought out using as target models the NMR structure of *KRAS* G4, and the X-ray structure of *KIT-1* G4 (PDB entries 5I2V and 3QXR, respectively). The 2D model of **I** was drawn using ChemDraw and the 3D coordinates were generated by the online SMILE Translator service. DockPrep tool from Chimera package was used for preparing the structures and the ligand, for Gasteiger partial charges assignment and polar hydrogens addition [28]. All torsions were set as rotatable. Box grids encompassing the whole G4s were defined and centered by AutoDock Tools (100 × 100 × 100 at 27.25, y = 27.37, z = 23.00 for *KRAS* G4; 70 × 70 × 70 at x = -4.50, y = 11.67, z = -11.09 for *KIT-1* G4). Ten AutoDock Vina 1.1.2 [29] runs for each model were performed by using random seeds, exhaustiveness 20, with each run returning 20 poses. The *KRAS* G4 underwent 500 conjugated gradient minimization steps prior docking.

2.7. Singlet oxygen quantum yield determination

The singlet oxygen ($^1\text{O}_2$) quantum yield (γ_Δ) of compounds **I–III** was determined as previously described [25,30]. Time-resolved photoluminescence of $^1\text{O}_2$ was measured at 1270 nm using the LIF-200 pulsed laser fluorimeter equipped with a nitrogen laser. A pulse frequency of 30 Hz, 20 μJ of energy and 2 ns impulse duration were used. The γ_Δ values were estimated both in pyridine and 1-octanol with a comparative method using *meso*-tetraphenylporphyrin as an appropriate standard [25]:

$$\gamma_\Delta/\gamma_{\Delta\text{st}} = I_0 \cdot D/I_{0\text{st}} \cdot D_{\text{st}} \quad (1)$$

where γ_Δ , I_0 , D and $\gamma_{\Delta\text{st}}$, $I_{0\text{st}}$, D_{st} were the quantum yield, the initial intensity of luminescence obtained from decay kinetics at $\tau = 0$, and the optical density of a solution of an appropriate photosensitizer and H_2TPP , respectively.

2.8. Biological assays

Toxicity of **I–III** towards tumor cell lines in the dark and under light irradiation was investigated using the HeLa cell model. HeLa cells were cultured at 37 °C in the DMEM/F12 growth medium (PAA Laboratories

GmbH, Cölbe, Austria) containing 10% v/v of fetal bovine serum (FBS) (HyClone, Logan, UT, USA) without antibiotics and under 5% CO_2 . All manipulations were similar to those described before [31]. Briefly, compounds **I–III** were dissolved in pure DMSO (Amresco, USA) and an appropriate amount of their stock solution was added to the growth medium containing 5000 cells for each plate, in order to reach final photosensitizer concentrations between 0.1 and 10 μM . Experiments to determine dark toxicity were run incubating the plates with HeLa cells for 72 h in the dark. For the analysis of light toxicity, cells incubated with the appropriate photosensitizer were exposed to red light for 20 min. A light diode panel emitting at $\lambda = 662 \pm 15$ nm and a total light dose of 12 J cm^{-2} were used. After irradiation, cells were incubated again for 70 h. Next, growth medium was removed, and cell culture washed with 200 μL of phosphate buffer solution (PBS). Immediately, 100 μL of a fluorescein diacetate solution (Sigma, USA) was added into each well and the plates were left inside the CO_2 incubator for 40 min. The relative number of living cells was determined by means of fluorescence intensity measurements using the “Fluorat-02-Panorama” spectrofluorometer (LTD “Lumex”, Russia) [31]. Excitation and emission wavelengths were set at 485 nm and 520 nm, respectively. Cell survival (%) was evaluated as ratio of the fluorescence intensity measured in the well containing the investigated compound with respect to the control well containing pure DMSO. All experiments were repeated 8–10 times.

3. Results and discussion

3.1. Circular dichroism experiments

Circular dichroism (CD) is a well-established method to study various aspects of G4s and of their interaction with ligands, like the presence and the overall topology adopted by a G4, and the capability of a ligand to induce a particular conformation [30]. CD is also a useful tool to investigate the thermal stability of G4s and the effect of a ligand on it.

Hence, CD was used for investigating the effects of **I–III** on the structure and thermal stability of the *KRAS* G4, as well as to check their selectivity towards other G4s and duplex DNA. TMPyP4 was also used for comparison. To check the proper folding of *KRAS* G4, its CD spectrum was recorded at 20 °C. A positive maximum at 263 nm and a negative minimum at 243 nm, which are diagnostic values of the parallel G4 topology, were observed (Fig. 2) [12]. Next, the potential of compounds **I–III** and TMPyP4 to alter the native folding topology of *KRAS* G4 was

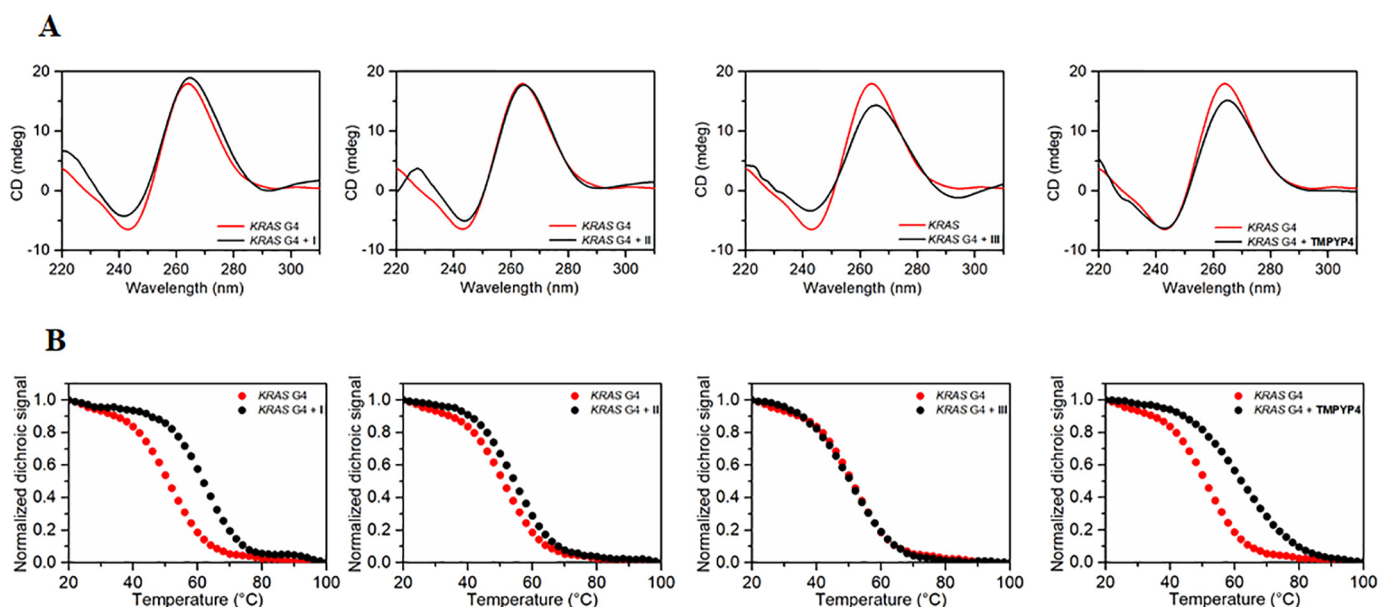


Fig. 2. (A) CD spectra and (B) CD melting profiles of *KRAS* G4 in the absence (red) and presence (black) of each ligand (10 mol equiv. of **I**, **II**, and **III**; 8 mol equiv. of TMPyP4).

Table 1
Ligand-induced thermal stabilization of *KRAS* G4 measured by CD melting experiments.

Ligand	ΔT_m (°C) ^a	
	<i>KRAS</i> G4 ^b	<i>Hairpin</i> ^b
I	+11	+1
II	+3	n.d. ^c
III	0	−21
TMPyP4	+11	n.d. ^c

^a ΔT_m values are the differences in the melting temperatures of DNA in the presence and absence of ligands. The error on ΔT_m is ± 1 °C.

^b The T_m values of *KRAS* G4 and *Hairpin* in the absence of ligand were 51.0 and 62.0 (± 0.5) °C, respectively.

^c Not determined.

analyzed. DNA/ligand mixtures were prepared by adding an excess of each ligand to the pre-folded G4 structure. No significant variations in the CD spectrum of *KRAS* G4 were observed upon addition of each ligand. The DNA-stabilizing properties of such compounds were hence evaluated by measuring the ligand-induced change in the melting temperature (ΔT_m) of *KRAS* G4 (Fig. 2). The results of these experiments are summarized in Table 1.

CD melting results show that, among the three investigated derivatives, **I** has the highest stabilizing effect on *KRAS* G4 with a ΔT_m of +11 °C. In order to compare the G4 stabilizing effect of compound **I** to that produced by TMPyP4, a CD melting experiment at 8:1 ligand/*KRAS* G4 ratio was performed, from which a ΔT_m of +10.5 °C was derived (Fig. S11). Interestingly, this value well matches with the one observed for TMPyP4 (Table 1), thus indicating a similar stabilizing effect for these two ligands.

On the other hand, compound **II** induced only a negligible thermal stabilization of *KRAS* G4 ($\Delta T_m = +3$ °C) despite the presence of three positive charges. Probably, the presence of such additional charges only contributes to establish unspecific electrostatic interactions with the outer phosphate backbone, preventing **II** to effectively bind to the G4 scaffold. Compound **III** proved to be ineffective in stabilizing *KRAS* G4 altogether. We speculate that the different position and geometry of the positively charged moiety affects, in this case, the possibility of forming the additional bonds required for the overall stabilization of the G4/ligand complex.

A 20-mer hairpin-duplex DNA consisting of two self-complementary 8-mer sequences connected by a TTTT loop (*Hairpin*, Fig. 1B), was also investigated. The CD spectrum of such hairpin is characterized by a positive band centered at ~280 nm and a negative one at 250 nm (Figs. 3A and S10), characteristic values of the duplex DNA. These bands were slightly shifted upon compound **I** addition. Conversely, compounds **II** and **III** induced significant changes to the CD band at 280 nm (Fig. S10). In particular, no effect was observed for **I** (Fig. 3B), while compound **II** was found to induce the unfolding of the duplex structure since the CD spectra of *Hairpin* in the presence of **II** at 20 and 100 °C were similar (Fig. S10), and **III** significantly destabilized *Hairpin* (Fig. S10 and Table 1).

Overall, these results indicate **I** to be comparable to TMPyP4 in stabilizing *KRAS* G4. However, unlike TMPyP4 that is known to indiscriminately bind to G4 and duplex DNA [17,32,33], **I** turned out to be selective.

A thorough characterization was then brought on solely for **I**, which was checked for its specificity towards other G4 structures. For this purpose, *KIT-1* and *Tel*₂₃ G4s were used as examples of parallel and antiparallel G4 conformations, respectively. First, CD spectra of these DNA sequences were recorded to verify their folding topologies (Fig. 3). The CD spectrum of *KIT-1* G4 showed a positive band at 260 nm and a negative one at 240 nm, in agreement with the formation of a parallel G4 conformation. On the other hand, *Tel*₂₃ displayed a positive band at around 290 nm with a shoulder at 270 nm, and a negative band at 240 nm, according to the formation of an antiparallel [3 + 1] hybrid G4.

As deducible from its relative CD signature, no significant conformational changes occur to *KIT-1* G4 upon addition of **I**. Conversely, **I** induced significant changes in the CD spectrum of the *Tel*₂₃ G4 structure, with the decrease of the band at 290 nm and the increase of the intensity of the band around 270 nm, thus suggesting a hybrid-to-parallel conformational change.

As far as thermal stabilization effects are concerned, **I** was found to stabilize *KIT-1* G4 to a smaller extent ($\Delta T_m = +5$ °C) than *KRAS* G4, while no effects were observed for *Tel*₂₃ G4. Interestingly, these results indicate the ability of **I** to discriminate among different G4 topologies, with a preference for the parallel conformations, and in particular for the *KRAS* G4 structure. This is also in agreement with the observed hybrid-to-parallel conformational change induced by **I** on *Tel*₂₃ G4.

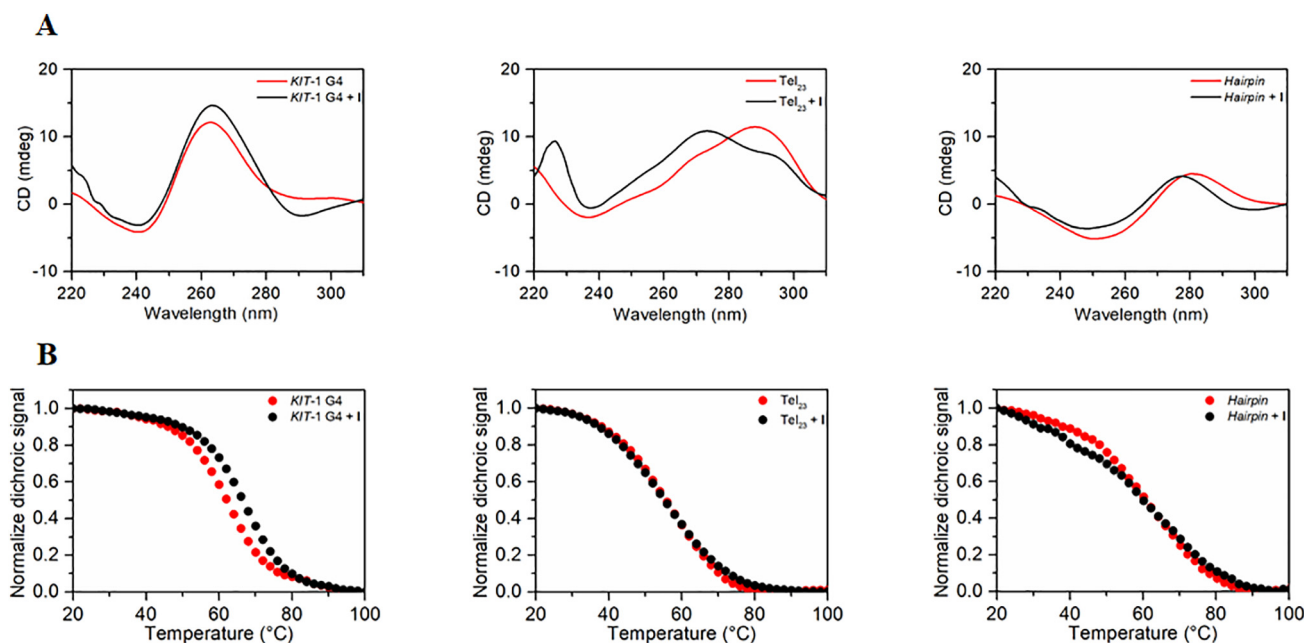


Fig. 3. (A) CD spectra and (B) CD melting profiles for *KIT-1* G4, *Tel*₂₃ and *Hairpin* in the absence and in the presence of **I** (10 mol equiv). The T_m values of *KIT-1* G4, *Tel*₂₃ G4, and *Hairpin* in the absence of ligand were 63.0, 56.2, and 62.0 (± 0.5) °C, respectively.

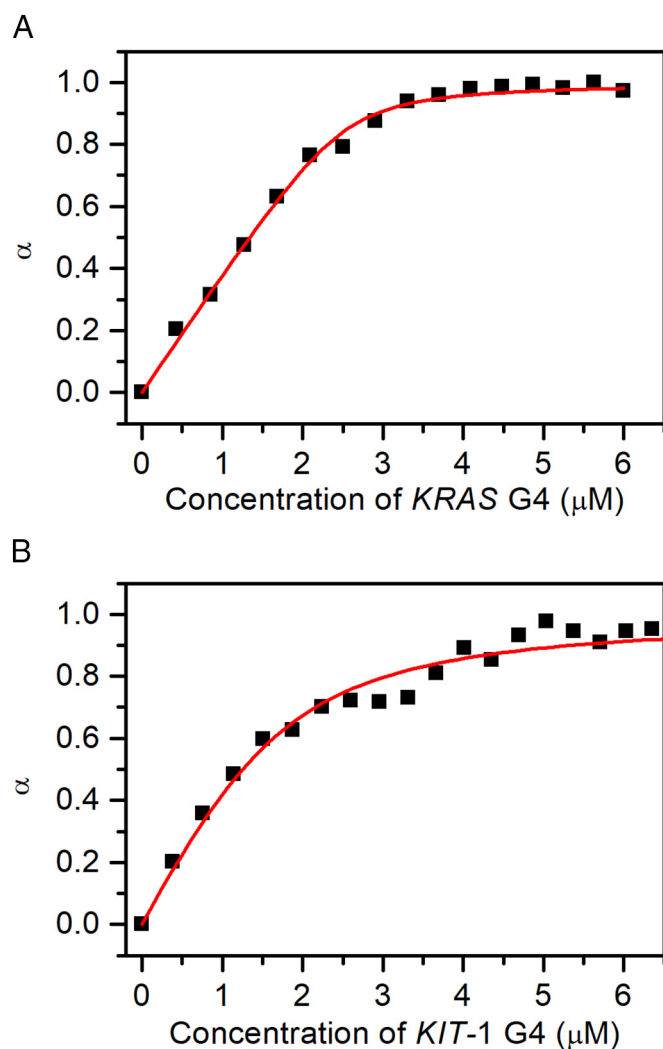


Fig. 4. Fluorescence titration curves obtained by plotting the fraction of bound I (α) as a function of (A) *KRAS* and (B) *KIT-1* G4 concentration. The experimental data (black squares) were fitted using an independent and equivalent-sites model (red lines).

3.2. Förster resonance energy transfer (FRET) melting assay

FRET melting analysis has been used to estimate the G4 over duplex selectivity of compound **I** and TMPyP4 [27]. The doubly-labeled F-*KRAS*-T G4-forming sequence was used. FRET experiments were performed both in the absence and presence of competing *Hairpin*. FRET-melting curves (Fig. S12) confirmed that both **I** and TMPyP4 are able to stabilize the F-*KRAS*-T G4 structure ($\Delta T_m > 15$ °C). Moreover, compound **I** showed a good degree of selectivity for the G4 over the duplex, with ΔT_m decreased by $0.7(\pm 0.6)$ °C in the presence of 10-fold excess of competing duplex (2 μ M) and of $1.7(\pm 1.0)$ °C at the level of a 50-fold excess of the duplex (10 μ M). Conversely, TMPyP4 showed less preference to bind to G4 compared to duplex DNA. Indeed, a strong decrease of T_m of the ligand-G4 complex was observed in the presence of competing duplex (Fig. S12).

3.3. Fluorescence binding experiments

Fluorescence titration experiments were carried out to quantify the ligand binding affinity for *KRAS* G4 and *KIT-1* G4. Fluorescence emission spectra of **I** in the absence and presence of increasing amount of G4s were recorded. Compound **I** has a fluorescence maximum at 668 nm when excited at 504 nm (Fig. S13). A decrease in fluorescence intensity

upon increasing DNA concentration was observed in both *KRAS* G4 and *KIT-1* G4 titrations. The binding constants were then determined from the variation of the fluorescence intensities. In particular, the binding curves were obtained by plotting the fraction of bound ligand (α) as a function of G4 concentration (Fig. 4), and binding constants (K_b) were obtained by curve fitting to an independent and equivalent binding sites model, by means of a nonlinear regression algorithm. The results of this interpolation analysis indicate in both cases a 1:1 ligand/DNA stoichiometry, and K_b values of $17.8 (\pm 4.4) \times 10^6$ and $1.9 (\pm 0.6) \times 10^6$

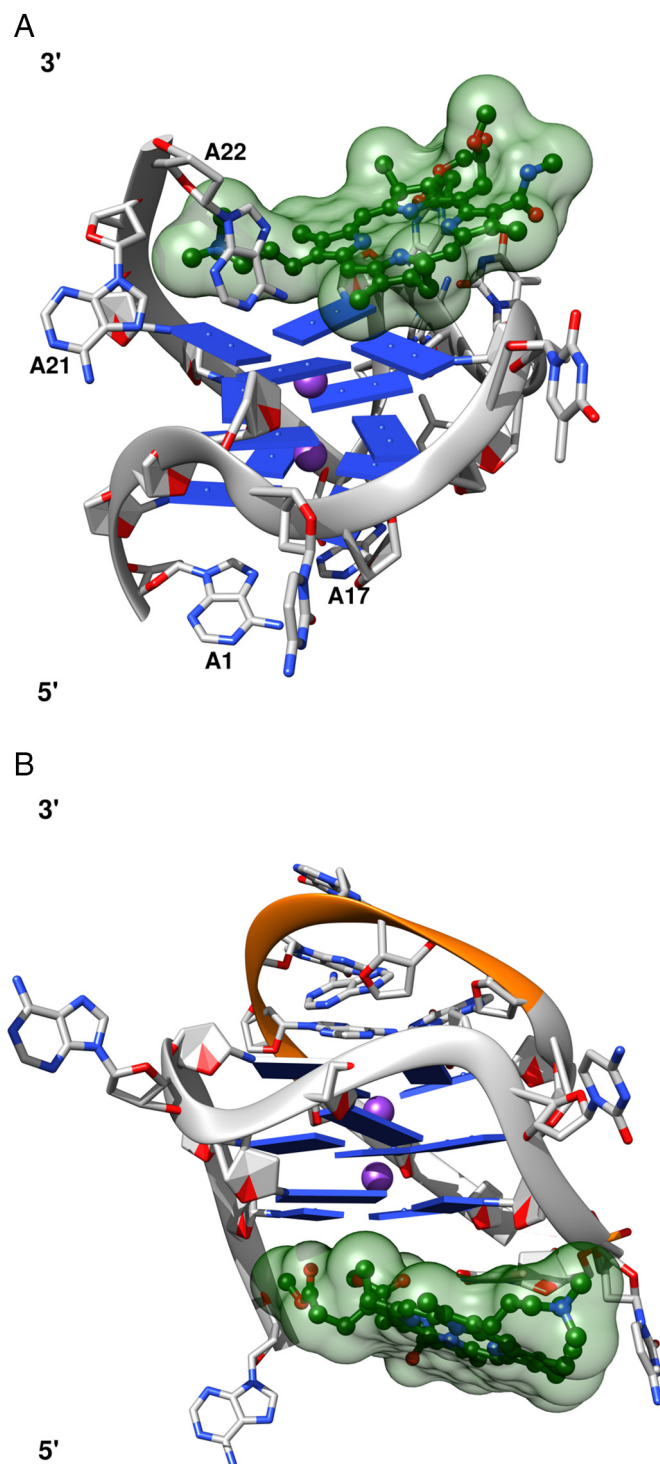


Fig. 5. Best scoring docking poses of **I** with *KRAS* G4 (-7.9 kcal mol $^{-1}$ - left) and *KIT-1* G4 (-8.2 kcal mol $^{-1}$ - right). Residues engaged in guanine-tetrads are represented and filled slabs. The *KIT-1* G4 loop hindering the 3' tetrad is highlighted in orange.

Table 2
Quantum yield of singlet oxygen 1O_2 for **I–III** in 1-octanol and pyridine.^a

Compound	Solvent	
	1-Octanol	Pyridine
I	0.66	0.62
II	0.53 ^b	0.59 ^b
III	0.65 ^b	0.56 ^b

^a Experimental errors are estimated to be within 10%.

^b These values were from [25].

M^{-1} for *KRAS* G4 and *KIT-1* G4, respectively, thus indicating a higher affinity of **I** for *KRAS* than *KIT-1* G4.

3.4. Binding mode by molecular docking

Molecular Docking calculation served to further evaluate the binding mode of **I** with either *KRAS* G4 or *KIT-1* G4, exploiting the recently deposited *KRAS* G4 NMR (PDB entry 5I2V) and the *KIT-1* G4 (PDB entry 3QXR) structures. Fig. 5 depicts the most energetically favored binding poses (-7.9 and -8.2 kcal mol⁻¹ for *KRAS* G4 and *KIT-1* G4, respectively). In both cases, docking models are consistent with the 1:1 stoichiometry found by fluorescence titrations, with the interaction widely driven by π - π end-stacking interactions, since the energetics of the poses on the opposite outer tetrad are severely unfavored (-5.6 kcal mol⁻¹ for *KRAS* G4, whereas no pose was found for *KIT-1* G4 – not shown). The 1:1 stoichiometry can be explained by the differences existing between the outer G4 planes. In the case of *KIT-1* G4, this is conceivably due to the hindrance to ligand interaction from the loop that crosses one of the planes. *KRAS* G4 does not feature such long, interfering loop, yet the outer G4 plane on the 5' side is less accessible to the solvent than its 3' counterpart because of hindrance from A1 and A17. A17 is “locked” by the stacking interactions it engages with the G4 plane below, whereas A1 is seemingly less restricted to move. Although A22 is sub-orthogonal to the 3' G4 plane with which it interacts by H-bond between N6 and O6 of either G4 or G20, this plane is still more accessible than its 5' counterpart. A22, and A21 alike, are therefore relatively free to flip and the ligand might compete for the G4 with ease. The binding face of *KIT-1* G4 has a similar condition with A1 and C12 stacking on the G4 plane. As in the case of *KRAS* G4, A1 is free to flip whereas C12 is stuck on the G4 plane. Anyhow, these inferences have to be taken carefully as conclusive given the intrinsic limitations of molecular docking and some concerns over the deposited 5I2V NMR structure (whose A21 and A22 appear in a very unstable arrangement). Furthermore, the system does not include any significant number of flanking bases as compared to the in-vivo system, whose behavior might sizably differ.

3.5. Generation of singlet oxygen

One of the most important properties of any photosensitizer is generation of singlet oxygen or other reactive oxygen species. The direct estimation of the quantum yield (γ_Δ) and lifetime of 1O_2 from compound **I** in pyridine and 1-octanol was performed by measuring the NIR luminescence emission of 1O_2 at around 1270 nm, which is considered as

the “gold standard” for PDT dosimetry. The corresponding γ_Δ values are listed in Table 2. The results obtained for compound **I** are in a good agreement with those of **II** and **III** reported by some of us in a previous study [25], and also fall within the range of γ_Δ values ($\gamma_\Delta = 0.55 \pm 0.1$) observed for any chlorophyll photosensitizer in any weakly polar solvent.

3.6. Photodynamic activity of compounds **I–III** in HeLa cells

The photodynamic activity of **I–III** in HeLa cell line was also evaluated. Results of such experiments, reported in Table 3, reveal several important features of these compounds. In particular, we observed no dark-toxicity for compound **II**. We speculate that **II**, having three cationic sidechains, may be not able to efficiently penetrate HeLa cell membranes, due to its high hydrophilicity. As for the other compounds, **I** showed a low dark-toxicity at 10 μM concentration, while **III** displayed a larger dark toxic effect towards cancer cells when used at 10 μM . On the other hand, by irradiating with red light, some damage towards cancer cells was observed with **II**, but its effect was small. Conversely, the mono-cationic compounds **I** and **III** displayed a good photodynamic effect providing the inactivation of 72 and 97% of tumor cells for **I** and **III**, respectively. The killing effect for **III** was larger, however, its dark-toxicity was also more pronounced. This may be ascribed to the unspecific binding of **III** to duplex DNA, with consequent off-target effects.

4. Conclusions

The discovery of photosensitizer molecules able to selectively interact with specific noncanonical DNA structures, like G4s, could represent an important strategy to enhance the effectiveness of the PDT treatment while preventing the toxicity effects due to off-target effects. G4-forming sequences are found in the promoter regions of many oncogenes where they are deeply involved in the regulation of their transcriptional activity and, therefore, in the development and progression of cancer. This notion is pushing towards the development of G4-targeting ligands as potential anticancer drugs. However, there are no approved anticancer drugs targeting such noncanonical DNA structures to date. This is at least in part due to the non-specific binding of most of G4 ligands to duplex and/or other DNA structures [34]. Moreover, all ligands bind to a target G4 reversibly, leading only to a transient effect on the expression of the respective oncogene [35]. In this context, the use of photosensitizers could represent an interesting approach to fight cancer by employing selective G4 binders that can irreversibly attack the target.

In this work, we have evaluated the interaction of three porphyrin-like photosensitizers with G4-forming DNA sequences. All three compounds were found to generate ROS in weakly polar media. Among them, compound **I** was shown to selectively stabilize G4 over duplex DNA and also displayed a marked preference for binding to parallel G4s (especially *KRAS* G4) over antiparallel ones. Indeed, CD experiments showed that **I** is a good *KRAS* G4 stabilizer that does not affect the pre-existing architecture of the target G4 upon interaction. For this reason, its binding to G4s was investigated in more detail. Fluorescence experiments provided the binding constant K_b of $17.8 \pm 0.5 \times 10^6 M^{-1}$ of **I** to the *KRAS* G4 and a 1:1 drug/DNA binding stoichiometry. Molecular

Table 3
Survival indexes for HeLa cells after treatment with compounds **I–III** (CPS, μM) in the dark and under irradiation with the light dose of 12 J cm⁻².^a

Compound	Dark toxicity			Photo-induced toxicity
	10 μM	1 μM	0.1 μM	1 μM
I	82.39 \pm 3.37	100.64 \pm 3.49	101.03 \pm 1.71	28.02 \pm 2.61
II	112.24 \pm 6.98	118.96 \pm 5.82	137.32 \pm 4.71	84.09 \pm 2.95
III	24.16 \pm 2.34	93.90 \pm 2.54	109.60 \pm 2.73	3.17 \pm 0.04

^a Survival index denotes the ratio between the number of living cells in the photosensitizer containing solution and the number of such cells in control, multiplied by 100. Uncertainties represent twice standard deviation.

docking results provided further insights into the recognition between **I** and the KRAS G4, highlighting the possible key structural elements involved in the interaction. Results of biological assays also revealed a strong enhancement of **I** activity on HeLa cells upon light exposure, providing the inactivation of around 72% of tumor cells.

Altogether, the reported results indicate that compound **I** could actually give the basis for the development of G4 ligands with effective photodynamic-induced cytotoxicity on cancer cells. The number and the position of cationic side chains can improve G4 ligand selectivity still preserving biological activity, to accomplish the desired result of achieving new potent but less toxic anticancer drug candidates.

Acknowledgements

This work was supported by the “Finanziamento della Ricerca di Ateneo 2016” from the University of Naples Federico II (prot. n. 0016505 to C.G.), and by Regione Campania-POR Campania FESR 2014/2020 (Project n. B61G18000470007).

Appendix A. Supplementary data

Supplementary data to this article can be found online at <https://doi.org/10.1016/j.ijbiomac.2019.12.152>.

References

- [1] M. Bochman, K. Paeschke, V. Zakian, DNA secondary structures: stability and function of G-quadruplex structures, *Nat. Rev. Genet.* 13 (11) (2012) 770–780.
- [2] S. Balasubramanian, L. Hurley, S. Neidle, Targeting G-quadruplexes in gene promoters: a novel anticancer strategy? *Nat. Rev. Drug Discov.* 10 (4) (2011) 261–275.
- [3] G. Biffi, D. Tannahill, J. McCafferty, S. Balasubramanian, Quantitative visualization of DNA G-quadruplex structures in human cells, *Nat. Chem.* 5 (3) (2013) 182–186.
- [4] A. Moye, K. Porter, S. Cohen, T. Phan, K. Zyner, N. Sasaki, G. Lovrecz, J. Beck, T. Bryan, Telomeric G-quadruplexes are a substrate and site of localization for human telomerase, *Nat. Commun.* 6 (2015).
- [5] P. Murat, S. Balasubramanian, Existence and consequences of G-quadruplex structures in DNA, *Curr. Opin. Genet. Dev.* 25 (2014) 22–29.
- [6] S. Cogoi, L.E. Xodo, G-quadruplex formation within the promoter of the KRAS proto-oncogene and its effect on transcription, *Nucleic Acids Res.* 34 (9) (2006) 2536–2549.
- [7] G. Hobbs, C. Der, K. Rossman, RAS isoforms and mutations in cancer at a glance, *J. Cell Sci.* 129 (7) (2016) 1287–1292.
- [8] R. Serra, M. Fang, S. Park, L. Hutchinson, M. Green, A KRAS-directed transcriptional silencing pathway that mediates the CpG island methylator phenotype, *Elife* 3 (2014).
- [9] M. di Magliano, C. Logsdon, Roles for KRAS in pancreatic tumor development and progression, *Gastroenterology* 144 (6) (2013) 1220–1229.
- [10] K. Haigis, KRAS alleles: the devil is in the detail, *Trends in Cancer* 3 (10) (2017) 686–697.
- [11] F. McCormick, KRAS as a therapeutic target, *Clin. Cancer Res.* 21 (8) (2015) 1797–1801.
- [12] Y. Zhang, M.H. Larraufie, L. Musavi, H. Akkiraju, L.M. Brown, B.R. Stockwell, Design of small molecules that compete with nucleotide binding to an engineered oncogenic KRAS allele, *Biochemistry* 57 (8) (2018) 1380–1389.
- [13] S. Cogoi, L. Xodo, G4DNA in ras genes and its potential in cancer therapy, *Biochimica Et Biophysica Acta-Genes Regulatory Mechanisms* 1859 (4) (2016) 663–674.
- [14] A. Kerkour, J. Marquieville, S. Ivashchenko, L. Yatsunyk, J. Mergny, G. Salgado, High-resolution three-dimensional NMR structure of the KRAS proto-oncogene promoter reveals key features of a G-quadruplex involved in transcriptional regulation, *J. Biol. Chem.* 292 (19) (2017) 8082–8091.
- [15] J. Marquieville, M. Kumar, J. Mergny, G. Salgado, H-1, C-13, and N-15 chemical shift assignments of a G-quadruplex forming sequence within the KRAS proto-oncogene promoter region, *Biomolecular Nmr Assignments* 12 (1) (2018) 123–127.
- [16] A. Siddiqui-Jain, C.L. Grand, D.J. Bearss, L.H. Hurley, Direct evidence for a G-quadruplex in a promoter region and its targeting with a small molecule to repress c-MYC transcription, *Proc. Natl. Acad. Sci. U. S. A.* 99 (18) (2002) 11593–11598.
- [17] J. Ren, J.B. Chaires, Sequence and structural selectivity of nucleic acid binding ligands, *Biochemistry* 38 (49) (1999) 16067–16075.
- [18] M.W. Freyer, R. Buscaglia, K. Kaplan, D. Cashman, L.H. Hurley, E.A. Lewis, Biophysical studies of the c-MYC NHE III1 promoter: model quadruplex interactions with a cationic porphyrin, *Biophys. J.* 92 (6) (2007) 2007–2015.
- [19] S. Tada-Oikawa, S. Oikawa, J. Hirayama, K. Hirakawa, S. Kawanishi, DNA damage and apoptosis induced by photosensitization of 5,10,15,20-tetrakis (N-methyl-4-pyridyl)-21H,23H-porphyrin via singlet oxygen generation, *Photochem. Photobiol.* 85 (6) (2009) 1391–1399.
- [20] Y. Margolin, J. Cloutier, V. Shafirovich, N. Geacintov, P. Dedon, Paradoxical hotspots for guanine oxidation by a chemical mediator of inflammation, *Nat. Chem. Biol.* 2 (7) (2006) 365–366.
- [21] M. Faudale, S. Cogoi, L.E. Xodo, Photoactivated cationic alkyl-substituted porphyrin binding to g4-RNA in the 5'-UTR of KRAS oncogene represses translation, *Chem Commun (Camb)* 48 (6) (2012) 874–876.
- [22] L. Martino, B. Pagano, I. Fotticchia, S. Neidle, C. Giancola, Shedding light on the interaction between TMPyP4 and human telomeric quadruplexes, *J. Phys. Chem. B* 113 (44) (2009) 14779–14786.
- [23] E. Boschi, S. Davis, S. Taylor, A. Butterworth, L.A. Chirayath, V. Purohit, L.K. Siegel, J. Buenaventura, A.H. Sheriff, R. Jin, R. Sheardy, L.A. Yatsunyk, M. Azam, Interaction of a cationic porphyrin and its metal derivatives with G-quadruplex DNA, *J. Phys. Chem. B* 120 (50) (2016) 12807–12819.
- [24] C. Romera, O. Bombarde, R. Bonnet, D. Gomez, P. Dumy, P. Calsou, J.F. Gwan, J.H. Lin, E. Defrancq, G. Pratiel, Improvement of porphyrins for G-quadruplex DNA targeting, *Biochimie* 93 (8) (2011) 1310–1317.
- [25] A. Kustov, D. Belykh, N. Smirnova, E. Venediktov, T. Kudayarova, S. Kruchin, I. Khudyaeva, D. Berezin, Synthesis and investigation of water-soluble chlorophyll pigments for antimicrobial photodynamic therapy, *Dyes Pigments* 149 (2018) 553–559.
- [26] C.R. Cantor, M.M. Warshaw, H. Shapiro, Oligonucleotide interactions. 3. Circular dichroism studies of the conformation of deoxyoligonucleotides, *Biopolymers* 9 (9) (1970) 1059–1077.
- [27] C. Giancola, B. Pagano, Energetics of ligand binding to G-quadruplexes, *Top. Curr. Chem.* 330 (2013) 211–242.
- [28] P.T. Lang, S.R. Brozell, S. Mukherjee, E.F. Pettersen, E.C. Meng, V. Thomas, R.C. Rizzo, D.A. Case, T.L. James, I.D. Kuntz, DOCK 6: combining techniques to model RNA-small molecule complexes, *RNA* 15 (6) (2009) 1219–1230.
- [29] O. Trott, A.J. Olson, AutoDock Vina: improving the speed and accuracy of docking with a new scoring function, efficient optimization, and multithreading, *J. Comput. Chem.* 31 (2) (2010) 455–461.
- [30] D. Berezin, D. Karimov, E. Venediktov, A. Kustov, V. Makarov, Y. Romanenko, The synthesis and singlet oxygen generation study of 13(1)-N-piperazinyl chlorin e6-15(2),17(3)-dimethyl ester, *Macrocyclics* 8 (4) (2015).
- [31] Y.I. Pylina, D.M. Shadrin, O.G. Shevchenko, O.M. Startseva, I.O. Velegzhaninov, D.V. Belykh, I.O. Velegzhaninov, Dark and photoinduced cytotoxic activity of the new chlorophyll-a derivatives with oligoethylene glycol substituents on the periphery of their macrocycles, *Int. J. Mol. Sci.* 18 (1) (2017).
- [32] H. Brito, A.C. Martins, J. Lavrado, E. Mendes, A.P. Francisco, S.A. Santos, S.A. Ohnmacht, N.S. Kim, C.M. Rodrigues, R. Moreira, S. Neidle, P.M. Borralho, A. Paulo, Targeting KRAS oncogene in colon cancer cells with 7-carboxylate indolo[3,2-b]quinoline tri-alkylamine derivatives, *PLoS One* 10 (5) (2015), e0126891.
- [33] M. Freyer, R. Buscaglia, K. Kaplan, D. Cashman, L. Hurley, E. Lewis, Biophysical studies of the c-MYC NHE III1 promoter: model quadruplex interactions with a cationic porphyrin, *Biophys. J.* 92 (6) (2007) 2007–2015.
- [34] A. Pagano, N. Iaccarino, M.A.S. Abdelhamid, D. Brancaccio, E.U. Garzarella, A. Di Porzio, E. Novellino, Z.A.E. Waller, B. Pagano, J. Amato, A. Randazzo, Common G-quadruplex binding agents found to interact with i-motif-forming DNA: unexpected multi-target-directed compounds, *Front Chem* 6 (2018) 281.
- [35] J. Amato, A. Pagano, D. Capasso, S. Di Gaetano, M. Giustiniano, E. Novellino, A. Randazzo, B. Pagano, Targeting the BCL2 gene promoter G-quadruplex with a new class of furopyridazinone-based molecules, *ChemMedChem* 13 (5) (2018) 406–410.